2013

A Prototype high resolution SiPM-based PET system for small volume imaging

Mitra Safavi-Naeini
University of Wollongong

A Prototype High Resolution SiPM-based PET System for Small Volume Imaging

A thesis submitted in fulfilment of the
requirements for the award of the degree

Doctor of Philosophy

from

THE UNIVERSITY OF WOLLONGONG

by

Mitra Safavi-Naeini
Bachelor of Engineering (Electrical)
University of Wollongong, 2005
Masters of Science (Medical Radiation Physics) with Distinction
University of Wollongong, 2006

CENTRE FOR MEDICAL RADIATION PHYSICS
2013

Abstract

Positron Emission Tomography (PET) is a molecular imaging technique which measures the distribution of positron-emitting radio-pharmaceuticals in a living subject by the detecting the γ-rays produced by positron-electron annihilations. Depending on the biological and chemical characteristics of the compound, many different functional processes within the living subject can be studied. Apart from the clinical applications of PET as a "routine imaging modality" in nuclear medicine, small-animal PET has become an important tool for preclinical studies, such as for the evaluation of new radiotracers and related therapies. The main requirements for small-animal PET are a uniform high spatial resolution, which is needed to resolve small structures in the reconstructed tracer distribution within the full field of view (FoV) and a high sensitivity, which allows the detection of small physiological changes and with the smallest levels of radiotracer uptake. The scintillator, detector, detector module, gantry, data acquisition systems and image analysis and reconstruction algorithms are all critical factors in the success of PET systems. In this Thesis, each of these aspects of system design are investigated, and an advanced low-cost small-animal PET system is designed and prototyped based on the results. The final imaging system, *Compact Millimetre Resolution Positron Emission Tomography* (CMRPET) is a high spatial resolution positron emission tomography (PET) scanner with full depth of interaction capability. Its pixellated scintillator and detector architecture allows the depth of interaction (DoI) of each 511 keV gamma ray event to be localised to a $3 \times 3 \times 3$ mm^3 scintillator voxel. The detector module configuration houses an edge-on 4×4 array of voxels, which ensures the high gamma ray detection sensitivity is not compromised. The incorporation of DoI in the design results in minimal degradation

of spatial resolution in the reconstructed PET image across the field of view (FoV) of the scanner. The average spatial resolution measured is 2.0 mm with a standard deviation of 0.3 mm, measured using a 1 mm diameter source placed at different radial displacements inside the FoV. The prototype was validated by comparing simulation results with experimental results.

Statement of Originality

This is to certify that the work described in this thesis is entirely my own, except where due reference is made in the text.

No work in this thesis has been submitted for a degree to any other university or institution.

Signed

Mitra Safavi-Naeini
Twelfth of August, 2013

Acknowledgments

First of all I would like to thank Professor Anatoly Rosenfeld and Dr. Michael Lerch for all of their support and guidance during my time as their student. Their wealth of scientific knowledge and advice has been indispensable during my doctoral research, and while they left me a lot of room, which I used to work on various topics, their gentle and kind "nudges" throughout the last couple of years were very much appreciated.

I am deeply grateful to Dr. Marco Petasecca for all his advice during the design and testing phase of the project, and later on during all those lengthy one-on-one conversations, trying to interpret the results. His guidance has helped me improve my problem solving techniques with troubleshooting electronics and running experiments. His knowledge of detectors and low noise electronics and his help with designing all custom made fixtures have been a great asset.

I would like to express my gratitude to Dr. Gareth Moorhead, Mr Robin Kirkham, Paul Dunn and Murray Jensen from the Manufacturing and Materials research group, CSIRO, for providing material support, technical advice and the extensive use of their laboratory.

The experimental part of this project would not have been possible without the generous assistance provided by Dr. Graeme O'Keefe and his team at the Centre for PET, Austin Health, Melbourne.

I am grateful to all other CMRP members, both staff and fellow students (postgrad-

uates in particular) for injecting the right amount of humour and excitement into our daily working days.

Last but not least, I would like to thank my husband, Dr. Daniel Franklin, for his help with all aspects of this project. This work would not have been possible without his unconditional support.

Dedication

To my family.

Contents

List of Figures

List of Tables

List of Abbreviations

3pl	3rd generation programming language
ADC	Analog to digital converter
ANSTO	Australian Nuclear Science and Technology Organisation
APD	Avalanche photodiode
ASIC	Application specific integrated circuit
BNL	Brookhaven National Laboratory
BGO	Bismuth germanate
CFoV	Centre, field of view
CMRP	Centre for Medical Radiation Physics
CMRPET	Compact Millimetre Resolution Positron Emission Tomography
CSIRO	Commonwealth scientific and industrial research organisation
CT	Computed tomography
DAC	Digital to analog converter
DoI	Depth of interaction
FBP	Filtered backprojection
FDG	Fludeoxyglucose
FET	Field effect transistor
FoV	Field of view
FPGA	Field-programmable gate array
FWHM	Full width at half maximum
HYMOD	Hybrid Modular Processor System
I2C	Inter-integrated circuit (bus)
JFET	Junction field effect transistor

LaBr	Lanthanum bromide
LSO	Lutetium oxyorthosilicate
LYSO	Lutetium yttrium oxyorthosilicate
MAC	Medium Access Control
MOSFET	Metal oxide semiconductor field effect transistor
MLEM	Maximum likelihood estimation method
MRI	Magnetic resonance imaging
NaI	Sodium iodide
OSEM	Ordered subset expectation maximisation
PD	Peak detector
PET	Positron emission tomography
PIN	P-intrinsic-N (diode)
PMT	Photomultiplier tube
RATCAP	Rat Conscious Animal PET
RoI	Region of interest
SiPM	Silicon photomultiplier
SPECT	Single photon emission computed tomography
SPI	Serial peripheral interface (bus)
TCP/IP	Transmission control protocol / Internet protocol
ToA	Time of Arrival
ToF	Time of Flight
ToT	Time over threshold
USB	Universal Serial Bus
VME	VERSAmodule eurocard

Chapter 1

Introduction

Röntgen's discovery of X-rays in 1895 created enormous excitement amongst scientists and started a flood of fundamental advances in physics, including the discovery of radioactivity, development of the modern understanding of atomic structure, special and general relativity, quantum mechanics and nuclear and particle physics. This event is famously recorded in the form of Röntgen's X-ray image of his wife's hand - the world's first "non-optical" image.

Over the next century, the range of available non-optical imaging systems has greatly expanded. One class of imaging modalities is particularly important in medical applications - namely emission-based imaging, in which tracer compounds labelled with positron-emitting radionuclides are injected into the subject of the study. These tracer compounds can then be used to quantitatively evaluate biochemical and physiological processes as they take place in the living organism. Emission-based imaging is used widely in both clinical and research in fields including oncology, neurology, cardiology and in the research and development of new pharmaceutical compounds. The earliest class of emission-based imaging is based on injecting a gamma-emitting radiopharmaceutical, the distribution of which is then imaged on a *gamma camera*. Subsequent developments provided the ability to obtain a three-dimensional distribution of radiopharmaceutical in the body, using tomographic techniques. The first of these methods to be developed was single photon emission computed tomography

(SPECT); this development was later followed by the introduction of positron emission tomography, in which the radiopharmaceutical must contain a positron-emitting isotope. Unlike SPECT, PET does not require the use of collimators in front of the detector, as each decay results in a pair of gamma photons with an energy of 511 keV being emitted in almost exactly opposite directions. Detection of a pair of simultaneous photons in the correct energy band indicates a very high probability that a positron decay occurred somewhere on the line joining the two detectors. More recent advancements include measuring the slight time difference between the detection of the photon pair to more precisely isolate the point of decay (time-of-flight PET).

PET and SPECT systems have traditionally utilised photomultiplier tubes (PMTs) coupled to discrete scintillators as the detection mechanism. PMTs provide high gain, but are bulky, fragile and highly susceptible to magnetic fields. More recent PET designs have sought to replace these detectors with a variety of solid-state photon detectors. This development has occurred in parallel with advances in scintillator technology, with new scintillator materials offering good sensitivity to 511 keV photons, with very high light output and short decay times. The current trend in PET, therefore, is to use these newer scintillators in conjunction with advanced solid-state detectors.

Like all other imaging systems, high sensitivity and uniform high spatial resolution across the entire field of view (FoV) are of utmost importance to PET. For PET systems optimised for small volumes, such as those used for PET mammography [13] and preclinical studies of small animals [14–17], the field of view may span almost the entire width of the detector ring. However, as the subject is moved closer to the detector ring, the problem of parallax error increases. This results in a significant degradation in spatial resolution near the periphery of the field of view. Current systems lack the ability to measure the depth of interaction (DoI) very precisely, and therefore must compensate for the known degradation in the spatial resolution by increasing the diameter of the ring, in order to maintain uniformity across the FoV.

However, increasing the ring diameter deceases the sensitivity of the scanner due to the smaller photon acceptance angle of photons emitted from the region of interest (RoI) of the object. As such, higher radiotracer activities must be injected or longer scanning times are required.

Parallax error and hence the resolution non-uniformity can be minimised if an accurate estimate of the DoI is available. The addition of DoI measurement capabilities also permits a larger crystal volume to be used, increasing the probability of photon detection and hence improving system sensitivity. Alternatively, a smaller ring radius with DoI capabilities can achieve the same FoV as a traditional larger-diameter non-DoI scanner, with a corresponding reduction in the required number of detectors and associated timing, signal routing and signal processing challenges. Additionally, improved detection efficiency results in an increased signal-to-noise ratio (SNR), resulting in more accurate visual detection of lesions, more accurate imaging of areas with lower amounts of radiotracer uptake, a potential reduction in imaging time, and/or the use of a lower-activity radiotracer, reducing the diagnostic dose received by the patient.

1.1 Objectives, Overview and Summary of Contributions of this Thesis

The fundamental objective of this Thesis is to develop a prototype of a compact, dedicated positron emission tomography system that provides a uniform high spatial resolution across its whole field of view through the use of DoI information. Given that the impact of parallax error is more significant close to the edge of the field of view, the resulting system is of particular interest to small volume imaging applications where the FoV approaches or equals the ring diameter.

The scintillator, detector, detector module, gantry, data acquisition systems and image analysis and reconstruction algorithms are all critical factors in the success of PET systems. In this Thesis, each of these aspects of system design are investi-

gated, and an advanced low-cost small-animal PET system is designed and prototyped based on the results. The final imaging system, *Compact Millimetre Resolution Positron Emission Tomography* (CMRPET) is a high spatial resolution positron emission tomography (PET) scanner with full depth of interaction capability. Its pixellated scintillator and detector architecture allows the depth of interaction (DoI) of each 511 keV gamma ray event to be localised to a $3 \times 3 \times 3$ mm^3 scintillator voxel. The detector module configuration houses an edge-on 4×4 array of voxels, which ensures the high gamma ray detection sensitivity is not compromised. The incorporation of DoI in the design results in minimal degradation of spatial resolution in the reconstructed PET image across the field of view (FoV) of the scanner. The average spatial resolution measured is 2.0 mm with a standard deviation of 0.3 mm, measured using a 1 mm diameter source placed at different radial displacements inside the FoV. The prototype was validated by comparing simulation results with experimental results.

The Thesis is divided into the following chapters:

- Chapter 2 presents a comprehensive review of relevant literature;
- Chapter 3 presents a range of different detector characterisation methods;
- Chapters 4, 5 and 6 present detailed characterisation of a variety of different silicon detectors. This work resulted in the following publications:

  M. Safavi-Naeini, M. Lerch, M. Petasecca, G. Pignatel, M. Reinhard, and A. Rosenfeld, "Evaluation of pixellated, back-sided planar photodetectors for high-resolution imaging instrumentation," *Nuclear Instruments and Methods in Physics Research Section A: Accelerators, Spectrometers, Detectors and Associated Equipment*, vol. 589, no. 2, pp. 259–267, 2008.

  M. Safavi-Naeini, D. Franklin, M. Lerch, M. Petasecca, G. Pignatel, M. Reinhard, G.-F. Betta, N. Zorzi, and A. Rosenfeld, "Evaluation of Silicon Detectors With Integrated JFET for Biomedical Applications," *Nuclear Science, IEEE Transactions on*, vol. 56, no. 3, pp. 1051–1055, Jun. 2009.

M. . Safavi-Naeini, G. Deeley, D. Franklin, M. Lerch, G. P. M. Petasecca, M. Reinhard, and A. Rosenfeld, "TCAD and IBIC charge collection modelling of a novel Silicon detector for use in medical imaging," *Nuclear Instruments and Methods in Physics Research Section A: Accelerators, Spectrometers, Detectors and Associated Equipment*, vol. 624, no. 1, pp. 73–77, Dec 2010.

M. Safavi-Naeini, D. R. Franklin, M. L. F. Lerch, M. Petasecca, G. U. Pignatel, M. Reinhard, R. Siegele, and A. B. Rosenfeld, "IBIC Characterisation of Novel Silicon Detectors for Imaging Applications," in *Nuclear Science Symposium Conference Record (NSS/MIC), 2008 IEEE*, Nov 2008, pp. 63–67.

- Chapter 7 discusses the design and development of a new small-volume PET system based on silicon photomultipliers, LYSO detectors and an advanced nuclear pulse processing and data acquisition system. Spectral and timing characterisation measurements for the key system components are presented. Detailed simulation studies are performed using GEANT4 Application for Tomographic Emission (GATE) with simulated point sources and phantoms, demonstrating the validity of the design. This work resulted in the following publication:

  M. Safavi-Naeini, D. Franklin, M. Petasecca, M. Lerch, R. Kirkham, G. Moorhead, P. Dunn, G. De Geronimo, and A. Rosenfeld, "SiPM based Detector Module and Digital Data Acquisition System for PET: Initial results," in *Nucl Sci Symp Conf Rec (NSS/MIC)*. IEEE, Nov 2009, pp. 2679–2682.

  M. Safavi-Naeini, D. R. Franklin, M. Petasecca, M. L. F. Lerch, and A. B. Rosenfeld, "Comparison of Correction Methods for Random Coincidence in CMRPET," *Nuclear Instruments and Methods in Physics Research Section A: Accelerators, Spectrometers, Detectors and Associated Equipment*, 2013 (submitted).

- Chapter 8 presents experimental results obtained using a prototype small-animal PET system based on the design and simulation studies in Chapter 7. Experiments using both point sources and a small ultra micro Jaszczak phantom are

performed, replicating the configurations studied in simulation. This work resulted in the following publications:

M. Safavi-Naeini, D. R. Franklin, M. Lerch, M. Petasecca, G. Moorhead, R. Kirkham, P. Dunn, G. O'Keefe, G. Degeronimo, and A. B. Rosenfeld, "Preclinical Studies Using a Prototype High-Resolution PET System with Depth of Interaction," in *Nuclear Science Symposium Conference Record (NSS/MIC), 2011 IEEE*, Nov 2011.

M. Safavi-Naeini, D. R. Franklin, M. Petasecca, M. L. F. Lerch, R. Kirkham, G. Moorhead, P. Dunn, G. D. Geronimo, and A. B. Rosenfeld, "Prototype High-Resolution PET System with DoI," *Journal of Instrumentation*, 2013 (submitted)

- Chapter 9 details remaining research challenges and potential future work related to this project.

1.2 Funding Support

This work is supported by the Australian National Health and Medical Research Council (NHMRC) under Development Grant 162722, entitled "A new positron emission tomograph detection system with improved image quality capabilities", which is a collaboration between the University of Wollongong's Centre for Medical Radiation Physics (lead investigator Prof Anatoly Rosenfeld), University of Melbourne (Prof Geoffrey Taylor), University of Sydney (Prof Steve Meikle) and St George Cancer Care Centre (Prof Barry Allen).

Chapter 2

Literature Review

This Chapter presents a comprehensive review of literature related to modern PET systems. Section 2.1 provides a brief history and overview of PET imaging. Section 2.2 discusses two of the key elements of PET systems: scintillators and photon detectors, with a particular focus on solid-state silicon-based detectors. Section 2.3 discusses the problem of determining the depth of photon interaction in PET systems, which has a significant effect on image resolution near the periphery of the field of view, and describes several solutions. Section 2.4 examines methods of data acquisition in PET systems, in which precise timing and noise minimisation are extremely important considerations. Section 2.5 compares and contrasts several complete clinical and preclinical PET systems optimised for small volume imaging. Finally, Section 2.6 summarises the key findings and the implications for the system to be developed in this Thesis.

2.1 Nuclear Medical Imaging

Nuclear medical imaging refers to a family of techniques for imaging organs and processes in the body by detecting particles emitted by biologically active radioactive tracer material administered to the patient. Nuclear medical imaging is distinct from other families of medical imaging such as ultrasound, X-ray computed tomography or magnetic resonance imaging, in which external ultrasonic, X-ray or electro-

magnetic energy sources are used to image tissues via absorption, reflection or other mechanisms. The emitted radiation is recorded and analysed, resulting in an image showing the distribution of radiotracer uptake. This image may be used for diagnostic purposes, or aid in development of new treatment methods and pharmaceuticals. The earliest types of nuclear imaging were based around a two-dimensional gamma camera; more sophisticated techniques such as SPECT and PET employ tomographic methods to provide high-resolution three dimensional images with high contrast and minimal imaging artefacts.

The main advantage of nuclear imaging over other radiological imaging techniques is that nuclear imaging can visualise *biochemical processes* taking place in the organ of interest (by tagging biochemically active tracers with an appropriate radionuclide), rather than simply showing structure and/or movement. Recent advancements in multi-modal imaging combine both techniques to provide biochemical and physiological information with great anatomical accuracy.

Positron Emission Tomography (PET) is a widely used medical imaging technique used in both clinical and preclinical applications for the study and diagnosis of different diseases. It is widely used in cancer diagnostics and assessing neurological diseases such as Alzheimer's and Parkinson's diseases and is increasingly employed to assist in radiotherapy planning and chemotherapy monitoring.

2.1.1 Positron Emission Tomography

A typical PET system is illustrated in Figure 2.1. The radiopharmaceutical emits positrons, which travel a short distance in the body before colliding with an electron and annihilating, converting all of the mass of both particles into energy in the form of a pair of 511 keV gamma photons travelling in opposite directions along the so-called *Line of Response* (LoR). If both of these photons interact with photon detectors, the event is registered as *coincident* [1]. Coincidence detection is the core concept of PET imaging, as it allows annihilation photons to be differentiated from other gamma radiation, allowing the point of annihilation to be isolated to somewhere along the

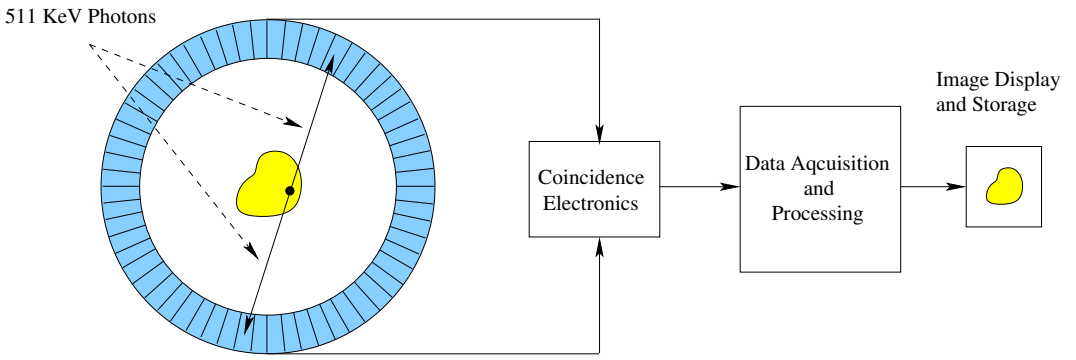

Figure 2.1 Diagram of PET imaging system [1]

LoR without the need for collimation (as is needed in SPECT). If the difference in time of arrival between a pair of coincident photons can be measured, the point of annihilation can be further isolated to a small region along the LoR. A complete three dimensional image can be constructed from coincidence events recorded from a series of detector rings (both within a single ring and between multiple rings).

While detection of positron annihilation requires the determination of whether two detected photons are truly simultaneous (a *true coincidence*), there are inevitably a certain number of *random* or *chance* coincidences which occur when photons from two independent annihilations are detected within a short interval. Additionally, when one or both photons from a single annihilation event are scattered prior to their detection, the event is called a *scatter* coincidence (Figure 2.2). In both cases, the two photons will be detected (if at all) within the coincidence interval (and so termed a *prompt* event), however the measured LoR is misplaced. The effect in the reconstructed image is a reduction in image contrast [18]. The *prompt rate* (true events plus scatter/random coincidences) is a linear function of the source activity in the patient. However, the rate of random events is proportional to the *square* of activity, hence these *randoms* become increasingly dominant with increased radiopharmaceutical activity [19].

Positrons emitted by the radionuclide travel a short distance from their source before annihilating with electrons in the surrounding tissue. The range of the positron

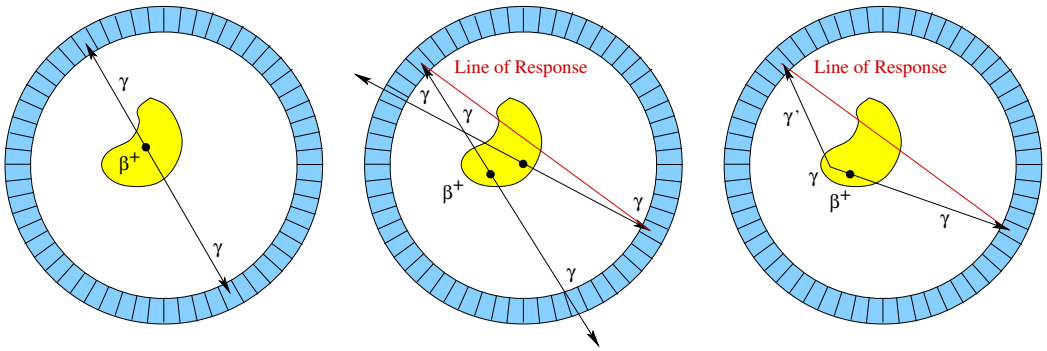

(a) True coincidence (b) Random Coincidence (c) Scatter Coincidence

Figure 2.2 True coincidences compared with randoms and scatter coincidences. The lines of response are acollinear with the actual location of positron annihilation.

depends upon its initial energy and the electron density of the matter, and is typically 1-2 mm in most animal tissue for a ^{18}F radionuclide [20]. This distance is the ultimate limitation on the spatial resolution for a PET imaging system [21]. It is worth noting that the positron range distribution are not well described by Gaussian functions, and thus FWHM is not the best indicator of effect of positron range on the spatial resolution. It is more accurate to use the *effective range*, defined as the perpendicular distance from the decaying radionuclide to the line defined by the two 511 keV annihilation photons. The most commonly used radionuclides, the energy of their emitted positrons and the effective range of the emitted positrons in water are listed in Table 2.1 [9, 22].

The small residual momentum of positrons at the end of their range results is another factor which affects the resolution of the system. The annihilating photons travel with an angle that is not quite 180°, with a semi-Gaussian angular distribution and a Full Width at Half Maximum (FWHM) value of approximately 0.5°. The resulting degradation of the spatial resolution is called the acollinearity, and is given by the following relation [5]:

Table 2.1
Numerical data for the radioisotopes most commonly used in PET. Electrons and positrons do not move along a straight line in matter because of the high number of interactions with small energy exchange; therefore their path length is always longer than their range.

Isotope	Half-life (min)	Average kinetic energy (MeV)	Maximum kinetic energy (MeV)	Mean effective range in water (mm)
^{11}C	20.4	0.385	0.960	1.7
^{13}N	10.0	0.491	1.198	2.0
^{15}O	2.0	0.735	1.732	2.7
^{18}F	109.8	0.242	0.633	1.4
^{68}Ge	68.3	0.783	1.880	1.7

$$R_{180^\circ} = 0.0022 \times D \tag{2.1}$$

where D is the diameter of the detector ring.

While PET systems based on direct detection of the annihilation photons by detectors have been proposed, it is difficult to directly detect the annihilation photons, as they do not strongly interact with most practical photon-detection device materials (such as silicon). By employing a suitable high effective-Z *scintillator* material, some or all of the gamma photon's energy can be absorbed (through photoelectric or Compton interaction), and its energy re-radiated as a shower of photons at longer wavelengths, allowing a much greater fraction of the energy to be absorbed and hence registered by the photodetector. A variety of materials can be used for the purposes of scintillation; these are discussed in detail in Section 2.2.1. The scintillator can be divided into small, optically isolated segments, each of which is optically coupled to a single pixel of a photodetection device, or a large slab of scintillator material can be shared between multiple pixels, with the point of interaction estimated from the recorded light distribution.

System sensitivity is one of the most important factors determining the performance of PET systems. Reduction of the ring diameter leads to an increase in the count rate,

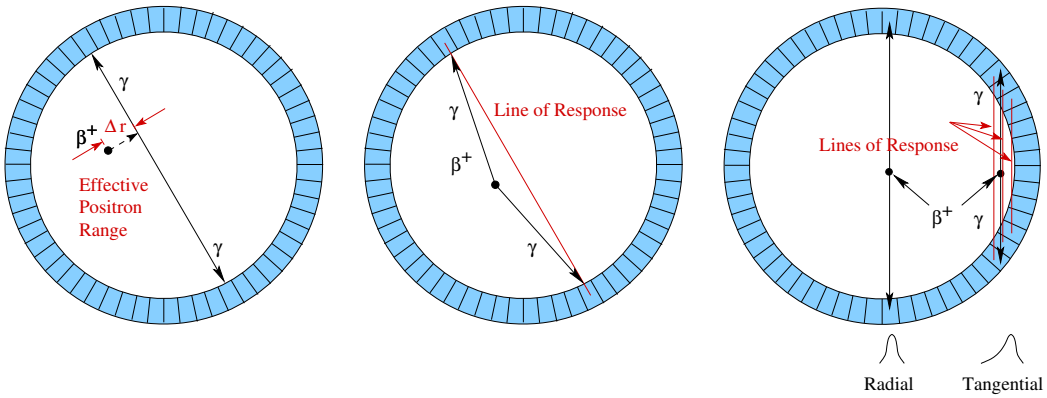

(a) Effective Range (b) Acolinearity (c) Parallax Error

Figure 2.3 The factors degrading the spatial resolution of a PET system.

and so is an increasingly popular strategy for PET systems designed to image small animals. However, as the proximity of the detector ring to the subject increases, and the field of view (FoV) becomes a larger fraction of the detector ring size, an artefact known as parallax error begins to seriously degrade the spatial resolution towards the outer part of the image. Also known as radial astigmatism or radial elongation, it is a result of the uncertainty in determining the depth of interaction (DoI) of the γ rays with the scintillator crystal, since near the edge of the FoV a gamma ray may penetrate more than one crystal segment [1]. The distance travelled by the gamma photons in the crystal prior to interaction is unknown, and it is unlikely that the point of interaction is exactly at the centre of mass or the point of entry into the crystal. This uncertainty grows as the source position moves radially outward from the centre of the scanner. The parallax effect is the limiting factor in reduction of the ring diameter [23, 24].

Figure 2.3 illustrates these three principal resolution degrading factors.

A number of approaches are available for increasing the rate of coincidence detection in a PET imaging system [1]:

- Administration of larger dose of radiopharmaceutical (i.e. an increase in isotope activity);

- Improvement of the efficiency of scintillator/detectors;
- Using more of the deposited energy spectrum; and
- Increasing the solid angle of detection.

An increase in the isotope activity is not a practical approach, since the radiopharmaceutical is administrated solely for diagnostic reasons, and it is essential to use the minimal practical dose. A limit of around 350-750 kBq (≈10-20 mCi) is employed by most PET imaging systems, although in the case of three-dimensional imaging the count-rate limitations of the system requires an activity of less than about 350 kBq (≈10 mCi) [1].

Increasing Z and the thickness of the scinitllator will improve the efficiency of 511 keV photon detection. The maximum detection efficiency of the 511 keV photons in commercial systems is 90% (or 81% coincidence efficiency), which is achieved by increasing the thickness of the scintillator crystal. Although this is an effective mechanism for increasing the detection efficiency, a thicker (deeper) scintillator will result in increased parallax error unless a mechanism is employed to measure the depth of interaction within the crystal.

Sensitivity may be increased somewhat by accepting a wider range of photon energies; however, the result is a higher rate of non-annihilation randoms and Compton-scattered photons being incorrectly detected and classified as true coincidence events. This degrades contrast and adds additional noise to the reconstructed image.

Perhaps the most practical method for increasing the rate of coincidence detection in PET systems is increasing the solid angle of PET systems by utilising scintillators whose segments are separated by smaller gaps and increasing the number of rings in the axial direction. However, there is a corresponding increase in fraction of scattered events counted amongst the true coincidences.

2.2 Detector Technology

2.2.1 Scintillators

Since the 1950s, various organic and inorganic scintillators have been used in detection of γ photons [1]. The scintillation process is based on the interaction of γ photons with matter, resulting in the generation of lower-energy photons (*scintillation photons*), which are more easily detected through the following interaction mechanisms:

- The photoelectric process, where the incident photon transfers all its energy to a bound electron and is completely absorbed;
- The Compton effect, in which the photon transfers a fraction of its energy to an electron and is re-radiated; the scattered photon and the electron share the energy of the incident photon; and
- Pair production, which occurs when the incident photon energy exceeds twice the rest mass energy of the electron: an electron/positron pair appears in place of the incident photon.

Of these, the first two interactions result in the deposition of a fraction of all of the γ photon energy within the scintillator. The deposition can occur in a single location via the photoelectric effect, or at several points within the same scintillator segment by successive Compton interactions, or in adjacent pixels in a pixellated scintillator array. Pair production is most likely to result in a further annihilation, which emits additional 511 keV gamma photons from the scintillator itself resulting in added noise and a reduction of the contrast of the energy spectrum; it is only relevant where the radiopharmaceutical has a decay mode involving the emission of very high-energy gamma rays (greater than 1.022 MeV), and is not possible with a pure positron emitter. Therefore, pair production is not normally a significant factor in PET systems.

Table 2.2 Properties of selected scintillator materials [1, 9–12].

Material	Density (g/cm^3)	Effective atomic number Z_{eff}	λ of maximum emission (nm)	Principal Decay Constant (ns)	Total Light Yield (photons/MeV)	Hygroscopic
NaI:Tl	3.67	51	415	230	37700	Yes
CsI:Tl	4.51	52	550	900	66000	Slightly
$Bi_4Ge_3O_{12}$ (BGO)	7.13	76	505	300	8200	No
Lu_2SiO_5:Ce (LSO)	7.40	65	420	40	30000	No
Gd_2SiO_5:Ce (GSO)	6.7	59	440	60	8000	No
$Lu_{1.8}O_2SiO_3$:Ce (LGSO)	6.5	59	420	40	23000	No
$Lu_{1.8}Y_{0.2}SiO_5$:Ce (LYSO)	7.1-7.3	65	420	41	27000-34000	No
$LuAlO_3$:Ce (LuAP)	8.3	64.9	365	18	12000	No
$YAlO_3$:Ce (YAP)	5.5	33.5	350	30	17000	No
$LaBr_3$:Ce (LaBr)	5.29	47	358	35	61000	Very

Each type of scintillator material has different characteristics which affect its suitability for different applications. For PET applications, some of the important characteristics include: good detection efficiency, high density (ρ) and effective atomic number (Z_{eff}), fast rise time and decay time, good energy resolution, emission wavelength, mechanical and hygroscopic properties, cost, and commercial availability [9, 25]. Self absorption of the scintillation photons by the scintillator is undesirable, and therefore the scintillator thickness must be less than the attenuation length of the 511 γ photons. The amplitude of the electronic signal produced in the detector is proportional to the number of absorbed scintillation photons, and hence to the energy deposited within the crystal. Since both photoelectric and Compton cross-sections are a function of the density (ρ) and the effective atomic number (Z_{eff}) of the crystal, scintillator material with a higher $\rho \times Z_{eff}$ is capable of a higher intrinsic efficiency and is the preferred option [1].

The main characteristics of the most common scintillator materials used in PET applications are summarised in Table 2.2.

[1]The atomic cross-section for photoelectric effect is proportional to $\frac{\rho \times Z_{eff}^n}{E_\gamma^m}$, where n and m are both function of the energy: n is gradually increases from 4 at 100 keV to 4.6 at 3 MeV and m decreases slowly from 3 at 100 keV to 1 at 5 MeV. The cross-section for Compton scattering is proportional to $\frac{\rho \times Z_{eff}}{A}$, where A is the mass atomic number. Z_{eff}/A is almost constant, at 0.45±0.05, for all elements except hydrogen [3, 9, 25]

Although LaBr, CsI and NaI produce the highest light output per MeV of incident radiation (amongst those listed in Table 2.2), their comparatively low $\rho \times Z_{eff}$ means that the rate of photoelectric interactions is relatively low, requiring a physically large crystal to achieve high detection efficiency. Additionally, they are hygroscopic, requiring careful handling to avoid damage by absorption of atmospheric moisture [1, 9, 26].

Daghighian et al. undertook a thorough evaluation of BGO and LSO scintillators compared to the baseline NaI(Tl) scintillator in 1993 [27], shortly after its discovery in the early 1990s by Melcher et al. [28]. The performance of LSO was found to be outstanding: coincidence timing and energy resolution was found to be of the order of two to three times superior to BGO. Despite the advantages of LSO, most PET systems of the mid-to-late 1990s used BGO, due to its high density (and hence detection efficiency), lower costs, and high availability. However, many more recent systems now use LSO due to its shorter decay time and superior light output. Since one of the isotopes of lutetium (^{176}Lu, which constitutes about 2.6% of natural lutetium [1]) in LSO is itself radioactive(simultaneously emitting a β particle at 420 keV and three gamma photons at 88, 202 and 307 keV [29]), it contributes a certain level of background radiation to the energy spectrum even when no external source is present. This background is not significant in comparison to count levels from the injected radiopharmaceutical [26].

Raylman et al. have investigated the performance of three scintillators for possible use in Positron Emission Mamography (PEM), a dedicated PET imaging system with a need for high spatial resolution and small Field of View (FoV) [2]: NaI(Tl), gadolinium oxyorthosilicate (GSO), and lutetium-gadolinium oxyorthosilicate (LGSO) [30]. In order to achieve compact physical construction, it is necessary to compromise between thickness, density, and the composition of scintillating crystals in order to efficiently stop high energy photons and cover the maximum solid angle [31]. The PEM systems consisted of two 30×30 arrays of pixelated scintillators ($3 \times 3 \times 10$ mm^3 for

[2]The system is very similar to the dedicated PET systems used in animal studies, detailed in Section 2.5.

GSO and LGSO and $3 \times 3 \times 19$ mm^3 for NaI(Tl)) coupled to arrays of square position-sensitive photomultiplier tubes. The scintillators were ranked based on their Compton scatter fractions, energy resolution, spatial resolution and detection efficiency. It was found that while there is minimal variation in the Compton scatter fractions (8%-9%), the NaI(Tl) system produced had the best system energy resolution (18.2%) and the GSO system the worst (28.7%), while the LGSO system offered the best mean spatial resolution (3.19 ± 0.04 mm for horizontal profiles and 3.20 ± 0.03 mm for vertical profiles) and delivered the best detection sensitivity (646.9 c/s/kBq/ml). By imaging a breast phantom containing various sized spheres, Raylman et al. demonstrate that the LGSO system detected the largest number of small spheres, and the NaI(Tl) system had the worst detectability [30].

Research interest in sub-millimetre resolution PET system combined with renewed interest in development of Time of Flight (ToF) PET has resulted in much of the recent work on scintillators for gamma-ray detection being focused on Ce or Pr doped lutetium based scintillators and lanthanum halides [25, 32–34].

Weber et al. compared the emission spectra, energy resolution and the light output of a LuYAP scintillator with LSO and BGO crystals to evaluate their potential for use in high resolution PET systems [33]. It was found that at room temperature, LSO has the highest light yield, followed by LuYAP and BGO, with energy resolutions of 15% (LSO), 20% (LuYAP) and 27.4% (BGO). It was found that the light yield of LSO is superior to all other tested scintillators [33].

Conti et al. performed a detailed evaluation of the intrinsic properties of these materials (namely LSO:Ce, LuAG:Pr, LuYAP:Ce, $LaBr_3$:Ce and $LaCl_3$:Ce) which have a direct effect on the timing resolution and thus the image quality of the system [25]. It was concluded that the the high density and high Z_{eff} of lutetium compounds made them more suitable than lanthanum halides for use in conventional PET. The relatively low light output of LuAG:Pr (9300 photons/MeV) and its slow decay component (594 ns) reduces the amount of light available for fast timing and is therefore unsuitable for high count rate applications [25]. $LaBr_3$ has optimal timing and bright-

ness characteristics, but its low density (5.1 g/cm^3) can be overcome only by using thicker detectors, which implies higher costs and depth-of-interaction problems.

Therefore, amongst the scintillator materials listed in Table 2.2, those based on lutetium-based are the materials of choice in PET applications due to their high density, fast decay and light production, in spite of the recent developments of bright, fast but relatively low density lanthanum bromide scintillators.

2.2.2 Radiation Detectors

Moses et al. have described the characteristics of a good photon detector for PET systems (ranked from most important to least important) [35]:

- High detector efficiency (higher than 85%);
- High spatial resolution (4 mm FWHM or better for clinical PET, with the goal of reaching sub-millimetre spatial resolution); and
- Timing resolution better than than 5 ns FWHM for conventional PET and better than 200 ps FWHM for ToF PET.

Since the optical pulse emitted from the scintillator crystal has a very limited number of photons and is of very brief duration, it is essential that the device used to convert this optical signal into an electrical signal is fast, has high quantum efficiency, and adds a minimum of self-generated noise. Ideally, it would also provide some internal gain, to ease the task of external electronics in amplifying the signal. The main alternatives for PET photodetectors include:

- Photomultiplier Tube (PMT);
- P-intrinsic-N (PIN) photodiode;
- Avalanche photodiode (APD); and

- Silicon Photomultipler (SiPM).

Photomultipler tubes work on the principle of converting the scintillation light into a very weak pico-ampere electrical signal at the photocathode, which is then amplified through an efficient low noise avalanche cascade process [1, 3]. A series of dynodes (electrodes) create a voltage gradient inside a vacuum tube, accelerating the electrons released from the photocathode, releasing more electrons upon contact from each dynode. This process repeats until the initial current pulse is amplified to the desired extent [3, 9].

While PMTs are still one of the most popular types of photodetectors used in emission tomography due to their reliability and high gain (of the order of $10^6 - 10^7$) and despite continued progress in photomultiplier tube technology, their performance is limited by their poor quantum efficiency (approximately 25%) and high sensitivity to even weak magnetic fields (including that of the Earth). They are also costly, bulky (resulting in a low packing factor), fragile and require a series of increasingly large positive bias potentials for successive dynodes [1, 9, 36]. These factors are particularly problematic in compact PET systems, such as those intended for small animal imaging, and where PET is to be combined with MRI imaging (which requires extremely powerful magnetic fields).

With availability of compact semiconductor radiation detectors in recent years, new design options have become available which offer superior spatial resolution, high detection efficiency, low power consumption and low cost. These advantages are particularly valuable for high-resolution small-volume PET imaging systems, such as those used for imaging small animals or for Positron Emission Mammography (PEM), where semiconductor detectors are now the preferred choice.

When compared to PMTs, semiconductor detectors have the following advantages:

- Monolithic fabrication allows the production of high-density planar detector arrays for high resolution applications;

- Insensitivity to magnetic fields;
- Large active area; and
- Quantum efficiency of up to 90% at wavelengths emitted by common scintillators.

In semiconductor photodetectors, incident light is converted to an electrical charge signal by generation of electron-hole pairs in the substrate [3]. The energy required for this process is greater than the band gap in semiconductors (the minimum energy of a detectable photon in silicon is 3.55 eV, while the bandgap is only 1.12 eV) [37, 38].

Silicon semiconductor diodes are normally fabricated by implanting or diffusing a thin positively doped (p-type) silicon layer on top of a negatively doped (n-type) silicon substrate [3, 37]. A reverse-biased $p - n$ junction has a highly resistive, positively charged depleted layer (in the case of n-type silicon) with a linearly decreasing electric field towards bulk silicon [2]. This region is almost devoid of mobile charge carriers and can be widened by applying an increasing reverse bias potential.

When exposed to photons or charged particles, electron-hole pairs are created within the depletion layer and immediately separated and swept out of the region by the electrical field, generating a pulse of electrical charge. The small amplitude of these charge pulses are the main drawback of silicon photodiode detectors, and necessitates further amplification via charge sensitive preamplifiers [39]. Other semiconductor detectors, such as APDs and SiPMs, can provide a large amount of internal charge gain, but require larger bias voltages and suffer from temperature stability problems.

For silicon, the penetration depth of optical photons with a wavelength of 420 nm is approximately 0.13 μm at a temperature of 300 K. In general, two main cut-off wavelengths are of particular interest: the upper cut-off wavelength, which is determined by the bandgap energy, and the short wavelength cut-off, caused by the very high absorption coefficient at short wavelengths, since the photons that are absorbed too

close to the surface do not contribute to the output signal [1,37]. This latter point is a motivation for the production of photodiodes with a shallow $p-n$ junction, leading to enhanced efficiency at blue light wavelengths typical for scintilltors of interest.

Although not the only option for semiconductor detectors, silicon has a number of properties which make it especially desirable as a detector material:

- Low ionisation energy (good signal);
- Long mean free path (good charge collection efficiency);
- High charge carrier mobility (fast charge collection);
- Low Z_{eff} (low multiple scattering);
- Very well developed technology and fabrication processes; and
- Low cost.

2.2.3 Silicon Detectors for PET Application

2.2.3.1 PIN Diodes

The simplest type of semiconductor detector is the p-intrinsic-n (PIN) diode. PIN diodes differ from a conventional $p-n$ junction in that there is a thick layer of undoped (intrinsic semiconducting) silicon separating the p-type and n-type layers. This results in the formation of a thick depletion layer in which large numbers of electron-hole pairs can be generated under conditions of reasonably low reverse bias potential.

Figure 2.4 shows a reverse-biased PIN diode, where its positively-doped side (p-side) is connected to the negative supply rail, and its negatively-doped side (n-side) is connected to the positive rail. The reverse-bias condition enhances the thickness of the depletion layer, since the thickness is proportional to the square root of the applied reverse-bias voltage and inversely proportional to the square root of the doping

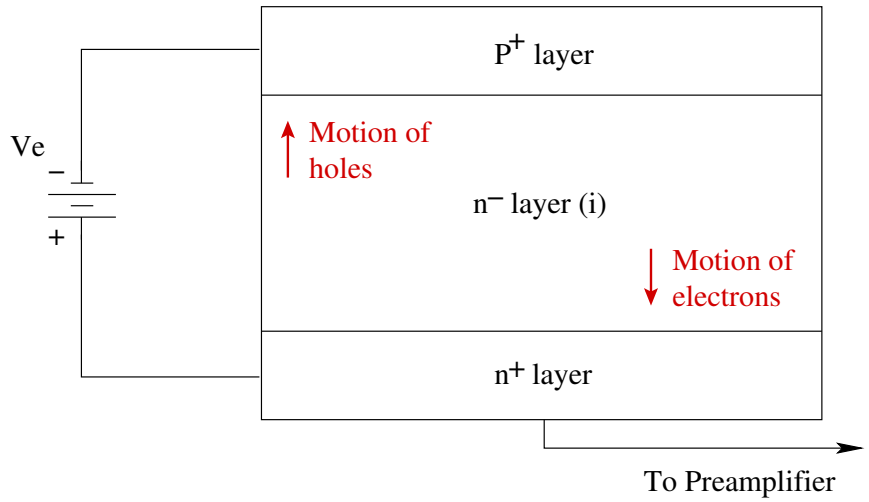

Figure 2.4 Schematic diagram showing a PIN diode [1, 2].

concentration [8, 37]. The junction behaviour can be modelled as a capacitor, with capacitance

$$C = \frac{\epsilon A}{d} \propto \frac{1}{\sqrt{V_e}} \tag{2.2}$$

where A is the area of the detector and V_e is the bias voltage. Since the radiation-induced electron-hole pairs are produced in this region, the quantum efficiency of the detector is increased when it is heavily reverse biased. The maximum possible reverse-bias voltage is limited by the diode breakdown voltage [1, 2, 37].

The PIN diode structure has the advantage of temperature stability, but has unity charge gain in comparison to the high intrinsic gain of PMTs, avalanche photodiodes (which are discussed in Section 2.2.3.2) and SiPMs [9, 40]. The signal to noise ratio (SNR) of PIN diodes is relatively poor in comparison to PMTs, APDs and SiPMs, however their structure allows for convenient integration of monolithic front-end transistors to improve their gain [8]. The poor SNR limits the energy resolution of PIN diode detectors, which may present a problem for their application in detecting photons in PET systems, especially those dedicated to small animal imaging.

A PET detector module based on a monolithic planar array of PIN diodes, a BGO scintillator and a photomultiplier tube has been developed by Moses et al. [40, 41]. In this detector design, the photosensitive area of an 8×8 array of silicon PIN diodes is attached to the front face of an 8×8 BGO scintillator crystal block, while the back side of the block is attached to a conventional PMT. The PMT is used for timing and energy spectrum measurements, while the PIN diode array is used to identify the scintillator element with which the gamma ray has interacted. The relative strength of the signals observed by the PIN diodes and the PMT allows the depth of interaction (DoI) to be estimated.

Moses discusses the noise characterisation procedure performed on a single BGO crystal segment coupled to a PIN diode and amplifier, and develops a model based on these measurements which relates detector noise, capacitance and dark current. The results were extrapolated to an array of 4, 36 and 64 segments using a Monte Carlo simulation technique. It was found that when the FWHM of the noise is below about 40% of the RMS value (approximately 300 e^-) of the 511 keV response, the rate of misdetection (incorrect pixel identification) remained constant (although non-zero due to Compton scattering); above this threshold the rates of misdetection progressively increased. Since a true interaction results in the generation of around 700 e^-, the minimum signal-to-noise ratio (SNR) for optimal detection is 2.33 (7.36 dB). The best accuracy for correct event position detection under these conditions was found to be about 82%.

The simulation results were experimentally validated by irradiating a 2×2 array of 3 mm$\times$3 mm crystal segments with a gamma-ray beam (electronically collimated with approximately 2 mm beam width) directed at the outer corner of one of four crystal segments). Coincidences were detected determined by arranging a single BGO crystal with optically coupled PMT immediately opposite the collimated source, and observing the response in each of the four crystals when coincident photons with energy greater than 250 keV were detected. The location accuracy of the test rig was found to be exactly 82%, which was in agreement with the simulation

results.

Once the minimum SNR for optimal detection accuracy was determined, the actual integrated amplifier could be fabricated. The reverse side of the silicon substrate upon which the PIN diodes are fabricated was also used to fabricate the charge-sensitive preamplifier components as well as circuits for calibration and readout, significantly reducing the need for external electronics. As an independent amplifier is required for each PIN diode, there is a tight constraint on the area of silicon available for each amplifier unit.

Testing of the completed detector/amplifier assemblies showed that the amplifiers had a noise floor of between 127 and 220 e^- for corresponding peaking times ranging from 4 to 0.5 μs [41], which gave an SNR significantly in excess of the minimum required for successful operation. Test measurements were performed using a single BGO crystal optically coupled to a single single PIN diode. The amplifier/detector modules were also characterised for capacitance and dark current.

A number of early devices achieved high quantum efficiency by using backside illumination. Holland et al. developed a silicon photodiode based on a high-energy physics detector with a very thin n^+ polysilicon layer on the backside coated with an anti-reflective indium-tin-oxide (ITO) layer [42, 43]. This combination achieves high carrier mobility, low resistivity and high optical transmittance properties, which are further improved by annealing at the relatively low temperature of 200 °C. Noise is minimised due to the low device capacitance resulting from a relatively thick substrate (300 μm) and low resistivity of the aluminium frontside and ITO backside contacts. Holland's device achieved quantum efficiencies of around 75% for LSO (450 nm) and 90% for BGO scintillators (480 nm).

Patt et al. have employed an alternative design to achieve low detector noise, based on a modified backside-illuminated X-ray silicon drift photodetector (SDP) [44]. SDPs are a specific type of planar PIN device exhibiting extremely low capacitance (of the order of 60 fF) but which suffer from a relatively large carrier drift time (of the

order of 230 μs). By choosing low-resistivity materials and modifying the structure and biasing of the SDP to produce a large uniform electric field, it is possible to reduce the drift time by an order of magnitude. This type of SDP is compatible with the response time of LSO scintillators, making it a potentially useful device for high-energy gamma imaging applications. The quantum efficiency realised by this detector was reported to be of the order of 40% at 460 nm, however this was without the benefit of an antireflective coating which should provide further performance improvements (up to around 70%) [44].

2.2.3.2 Avalanche Photodiodes

A promising alternative to PIN diodes and photomultiplier tubes is the avalanche photodiode (APD). APDs are reverse-biased at a voltage several volts above their breakdown voltage ($V_{breakdown}$). Breakdown is rapidly triggered after interaction with a photon, after which the reverse-bias current increases rapidly and is sustained until the reverse-bias voltage is reduced to below the breakdown voltage [3]. This effect is achieved by the creation of a region with a very strong electric field (as shown in Figure 2.5). Photoelectric interactions with the absorption layer release charge, which triggers an effective charge multiplication via avalanche breakdown upon reaching the high-field area.

APDs offer considerably higher gain in comparison to PIN diodes (typically around 1000; gain is a function of the bias voltage, compared to unity gain for the PIN diode) resulting in a high SNR and a faster response relative to PMTs and PIN detectors. However, they are sensitive to temperature, and require a high operating voltage (although not as high as PMTs) [9,38]. Maximum gain for an APD is achieved when operating in so-called Geiger mode (where a voltage in excess of the breakdown voltage is applied, and the current avalanche is rapidly quenched (as with a Geiger-Müller tube) to prevent damage to the device). This mode of operation is highly non-linear, however it does offer considerably more gain than when operating in linear mode.

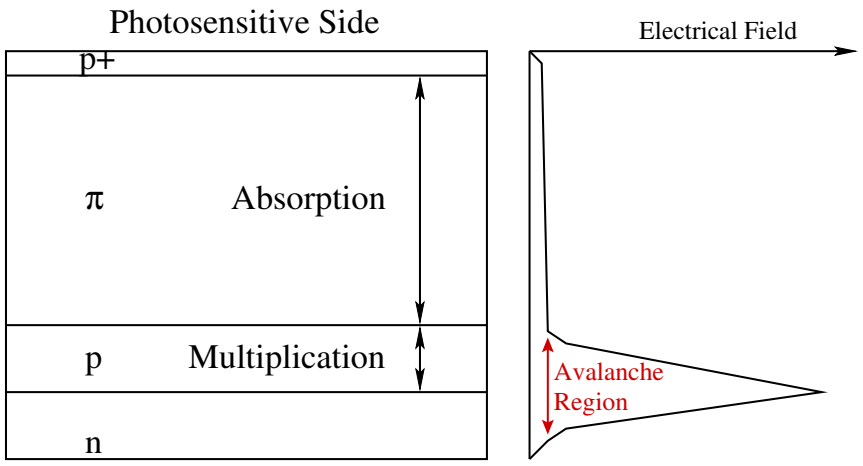

Figure 2.5 Structure of an Avalanche Photodiode (APD). A graph showing electric field strength versus depth is also shown. [1, 3, 4].

Sciacca et al. discuss the issues in designing single-photon APD detectors [45]. The authors detail one of the most important aspects of APD circuit design: the quenching circuit, since this controls both the dead-time of the circuit and its sensitivity to secondary random events (due to incomplete release of trapped charge during the initial avalanche). Quenching may be passive (in which a resistor serves to quench the APD) or active (in which the current is automatically switched off by a FET).

Techniques for minimising the dark count rate (which results from thermal carrier generation), including careful doping of the photosensitive layers, must be utilised to reduce the internal noise of the detector. As a result of avalanche amplification, APDs have a large Excess Noise Factor (ENF) which grows with the gain. Voltage and temperature sensitivities of device gain also grow with as gain increases. Therefore, special care needs to be taken when operating APDs with a gain factor of more than a few hundred.

Several APD based detector modules for use in PET scanners have been proposed. Bérard et al. have developed an APD detector module (LabPET II) with sub-millimetre spatial resolution [46] based on two monolithic APD arrays of 4×8 pixels, each with an active area of 1.1×1.1 mm^2 coupled to an 8×8 LYSO scintillator array [46]. Tim-

ing, energy and spatial resolution (at the centre of the field of view) were measured to be 5.0±0.2 ns, 27.5±2.1% and 0.73 mm respectively. The poor energy resolution is due to optical cross talk, mismatched scintillator geometry which prevented piping of the scintillation light directly to the APD and high-voltage ripple coming from the analog test board.

2.2.3.3 Silicon Photomultipliers

A further development of the APD is to construct a large array of small APD cells with integrated quenching resistors, each with a dimension of 20-100 μm, on a common silicon substrate [36, 47–51]. The current pulses from individual microcells can either be summed to provide a single current pulse whose total charge is proportional to the number of triggered microcells or counted digitally and timestamped. This results in a solid-state device with an effective gain comparable to a PMT (up to 10^7), but with a much lower biasing voltage (typically below 100 V, compared to several thousand volts for a PMT). Due to the small size of each microcell, the probability of multiple photon intreactions with a given microcell is much lower than with a single large APD. In this way, the non-linear characteristic of the APDs are averaged out, leading to a current output or photon count which varies linearly over a wide intensity scale. By contrast, a single APD operating in the high-gain Geiger mode has an output current which does not increase linearly with light intensity [49]. These multi-pixel APD arrays operating in Geiger mode were first developed in Russia [52], and are now produced by many companies under different names such as Silicon Photo-Multiplier (SiPM), MRSAPD, MPPC, MAPD, etc. The generic name SiPM will be used for all of these devices throughout the rest of this Thesis.

SiPM gain (G) can easily be determined by measuring a single electron peak which corresponds to one pixel discharge and is proportional to single-pixel capacitance (C) and $\Delta \mathrm{V} = V_{bias} - V_{breakdown}$ [47, 50]:

$$G = \frac{Q}{e} = \frac{\Delta V \times C}{e} \tag{2.3}$$

A typical value of C of $\approx$ 100 pF and ΔV of a few volts (per pixel) result in a deposited charge of a $\approx$ 100 fC for each electron. The relative gain variation $\frac{\Delta G}{G}$ is proportional to ΔV. Therefore SiPMs operated at smaller ΔVs have larger gain sensitivity to the voltage variation and require better bias voltage stabilisation. Another issue is the SiPM's gain sensitivity to temperature: a 2 K decrease in temperature results in a drop in $V_{breakdown}$ of $\approx$0.1 V resulting in an increase of the value of G. It is thus important to minimise temperature fluctuations throughout all SiPM based measurements.

Recently, SiPMs have been developed which are optimised for detecting wavelengths of light emitted by the LSO-family scintillators often used for PET applications (blue light, around 420 nm). These detectors offer a photon detection efficiency which compares favourably with that of the PMTs (up to 30%) [36, 53].

2.3 Spatial Resolution and Depth of Interaction

One of the most active fields of detector research is developing a detector module capable of measuring the depth of interaction (DoI) in the scintillator crystal [23, 54]. As discussed in Section 2.1.1, for PET detectors in which the radius of the subject approaches the radius of the detector ring, annihilations occurring near the periphery of the field of view are likely to interact with multiple crystal segments in the detector. This results in an ambiguity in the line of response, which manifests itself as a blurring of the sinogram in the radial direction. Correction of this aberration requires a more accurate estimate of the line of response, which can be accomplished by measuring the depth of interaction (DoI) in the scintillation crystal.

The depth of interaction is described by a multiplicative factor applied to the value of detector resolution at the midpoint between a pair of directly opposed detectors [5]. The intrinsic spatial resolution R_{det} of a PET system is determined by the apparent width of the detector (d'). For a source placed in the centre of the FOV, this is given by [5]:

$$R_{det} = \frac{d'}{2} \tag{2.4}$$

As the source moves towards the periphery of the detector ring, the lack of information about the depth at which the detection occurs and the relative placement of the detectors changes the apparent width of the detector, hence degrading the intrinsic spatial resolution [5]:

$$d' = d\cos\theta + x\sin\theta \tag{2.5}$$

and

$$R'_{det} = \frac{d}{2}\left(\cos\theta + \frac{x}{2}\sin\theta\right) \tag{2.6}$$

where x is the width of the scintillator crystal, d the width of the detector and θ is the radial angle between the planar axis of the detector and y-axis (Figure 2.6). The intrinsic resolution calculated by Equation 2.6 is an approximation, since it does not account for the variations in detector thickness.

One interesting conclusion which may be drawn from Figure 2.6 is the relation between the DoI and the geometry of the ring. Systems which employ a hexagonal or octagonal ring configuration are less prone to parallax error, and hence provide superior peripheral spatial resolution. However, at the centre of the FOV, they have a somewhat worse spatial resolution compared to a circular ring of detectors [5].

Moses' detector [40, 41, 55] provides an estimate of the DoI via distance-dependent intensity attenuation along the length of the crystal. The outside of each scintillator block is covered by a lossy semi-reflective material which progressively attenuates the light pulse as it travels via internal reflection down the length of the crystal. A PMT is coupled to one end of the crystal, and a PIN detector to the opposite end. Therefore, by measuring the ratio of light intensity detected by the PMT to

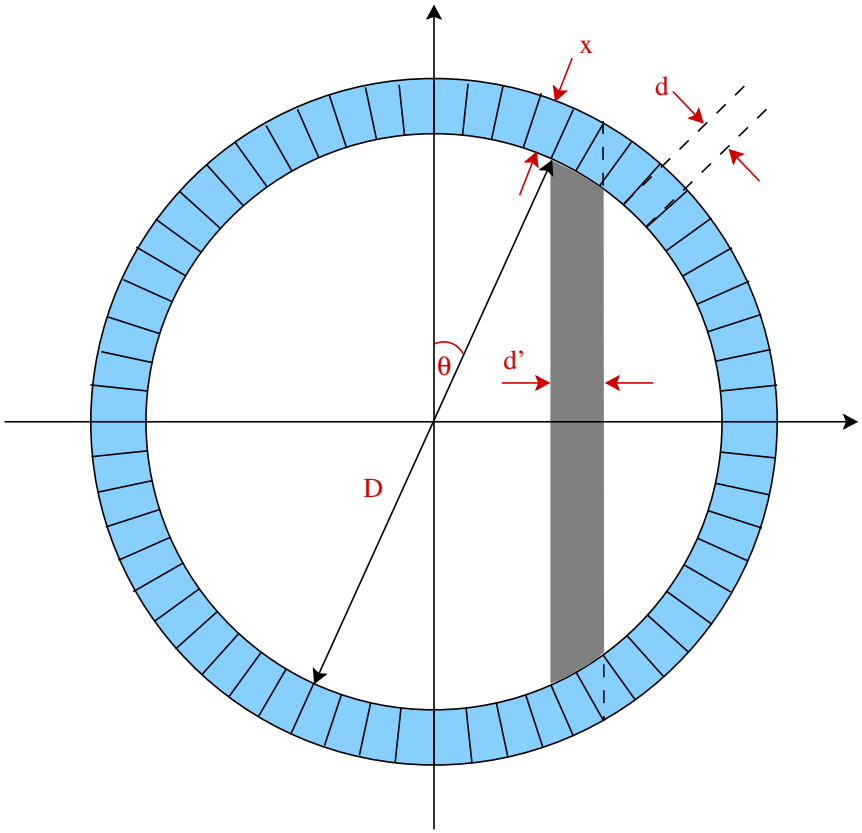

Figure 2.6 Depth of Interaction (DoI) and its dependence on the apparent width of detector (d') [5]

that observed by the corresponding PIN diode, the DoI may be estimated [55]. As with the estimate of minimum SNR requirements, Moses performs experiments using a single-crystal detector and extrapolates those results to a multi-element detector array. The test configuration for measuring DoI uses two single-crystal detector units, one fitted with a PMT and single PIN photodiode and placed at a fixed location, the other at right angles, separated by a short distance from the first, with only a PMT. A positron source is placed between the second detector and the first, and the moved together with the second detector via an adjustable stage. This assembly allows for coincidence detection with a controllable depth of interaction in the first scintillator crystal.

Moses' experimental results show a highly linear relation between the DoI and the measured light intensity for both PIN photodiode and PMT, with gradients of opposite polarity due to increasing vs. decreasing proximity to the detector as DoI increases for each respective detector. After normalising the energy response of the detectors to the same scale, it is possible to make a meaningful comparison between energy deposited in each detector. A near-linear relation exists between the DoI and the ratio between the energy deposited in the photodiode and the total energy deposited in both detectors. The DoI resolution achieved with Moses' LSO detector [55] was comparable to the BGO devices developed previously [41], of the order of 5 mm FWHM. Although this is a relatively coarse estimate of the DoI, it is sufficient to considerably reduce the radial blurring near the periphery of the FoV which occurs without the use of DoI information. As the signal detected by the photodiode decreases as DoI increases while the noise level remains constant, the spread of the photopeak increases, reducing the effective DoI resolution for large DoI. However, due to the high linear attenuation coefficient of BGO (0.92 cm^{-1}) and LSO (0.86 cm^{-1}), the majority of interactions are relatively shallow.

Moses goes on to extrapolate the function of a single-crystal detector to the multi-crystal case using Monte Carlo analysis, and simulate the improvement in point spread function when DoI is taken into account.

Several groups have proposed different SiPM based detectors for PET applications [36, 49, 56, 57] which are capable of providing DOI information. Del Guerra et al. have proposed a SiPM based detector concept which employs a slab of LSO scintillator sandwiched between two arrays of SiPMs with different pixel sizes. The array with larger pixels provides the timing information, while the finely pixellated array resolves the hit position in two dimensional space with sub-millimetre accuracy. The DoI position within the scintillator block can be found by combining both detectors' response [36]. The design is yet to be simulated or analytically evaluated.

Another proposed design by Beltrame et al. incorporates LYSO crystals aligned along the axial coordinate and wavelength shifter strips (WLS) orthogonally placed with respect to the crystals, both read out by SiPMs [56, 58]. The design provides both axial and radial information and is suitable for multi-modal imaging. Preliminary simulation and experimental characterisation of the module have been carried out with two modules in coincidence, and an energy resolution of 12.5% and spatial resolution of 1.5 mm in the middle of the field of view have been reported [56].

2.4 Data Acquisition Systems

As the resolution of PET systems increase, the volume of data which needs to be processed also increases. Some highly compact systems (such as RatCAP [14–17]) do minimal data processing on the detector boards, and shift the responsibility for coincidence detection to external computer hardware. Therefore, it is necessary to have an efficient and scalable data transmission system to transfer data to the storage and processing host for image reconstruction.

A number of different approaches have been applied to this problem. The earliest PET systems required the use of expensive and highly specialised VME (VERSAmodule Eurocard) based backplanes, which, at the time, were one of the few bus technologies with the necessary bandwidth to manage the flow of data. A host PC would typically interface to this bus to acquire data buffered in readout units con-

nected to the bus. Cherry's MicroPET system is an example of a VME-based PET machine [59, 60].

More recent work has looked at ways to reduce the cost of data acquisition and management systems, by replacing the expensive VME bus with a low-cost commercial-off-the-shelf interconnection technology. Hegyesi et al. have recently published a design for a PET system which used an Ethernet-based data acquisition scheme. Their detector utilises a rotating gantry with an array of four 8×8 LSO scintillators and position-sensitive PMTs, which are coupled to preamplifiers, high-speed analog-to-digital converters, and field-programmable gate arrays (FPGAs) for digital signal processing. Each module is then connected to a 16-bit PIC microprocessor and 10 Mb/s 10baseT Ethernet (IEEE 802.3) network interface card (NIC) [61]. The effective throughput of each detector in this system is therefore limited by hardware to 720 kB/s, which is sufficient to handle approximately 90000 events per second per detector (although this could be increased to more than 500000 events per second per detector if the Ethernet interface is upgraded to 100baseT). The four detector modules are thus connected to a central 100baseT Ethernet switch, which also has two 1000baseT ports (although the aggregate traffic from four detectors should not unduly tax a single 100 Mb/s port).

The Ethernet-based modules communicate with a server PC, using Transmission Control Protocol (TCP) for low-rate inter-module communication and UDP for sending event information to the central server. This architecture also allows a multi-server cluster to be used for data processing, which should allow the design to be scaled to support many more detectors. Coincidence detection is performed entirely in software on the server PC.

Since open-source hardware implementations of 100 Mb/s 802.3 medium access control (MAC) are available as VHDL/Verilog code, it would be quite straightforward to integrate an Ethernet interface into any future FPGA-based coincidence detection system at a cost of around 2400 gates [62].

An alternative physical-layer approach is used by Lewellen et al. , who have developed a data acquisition system for their LSO/PMT-based PET system. Lewellen's data acquisition system is based on IEEE 1394a (firewire) [63]. Firewire is a popular high-speed serial bus designed for interconnecting multimedia devices. As with Hegyesi's system, an FPGA is used to perform much of the signal processing work, however in this case, coincidence detection is also performed within the FPGA. Two detector modules are supported by each electronics block, which also include an integrated microprocessor, ADC, VA32_75 preamplifier/shaper ASIC and 1394a controller.

Each coincidence event is stored in a 32-byte data structure, and when 64 such structures are accumulated they are transmitted on the bus to the host computer. The 2048-byte packet size was selected to maximise the utilisation of the 1394a bus. Although this approach puts a smaller computational burden on the host computer, this comes at the cost of needing significantly more sophisticated hardware associated with each detector module.

One promising candidate data acquisition system is the Hybrid Modular Processor System (HYMOD), a flexible fast signal processing and data acquisition platform, developed at Australia's CSIRO [64]. HYMOD was originally developed for automatic vehicle number plate recognition, for the monitoring of truck driver fatigue by determining average vehicle speeds between checkpoints on major highways. The HYMOD platform consists of a Field Programmable Gate Array (FPGA) connected to 6 large static RAM blocks, a PowerPC processor running an embedded Linux operating system, two gigabit Ethernet ports and 12 high-speed serial ports (3.125 Gb/s). The embedded operating system running on the PowerPC can load arbitrary code to the FPGA; CSIRO has developed its own pipelined, parallel processing language for this purpose called 3PL (3rd-generation Programming Language), which is ideally suited for data-processing applications. The PowerPC also handles network I/O, buffering for display and logging of detector events to a remote binary log server; it also provides a TCP/IP endpoint for remote configuration requests for the

control and management of other electronics interfaced to HYMOD. The powerful capabilities of HYMOD have allowed it to be adapted to perform a variety of imaging and spectroscopy data acquisition tasks for a synchrotron X-ray microprobe. In this application, HYMOD processes up to 10^8 events per second. As it has an Ethernet network interface, a data acquisition system with multiple HYMOD units would be straightforward to assemble; a single high-bandwidth binary log server would be able to service all of the boards. In this application, HYMOD utilises a dedicated nuclear pulse processing ASIC which is also suitable for this project; this ASIC is discussed in detail in Section 2.4.6.

2.4.1 Discrete Analog Electronics and Nuclear Pulse Processing

PIN photodiodes, APDs and (analog) silicon photomultipliers all produce an output in response to a photon interaction which is in the form of a current pulse (or charge burst). For example, a single gamma photon interacting with an LSO scintillator optically coupled to a reverse-biased PIN photodiode produces a charge burst of around 600-700 electrons over a period of a few tens of nanoseconds [6]. This brief pulse needs to be amplified and shaped with a Gaussian filter whose time constant is chosen to minimise the total noise, such that the signal to noise ratio is maximised.

Once the pulse is amplified and shaped, it needs to be fully characterised in terms of arrival time and energy (i.e. pulse height), for digital readout and analysis.

2.4.2 Charge Sensitive Preamplifier

A preamplifier module is connected between the detector output, isolating the detector from the shaping circuit and converting the the current pulse by integration to a voltage pulse with amplitude proportional to total collected charge. Two types of amplifiers can be used for this purpose: current-to-voltage and charge sensitive amplifiers. The latter is preferred in most applications as it produces less noise.

Figure 2.7 shows the basic circuit diagram of a charge sensitive preamplifier. This device is essentially an integrating transimpedance amplifier with very large unity

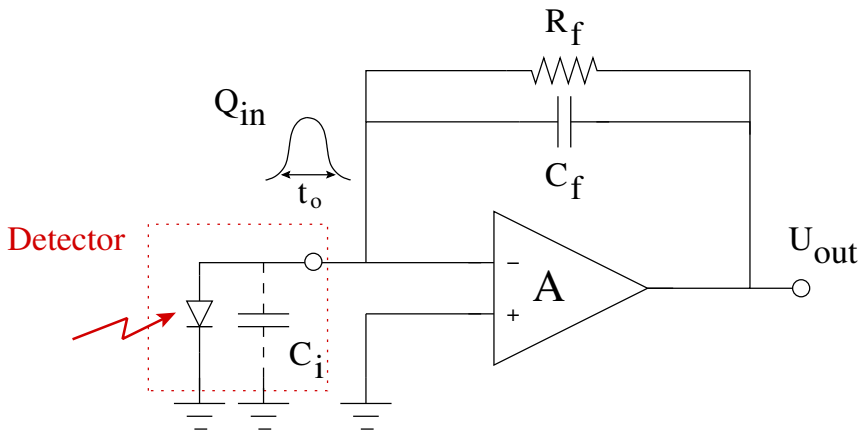

Figure 2.7 Basic circuit schematic of a charge sensitive preamplifier.

gain bandwidth and extremely high input impedance. The amplifier is based around a wideband operational voltage amplifier with a parallel resistor-capacitor circuit in the feedback path. Hence a short current pulse (the charge burst from the detector) at the input results in an output voltage which rises rapidly and exponentially decays relatively slowly. The rise-time of the amplifier output is determined by

$$\tau_r = R_i C_{det} \tag{2.7}$$

where R_i is the input impedance of the amplifier and C_{det} is the capacitance of the detector. The decay time constant is determined by the feedback network:

$$\tau_f = R_f C_f \tag{2.8}$$

where R_f is the feedback resistor and C_f is the feedback capacitor.

The charge gain C_G (expressed as the ratio between the peak voltage at the output to the charge deposited at the input) for a charge-sensitive preamplifier with feedback capacitance C_f is approximately given by

$$C_G \approx -\frac{1}{C_f} \tag{2.9}$$

The input capacitance of the charge-sensitive preamplifier described above is given by

$$C_i \approx (1 + A_v)\, C_f \tag{2.10}$$

where C_f is the feedback capacitance and A_v is the open-loop voltage gain of the amplifier. Provided that this input capacitance is significantly larger than the detector capacitance, almost all of the charge pulse from the detector can be measured [65].

The output signal (U_{out}) is a function of the feedback capacitor and the input charge [1, 3, 37]:

$$U_{out} \approx \frac{Q_{in}}{C_f} \tag{2.11}$$

2.4.3 Noise in the Preamplifier

There are a number of independent noise sources in the detector and charge-sensitive preamplifier stage. Some of these noise sources can be controlled; others are fundamental physical properties of the devices. The main noise sources can be modelled as shown in Figure 2.8.

The first noise source is thermal noise, which is thermal noise present in the (usually very large) feedback resistor in the preamplifier [6]. Thermal noise can be approximated as the voltage

$$V_{nt1} = \sqrt{4KTR_f}\ \mathrm{V.Hz}^{-1/2} \tag{2.12}$$

where K is Boltzmann's constant, T is the temperature in Kelvin, and R_f is the

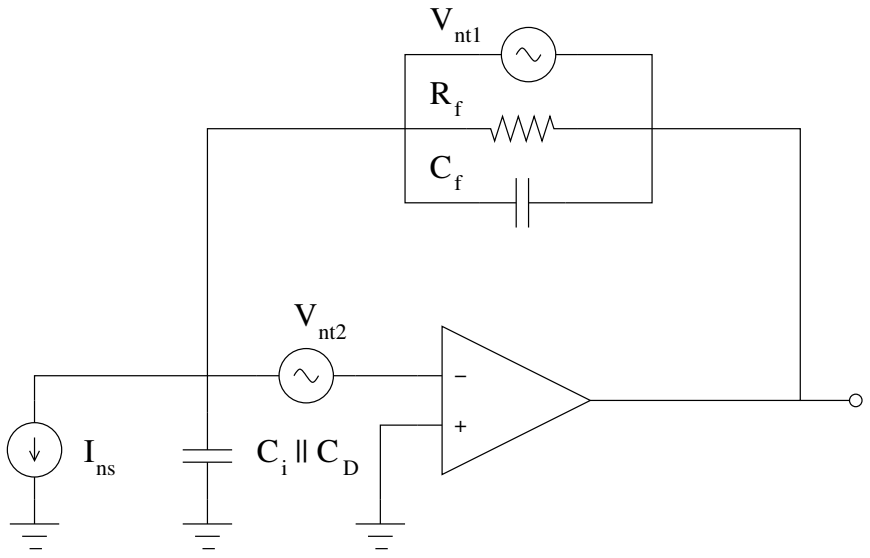

Figure 2.8 Noise sources in the detector and charge-sensitive preamplifier stage [6].

feedback resistance.

Practical charge-sensitive amplifiers are frequently not directly coupled to the detector; rather, the charge pulse is injected into the gate of a junction field-effect transistor (JFET), which amplifies the pulse while providing very high input impedance to the detector. This contributes two types of noise: firstly, thermal noise, which can be approximated as a voltage:

$$V_{nt2} = \sqrt{\frac{8}{3}\frac{KT}{g_m}}\ \mathrm{V.Hz}^{-1/2} \tag{2.13}$$

where K and T are Boltzmann's constant and the temperature in Kelvin, and g_m is the transconductance of the JFET; and secondly, shot noise - which can be combined with the shot-noise contribution from the detector:

$$I_{ns} = \sqrt{2q(I_g + I_D)}\ \mathrm{A.Hz}^{-1/2} \tag{2.14}$$

where q is the charge on an electron ($1.602 \times 10^{-}19$ C), I_g is the gate leakage current

of the JFET, and I_D is the dark current of the detector.

This leads to a complete noise model, expressed as a function of frequency:

$$V_n^2(j\omega) = V_{nt1}^2 \left(1 + \frac{C_i + C_D}{C_f}\right) + \left(I_{ns}^2 + \left(\frac{V_{nt2}}{R_f}\right)^2\right) \frac{1}{(j\omega C_f)^2} \tag{2.15}$$

The first term is independent of frequency and scaled by the ratio $1 + (C_i + C_D)/C_f$, while the second term *decreases* in proportion increased frequency and is independent of capacitance at the input [6, 66, 67].

2.4.4 Shaping Amplifier

The output of the charge-sensitive preamplifier is a voltage waveform, which consists of a series of short rise-time, slowly decaying pulses. The signal also includes broadband noise (additive white Gaussian noise) from a variety of sources (including the detector itself and the associated analog electronics).

If enough of these pulses occur within a short period, then due the integrating action of the preamplifier, the pulses will tend to 'pile up'. Since the amplitude of the output pulses contain important information (gamma-ray energy), this piling-up of pulses is problematic. It is also desirable to attenuate noise as far as possible. Therefore, the charge-sensitive amplifier output is coupled to a shaping amplifier whose impulse responses is an approximately Gaussian pulse with a particular pulse width known as the *shaping time*. For a pulse of the form

$$G(t) = Ae^{-\left(\frac{t-t_0}{\tau}\right)^2} \tag{2.16}$$

the shaping time is given by τ. Shaping time is also frequently expressed in terms of the full width at half maximum (FWHM) of the pulse, the width of the pulse measured from half the pulse height on the rising and falling edge. For a true Gaussian pulse, the FWHM is 2.35τ.

A Gaussian filter has the following desirable characteristics:

- Very linear phase response (almost as good as Bessel);
- Lower complexity than equivalent magnitude-response Bessel filter;
- Ripple-free passband frequency response; and
- No overshoot with minimal rise-time and fall-time (critical dampening).

Generally, a shaping voltage amplifier should be a band-pass filter, since it is essential that the output pulse decays more rapidly than the output of the charge-sensitive preamplifier, while it still has a fast rise-time. This can be achieved using a differentiator followed by one or more low-pass stages (for example, Sallen and Key biquadratic low-pass filter stages) [68]. It may also provide any level of desired gain. Gaussian shaping amplifiers are available with a variety of pre-determined shaping times - typically between 250 ns and 4 μs [68].

After filtering, it is possible to make the following observations on noise terms from the detector/preamplifier circuit which are present in the output from the shaping amplifier:

- Thermal noise from the input FET is inversely proportional to shaping time;
- Thermal noise from the feedback resistor is proportional to shaping time; and
- Shot noise from the detector is also proportional to shaping time;

The frequency at which the shaping amplifier with shaping time τ provides maximum gain is given by

$$f \approx \frac{1}{2\pi\tau} \tag{2.17}$$

Hence, τ should be carefully selected to avoid amplifying environmental noise sources, which are frequently narrowband (e.g. radio transmissions, RF regress from computers, wireless networks etc.), while minimising the sum of internally-generated noise [65, 68].

2.4.5 Constant Fraction Discrimination

The output from the shaping amplifier is (ideally) a Gaussian pulse, whose amplitude is determined by the energy of the incident photon. If the timing of analog-to-digital conversion of the pulse is to be performed on the basis of the pulse crossing a certain amplitude threshold, for large-amplitude pulses, the ADC will begin conversion early, while for smaller pulses, conversion will be delayed. This time-walk is undesirable and needs to be corrected. The standard approach to this is to apply constant fraction discrimination, in which an attenuated version of the input signal is added to a delayed and inverted version of the input signal, with the sum fed into a zero-crossing detector [3]. The net effect is similar to a differentiator, with the difference being that the zero-crossing point indicates the point at which the pulse has reached a certain fraction of its maximum rather than the maximum or minimum [65]. The output of the zero-crossing detector can then be used to start the data acquisition process. Further reduction in timing jitter may be achieved through the use of a Schmitt trigger circuit on the discriminator (if the output of the shaping amplifier includes a significant amount of additive noise) [69, 70].

2.4.6 SCEPTER Integrated CMOS Nuclear Pulse Processing ASIC

An interesting approach to automatic analysis of incoming nuclear pulses is the use a dedicated hybrid analog/digital ASIC. A number of advanced CMOS nuclear pulse processing ICs have been designed at Brookhaven National Laboratory; one in particular is of great relevance to this project. This device is a 32-channel hybrid analog/digital CMOS IC called SCEPTER (Simultaneous Capture of Events with Programmable Timing and Energy Readout) [71, 72].

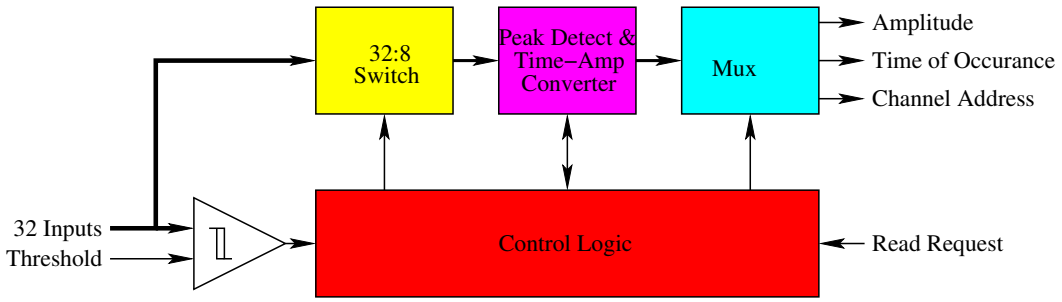

Figure 2.9 SCEPTER pulse capture system

Each channel of SCEPTER detects shaped and preamplified pulses arriving from photon detectors and converts the pulse height and time of arrival to an analog voltage representation via a peak detect and Time to Amplitude Converter (TAC) system [72]. It can record up to eight simultaneous pulses arriving within a single read request period (the read request clock rate can be configured to one of a limited number of fixed values). The time of arrival and pulse height information for any pulses received during a given read request interval are then sequentially read out as analog voltages in successive read request intervals. Hence, two ADCs can measure the pulse amplitude and time of arrival by reading the appropriate analog outputs in the middle of read request intervals at the same time as channel addresses are read out digitally. The readout process, which is independent from the pulse recording method, minimises the deadtime of the system.

A block diagram of this IC is shown in Figure 2.9.

The time of arrival can be recorded by SCEPTER using two different methods: Time over Threshold (ToT) and Time of Occurrence (TOc). The former limits the resolution to the system clock rate, making it unsuitable for applications in need of sub-microsecond resolution. Therefore, for this project, TOc mode is the most appropriate timing method to use.

In response to an input threshold-crossing, the channel analog input is routed to the next available Peak Detect (PD) block via a 32:8 analog multiplexer/crosspoint

switch matrix. This process is completed within a few nanoseconds, and the ASIC is ready for the next pulse; if two pulses exceed the input threshold within 3 ns of each other, priority is always given to the lower-numbered channel. This is particularly important for PET applications, in which events of interest are those which do occur within a few nanoseconds.

Once the cross-point switch is set, the selected peak detector enters the *tracking* state, which lasts until a peak is found or a configurable time-out expires. During this time the remaining free peak detectors can simultaneously process other pulses arriving on any input channel. When the PD detects a peak, it enters the *buffering* state. At this instant, the address of the channel being processed is stored in a latch and the crosspoint switch is reset. The triggered peak detector remains *occupied* until it is read out.

The arbitration logic also maintains a time-ordered list of occupied peak detectors pending readout. This list is updated whenever a change in the number of occupied peak detectors occurs, either by a new event or by a readout operation. `FULL` and `EMPTY` flags are available to indicate when all the peak detectors are occupied and unoccupied, respectively.

A read request is initiated by a rising edge of Chip Select (`CS`). In response to a read request, a count of all PDs is performed to establish which are in the occupied and pending readout state. PDs with no valid sample simply tie their `PDOUT` and `TDOUT` analog outputs to GND, thus routing a 0 V sample to the respective ADC inputs. PDs with valid peak sample present their peak amplitude and TACs at the `PDOUT` and `TDOUT` analog outputs, the latched channel address appears at the the PIXADDROUT outputs, and the `VAL` flag is set. Once the external ADC has completed its conversion, the downstream electronics acknowledges that it acquired the peak height and channel address by lowering the CS. This resets the appropriate peak detector and designates it as ready to receive subsequent pulses.

SCEPTER is reported to have high accuracy in both timing and energy measurements

with low power consumption. Initial prototypes reported [73]:

- Power consumption of less than 2 mW/channel;
- Good linearity (0.05% deviation from nominal linear response); and
- High absolute timing and energy measurement accuracy (nominally a maximum error of 0.3% of full scale for both.

2.5 Full System Evaluation: Dedicated PET Systems for Small Animal Studies

Development of PET systems for small animals is difficult for a number of reasons. When the radius of the subject approaches that of the detector ring, resolution at the edge of the subject cross-sectional area is significantly worse than at the centre due to parallax error (as discussed in Section 2.3).

Moses et al. discuss a small-animal PET system with a ring diameter of 35 cm and axial field of view of 15 cm [74]. Unlike Moses' previous work, this PET system uses a LSO scintillator crystal, which offers considerably greater light output and shorter decay time at room temperature (BGO must be cooled to about -20°C to obtain the maximum light output, but this also increases its decay time compared to room temperature operation [41]). The LSO scintillator crystal is operated without septa, hence efficiency is relatively high. The short dead-time is beneficial in accurately measuring the high count-rate which occurs due to the proximity of the detectors to the patient. This proximity also necessitates the estimation of Depth of Interaction, which is accomplished by utilising the same combination of PMT and PIN-diodes as used in [41].

The lack of septa allows for the detector to be operated in 3D mode - in which annihilation photons may be detected in two different detector rings. This allows for many more lines of response to be generated as more events will be detected.

In more recent work, Rouze et al. propose a very small PET imaging system designed for mice, with a field of view of approximately 40 mm [75]. To minimise the parallax error associated with the outer part of the FoV, Rouze uses six pairs of planar detector banks mounted on a rotating gantry. Three detector pairs are positioned directly opposite each other, while the other three are offset by one-quarter of the width of a pixel. The offset allows an effective enhancement in resolution by approximately 20%.

Rouze's system does not attempt to measure DoI; instead, it tries to reduce the problem of parallax error by ignoring coincidences in which the parallax error will be too high (i.e. the LoR passes though too many crystal segments). Events are detected using PMTs which are coupled to the scintillator via optical fibres.

The simulated performance of the detector indicates that with a LSO scintillator, it should be possible to achieve spatial resolution of approximately 1 mm FWHM in axial, radial and tangential directions.

Correia et al. discuss design issues relating to a single axial plane PET imaging system for small animals designed to have a spatial resolution of around 1 mm FWHM [76]. Although not as small as Rouze's system of 2004, Correia's system is interesting for another reason: DoI calculation is unnecessary as the LSO scintillator crystals are relatively thin (5 mm). This reduces the sensitivity of the detector array, however the detector can achieve increased spatial resolution. The image is acquired using an array of PMTs and digitised using an 8-bit flash ADC. Energy thresholds are set deliberately low as due to the physical construction of the system, the response of different segments in each crystal block are not equal.

Practical measurements of the spatial resolution show that it actually varies between 1.24 mm and 1.72 mm FWHM (as the source moves from the centre to a radial offset of 2.5 cm). Some preliminary imaging work had been performed using the system at the time of publication.

A second-generation version of the Correia PET system is discussed in [77]. It uses longer (7 mm as opposed to 5 mm) and wider (1.2 mm as opposed to 1 mm) crystal segments in order to improve detector sensitivity; the cost of this design choice is somewhat reduced spatial resolution at the edge of the FoV. However, the sensitivity of the detector was improved approximately two-fold. The practicality of the detector remains limited as it only has a single detector ring.

Li et al. discuss a fixed-gantry PET system in which costs are reduced by sharing PMTs between scintillator crystal blocks, and using commercial off-the-shelf technology and software rather than custom hardware as far as possible [78]. Li's system also integrates a low-cost calibration system based on LEDs, and a novel programmable voltage-divider system for providing the bias voltages for the PMT dynodes.

Several dedicated small animal PET prototypes (e.g. MicroPET II, RatCAP, SiliPET) and a number of fully engineered scanners (Siemens Iveon, Siemens MicroPET Focus 120 and GE eXplore Vista) have been released commercially [14, 79–81]. All three commercial systems offer high spatial resolution and good sensitivity, but are based on PMTs and are therefore bulky and extremely sensitive to magnetic fields. Of the three systems, the MicroPET Focus 120 uses the thinnest crystal elements with the largest gantry (15 cm in diameter with 10 cm transaxial FoV), using a large number of LSO crystals for large solid angle coverage in order to achieve good sensitivity [82]. The Inveon scanner is an updated version of the MicroPET Focus 120, which uses larger LSO scintillator blocks, resulting in improved sensitivity; however, this is at the cost of a larger line of response (LoR) acceptance angle [81]. The Vista scanner employs the more complex phoswich technology to reduce the diameter of the gantry (11.8 cm) while providing DoI information [83]. All three systems provide good spatial resolution (respective resolutions of 1.18 mm, 1.51 mm and 1.48 mm in the radial direction at the centre of the FoV).

At 27%, The energy resolution of the Vista is somewhat degraded in comparison to comparable single-scintillator (non-DoI correcting) small-animal PET scanners

(by around 20%) [82, 83]. However, the energy resolution of a scanner used for imaging smaller volumes is seen as less critical, since fewer photons are scattered in the subject when compared to whole body human imaging systems [84].

2.5.1 MicroPET

The MicroPET series of 3D PET imaging systems developed by Cherry et al. were the first to make use of LSO scintillator crystals [59]. The first-generation MicroPET system used 30 8×8 arrays of LSO crystal scintillator blocks, each 10 mm in length, optically coupled to pixellated PMTs via optical fibres. It only had a single ring of detectors and therefore had limited field of view (18 mm). The resolution achieved was between 2 mm and 4 mm FWHM (axial, radial and tangential). Chatziioannou et al. have developed a technique for effectively enhancing the spatial resolution of the MicroPET system by inducing a 300 μm wobble in the scanner bed in the transverse plane [85]. This effectively adds additional lines of response, yielding an increased spatial resolution by 19% in the tangential direction and 13% in the radial direction. However, this comes at the cost of a 50% increase in image noise. The noise floor may be reduced to the original (unwobbled) level by using a longer image acquisition time.

The successor to the first-generation MicroPET, MicroPET II, uses a different crystal geometry to provide improved spatial resolution (by a factor of more than two, to between 1.04 mm and 1.92 mm) and peak sensitivity (by a factor of three, to about 2.26%) compared to the original MicroPET system [60, 79]. It also increased the number of detector rings to three to increase the axial FoV.

The original MicroPET design proved extremely successful and has been commercialised for use in research in the field of animal biology. In 2004, Laforest et al. published a performance evaluation and characterisation of an upgraded commercial version of the MicroPET, the Focus F-120 [86]. Results were compared with the original MicroPET R4, which showed a considerable improvement in spatial resolution, sensitivity and noise-equivalent count rate.

2.5.2 RatCAP

To date, the ultimate in miniature PET systems is a device known as the Rat Conscious Animal PET system (RatCAP) [15]. RatCAP is designed to be small enough that it can be worn by a RAT and suspended on a counterbalance system such that the rat may move about its enclosure - fully conscious - while brain activity is observed. This promises to greatly expand the range of studies which may be performed on animals in vivo, since conventional small-animal PET requires that the subject is anaesthetised. Implementation of the RatCAP system requires that a large number of technical problems are addressed, primarily related to the very small size to which the imaging hardware is constrained. A number of simplifications to conventional PET are proposed which allow RatCAP's design objectives to be met.

Vaska et al. present an overview of the design of RatCAP and discuss the main challenges in the project [15]. RatCAP uses twelve planar 4×8 arrays of avalanche photodiodes (APDs), which provide higher gain than PIN detectors at the cost of reduced temperature stability. The scintillator material is LSO, with each crystal having a square cross-section of 2 mm$\times$2 mm and a thickness of 5 mm. The signal from each of the APDs is coupled to a custom ASIC which performs necessary amplification, shaping and discrimination, then encodes the address of the crystal generating the event and transmits it serially to a VME data acquisition system. Coincidence detection is not performed in hardware, as this would significantly increase the complexity, size and power requirements for the detector electronics. Instead, all events are acquired and recorded to disk for later off-line analysis, in which singles are discarded and true coincidences are used to reconstruct the image. This is feasible only because of the relatively small number of detectors in the ring, which generate an aggregate data rate of the order of several hundred megabits per second - well within the capabilities of modern computer systems.

Unlike most PET systems, RatCAP does not use an analog-to-digital converter for signal acquisition - only an analog discriminator system. This saves a considerable

amount of power and hence reduces thermal load on the sensitive APDs. The cost of this is a significant reduction in coincidence sensitivity (around 30%). In the event that this is unacceptable, the system has provision for routing the analog signals from the amplifier outputs to external ADCs, although this comes at the obvious cost of considerably more complex wiring and hence reduced mobility for the rat.

RatCAP suffers from an inherently large parallax error, since the device is designed to be worn directly around the animal's head. This leads to relatively low radial resolution. Simulation results indicate that the 5 mm crystal depth results in a worst-case radial resolution of around 2 mm FWHM.

Pratte *et all* discuss the ASIC containing the front-end electronics used in RatCAP [16]. The main design constraints are a minimisation of power consumption and heat generation, a minimum number of interconnects, minimum size, and maximum timing resolution. The ASIC is clocked at 100 MHz and includes an integrated voltage regulator. Data is transmitted as a 64-bit word, including a 43-bit timestamp, 13-bit channel address (identifying the specific APD which has registered the event), 7-bit timer/counter/overflow detector, and finally, a 3-bit event classification field.

The APD is coupled to a charge-sensitive preamplifier and pulse shaper, which includes a pole-zero cancellation network (to compensate for FET nonlinearity and reduce the parallel noise contribution) and a 3rd-order Gaussian shaper (implemented as a first-order low-pass filter and a second-order biquadratic bandpass filter). This is followed by a timing discriminator which transmits the data packet asynchronously. A simple bus-arbitration mechanism is used, so that in the event that two events occur simultaneously, the highest-value address is given priority.

A mathematical model of the timing resolution and noise characteristics of the front-end ASIC is presented, with experimental and simulation data estimating linearity, timing resolution and energy resolution.

Shokouhi et al. have performed a series of simulations on the RatCAP system us-

ing SimSET [87] [17]. Monte Carlo simulations of detector performance are made, which indicate that a radial spatial resolution of around 1.8 mm FWHM is achievable. One important conclusion of this work is that due to non-uniform sampling of the lines of response, it is essential to interpolate between the available data sets prior to filtered backprojection. This results in dramatically reduced levels of image artefacts.

2.6 Conclusion

This chapter provided an overview of the background to this project, and illustrated the major research opportunities related to development of a high resolution PET scanner which provides a uniform spatial resolution across its field of view. It identified some key technologies which would be ideal for the development of a prototype system. These are summarised below.

Amongst the scintillator material listed in Table 2.2, Lu-based scintillators still remain the materials of choice in PET applications due to their high density, fast decay and high light output, in spite of the recent developments of bright, fast but relatively low density lanthanum bromide scintillators.

A variety of silicon detectors may be appropriate for this project, ranging from simple PIN diodes (which provide low intrinsic gain but are well-understood and easy to integrate on a large scale) to advanced silicon photomultiplier devices. A review of current literature indicates that SiPMs offer a good combination of desirable characteristics including high gain and sensitivity; however this needs to be verified through detailed experimental characterisation and analysis. This work is undertaken for three interesting photon detector devices in Chapters 4, 5 and 6, with the conclusion that a SiPM detector would be the best choice for this project.

The HYMOD platform has the advantage of previously having been used in conjunction with the advanced SCEPTER mixed-mode analog/digital nuclear pulse process-

ing ASIC. A single HYMOD module and SCEPTER chip will be capable of handling the high data rate and 32 detector channels needed for this project, and thanks to its standard Ethernet network interface, can be easily interfaced with a high-bandwidth binary data logging system. A design for a prototype high-resolution small-volume PET system based on HYMOD and SCEPTER with SiPM detectors and LYSO scintillators is presented in Chapter 7 and experimentally evaluated in Chapter 8.

Chapter 3

Photodetector Characterisation Techniques

One of the key components of all gamma-ray imaging systems is the mechanism by which the gamma photons are converted into an electrical signal for processing and image reconstruction. A pixellated photodetector, coupled to a matrix of scintillator crystal segments, can thus be used to infer the point of origin of a nuclear event in the patient through indirect observation of the emitted gamma-ray photons, either via the use of collimators (for example, in SPECT) or through coincidence detection (as used in PET).

While the photomultiplier tube (PMT) remains one of the most popular types of photodetector due to its reliability and high intrinsic gain (of the order of $10^6 - 10^7$), the performance of PMTs is limited by their poor quantum efficiency (approximately 25%) and their high sensitivity to magnetic fields, which precludes their use in combined PET/MR and SPECT/MR systems. They are also bulky, fragile and require a progressively higher series of bias potentials for each successive dynode.

Solid-state photodetectors are now widely employed for gamma-ray imaging applications due to their robustness and compactness in comparison to vacuum-tube PMTs. A variety of semiconductor devices have been developed for gamma-ray imaging, including p-intrinsic-n (PIN) photodiodes, avalanche photodiodes (APDs) and silicon

photomultipliers (SiPMs). With the introduction of these devices, new design options have become available for gamma imaging systems, offering excellent spatial resolution, high detection efficiency, low power consumption and low cost. These advantages are particularly beneficial in high resolution / small volume imaging applications, such as small animal and breast imaging.

In order to achieve maximum detection efficiency, the quantum efficiency and quality of optical coupling of the detector module must be optimised. Ideally, detectors should also add a minimum of self-generated noise and provide some intrinsic gain. This improves the signal to noise ratio (SNR) and reduces the need for multiple further stages of amplification, thereby reducing the required complexity of the external electronics.

In this Chapter, a range of different experimental and simulation-based detector characterisation methods are introduced. These techniques will be used to measure the key characteristics of the devices being tested, in particular evaluating the suitability of each device for use in positron emission tomography applications. The simplest device, a planar PIN photodetector, will be characterised in Chapter 4, while a PIN photodetector with integrated JFET and feedback capacitor will be evaluated in Chapter 5 and a silicon photomultiplier in Chapter 6. Not all devices are characterised using each method, as some methods are inappropriate, irrelevant or impractical for certain devices.

Performance of the detectors in nuclear event detection and spectroscopic applications is assessed, both with scintillation and, in some cases, additionally via direct interaction of low-energy gamma photons. The characterisation techniques to be introduced in this chapter include:

- ISE-TCAD computer simulation of charge distribution, electric field structure and transient current response (Section 3.1 - note that only the simplest device, the planar PIN photodetector, is simulated due to its simple internal structure);

- Electrical characterisation, including capacitance-voltage and current-voltage relations and transient current analysis (Section 3.2);
- Spectroscopic characterisation, including measurements of energy resolution with a variety of photon energies with and without the use of scintillators (Section 3.3); and
- Ion beam induced charge (IBIC) imaging, which characterises the response of the detector to incident high-energy alpha radiation as a function of the point of interaction under varying bias conditions (Section 3.4).

3.1 TCAD Simulation

Technology computer aided design (TCAD) is a powerful tool for predicting both qualitative and quantitative characteristics of complex semiconductor device structures. It is possible to use TCAD for simulation of structures with complex doping profiles and features such as guard rings and implants, and studying the charge carrier and electric field distribution. TCAD can also perform simulation studies of transient response to radiation (for example, transient current analysis in an irradiated reverse-biased semiconductor junction) by applying a stress to a DC-stable system and allowing it to relax back to equilibrium [88–91].

TCAD simulations divide a geometric model of a semiconductor (in two or three dimensions) into a finite number of discrete elements. Assuming continuity at the boundaries of adjacent elements, a numerical approximation of the well-known drift-diffusion charge transport model is used to solve for the internal charge distribution and hence the electric field at all points inside the device, in either two or three dimensions. Selecting the optimal simulation mesh density is a critical consideration when constructing a detector model in TCAD - the upper limit of the mesh size is set by the feature size of the simulated device (electrodes, implants, high electric field area) and the lower limit is set by computational complexity constraints (and possibly software limitations as well). It is recommended that the mesh dimensions do not

exceed one quarter of local feature lengths. The mesh should be locally adjusted to suit the characteristic lengths of the studied physical phenomena [91, 92].

In this work, TCAD simulations were performed using Synopsys TCAD for the planar PIN device only (Section 4.2), as the relatively simple and symmetric geometry greatly simplifies the simulation. The simulated detector model was based on models developed by Petasecca et al. for studying the radiation hardness of of p-type silicon substrates for use in high fluence radiation fields [90]. The simulated detector was modelled by a 300 μm thick and 40 μm two-dimensional $p^+/n/n^+$ structure, with the substrate doped at a concentration of $N_D = 10^{11}$ cm^{-3}. The p^+ region (front side) is separated by a 15 μm gap from a 6 μm wide and 1 μm deep p^+ implant with a Gaussian profile to model the guard ring. A two-dimensional grid-type mesh consisting of 11010 vertices and 22178 edges was used; five separate regions were defined (one silicon, two oxide regions, two contacts).

Simulation results for the diode capacitance as a function of the reverse-bias potential applied to the photodetector were used to predict its full depletion voltage. Leakage current density as a function of the applied reverse-bias potential was also investigated. The internal electric field and charge carrier density inside the device were studied under a variety of bias conditions, both before and after interaction with an incident charged particle. Transient current waveforms were also generated by simulating a 5.5 MeV α-particle incident on the front and backside of the detector. The particle generates a cylindrical distribution of charge within the detector substrate which drifts along the electrical field lines and is collected by the detector electrodes. The resulting pulse is used for comparison with experimental results obtained using methods described in Section 3.2.

3.2 Electrical Characterisation

Radiation detectors based on a reverse-biased diode structure, such as PIN detectors, may be modelled electrically as a small a small capacitor whose capacitance is a non-

linear function of the applied bias voltage. Photons interacting with the silicon body of the diode produce a small burst of electron-hole pairs at the point of interaction. Due to the electric field inside the device, the charges separate, with the electrons drifting rapidly towards the positive electrode and the holes drifting relatively slowly towards the negative electrode. This results in a current pulse with a short rise time (primarily due to the electron current) and a long tail (due to hole current). The total amount of charge in the current pulse depends on the number of electron-hole pairs generated by the interaction, which is proportional to the energy of the incident photon, while the precise shape of the pulse also depends on the geometry of the detector, the location of the point of interaction and the strength of the applied electric field [93]. The current pulse must be amplified and shaped and/or integrated in order to estimate the total amount of charge and hence the energy of the original event (refer to Section 2.4.2 for a more detailed discussion of this process).

As discussed in Section 2.4.3, three principal noise sources degrade the SNR of the resulting pulse measurement: *current* or *parallel* noise (shot noise intrinsic to the detector resulting from leakage current plus thermal noise from the bias resistor and preamplifier), *voltage* or *series* noise (thermal noise from the amplifier and amplifier input series resistance), and *low frequency* or $1/f$ noise (a result of charge-trapping effects within semiconductors and other physical properties of electronic devices, with one or more time constants) [94]. The contribution of both voltage noise and $1/f$ noise to the Equivalent Noise Charge (ENC - the input charge for which the output signal is equal to the output noise) are proportional to the square of total input capacitance (i.e. the sum of detector, input and stray capacitance at the preamplifier input, normally dominated by detector capacitance) [95]. The current noise is independent of this capacitance, but is a linear function of detector leakage current. These factors are therefore critical to determining the performance of the entire signal processing chain [96, 97]. It is also important to note that current and voltage noise are proportional and inversely proportional to shaping time respectively, while $1/f$ noise is independent of shaping time. Overall ENC is the sum of these three functions; therefore, the shaping time which results in the minimum overall noise is

that for which the contribution to ENC from voltage and current noise is equal [94].

PIN detectors are designed to operate when fully depleted, as this maximises uniformity of internal electric fields and hence charge collection efficiency; therefore, accurate determination of the full depletion voltage is essential for proper operation. As discussed in Section 2.2.3.1, the relationship between the capacitance of a PIN detector (C_{det}) and the applied voltage (V_e) is given by

$$C_{\mathrm{det}} = 2\sqrt{\frac{\epsilon}{2\rho_n \mu_n V_e}} \tag{3.1}$$

and

$$V_e = \frac{d^2}{2\epsilon\rho_n\mu_n} \tag{3.2}$$

where ρ_n is the resistivity of the bulk region, μ_n is the electron mobility [38, 98]. According to Equations 3.1 and 3.2, the capacitance of a PIN detector will reach an almost stable value when the bulk region is fully depleted. Therefore, the depletion voltage can be determined from the capacitance-voltage characteristic curve of the detector.

The current flowing through a reverse biased detector in the absence of any external radiation source is defined as the *leakage* or *dark* current [38,98,99]. The total current I in a forward or reverse biased ideal diode, defined as the sum of the electron and hole current densities (I_n and I_p) is given by the Shockley equation [38, 100]:

$$\begin{aligned} I &= I_p + I_n \\ &= I_0[\exp(\frac{qV}{kT}) - 1] \end{aligned} \tag{3.3}$$

where q is the electron charge magnitude, V is the applied bias voltage, k is Boltzmann's constant and T is the absolute temperature of the lattice. While Equation

3.3 provides an accurate estimate of the current-voltage characteristics of an ideal semiconductor junction, it ignores a number of processes which are significant in radiation detectors. These include photon-induced generation (and, to a minor extent, recombination) of the carriers in the depletion volume, avalanche breakdown and tunnelling and surface effects. These processes result in domination of the reverse-bias current of a fully depleted photodiode by the generation currents and the surface leakage currents [3, 38, 98]. The leakage current is usually dominated by the thermal generation of the carriers within the depletion volume (I_{vol}), and is proportional to the square root of the bias voltage (V) [38, 98]:

$$I_{vol} \approx -eA\frac{n_i}{\tau_g}\sqrt{\frac{2\epsilon_0\epsilon_{Si}}{eN_D}V} \tag{3.4}$$

where A is the cross-sectional area, n_i is the intrinsic carrier concentration, τ_g is the carrier generation lifetime, N_D is the donor concentration, V is the depletion volume and ϵ_{Si} is the relative dielectric permittivity of silicon. Once the volume is fully depleted ($V > \frac{3kT}{q}$) (as predicted by Equation 3.3) the leakage current saturates at I_0; the current increase remains very small with increasing voltage (i.e. a plateau region) before reaching the *breakdown voltage*, characterised by a rapid increase of the leakage current. The current-voltage plot can be used to identify problems which may have occurred during the production process.

For both current-voltage and capacitance-voltage measurements, each detector under test was biased using an ORTEC 719 precision DC supply, with bias voltages adjusted over a range of zero to 100 V. The leakage current was then measured as a function of the applied bias voltage using a Keithley 614 electrometer, while detector capacitance was measured using a Boonton 7200 capacitance bridge.

3.2.1 Capacitance-Voltage Measurements

The Boonton 7200 capacitance meter utilises two phase-sensitive detectors to extract and display both the parallel capacitance and conductance of the device being char-

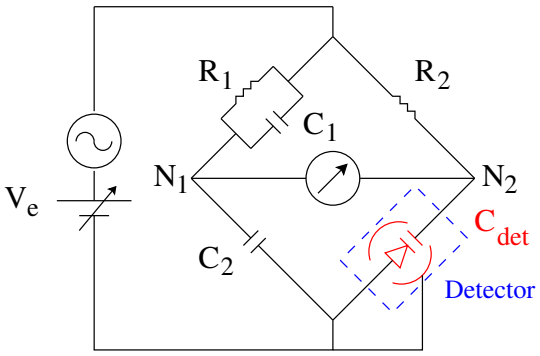

Figure 3.1 Schering's bridge circuit with the device being characterised.

acterised [101]. This instrument uses an AC bridge similar to the Schering circuit shown in Figure 3.1. The bridge is a four-arm alternating current (AC) bridge circuit where measurements are performed by balancing the loads on its arms such that zero current flows between them. An additional variable DC source is used to supply bias the detector - as both branches of the bridge have a series capacitance, this does not affect the measurement.

The bridge is "balanced" when no current flow between nodes N_1 and N_2, or when the magnitude and phase of the voltage waveforms at these nodes are exactly equal. Given that the values of resistance of R_1 and R_2 and the capacitance C_1 and C_2 are known, the detector capacitance (C_{det}) is obtained by:

$$C_{det} = \frac{R_1.C_2}{R_2} \tag{3.5}$$

Figure 3.1 shows the tested device connected to the bridge, with its guard ring grounded.

3.2.2 Timing Characterisation

Transient current analysis is the measurement of time-domain current pulse shapes in silicon detectors resulting from collection of charge carriers released through interaction of incident charged particles with the detector. In the case of a simple

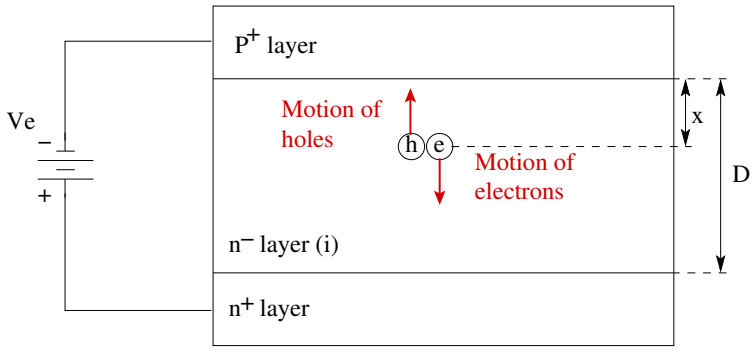

Figure 3.2 Charge carrier motion in a simple PIN detector.

PIN detector (Figure 3.2), the measured current pulse shape $i(t)$ depends on the deposited charge $Q(t)$, the electric field profile **E**, the distance that each charge carrier traverses $x(t)$, and its drift velocity (v_{drift}), as described by the Ramo-Shockley equation [102–104]:

$$\begin{aligned} i(t) &= \frac{Q(t)}{D}.v_{drift}(x(t)) \\ &= \frac{Q(t)}{D}.\mu E(x(t)) \end{aligned} \tag{3.6}$$

where μ is the charge carrier mobility and D is the detector thickness. At high field intensity, where the drift velocity reaches saturation, the location at which the charge carriers were produced impacts the shape and the rise time of the output pulse (although the total deposited charge within the detector volume remains the same). This is due to the fact that the mobility of electrons is approximately three times greater than that of holes. For the PIN detector model shown in Figure 3.2, the electron and hole collection times (t_e and t_h respectively) are given by:

$$t_e = \frac{D - x}{v_{el}} \tag{3.7}$$

and

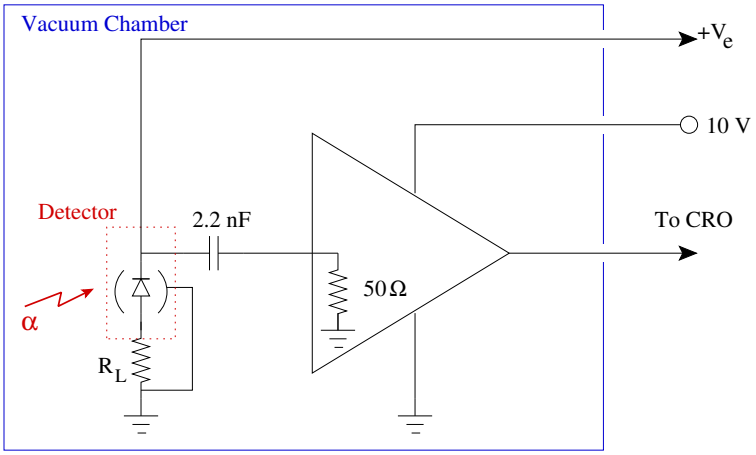

Figure 3.3 The schematic showing the Transient Current Technique (TCT) experimental apparatus.

$$t_h = \frac{x}{v_{hl}} \tag{3.8}$$

where v_{el} and v_{hl} are the saturation velocities of the electrons and holes. Since the position at which the electron-hole pairs are generated influences their time of arrival at their respective collecting electrode, the shape of the rising edge of the transient current pulse is an indication of the contribution of each type of charge carriers to the electrical signal and the shape of the electric field within the detector volume.

Carrier collection time was evaluated by measuring the transient current response of the device under test. The detector was connected to the input of a fast current amplifier (Philips scientific 6954 wideband amplifier) with an input impedance of 50 Ω and a voltage gain of 10. Pulses are recorded by a LeCroy digital oscilloscope in averaging mode, to improve the signal to noise ratio. Figure 3.3 depicts the experimental apparatus. The signal is generated by collection of the charge deposited from direct interaction of the 5.47 MeV α particles emitted by an ^{241}Am source placed on the front and the backside of the detector. The short range of the alpha particles in silicon (up to a depth of approximately 25 μm for 5.5 MeV α) ensures the signal generation close the irradiated detector side, which in turn allows the observation of

electron and hole contribution to the induced signals. The experiment was conducted inside a shielded vacuum chamber to minimise the noise and maximise the deposited charge in the detector.

3.3 Spectroscopic Characterisation

Energy resolution is an important characteristic of any photon detector. At low energies (up to a few tens of keV) it is possible to detect gamma photons directly, as the probability of interaction between an incident photon and the silicon detector is high. For higher energies, due to the low probability of direct photon interaction it is necessary to optically couple the detector to some form of scintillator. The most appropriate scintillator for a given application depends on a variety of factors, including the peak response wavelength of the detector, the light output of the scintillator, the scintillator's response time, the energy of the gamma source of interest and the effective atomic number of the scintillator.

Energy resolution is measured by acquiring a pulse amplitude spectrum (with or without scintillator) from a detector under desired test conditions (bias, guard ring potential etc.). The detector is normally connected to a preamplifier (in the case of a simple PIN diode, this is preceded by an additional JFET amplifier stage) followed by a shaping amplifier with its time constant adjusted to minimise noise (as described in Section 3.2).

For all spectroscopic characterisation methods detailed in this Chapter, a spectroscopic (shaping) amplifier (either Ortec 2021 or Canberra 2025) coupled to an Amptek portable digital multi channel analyser (MCA) was used to acquire the amplitude spectrum. The bias voltage was provided by the same supply as used in Section 3.2. Preamplification was performed using an Amptek A250 amplifier; for the PIN diode experiments this was preceded by a 2SK147 JFET amplifier stage (chosen to ensure a large gain-bandwidth product). The complete schematic is shown in Figure 3.4 [7].

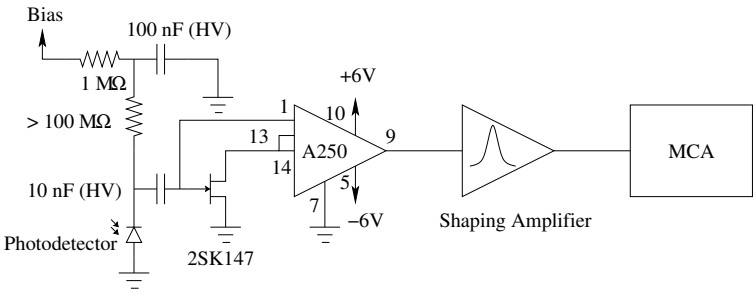

Figure 3.4 Test circuit for spectroscopic characterisation [7].

Energy calibration was performed using either two or three radioactive sources with known spectral peaks; depending on the number of calibration points, the energy axis was calibrated using a linear or second-order polynomial. Energy resolution was then calculated for the most significant spectral peaks by measuring the full width at half maximum (FWHM) directly from the spectral curve.

3.4 Ion Beam Induced Charge (IBIC) Collection

Ion Beam Induced Charge (IBIC) imaging is used to study charge collection and transport within a semiconductor device as a function of the location (and possibly angle) of particle ingress through the face of the detector. This can be used to infer properties of a photodetector under varying bias conditions, and gives an indication of the spatial uniformity of the detector's imaging properties. In IBIC imaging, a narrow beam of charged particles (typically α particles, protons or electrons) is scanned across a semiconductor device in a vacuum [105]. Beam energy and current can be adjusted as desired, and the amplitude spectrum of events detected at each beam position are recorded. This measurement quantifies the electron-hole charge transport resulting from the incident energetic ions within the biased detector, potentially down to micron-scale resolution. Charge collection with respect to position can be illustrated by reconstructing an image based on the peak energy observed at each point of the detector surface where the pixel intensity or colouration is indicative of its charge collection efficiency. It is also possible to pass the spectra through an energy window

and quantify how major impurities present within the detector bulk affect the charge collection of the detector.

Heavy charged particles - that is, those heavier than electrons - interact with the electrons of absorbing material along their path, mainly through scattering. This process is described by the *Bethe-Bloche formula* [98, 99, 106]:

$$-\langle\frac{dE}{dx}\rangle = Kz^2\frac{Z}{A}\frac{1}{\beta^2}\left(\frac{1}{2}\ln\frac{2m_ec^2\beta^2\gamma^2T_{max}}{I^2} - \beta^2 - \frac{\delta(\beta)}{2}\right) \tag{3.9}$$

where

- $\frac{dE}{dx}$ is the energy loss of the particle per unit length;
- K, $4\pi N_{AV}r_e^2m_ec^2 = 0.307075$ MeV.cm^2;
- z is the atomic number of the incident particle;
- Z is the atomic number of the traversed medium ($Z_{Si} = 14$);
- A is the atomic mass of the traversed medium ($A_{Si} = 28$);
- m_ec^2 is the rest energy of electron (0.511 MeV);
- β is the velocity of the particle in units of speed of light;
- γ is the Lorentz factor $\frac{1}{\sqrt{1-\beta^2}}$;
- I is the mean excitation energy ($I_{Si} = 137\ eV$);
- T_{max} is the maximum energy transfer to the electron; for all traversing particles except an electron, it can be approximated by $\approx\ 2\ m_ec^2\beta^2\gamma^2$. T_{max} of an incoming electron its energy; and
- $\delta(\beta)$ is a correction term that includes the density correction for high particle energies.

There are two key consequences of the Bethe-Bloche formula: firstly, particles with a higher atomic number have a higher rate of energy loss with respect to distance travelled; and secondly, the rate of energy loss for high energy particles is inversely proportional to their velocity. For an alpha particle, the loss of energy per collision is so small that the rate of energy loss remains approximately constant; as the particle loses most of its energy, the rate of energy loss increases rapidly and reaches a peak (the *Bragg peak*) before the particle is brought to rest [98, 99, 106].

The electron-hole pairs produced by the incident charged particle are collected at the electrical contacts of the device under test; this burst of charge is a current which can be integrated using a charge-sensitive amplifier to obtain an output voltage pulse whose peak is proportional to the total charge released. This is similar to the external electronics used to perform timing and spectroscopy characterisation. Thus by steering the beam across the detector in a raster pattern and logging observed pulse amplitudes, it is possible to obtain a spatial distribution of charge collection throughout the detector for a given particle energy. The same experiment can be repeated for different beam energies, bias conditions and detector orientations if desired.

The experiment was conducted using the High Energy Heavy Ion Microprobe (HIMP) of the ANTARES tandem accelerator at ANSTO [107]. The general experimental configuration is shown in Figure 3.5. Specific preamplifier circuits differ depending on the detector under test; the preamplifier circuit used with the planar PIN detector and the PIN detector with integrated JFET are shown in Figure 3.6.

IBIC measurements were performed using the Australian Nuclear Science and Technology (ANSTO) microprobe, where a 3 MeV He^{2+} beam with a spot size of 12 μm was scanned over the detector with a normal incident angle to the detector [107]. A CANBERRA 2025 spectroscopic shaping amplifier was used for subsequent charge pulse amplification, with a gain of 1000 and a shaping time of 4 μs. High voltage bias is provided by an ORTEC 710 quad bias supply. The data acquisition ADC has a resolution of 11 bits, linearly mapped to 2048 voltage levels in the range 0 to 10 V. The detector and its readout circuit was positioned in an evacuated chamber, reverse-

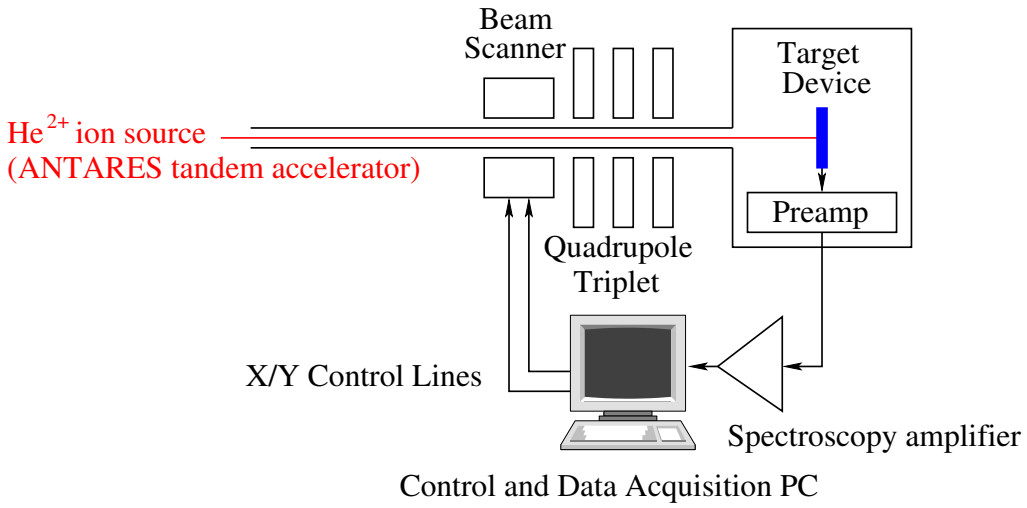

Figure 3.5 IBIC experimental configuration. Note that the sample board is electrically isolated from its mounting supports by perspex nuts.

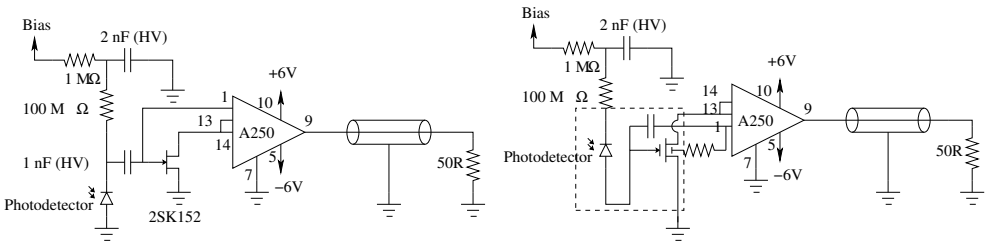

(a) PIN (b) PIN+JFET

Figure 3.6 IBIC preamplifiers for the devices tested in Chapters 4 and 5. The circuits are similar to the spectroscopic characterisation circuit in Figure 3.4. ±6 V supply rails are provided by a battery source to minimise extraneous noise.

biased at various potentials, and scanned in a 512 $\times$ 512 pixel matrix, at a spatial resolution of 2000 lines per inch (78.74 lines per mm).

Spectroscopic energy calibration was performed using a precision pulse generator and the low energy gamma peak from an $^{241}\mathrm{Am}$ source. Spectra were collected using the same Amptek MCA as used in Section 3.3.

3.5 Summary and Conclusion

In this chapter, methods for evaluation of the electrical, temporal and spectroscopic parameters of detectors were introduced. These methods will be applied in Chapters 4, 5 and 6 for the characterisation of three advanced solid-state detectors so that the most appropriate device can be selected for this project.

Chapter 4

Characterisation of a Planar PIN Detector

The simplest type of semiconductor photon detector suitable for use in PET applications is the p-intrinsic-n (PIN) photodiode [108]. These devices have a number of positive attributes, including uniformity of performance, high reliability and low production costs. However, their charge gain is unity. By contrast, devices such as PMTs, APDs and SiPMs have high intrinsic gain [109]. The intrinsic SNR of the PIN photodiode is thus relatively poor in comparison to these devices - however, its structure allows for convenient integration with monolithic front-end FETs [110] to provide direct, low noise coupling with an external readout electronic circuit at room temperature, as proposed by Kemmer and Lutz in 1987 and confirmed by Kemmer et al. in 1990 [111, 112]. It is also straightforward to integrate multiple PIN devices into a single detector array.

This chapter discusses the design and performance of a specific detector configuration based on a PIN photodiode optically coupled to a CsI(Tl) scintillator on its backside. The novel feature of this detector is that all electrodes and metallisation layers are on the detector frontside, resulting in a uniform optical window on the detector back side. The design can be easily extended to produce detector arrays of arbitrary size with maximum packing factor, making this device ideal for imaging applications [113].

4.1 Device Description

A diagram illustrating the internal structure of one detector segment is shown in Figure 4.1. The total optically-sensitive area is approximately 3×3 mm^2. The detector is fabricated on 300 μm n-type high resistivity (5 kΩ·cm silicon substrate. Surface passivation is achieved by a 0.7 μm thermally-grown oxide layer. The anode of the PIN photodiode (p^+ doped silicon produced by boron ion implantation) is located on the detector front side and is surrounded by a p^+ guard ring. The guard ring is maintained at the same potential as the anode to minimise the leakage current between the cathode and anode of the reverse-biased diode [114]. A 200 μm n^+ arsenic region is implanted along the pixel edge at a distance of 100 μm from the guard ring, which serves as a front side substrate contact [115]. A shallow, uniform n^+ arsenic ion implantation on the detector backside provides a good ohmic contact without the need for a metal layer, thus achieving good optical transmittance whilst also allowing the backside to be optically bonded to the scintillator. This implantation, in conjunction with an antireflective coating of alternating layers of silicon oxide and silicon nitride, provides a very high light collection efficiency [115, 116] and allows the potential applied at the substrate from the front-side contact to spread out to the entire photodetector matrix [115]. Using a multilayer anti-reflective coating of silicon oxide and silicon nitride also improves quantum efficiency, which has been measured to be 82% at 420 nm [116, 117]. All electrodes are fabricated with aluminium thin films and patterned on the front side of the device.

4.2 Simulation Results

In order to establish that the detector is fully depleted from the backside while reverse biased from the frontside, simulations were performed using the ISE-TCAD semiconductor simulation package [118]. A simplified two-dimensional model of the detector was constructed; due to the three-dimensional structure of the planar device (the sensitive area is square) it is expected that there will be some small differ-

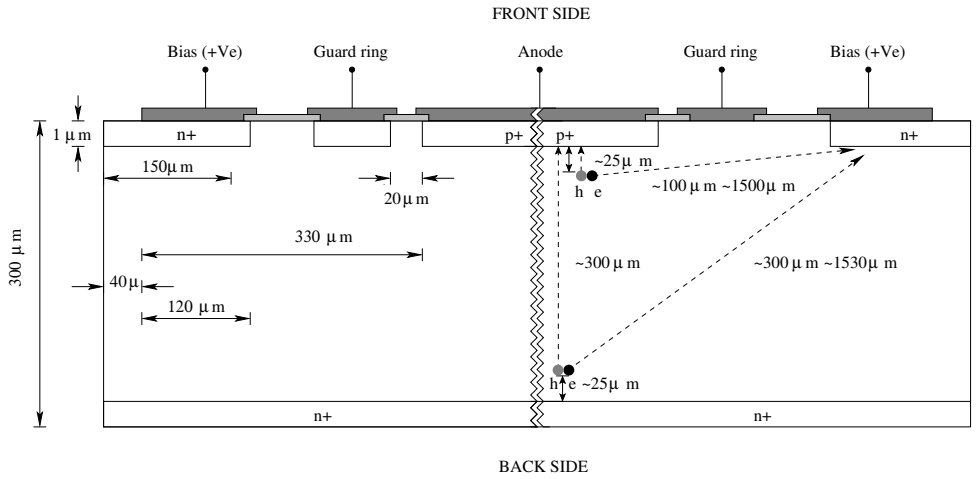

Figure 4.1 Planar PIN detector: cross-section (side elevation)

ences between the simulation and experimental results. Nevertheless, the simulation provides an insight into the internal behaviour of the device under a range of bias conditions and particle interactions.

Figure 4.2(a) shows the simulated electric field inside the detector when it is biased at a relatively low potential (10 V) and therefore underdepleted, while Figure 4.2(b) shows the electric field when the detector is fully depleted (biased at 50 V). The simulation shows that although the detector is underdepleted when biased at 10 V, the n^+ backside contact is maintained at nearly the same potential as the bias terminal - a condition that also holds when the detector is fully depleted.

Figures 4.3(a) and 4.3(b) show the electron density inside the detector when biased at 10 V and 50 V respectively. The regions with minimal electron density (which also are regions of maximal hole density) correspond to positive charge build up of the fully depleted PIN photodiode. This region is clearly defined in each figure, confirming that the entire detector volume (including lateral) is fully depleted at 50 V. Note that as this device has reached steady-state, the hole distribution is the complement of the electron distribution.

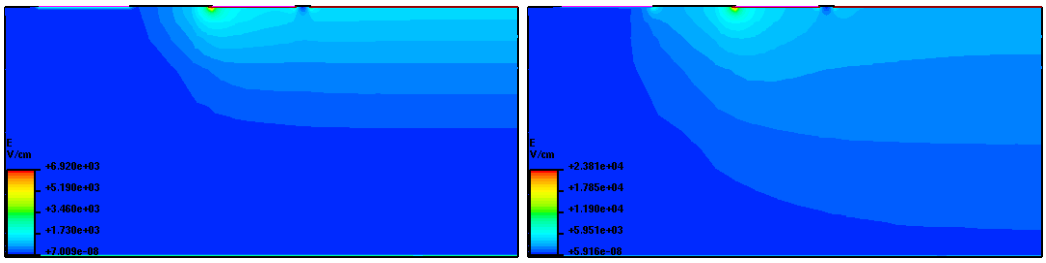

(a) Underdepleted at 10 V (b) Fully depleted at 50 V

Figure 4.2 Simulated electric field inside the planar detector at various bias potentials, prior to particle entry.

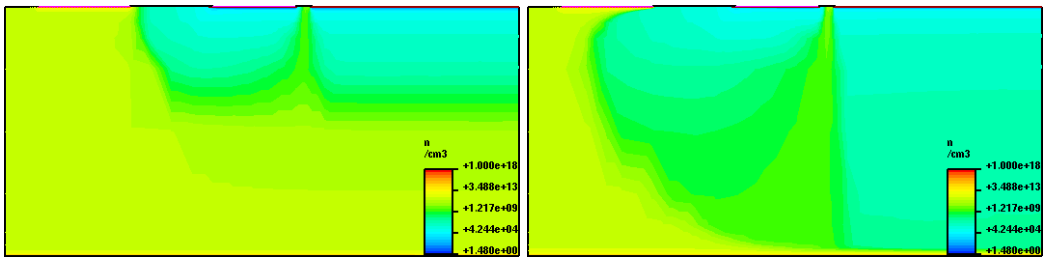

(a) Underdepleted at 10 V (b) Fully depleted at 50 V

Figure 4.3 Simulated electron density inside the planar detector at various bias potentials, prior to particle entry.

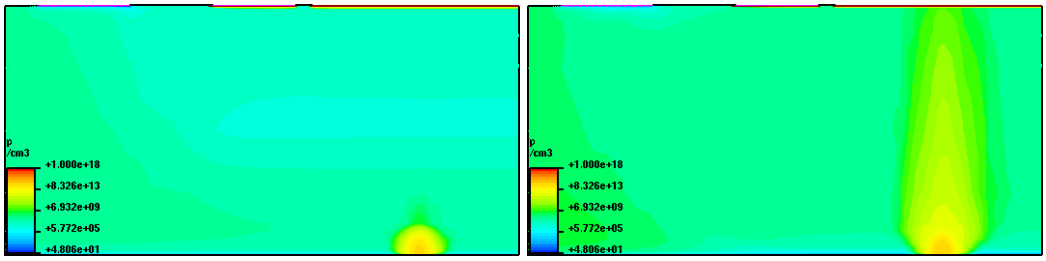

(a) Underdepleted at 10 V (b) Fully depleted at 50 V

Figure 4.4 Simulated hole density inside the planar detector at various bias potentials, post back side particle entry.

Transient current simulations were performed to evaluate the charge production at various points of entry within the device, and to test the operation of the guard ring. A single 3 MeV alpha particle was simulated to make an entry perpendicular to the back side of the device at time $t = 10$ ns. Hole distribution post-incidence of the alpha particle is shown for both the underdepleted and fully depleted device in Figure 4.4.

The simulation was repeated for front-side particle entry - however, electron and hole collection is much faster from the front side due to the shorter distance to the electrodes. Results of this experiment are shown in Figure 4.5 at $t = 2$ ns.

Transient current pulses for backside particle penetration are shown in Figure 4.6 for bias voltages between 50 and 100 V. Figure 4.6(b) illustrates the difference in transient current response where the particle is incident to the centre of the sensitive region and near the guard ring. The guard ring clearly collects almost all induced charge for this entry point, as the resulting current pulse is virtually flat.

4.3 Electrical Characterisation

All electrical measurements were performed both with a floating and grounded guard ring.

The measured leakage current is shown as a function of bias voltage in Figure 4.7.

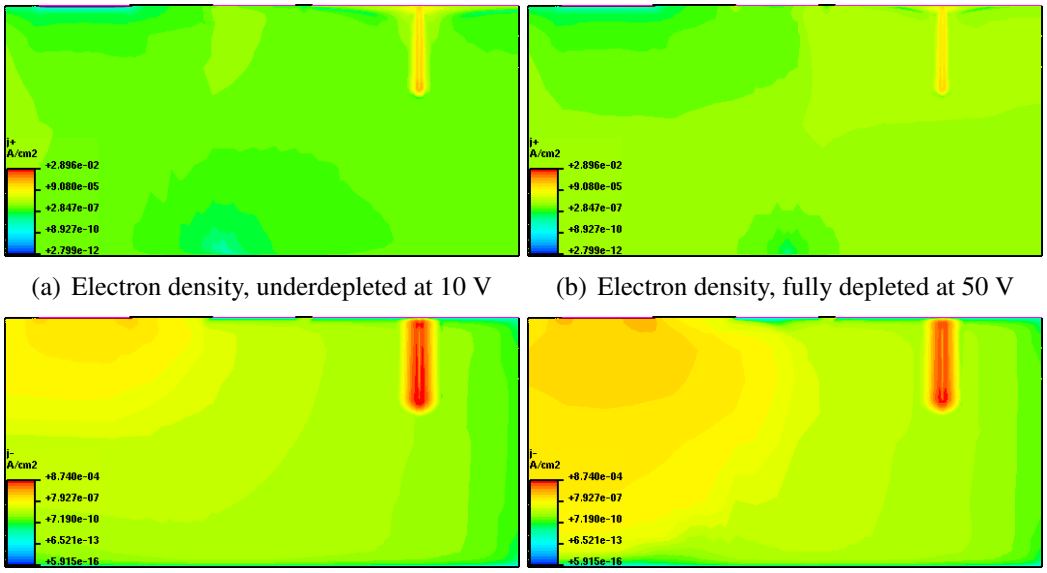

(a) Electron density, underdepleted at 10 V

(b) Electron density, fully depleted at 50 V

(c) Hole density, underdepleted at 10 V

(d) Hole density, fully depleted at 50 V

Figure 4.5 Simulated electron and hole density inside the planar detector at various bias potentials, post front side particle entry.

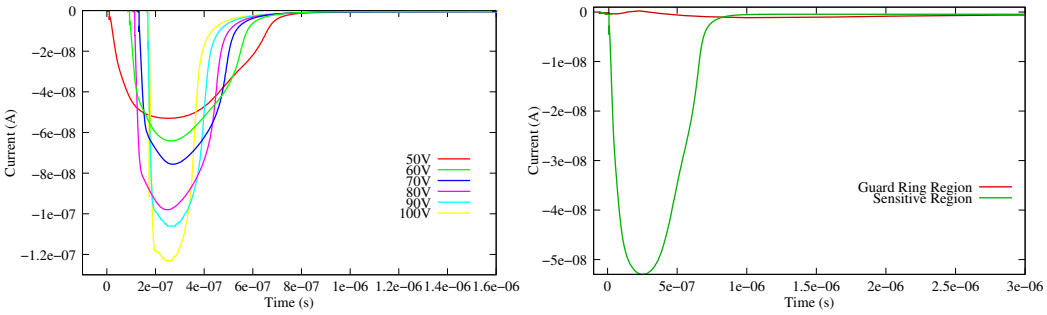

(a) Simulated backside transient current pulse waveforms

(b) Transient current response in the vicinity of the guard ring and sensitive region

Figure 4.6 Simulated transient current response of the planar photodetector; The point of entry was chosen in the middle of the sensitive region and close to the guard ring (Figure 4.6(b)) to test the guard ring's effectiveness.

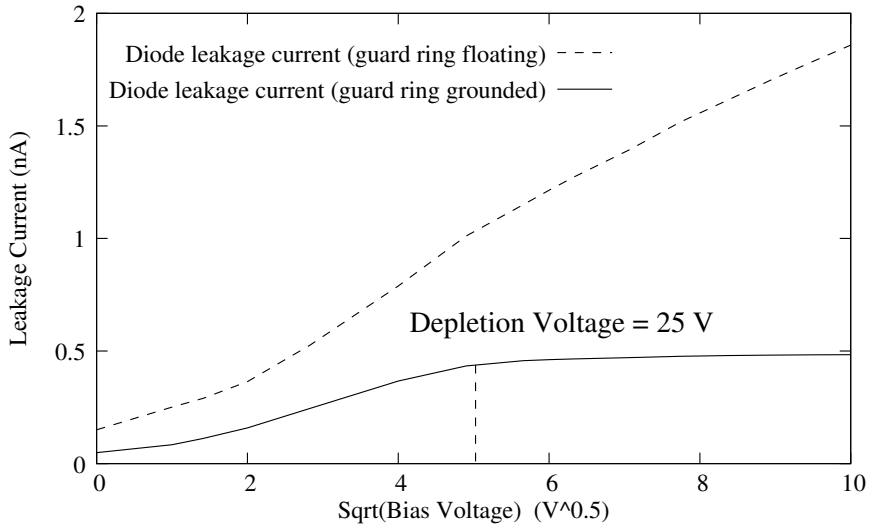

Figure 4.7 Leakage current versus square root of the bias voltage.

Leakage current initially increases rapidly with increasing bias voltage, then levels off as the bias voltage exceeds approximately 25 V (5 $\sqrt{\text{V}}$), asymptotically approaching a limit of 0.5 nA.

The behaviour of the leakage current with respect to bias voltage (I-V curve) depends on the electron-hole recombination current, which in turn depends on volume of the depleted region. This is clear from the almost linear behaviour of the curve up to a bias potential of 25 V, at which point the leakage current levels off (saturates) indicating full depletion (i.e. further increasing the bias potential will not result in a further increase the depletion volume, thus the leakage current saturates at 0.5 nA). With a bias potential of 50 V, no further increase in leakage current is observed.

Figure 4.7 also demonstrates the ability of the photodetector to be biased at voltages significantly above its depletion voltage, with no breakdown observed even at 100 V (75 V above full depletion voltage). Given that the leakage current is not growing, this provides an option for fully depleting the diode laterally, and thus gaining higher readout performance when used in combination with a scintillator (since detection of incident photons will be nearly uniform across the entire front area of the photodiode - an important property for imaging instrumentation).

As can be seen from Figure 4.7, when the guard ring is grounded, the dark current is reduced significantly - by a factor of more than 4.5 for large bias voltages. The difference in the measured diode leakage current with and without the guard ring grounded demonstrates its effectiveness in limiting the leakage current measured through the active volume of the diode. In this configuration, the grounded guard ring collects the majority of the leakage current related to surface electron-hole recombination and from the fraction of the detector volume outside the guard ring. The remaining leakage current is thus mostly contributed by the bulk of the photodiode within the region surrounded by the guard ring.

Figure 4.8 shows the measured and simulated capacitance values of the planar PIN diode structure, with the bias voltage applied to the n^+ contact on the detector's front side (bias contact). Bulk capacitance initially decreases rapidly with the increasing bias voltage, finally levelling off at approximately 3.5 pF. This capacitance is almost reached at a bias potential of 25 V, with a small further decrease as the bias voltage increases to 50 V, indicating that the device is fully depleted at this point, which agrees with the estimate based on the I-V characterisation (Figure 4.7). Results obtained from the simulation model (also shown in Figure 4.8) are in good agreement with the experimental results, with the small error being due to geometric simplifications used in the simulation model.

The theoretical capacitance of a 300 μm-thick 2.2×2.2 mm^2 fully-depleted vertical silicon PIN diode with grounded anode and guard ring (the former placed on the detector back side) is 1.6 pF. By contrast, the capacitance of the planar photodiode (biased at 50 V, thus fully depleted) was measured experimentally and found to be 3.5 pF. The p^+ region consists of a 2×2 mm^2 p^+ pixel connected in parallel with the surrounding 0.1 mm wide p^+ guard ring. Given the planar structure of the deviceand that the electrodes are placed on the frontside (see Figure 4.1), the additional component of the device capacitance is most likely a result of the lateral depletion, which extends to a distance of approximately 350 μm, and parasitic capacitance from the measuring equipment. The guard ring will also add slightly to the measured capaci-

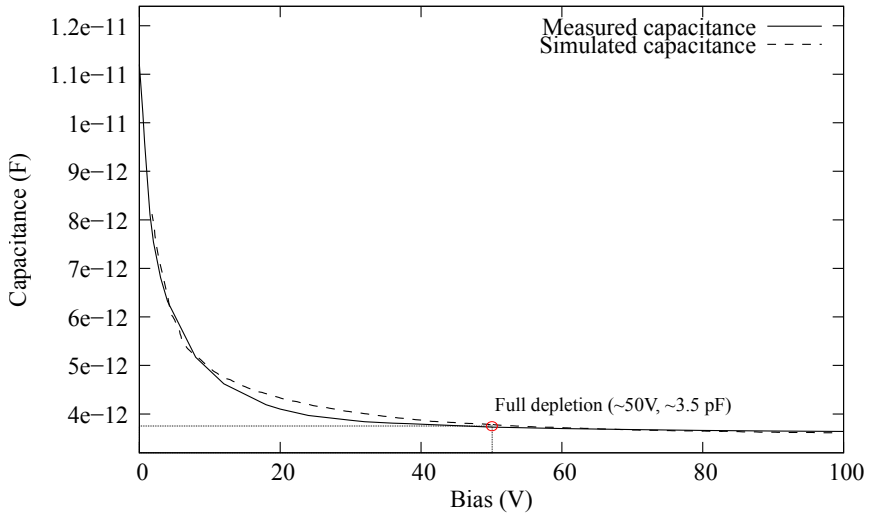

Figure 4.8 Capacitance (C) versus bias voltage - both the simulated and measured detector capacitance are shown. The guard ring is grounded.

tance.

4.4 Timing Characterisation

Carrier collection time was evaluated by measuring the transient current response of the system. The diode was connected to the input of a fast voltage amplifier (Phillips Scientific 6954 wideband amplifier) with an input impedance of 50 Ω and a voltage gain of 10. Amplified current pulses (measured as a voltage waveform) resulting are recorded by a LeCroy digital oscilloscope in averaging mode, to improve the signal to noise ratio. Figure 4.9 shows the current pulse responses resulting from direct interaction between alpha particles ($^{241}\mathrm{Am}$, 5.47 MeV) and the detector, with the detector biased at various potentials between 36 V and 100 V and the source placed on the front side in a vacuum chamber.

The electron-hole pairs are created near the surface of the active volume of the detector (a maximum depth of 25 μm for the 5.5 MeV alpha particles emitted by the ^{241}Am source). Since the electron-hole pairs are produced very close to the detector's p^+ region, the holes only have a short distance to travel before they are collected. How-

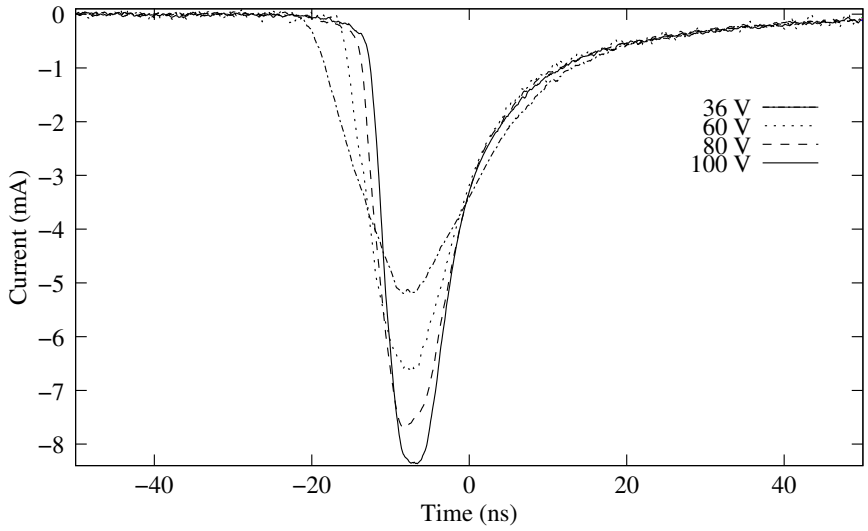

Figure 4.9 Transient current response - frontside illumination by 5.43/5.47 MeV α-particles (^{241}Am). Average of 500 pulses.

ever, the electrons must travel a considerably greater distance to reach their point of collection (at the n^+ bias terminal) - between 100 μm and 1500 μm, depending on the point of interaction (as shown in Figure 4.1). Therefore, while the time of collection of the holes remains relatively short and constant with respect to changes in bias voltage, the greater (and more variable) distance of electron travel prior to collection manifests itself as a long-tailed region on the average current response profile (Figure 4.9). The pulse shape is comparable to the results obtained in Section 4.2, although the scale is different due to the different energy of the incident alpha particles and the fact that the simulation was of a 2 dimensional partial slice of the edge of the detector only (for reasons of computational tractability).

Current pulses resulting from alpha-particle interactions when the source is placed on the detector back side are shown in Figure 4.10. The electron-hole pairs are generated near the surface of the detector's back side, and are collected by the front side electrodes (Figure 4.1). While the distance travelled by the electrons (moving towards the positively-biased n+ electrode) is only slightly greater than for the front-side situation ($\approx$ 300 μm - 1530 μm), the slower-moving holes must all travel a greater distance to be collected ($\approx$ 300 μm). This difference in travel distance for

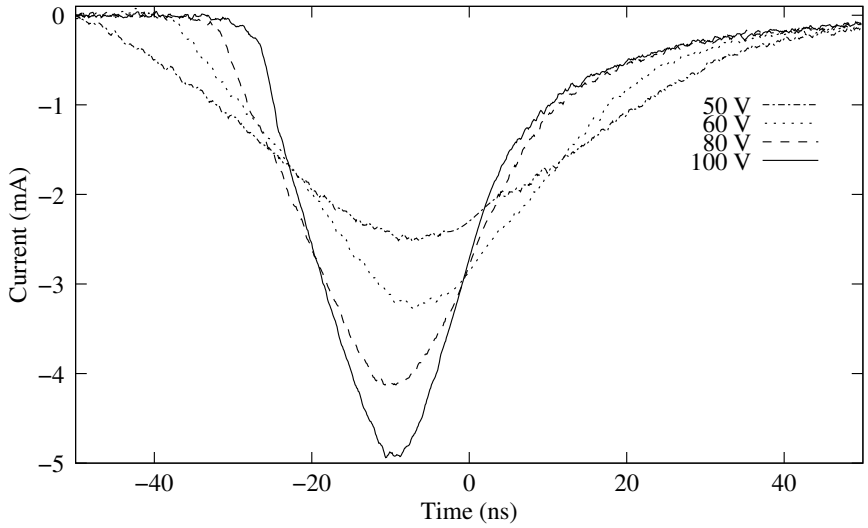

Figure 4.10 Transient current response - *in vacuo* backside illumination by 5.43/5.47 MeV α-particles ($^{241}\mathrm{Am}$). Average of 500 pulses.

the charge carriers affects the pulse shape, with greater temporal symmetry about the pulse peak (i.e. a smaller difference in rise and fall times). Specific rise times (10%-90% peak) and fall times (90%-10% peak) for a variety of bias voltages are listed in Table 4.1 for both front and back side illumination. The relatively small variation in fall time for front-side illumination (33% from underdepletion to full depletion) is a reflection of the relatively small variability in travel distance for the holes, while the rise time varies significantly due to the greater and more variable distance (with respect to the particle's ingress point and bias voltage) travelled by the electrons. With back-side illumination, fall times are greater than for front-side illumination but still relatively constant (as holes will move a relatively constant distance to the collection point compared to electrons) while rise times are also significantly greater and than for front side illumination and more variable with respect to bias voltage and ingress point compared to the fall time.

The results shown in Figures 4.9 and 4.10 demonstrate the fundamental difference between the transient responses of the planar PIN detector and a fully depleted vertical-structure PIN diode. In a vertical-structure PIN diode, alpha-particle interaction with the *back* side results in a current pulse dominated by *hole* drift through the entire

Table 4.1
Rise times (10%-90% peak) and fall times (90%-10% peak) for front and back side illuminated planar PIN diode at various bias voltages

Bias Voltage (V)	t_r **(front, ns)**	t_f **(front, ns)**	t_r **(back, ns)**	t_f **(back, ns)**
36	9.8	29.5	N/T	N/T
50	N/T	N/T	30.8	42.0
60	4.9	24.6	23.7	38.0
80	3.1	20.1	15.6	33.5
100	3.1	20.1	12.5	32.2

depletion region towards the p^+ front electrode. This results in a pulse duration of ≈ 20 ns, governed by the time taken for the holes to drift through the depletion region from the point of generation to the point of collection [119]. By contrast, when alpha particles interact with a vertical-structure PIN detector's *front* side, *electron* drift is the main contributor to the pulse, making it shorter (≈ 12 ns when biased at 150 V) due to the higher mobility of electrons [119]. However, for the planar detector discussed in this work, the n^+ electrode is located on the front side. Therefore, while the contribution from holes remains similar to that of the vertical-structure PIN diode, the electron path varies between 300 μm and 1500 μm. This makes the time of collection longer for the planar device, with the pulse lasting around 80 ns when illuminated from the back and 65 ns when the source is placed on its front side (biased at 100 V).

An additional factor affecting the current pulse profiles tending to make the back and front side pulses look alike is domination of electron drift - which depends on the precise point of interaction of the alpha particles in the planar PIN diode. Given the long range of electron paths, the shape of the average of a large number of backside pulses is not primarily determined by the holes, but by the electrons.

The effects of increasing the bias voltage are evident in Figure 4.10. Since depletion is occurring from the front side, the amount of collected charge is strongly dependant on the bias voltage. The electric field increases in strength in the same direction as the depth of depletion, reaching a maximum immediately adjacent to the electrodes

and a minimum in the backside region. Since the velocity of the charge carriers depends on the strength of the electric field, collection time decreases as the applied bias potential increases.

4.5 IBIC Characterisation

The device was connected to the same bias supply, JFET/A250 preamplifier, shaping amplifier and MCA as described in Section 3.3. Scans were performed at bias voltages of 10 and 50 V, which result in underdepletion and full depletion respectively. The experiment was performed twice: once with backside illumination, and again with frontside illumination.

Figures 4.11-4.12 show a succession of IBIC images in which the detectors illuminated from the back side and front side respectively. The upper subfigures in each case show the charge collection resulting from the detector being biased below full depletion voltage, while the lower subfigures show the detectors at full depletion. The left-hand subfigures in each case illustrate charge collection for the case where the guard ring is floating (open circuit), while the right-hand subfigures show the results obtained with a grounded guard ring. Red, green and blue colouration indicates areas with progressively higher charge collection. The IBIC maps clearly show the effect of the guard ring on the charge transport properties of the detectors: when the guard ring is grounded, no charge is collected around the edge of the detector.

Some non-uniformity in charge collection is noted on the underdepleted planar PIN device's backside. This is due to slight irregularities in majority carrier doping density over this region in the bulk of the semiconductor material. The horizontal discontinuities visible in Figure 4.11(c) and 4.11(d) are a result of stitching together multiple images with different sample densities.

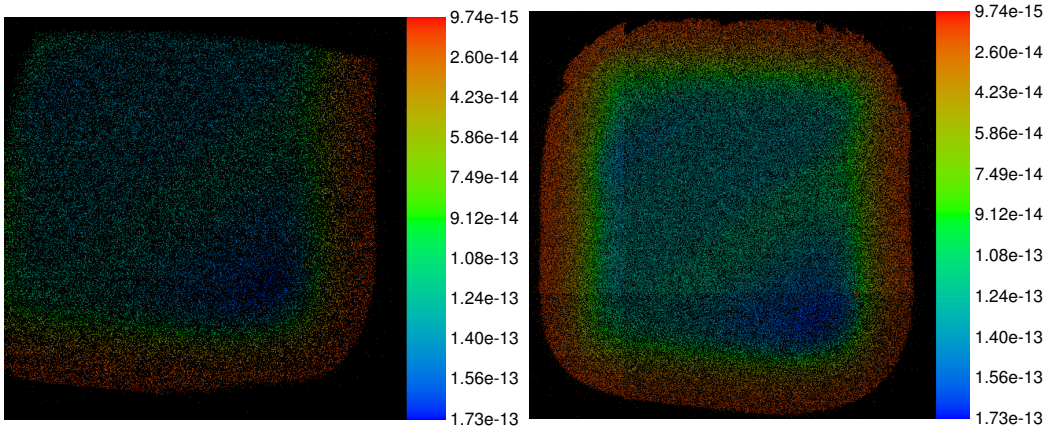

(a) Underdepleted photodetector (partial view) biased at 10 V - floating guard ring

(b) Underdepleted photodetector (full view) biased at 10 V - grounded guard ring

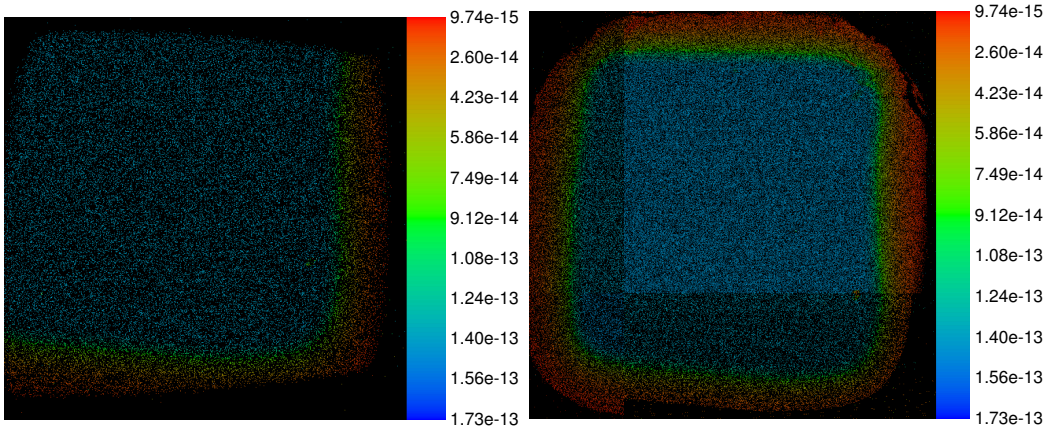

(c) Fully depleted photodetector (partial view) biased at 50 V - floating guard ring

(d) Fully depleted photodetector (full view) biased at 50 V - grounded guard ring

Figure 4.11 IBIC images of the the planar PIN device, backside illuminated, biased at 10 V and 50 V. Black represents zero charge collection, while red, orange, yellow, green and blue indicate areas with progressively greater levels of charge collection. The colourmap shows the charge calculated for each colour in coulombs.

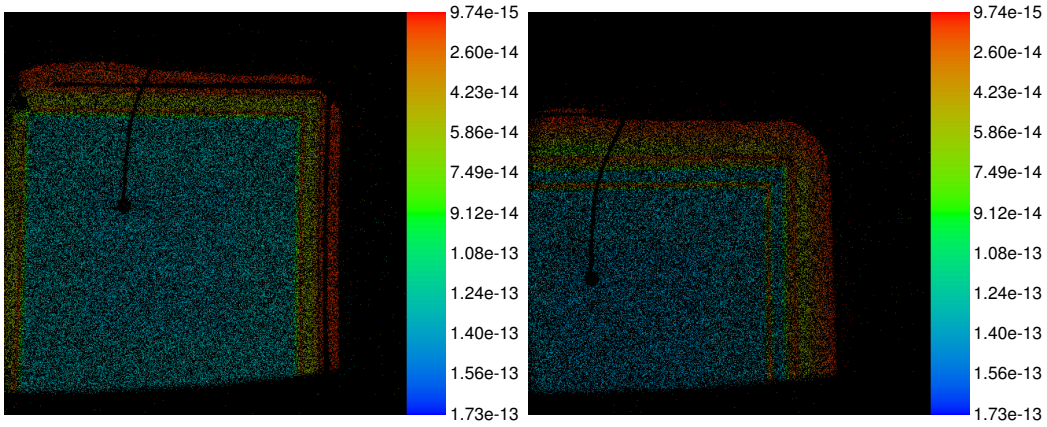

(a) Underdepleted photodetector (partial view) biased at 10 V - floating guard ring

(b) Underdepleted photodetector (partial view) biased at 10 V - grounded guard ring

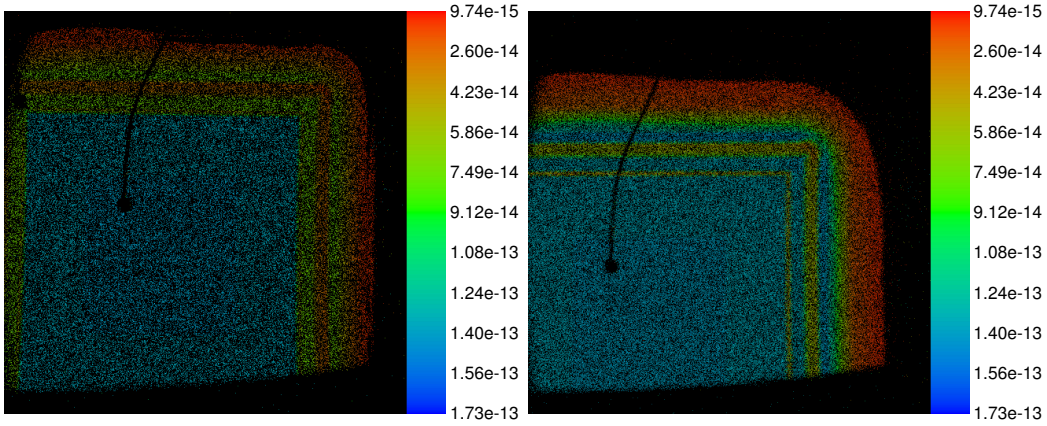

(c) Fully depleted photodetector (partial view) biased at 50 V - floating guard ring

(d) Fully depleted photodetector (partial view) biased at 50 V - grounded guard ring

Figure 4.12 IBIC images of the the planar PIN device, frontside illuminated, biased at 10 V and 50 V. Black represents zero charge collection, while red, orange, yellow, green and blue indicate areas with progressively greater levels of charge collection. The colourmap shows the charge calculated for each colour in coulombs.

4.6 Spectroscopic Characterisation

The detector was reverse-biased at 40 V (well into the region of full depletion) at room temperature, and coupled to the preamplifier, shaper, and MCA chain via a 2SK147 JFET, chosen for its low voltage noise density (0.5 nV.Hz$^{1/2}$). A shaping time of 4 μs was selected as this was found to provide the best energy resolution when used in conjunction with the customised optically coupled $2 \times 2 \times 3$ mm^3 CsI(Tl) crystal (for those spectroscopic measurements made using a scintillator). The guard ring was grounded during all measurements.

4.6.1 Low Energy Photon Sources (Direct Interaction)

The spectroscopic response of the detector to low energy γ-rays via direct interaction was measured at room temperature (21° C) using two sources: ^{125}I (using the 27 keV peak) and ^{241}Am (using the 14 keV peak). The resulting spectra are shown in Figures 4.13 (^{125}I) and 4.14 (^{241}Am), with their energy resolutions being 1.9 keV (7%) and 1.37 keV (9%) full width at half maximum (FWHM) respectively. The noise contribution of the readout electronics alone was evaluated by observing the output in response to an ORTEC 914 precision pulse generator coupled to the readout circuit via a 1 pF capacitor (with the detector disconnected), resulting in a FWHM of 1.25 keV (4.6%, also at 27 keV).

The energy resolution was also investigated using direct interaction with alpha particles from an ^{241}Am source. Both the source and detector were placed in a vacuum chamber for this experiment to prevent the attenuation of the alpha source by interaction with air molecules. The resulting spectrum is shown in Figure 4.15 - the minor 5.443 MeV and 5.388 MeV peaks are clearly visible. The energy resolution achieved for the main 5.486 MeV peak is 17 keV FWHM (0.31% FWHM), compared with 5.85 keV FWHM (0.1% FWHM) for the peak from the pulse generator.

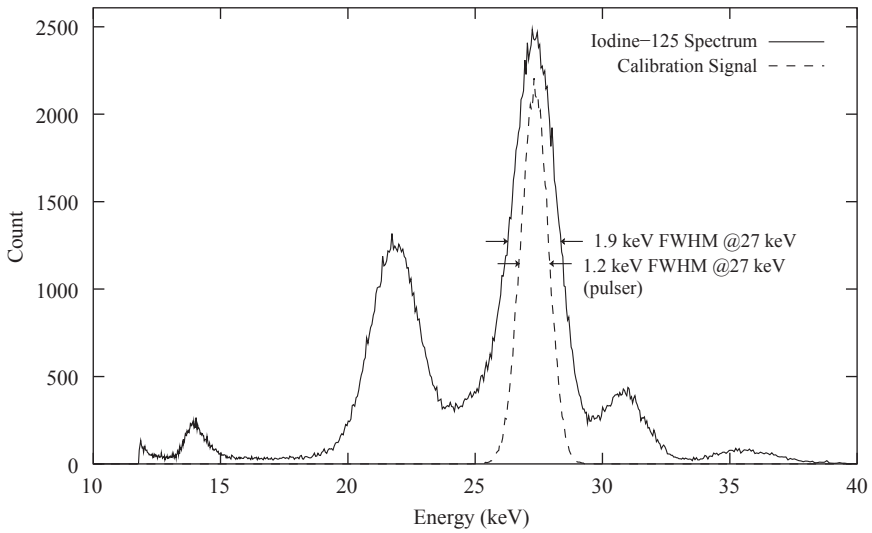

Figure 4.13 $^{125}\mathrm{I}$ spectrum obtained from the planar PIN diode detector. The backside-illuminated gamma spectrum is superimposed on the shaped spectrum of a test pulse from a precision pulse generator, for the purpose of electronic noise and energy calibration.

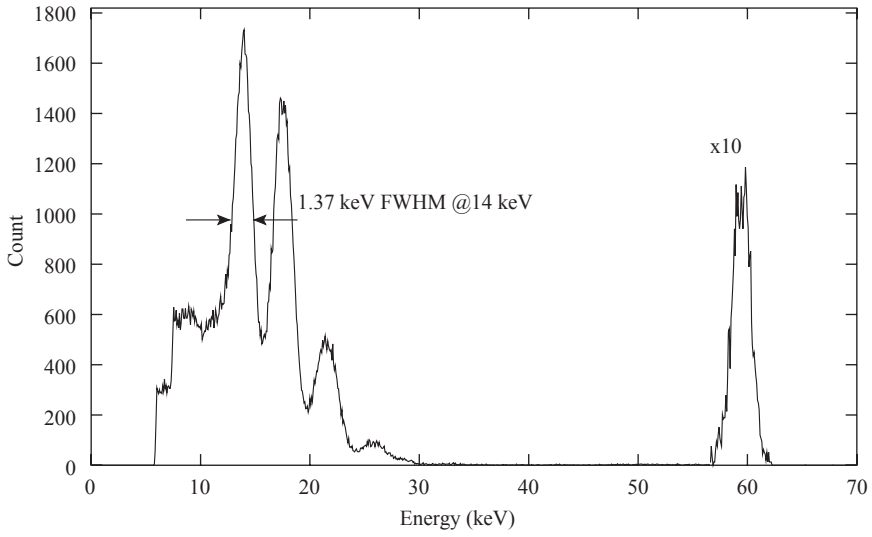

Figure 4.14 $^{241}\mathrm{Am}$ low energy gamma spectrum obtained from the planar PIN detector, with the source placed on detector's backside.

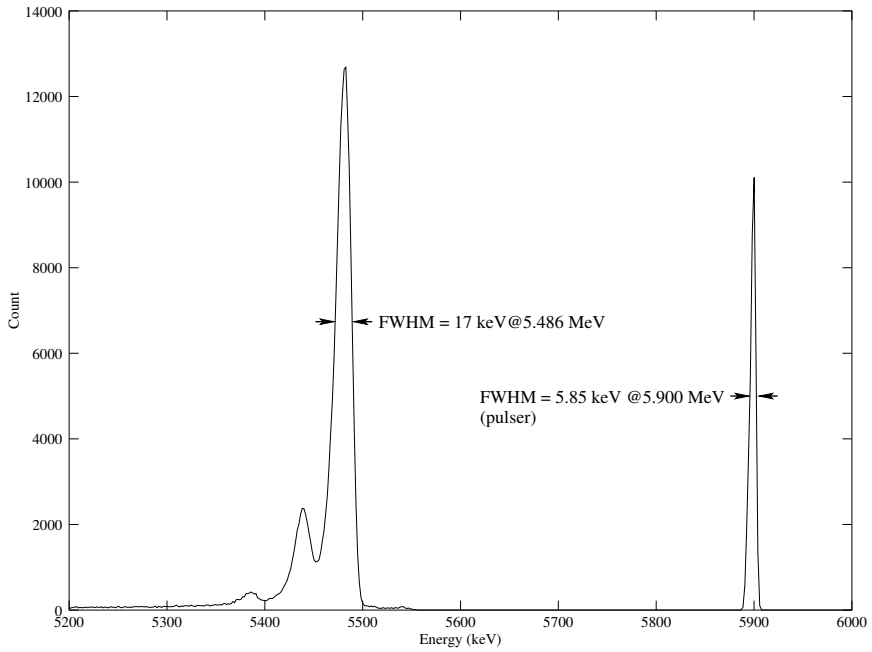

Figure 4.15 $^{241}\mathrm{Am}$ alpha spectrum. The 5.486 MeV, 5.443 MeV and 5.388 MeV peaks are clearly resolved. The peak at 5.9 MeV is produced by the precision pulse generator.

4.6.2 High Energy Photon Sources (CsI(Tl) Scintillator)

The detector performance was further evaluated in conjunction with a customised CsI(Tl) scintillator. This scintillator material was selected due to its high light output (of the order of 60000 photons per MeV, varying between samples [120]) and the fact that its peak output is at 530 nm - an ideal wavelength for silicon detectors as it is in the middle of the sensitive wavelength range (190-1100 nm [121]). The scintillator crystal is optically coupled to the back side of the photodiode with optical grease (NYE OC-431A), with a refractive index of 1.46 at 589.3 nm [122]. The grease prevents air from being trapped in the junction, which minimises losses due to discontinuities in refractive index (at the scintillator-air and air-detector interfaces). This maximises photon detection efficiency.

The energy resolution with the CsI(Tl) scintillator measured to be 27 keV FWHM (4% (FWHM)) for the 662 keV emission peak of a $^{137}\mathrm{Cs}$ gamma source (Figure 4.16), which represents an improvement on results previously reported for compara-

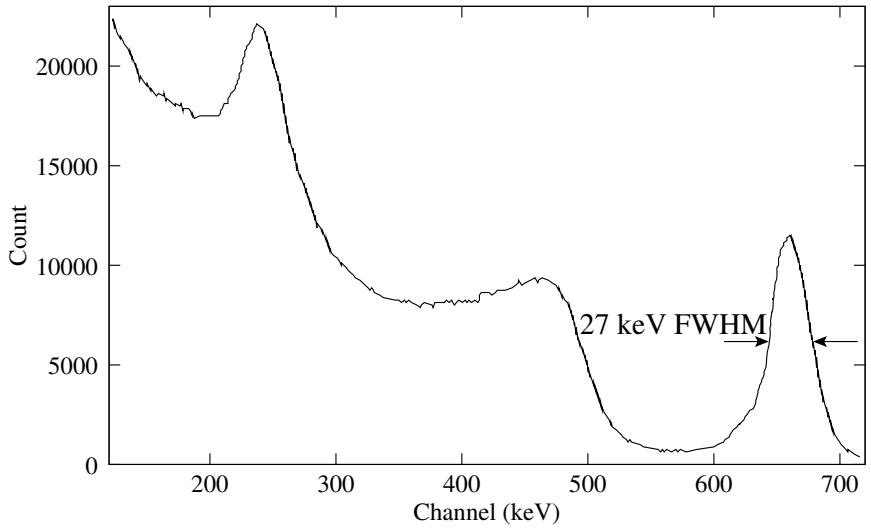

Figure 4.16 ^{137}Cs spectrum with detector biased at 50 V and coupled to a customised $2 \times 2 \times 3$ mm^3 CsI(Tl) scintillator (courtesy of Prof. Alberto Fazzi).

ble devices (such as the 5.8% FWHM reported by Patt et al. [44]). This demonstrates that coupling of the PIN diode's backside to the CsI(Tl) scintillator maximises both quantum efficiency and light collection efficiency.

4.7 Summary and Conclusion

The planar PIN photodiode with front side p^+ and n^+ electrodes, back-sided scintillator coupling and near-100% fill factor presented in this chapter is an efficient, modular, scalable design which is ideally suited for use as the imaging element in a pixellated gamma-ray detector.

The ISE-TCAD simulation of the electric potential and charge distribution in the detector under different bias voltages shows that the backside potential remains quite uniform and is approximately equal to the potential applied to the n^+ front-side region. This is a result of the the shallow n^+ implantation on the detector back side, which provides a low resistivity plane across the back surface of the device.

The front side pulses shown in Figure 4.9 exhibit a fast rise time, which corresponds

to initial fast drift of electrons in the strongest part of the internal electric field, and a long tail, related to the slower drift of electrons in the weaker field nearest to the front side $n+$ region. By contrast, the back side pulses shown in Figure 4.10 exhibit a slower rise time and decay time. This is due to the electrons' slower drift from the weak electrical field near the back side towards the front side $n+$ region, which results in a bell-shaped transient current pulse, in contrast to the constant slope pulse of a vertical-structure PIN diode.

Investigation of the electrical, spectroscopic and timing characteristics of the developed planar photodiode show that its performance is comparable to a vertical-structure back-side biased silicon photodiode of the same size (3×3 mm^2).

Optical coupling of CsI(Tl) on the photodiode's back side provides an energy resolution of 4% for 662 keV, indicating that the device offers high quantum efficiency. This makes the detector suitable for many nuclear imaging applications such as SPECT and gamma cameras. Use of this photodiode for PET applications, where fast scintillators such as LGSO are required, could therefore be considered. In contrast to the 530 nm peak wavelength of photons emitted by the CsI(Tl) scintillator, the much shorter wavelength of photons produced by LGSO scintillators means that they will be absorbed much closer to the detector surface due to their higher absorption coefficient. Taking into account the specific characteristics of the electric field in a planar photodiode (namely, the reduced electric field near the n^+ back side, confirmed by the transient current pulse response of the detector when illuminated from the back side) further studies with coupled LSO and LGSO scintillators will be used to evaluate the quantum efficiency of this device in response to shorter wavelengths.

A full pixellated detector module based on this PIN diode connected to an application-specific integrated circuit (ASIC) on the front side is expected to be an excellent option for gamma imaging cameras. For PET applications in particular, the main limitation of this device is the lack of intrinsic gain. This limitation will be overcome in two different ways by the devices described in the following Chapters.

Chapter 5

Characterisation of a Hybrid Detector

Modern solid-state radiation detectors and their associated readout electronics can now be fabricated on a common high-resistivity silicon substrate using a single manufacturing process [111]. This results in a reduction in the electronic noise, since the parasitic capacitance associated with preamplifier-detector connection is minimised. Furthermore, it reduces the need for shielding against capacitively-coupled pickup noise [111] and simplifies the circuit process assembly [67, 123, 124]. However, these benefits must be traded off against the increased complexity (and potentially cost) of fabrication. Therefore, the monolithic approach is normally only worth pursuing for detectors with a very low capacitance, such as pixel detectors and silicon drift chambers [125, 126].

As discussed in Chapter 4, discrete silicon PIN detectors are normally coupled to a charge-sensitive preamplifier circuit. In a standard detector preamplification configuration, this takes the form of a low-noise junction field-effect transistor (JFET) coupled to a specialised charge-sensitive operational amplifier such as the Amptek A250 with a capacitive feedback network. The idea of fabricating this JFET on high-resistivity silicon utilising detector-compatible processes dates back to the late 1980s. Early works by Radeka et al. [67, 123] and Holland et al. [42] resulted in successful implementation of Single Sided JFETs (SSJFETs) by applying the same

technological steps used for producing Charge Coupled Devices (CCDs) [43]. Another example of a detector with embedded electronics (a Depleted Field Effect Transistor (DEPFET)) was proposed by Kemmer and Lutz and successfully fabricated [111, 112].

The detectors used in this chapter are the result of ten years of research and development undertaken at FBK-irst (Trento, Italy) [127]. The device is based on a silicon PIN detector, featuring an on-chip n-channel JFET and matched feedback capacitor integrated on its p-side (frontside). This structure reduces electronic noise by minimising stray capacitance and enables highly efficient optical coupling between the detector back-side and scintillator, providing a fill factor of close to 100%. The detector is specifically designed for use in high resolution gamma cameras, where a pixellated scintillator crystal is directly coupled to an array of silicon photodetectors. The on-chip JFET is matched with the photodiode capacitance and forms the input stage of an external charge sensitive preamplifier (CSA). The integrated monolithic feedback capacitor eliminates the need for an external feedback capacitor in the external electronic readout circuit, improving the system performance by eliminating uncontrolled parasitic capacitances.

5.1 Device Description

The three-dimensional structure of the PIN and JFET detector is shown in Figure 5.1, while Figure 5.2 shows a photograph of front side of the detector, illustrating the monolithic circuit elements. The device includes a PIN diode detector with a p^+ implantation on the top side of the chip (with an area of approximately of $2 \times 0.4\ \mathrm{mm}^2$), coupled to an integrated n-channel JFET.

The JFET is a based on a double-gate (tetrode) structure and is fabricated on high resistivity (6 kΩcm) 300 μm n-type substrate [128]. The JFET has radial symmetry and is realised by triple implants on the top side of the chip. The conducting n-channel is a phosphorus n-implantation, in which the drain, source (n^+) and top-gate

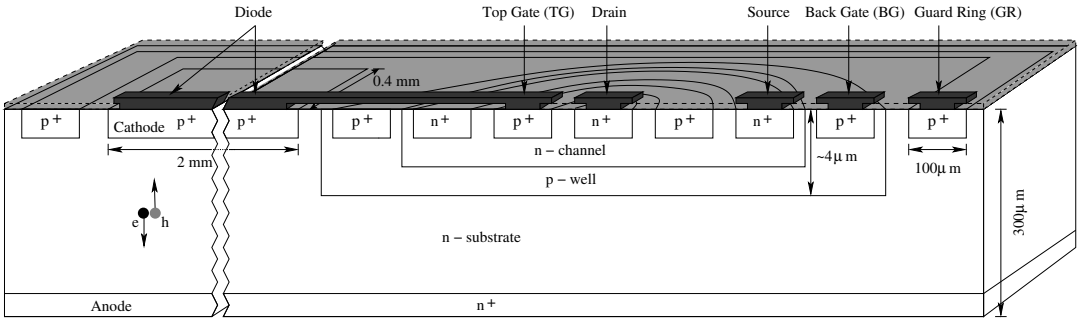

Figure 5.1 PIN+JFET detector: cross-section (not to scale)

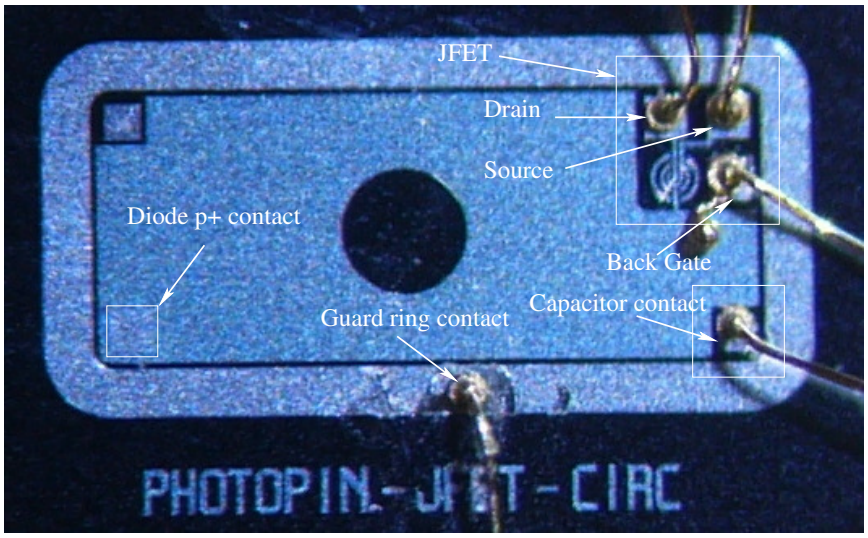

Figure 5.2 Layout of the PIN+JFET structure

(p^+) implants are embedded in successive concentric annular regions. Surrounding the n-channel is a p-well with an annular p^+ implantation which forms the back gate region.

The PIN diode's p^+ cathode, which collects the hole component of the event signal, is directly coupled to the JFET top gate through a metal strip [8]. A phosphorus-doped poly-silicon layer is present on the back-side to provide the n^+ substrate ohmic contact.

The JFET gate-source junction is forward biased and the drain current is stabilised by a low frequency feedback path to the JFET p^+ well contact (which serves as a secondary or back gate for the JFET). JFET channel conductivity is modulated by the bias voltages applied to the top gate and the p-well / back gate [8]. A 100 μm wide p^+ implanted guard ring surrounds the entire diode and JFET structure, collecting the leakage current and shaping the electric field. Since the detector is intended for spectroscopic applications which will require it to be coupled to a charge sensitive preamplifier (CSP), a feedback MOS capacitor of approximately 0.2 pF is incorporated in the device structure. The proximity of the feedback capacitor to the JFET minimises stray capacitance due to external wiring which would otherwise be needed [8]. A circular opening on the diode metal layer (300 μm diameter) is also present in the prototype samples and is used for evaluation of the electro-optical properties of the device.

The p-well allows the channel to be depleted simultaneously from both above and below, by applying the same negative voltage to the top gate and p-well contacts. Furthermore, it provides good confinement of the electrons flowing through the channel from source to drain, due to the high potential barrier existing at the channel-well junction [127].

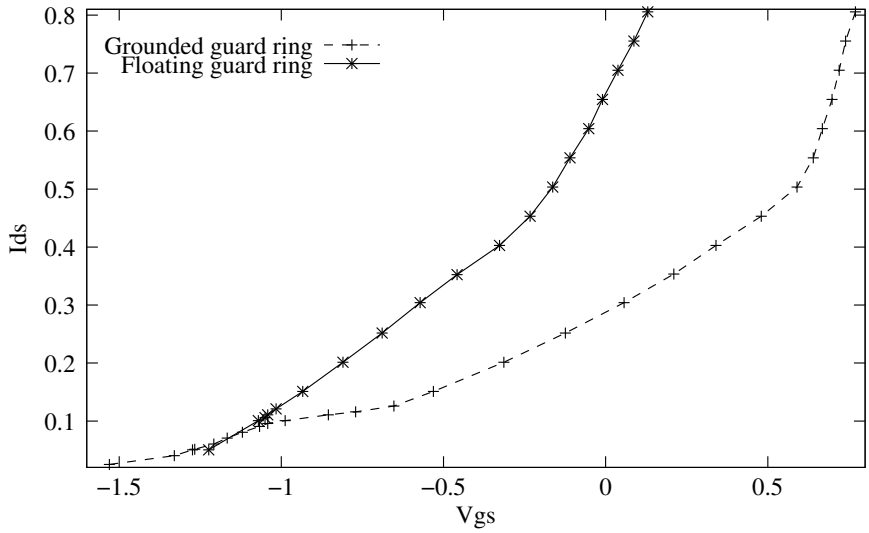

Figure 5.3 JFET $V_{gs} - I_{ds}$ transfer characteristics. The bottom gate is grounded (0 V), the drain voltage is +5 V and the substrate was biased at 32 V.

5.2 Electrical Characterisation

The relation between V_{gs} (the potential between the top-gate and the source electrode) and drain-source current I_{ds} is shown in Figure 5.3 (the drain voltage is held at 32 V and the p-well (back gate) is grounded). The curve exhibits the quadratic behaviour typical of field-effect transistors. The superficial component of the I_{ds}, contributed by the leakage current is removed when the guard ring is grounded.

Figure 5.4 shows the complete preamplifier circuit, which utilises a 'double feedback' configuration [8]. The cathode (which collects the holes) is connected to the top-gate of the JFET, providing a path to the grounded source via the $p - n$ gate-source JFET junction. The drain is coupled to the input of an A250 charge-sensitive preamplifier, whose output is capacitively coupled back to the top-gate of the JFET to complete the charge-integrating feedback loop. The resistive feedback path connecting the output of the A250 to the back-gate (BG) stabilises the drain current (I_d), which is strongly affected by variations in the quiescent leakage current [8].

A simplified schematic of the preamplifier circuit is shown in Figure 5.4, where the

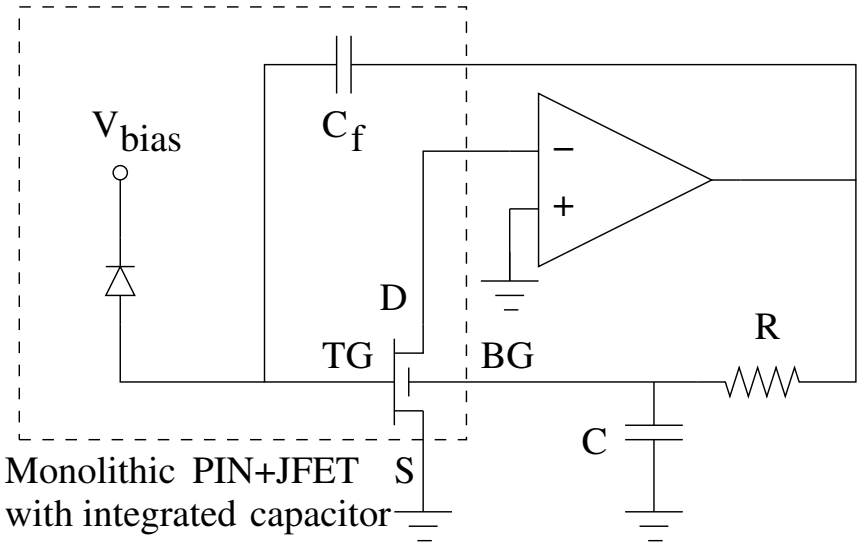

Figure 5.4 Simplified schematic of the preamplifier circuit with the monolithic device replaced by an equivalent discrete-component model; TG and BG refer to Top Gate and Bottom Gate respectively [8].

device is modelled by the discrete components inside the dotted region.

As discussed in Section 3.2, the two principal components of the equivalent noise charge (ENC) are leakage current (modelled as a parallel-connected noise source) and the bulk capacitance (modelled as a series-connected noise source) [95]. The asymptotic straight lines in Figure 5.5 show the individual contribution to the total noise from the series and parallel components. Series noise is dominant for short shaping times, while for long shaping times, the parallel component dominates. A minimum ENC of 152 electron RMS is obtained with a shaping time of 2 μs. This shaping time is therefore used for the spectroscopic characterisation in Section 5.4.

5.3 IBIC Characterisation

Figure 5.6 shows four IBIC images in which the detector was biased below and above the full depletion voltage and the guard ring was either floating (Figures 5.6(a) or 5.6(c)) or grounded (Figures 5.6(b) and 5.6(d)). The IBIC maps clearly show the effect of the guard ring on the charge transport properties of the detector: when the

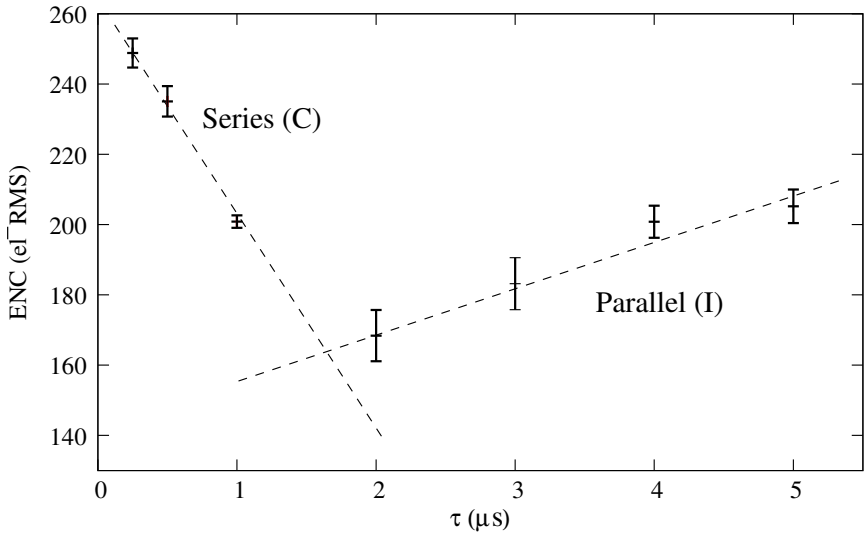

Figure 5.5 Equivalent Noise Charge (ENC) measured for different shaping time constants. The fitted dotted lines show the parallel and series components of the ENC.

guard ring is grounded, no charge is collected around the edge of the detector. The circular area visible within the p^+ region is caused by a fabricated gap in the aluminium metallisation, providing an optical window for electro-optical testing. The lack of aluminium layer results in a higher deposited energy (dark blue) in the photodetector.

The square region in the upper right-hand corner of the detector frontside (shown in Figures 5.2 and 5.6) is the monolithic JFET. The bonding pads (ohmic contacts) are visible as small dark regions in the IBIC images due to their total lack of charge collection. As the bias voltage increases, the collected charge from the area under the JFET (p-well) decreases, reaching zero at 20 V. As shown in Figure 5.1, the back gate contact (which is another p^+ region) surrounds the JFET's main electrodes. Therefore, the back gate contact behaves as a pseudo-guard ring around the JFET.

There are three separate P-N junctions in this device, each of which should be considered in order to fully understand the charge collection profile seen in the IBIC images. Specifically, these are the junctions between the cathode and anode, the guard ring and anode, and the pseudo-guard ring (p-well) and anode. When the bias potential

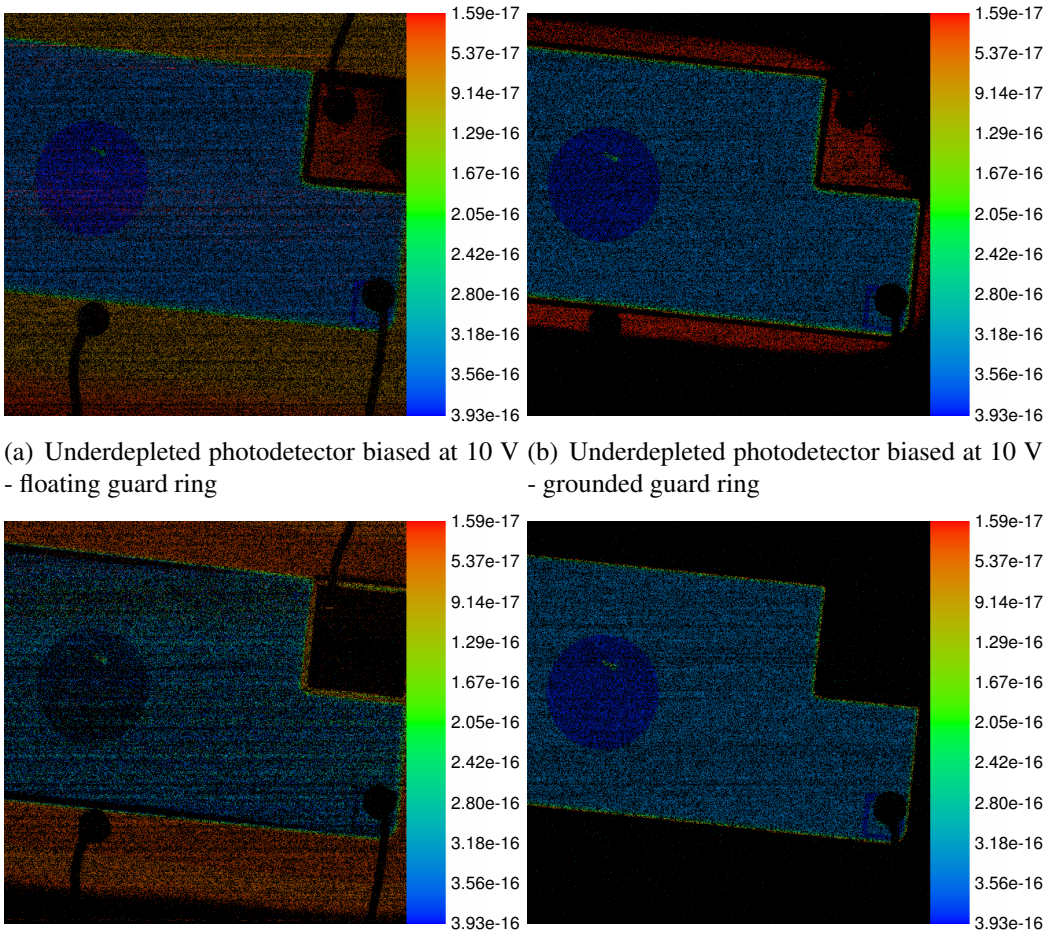

(a) Underdepleted photodetector biased at 10 V - floating guard ring

(b) Underdepleted photodetector biased at 10 V - grounded guard ring

(c) Fully depleted photodetector biased at 20 V - floating guard ring

(d) Fully depleted photodetector biased at 20 V - grounded guard ring

Figure 5.6 IBIC images of the the PIN+JFET device biased at 10 V and 20 V. Black represents zero charge collection, while red, orange, yellow, green and blue indicate areas with progressively greater levels of charge collection. The colourmap shows the charge calculated for each colour in coulombs.

is less than that required for full depletion, some of the electron hole pairs generated under the latter two junctions are collected by the cathode/anode junction (diffusion), and read out through the charge sensitive preamplifier circuitry. This is clearly seen across the partly illuminated JFET structure in Figures 5.6(a) and 5.6(b): charge collection is greatest at the corner of the JFET which is closest to the p^+ detector region (the upper-left corner of the square area), and zero at the opposite corner.

As the bias potential increases, all three $p - n$ junctions approach full depletion. Therefore, the electron-hole pairs which are generated within the substrate drift to the closest respective p^+ regions, and only those collected by the p^+ detector region are read out by the charge sensitive preamplifier. This lack of collected charge from underneath the JFET region is seen in Figures 5.6(c) and 5.6(d), where the square area corresponding to the JFET is uniformly black. However, since the detector is designed to be illuminated from the backside, this apparent dead region will not significantly impede the collection of charge carriers at the detector frontside.

5.4 Spectroscopic Characterisation - Low Energy Photon Sources (Direct Interaction)

The spectroscopic response of the detector to low energy γ-rays via direct interaction was measured using an ^{125}I source (27.47 keV) at room temperature (21°C). The resulting (calibrated) spectra are shown in Figure 5.7, with the guard ring potential set to -5 V, 0 V and +5 V and the detector reverse biased at 22 V. The best energy resolution achieved was 1.40 keV full width at half maximum (FWHM) (or 5.09%) at 27.47 keV, which was obtained with a grounded guard ring. This is because the guard ring can only efficiently remove surface leakage current when biased at the same potential as the cathode. Therefore, when the guard ring is grounded, leakage current (and noise) are reduced in comparison to the floating guard-ring state, hence improving the energy resolution of the detector. The noise contribution from the post-JFET analog signal processing chain was previously measured in Section 4.6.1

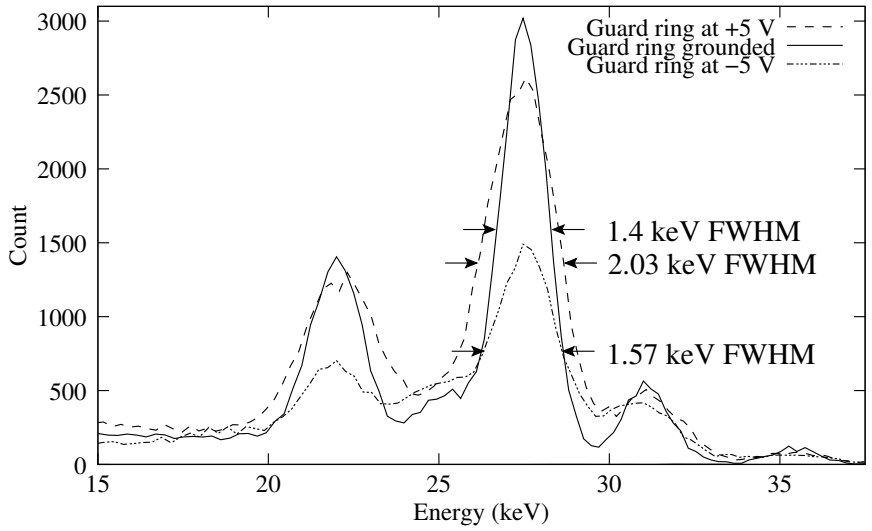

Figure 5.7 Calibrated ^{125}I spectrum obtained from the PIN diode detector biased at 22 V with integrated JFET and capacitor. The frontside-illuminated gamma spectra acquired at three different guard ring potentials are shown superimposed. The best resolution was achieved when the guard ring is at zero volts.

and found to be 1.25 keV FWHM at 27.47 keV (4.55% FWHM).

The same spectra are also shown *without* calibration in Figure 5.8. The progressive right shift in the spectrum as the guard ring potential becomes more positive shows that the gain of the charge-sensitive preamplifier circuit has also increased. This is because the capacitance of the monolithic feedback capacitor $\mathrm{C_f}$ has effectively decreased in value due to the modification of the depletion under the p^+ region of the detector close to $\mathrm{C_f}$. This decrease in C_f results in an increase in gain of the charge-sensitive amplifier (since the gain of such an amplifier configuration is proportional to $1/C_f$).

It is noted that in its present form, this detector is not suited to use with a scintillator as the integrated JFET and feedback capacitor are on the sensitive front side of the detector. Therefore, high-energy spectral characterisation with a scintillator has not been performed.

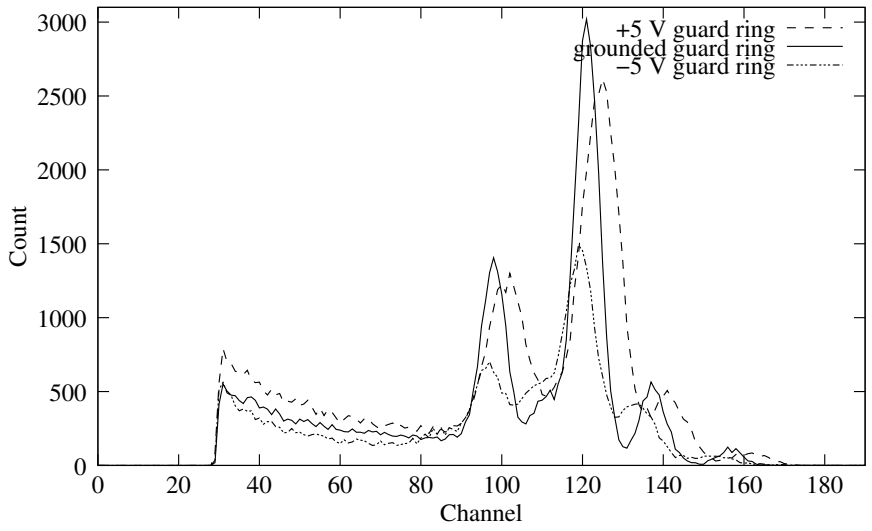

Figure 5.8 Uncalibrated ^{125}I spectrum obtained with at various guard ring bias potentials. The progressive shift in the gain is due to the increase in the effective capacitance of monolithic feedback capacitor as the guard ring potential becomes more positive.

5.5 Summary and Conclusion

The integration of a JFET and monolithic capacitor results in an excellent low energy gamma resolution, mainly due to the reduction of the electronic noise. The IBIC images show a uniform charge collection in the p^+ detector region, while grounding the guard ring removes the collected charge around the detector edge. The noise level of a single pixel (152 e^-) is comparable to systems with non-integrated readout electronics. However, the ultimate objective is to extend this design to a pixellated detector array (of 8x8 or 16x16 pixels) for medical and spectroscopic applications in which the use of fully-external electronics is undesirable due to the variability of parasitic capacitances in the external feedback path. The use of an integrated JFET and monolithic feedback capacitor therefore will provide improved uniformity of gain across all pixels.

The effect of guard ring biasing on the MOS capacitance and therefore the detector resolution can be easily reduced by moving the capacitor away from the guard ring. The JFET could be surrounded by a low resistivity n^{++} pocket to effectively isolate

it from the rest of the device.

For future PET systems, a PIN device with integrated JFET and monolithic capacitor may be a good choice; however, at present such devices are not commercially available in a suitable densely-packed matrix layout suitable for PET detector block modules. Therefore, an alternative device, the silicon photomultiplier, which provides intrinsic gain through a different mechanism, will be investigated in the next Chapter.

Chapter 6

Characterisation of a Silicon Photomultiplier Detector

Silicon photomultipliers (SiPM) are a new class of photo-detector which provide an intrinsic gain for a single photo-electron of the order of 10^6 [47, 48, 129, 130]. The performance of SiPM devices (such as gain and response time) is comparable with that of a vacuum photomultiplier tube. The SiPM is based on an array of independent p-n junction avalanche photodiode (APD) micro-cells with an integrated quenching resistor and a common substrate. The APDs operates in limited Geiger mode with a bias voltage a few volts above breakdown [131].

The signal produced by an individual micro-cell contains digital information; when a photon hits the micro-cell, it generates a single current pulse. However, when an array of identical micro-cells is hit by incident light, the amplitude of the resulting current signal (summed across the whole matrix) is quantised and proportional to the number of incident photons. Hence, direct measurement of low-energy photons is not practically possible, as any single photon interacting with any cell will result in essentially the same current pulse. Therefore, even for low energy photon detection, the SiPM must be used in conjunction with a scintillator with matching optical characteristics. More recent devices provide a timestamped digital count of the number of triggered cells rather than an amplitude-quantised current pulse [132].

The main parameters which characterise the performance of a SiPM sensor are the leakage current, the dark rate and the internal gain. The leakage current and the dark rate determine the level of noise in the detector. The leakage current is defined as the sum of bulk and superficial currents of the reverse biased device before its breakdown while the dark count is the number of avalanche current pulses produced by thermally generated electrons. Hence the dark count rate is the number of such false events per second. The dark count rate is determined by the sensitive area of the SiPM, the bias voltage and the operating temperature [53, 133].

This section focuses on the characterisation of a silicon photomultiplier, optically coupled to an LGSO scintillator. The device is an FBK-Irst SiPM sample, developed in the framework of the INFN/PAT DASiPM2 Collaboration (MEMS Project) [134]. Energy resolution for low and high energy gamma radiation has been measured using ^{241}Am, ^{57}Co, ^{109}Cd, ^{22}Na and ^{137}Cs gamma sources. Linearity and saturation results are also reported.

6.1 Device Description

The SiPM detector was fabricated on a p-type epitaxial layer. It consists of an array of 625 micro-cells covering an active area of 1×1 mm^2. Each micro-cell (40×40 μm^2) is composed of a shallow n$^+$-p junction in series with a poly-silicon quenching resistor (Figure 6.1), the resistance of which was estimated to be approximately 300 kΩ [135]. The isolation trench is covered by an aluminium grid which acts as an optical reflector of the photons incident on the neighbouring cells as well as an electrical connector between the micro-cells.

The sample referenced throughout this section is from the second production batch fabricated by the FBK-irst in October 2006 and is identified by code BiT3V1PD9.

Electrical and gamma ray spectroscopy characterisation has been performed using an electronic readout system including a high bandwidth (600 MHz) ORTEC 474 fast

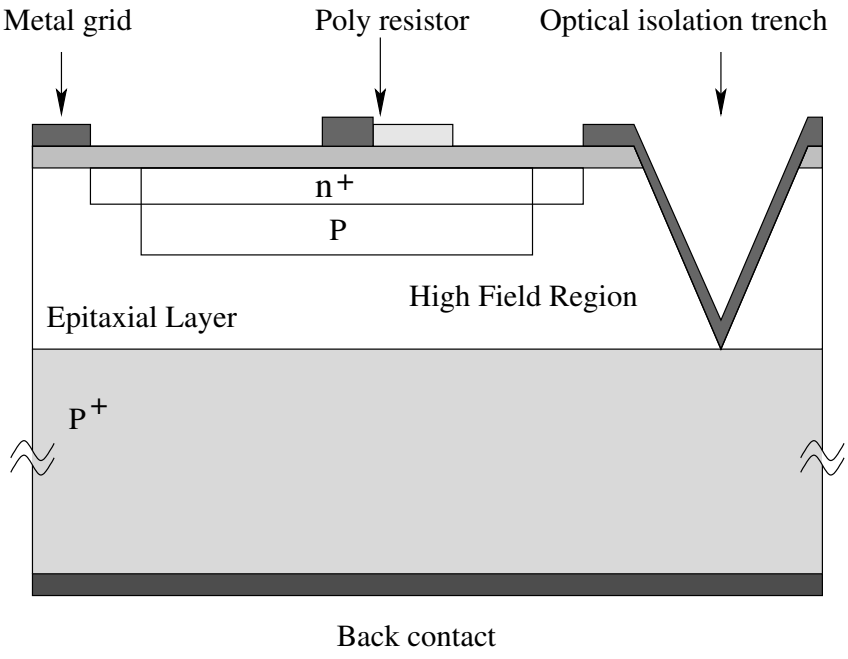

Figure 6.1 Silicon Photomultiplier: peripheral cross-section (not to scale)

timing amplifier (FTA) with an input resistance of 50 Ω and a gain of two. The FTA is followed by an ORTEC 671 spectroscopy amplifier with a shaping time of 500 ns and a gain of 1000. The second amplifier stage was necessary to match the input impedance and the dynamic range of the Multi Channel Analyser (AMPTEK MCA 8000A). Leakage current was measured by a Keithley 614 Electrometer.

6.2 Electrical Characterisation

The leakage current of the SiPM is plotted as a function of applied bias voltage in Figure 6.2. The graph shows two distinct regions: between zero and the breakdown voltage, where the I-V characteristic resembles a depleted p-n junction; and beyond the breakdown voltage, where it grows exponentially due to the generation of the discharge pulses caused by thermo-exited electrons at room temperature [53, 133, 136, 137]. Based on the results shown in Figure 6.2, the breakdown voltage is 34.5 V, at which point the leakage current is approximately 10 nA.

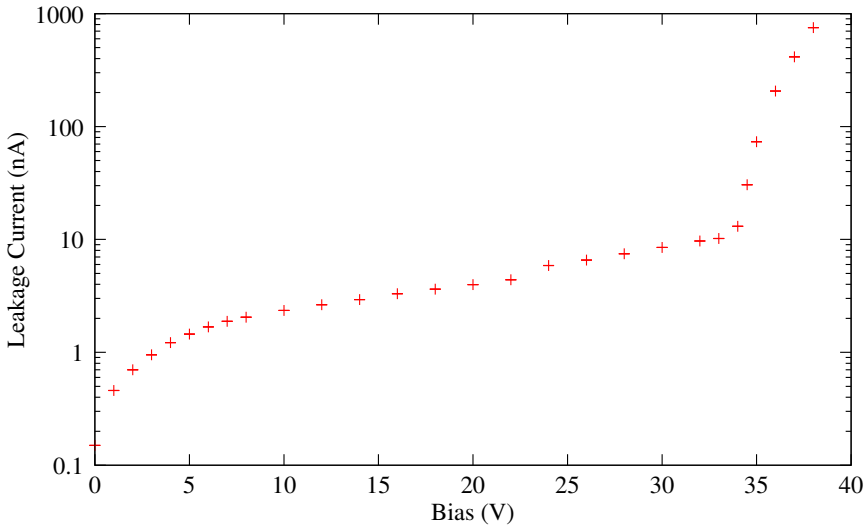

Figure 6.2 Leakage current, measured prior to the application of the optical gel and scintillator.

Like all solid-state photo-detectors, the SiPM intrinsically generates a certain level of background noise. Dark current originates from thermally generated electrons; it is measured in dark conditions at room temperature using an electrometer directly connected to the device.

The dark noise was measured for different bias voltages. Figure 6.3(a) shows the normalised pulse amplitude spectra for different values of bias voltage slightly greater than the breakdown voltage. Measurements were performed without any scintillator

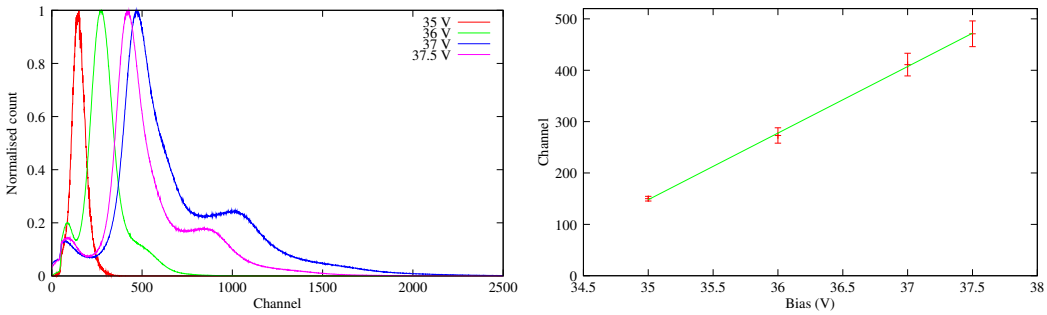

(a) Dark noise spectra measured at different bias voltages.

(b) The peaks of noise spectra plotted as a function of the bias voltage.

Figure 6.3 Noise characteristics of the SiPM detector.

attached. The dark pulse rate was found to be approximately 1 MHz at room temperature. The low amplification gain makes it impossible to resolve the discrete peaks associated with the contribution of a single or multiple electrons to the background dark current. However, it is possible to see the Gaussian distribution of the dark pulse amplitude produced by the photo-electrons.

The gain of a SiPM is known to increase linearly as the bias voltage is increased [53]. The relative position of the peaks of the dark count rate spectra as a function of the bias voltage is shown in Figure 6.3(b). The shift in the spectra clearly follows a linear model as expected.

The appearance of an extra peak in the dark count spectra measured at 37 V and 37.5 V in Figure 6.3(a) is due to the after-pulsing phenomena [134]. The peak begins to appear when the applied bias exceeds the breakdown voltage ($\mathrm{V_{BD}}$) by 1.5 V, and becomes pronounced at 37.5 V (3 V above $\mathrm{V_{BD}}$). Achieving the best energy resolution relies on choosing an optimum bias voltage.

6.3 Scintillated Pulse Characterisation

The avalanche process in the SiPM generates an output current pulse shaped by the sub-pixel capacitance and with a very short rise time (less than 1 ns). The decay time of the pulse is dominated by the quenching resistance and the input impedance of the preamplifier stage, providing a total recovery time of approximately 20 ns [138]. With a decay time constant in the range of 40 ns for fast scintillators (LSO family), it is the intrinsic timing properties of the scintillator that determines the response time of the whole system.

The SiPM has been designed to reach maximum photo-detection efficiency at a wavelength of 420 nm, typical of the LSO scintillator family. Therefore, a $1 \times 1 \times 3\ \mathrm{mm}^3$ LGSO scintillator (from Crystal Photonics Inc. - USA) was coupled to the sensor using optical grease with a refractive index of 1.62 (NYE Optical Inc.). All other faces

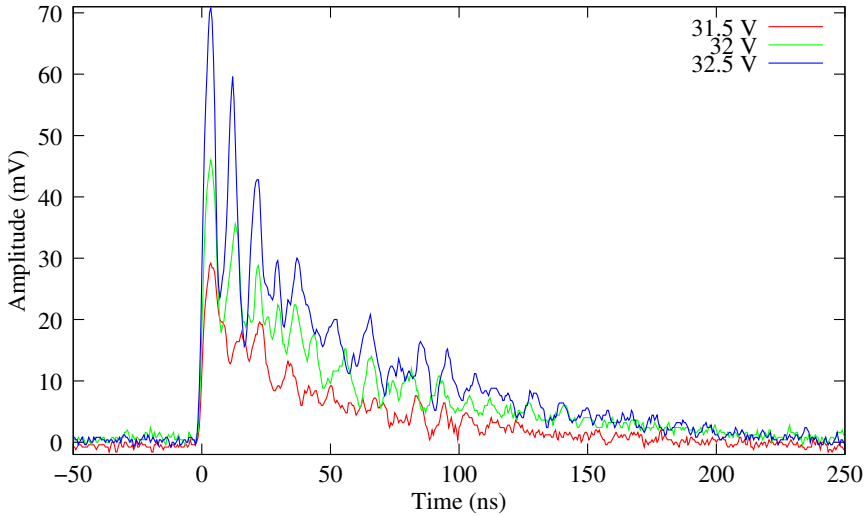

Figure 6.4 Current pulse generated by a 122 keV photon, detected by the SiPM coupled to an LGSO scintillator with a 40 ns decay time constant and amplified by the FTA.

of the scintillator were painted with a white reflective coating. The output pulses of the SiPM when exposed to 122 keV gamma photons are shown in Figure 6.4. The current pulses generated by the SiPM are amplified by the previously mentioned fast timing amplifier to prevent any distortion of the output pulse shape.

The SiPM output pulse differs in shape from that of a silicon PIN diode or a photomultiplier tube (PMT), whose outputs are smooth analog signals. The rise time of a pulse generated by a fully depleted PIN photodiode connected to a charge sensitive amplifier is dominated by the emission rate of its coupled scintillator, while the decay time depends on the time constant of the shaper, which is of the order of several μs. The output pulse of an SiPM detector coupled to an LGSO crystal is the convolution of the decay time of the scintillator and the recovery time of the sub-pixel. Therefore, the output of the fast timing amplifier is composed of short pulses modulated by the decay time constant of the photons emitted by the scintillator. The LGSO decay time constant ($\tau \approx 40$ ns) requires the use of a shaping time greater than 120 ns (3τ) for complete pulse integration and shaping, which results in a smooth pulse shape easily processable by the MCA.

6.4 Scintillator Optical Characterisation and Calibration

[139].

Since the dynamic range of the SiPM is determined by the number of pixels per unit area, a crucial step in the design of the experimental configuration was to correctly estimate the number of photons hitting the sensitive area of the sensor to avoid overloading and thus saturating its response. The effective scintillator light collection efficiency (SLICE), which represents the fraction of total incident photons that are absorbed by the sensitive area of the detector [139], was evaluated by coupling it to a silicon PIN photodiode with an active area of $1 \times 1\ \mathrm{mm}^2$ and an anti-reflective coating which fits well the optical response characteristic of the surface of the SiPM sample [116]. The detector was reverse biased at 30 V and irradiated with 511 keV and 662 keV gamma photons emitted by $^{22}\mathrm{Na}$ and $^{173}\mathrm{Cs}$ sources, respectively. Calibration of the PIN photodiode (in terms of the number of photoelectrons generated) was performed using a precision pulse generator and a $^{125}\mathrm{I}$ gamma source, with the 22 keV and 27 keV gamma photons directly interacting with silicon. The spectra obtained are shown in Figure 6.5.

511 keV annihilation photons which interact with an LGSO scintillator produce a peak in the blue part of the optical spectrum equivalent to direct interaction of 9 keV photons with silicon [116]. This peak, when combined with the detection quantum efficiency of 85% measured at a wavelength of 470 nm, results in an estimated total of 2940 photons reaching the sensitive area of the photodiode for each 511 keV photon incident on the scintillator. This corresponds to a SLICE for the LGSO scintillator of $22.3 \pm 4\%$.

The Signal to Noise Ratio (SNR) of a SiPM detector is a function of the number of photons emitted by the scintillator due to the incident gamma photon and the number of dark electrons generated thermally by the sensor [140, 141]:

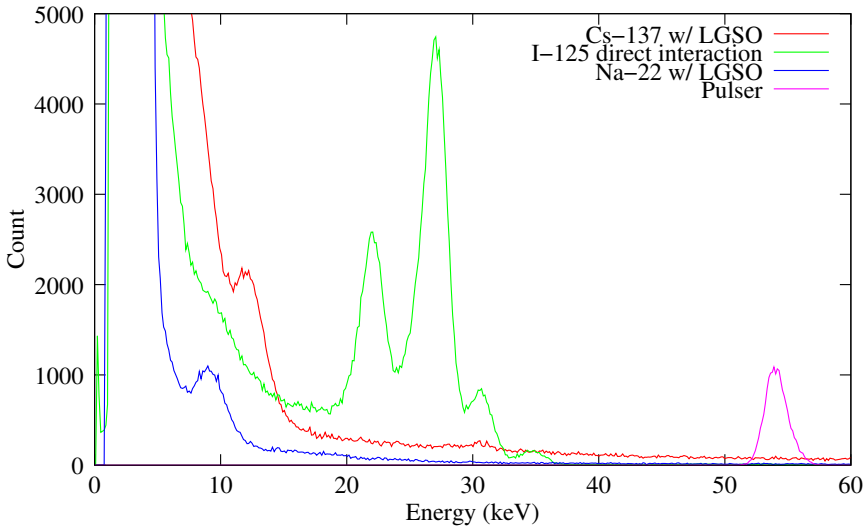

Figure 6.5 ^{22}Na, ^{173}Cs (from LGSO scintillation) pulse height spectra, read out by a PIN diode coupled to the $1 \times 1 \times 3$ mm^3 LGSO scintillator. The 27 keV peak is the result of the direct interaction of low energy gamma photons (^{125}I) in the PIN diode substrate

$$\mathrm{SNR} = \sqrt{PDE}\frac{N_{signal}}{\sqrt{N_{background}}}$$

where $PDE = QE \cdot \epsilon_G \cdot A_{pixels}/A_{total}$ is the photon detection efficiency of a silicon photomultiplier (where QE is the quantum efficiency, ϵ_G is the probability of a photon activiating a SiPM cell, A_{pixels} is the total sensitive area, and A_{total} is the total detector area), N_{signal} is the number or rate of photons emitted by the scintillator and $N_{background}$ is the thermally-generated dark electrons.

Typically, PDE for high-QE SiPM devices is around 15-20% [140, 141]. A maximum of four simultaneous dark electrons was observed with this device. Assuming a constant SLICE for the energies ranging from 60 keV up to 511 keV [142], the expected light yield for the 60 keV (^{241}Am), 88 keV (^{109}Cd) and 122 keV (^{57}Co) photon energies are 110, 160, 220 photo-electrons respectively. Thus, the estimated SNR of the SiPM detector is in the range of 25 to 50.

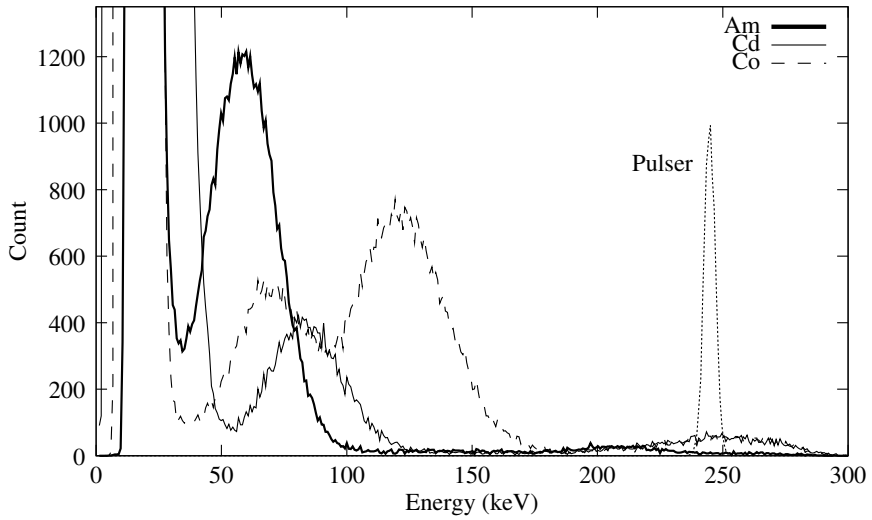

Figure 6.6 Calibrated ^{241}Am, ^{109}Cd and ^{57}Co spectra obtained from the SiPM coupled to the LGSO scintillator, at room temperature.

6.5 Spectroscopic Characterisation

6.5.1 Low Energy Photon Sources (LGSO Scintillator)

The low energy gamma spectroscopic characterisation of the SiPM were performed by optically coupling the sample to the previously characterised LGSO scintillator, assuming the same optical coupling conditions used with the PIN diode (see Section 6.4). The energy resolution and linearity of the SiPM was studied using three low energy gamma ray sources. The best energy resolutions were obtained while the detector was biased 2.5 V above the breakdown potential (37 V).

Figure 6.6 shows the low energy gamma spectra of $^{241}\mathrm{Am}$, $^{109}\mathrm{Cd}$ and $^{57}\mathrm{Co}$ sources obtained from the SiPM detector coupled to the LGSO scintillator. The energy axis was calibrated using the 122 keV gamma photo-peak ($^{57}\mathrm{Co}$) and a precision pulser. A 50 Ω load was used as the interface between the pulser and the FTA to evaluate the electronic noise contribution. The low energy peak observed in the $^{57}\mathrm{Co}$ spectrum is due to the fluorescent X-rays emitted by the lead (Pb) in the sensor's package [143]. The spectra demonstrate good linearity (less than 4% deviation from the nominal

Table 6.1
The energy resolutions obtained from the 1×1 mm^2 SiPM sample biased at 37 V

Source	Energy (keV)	FWHM (keV)	Resolution (%)
^{241}Am	60	24	40.5
^{109}Cd	88	29	33.0
^{57}Co	122	30	24.5

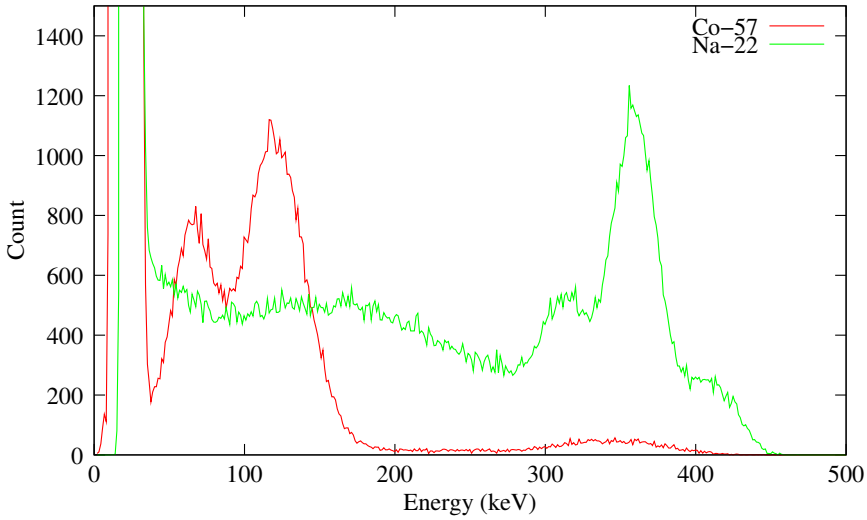

Figure 6.7 Calibrated ^{22}Na and ^{57}Co spectra. The spectral shift of the 511 keV peak is due to the saturation of the detector response.

peak value) between the intensity of light emitted by the scintillator and the output pulse amplitude for gamma photons with energies ranging from 60 to 122 keV. The full width at half maximum values corresponding to the photo peaks are summarised in Table 6.1, along with the calculated energy resolution expressed as a percentage.

6.5.2 High Energy Photon Sources (LGSO Scintillator)

The same procedure was repeated to obtain the ^{22}Na spectrum (photo-peaks at 511 keV and 1.27 MeV) shown in Figure 6.7 together with the ^{57}Co spectrum. The spectra show that the 511 keV peak has been shifted to 358 keV, due to detector saturation. Considering the calculated SLICE value of 22.3$\pm$4% for the LGSO scintillator, the estimated number of photons detected by the sensor is 2900$\pm$110, which exceeds the number of sub-pixels, saturating the dynamic range of the device.

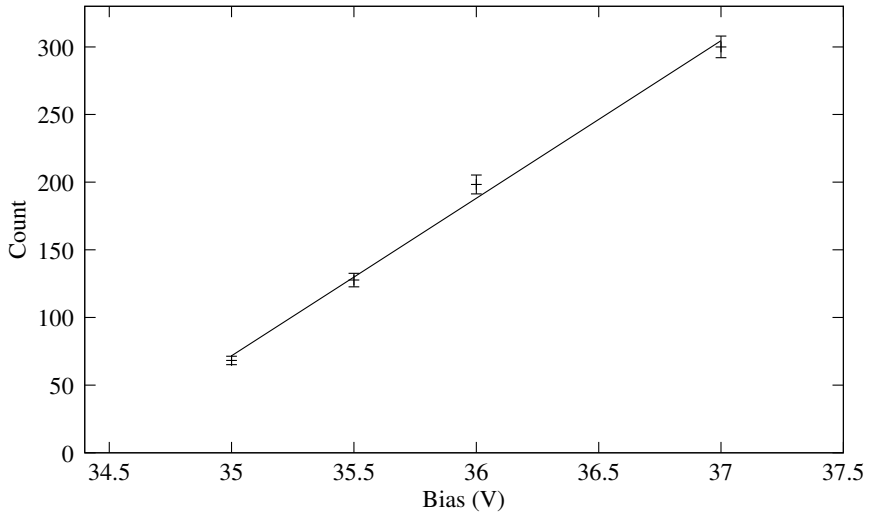

Figure 6.8 The 511 keV photopeak centroid is plotted as a function of the applied bias. The curve demonstrates that the preamplification stage (readout electronics) does not have any effects on the saturation phenomena.

Taking into account also the nominal photodetection efficiency of SiPM of 30%, it is expected that approximately 900 photo-electrons should be detected by the sensor [135]. The $^{22}\mathrm{Na}$ spectrum also shows a distorted tail at higher energies due to the multi-triggering of sub-pixels during the emission process (corresponding to the scintillation event of the gamma ray interaction with the LGSO crystal).

To investigate the linearity of the device response, its pulse height response to the $^{22}\mathrm{Na}$ source was recorded under different bias voltages. The channel corresponding to the 511 keV peak was plotted versus the applied bias voltage and is shown in Figure 6.8. The linear behaviour of the curve demonstrates that the saturated output is not related to the readout electronics and is caused by the detector. The estimated number of effective photons generated by a 511 keV event indicates that a minimum number of 900 sub-pixels is required to detect such gamma events.

6.6 Discussion

Figure 6.4 shows that the structure of a SiPM pulse is composed by short pulses shaped by the dead time characteristic of the subpixels, modulated by the decay time of the scintillator. It means that the amplitude of the first pulse generated by SiPM is not related to the total amount of photons generated in the scintillator but only by the rate of emission characteristic of the crystal. Assuming that the emission rate of a LGSO crystal is described by

$$\frac{dN}{dt} = -\frac{N_0}{\tau} e^{-\frac{t}{\tau}} \tag{6.1}$$

where N_0 is the number of photons (2900) emitted at 511 keV considering the SLICE of the scintillator and $\tau = 40\ \mathrm{ns}$ the decay time for the LGSO. The number of the photons incident on the SiPM corresponding at the amplitude of the only first short pulse of the response of the sensor will be

$$N_{\Delta t} = \int_0^{\Delta t} \frac{N_0}{\tau} e^{-\frac{t}{\tau}} dt = N_0 (1 - e^{-\frac{\Delta t}{\tau}}) \tag{6.2}$$

where $\Delta\mathrm{t} \in [10, 20]\ \mathrm{ns}$ is the range of the width of the first pulse evaluated experimentally. The number of photons $\mathrm{N}_{\Delta\mathrm{t}}$ estimated for the range $\Delta\mathrm{t}$ is equal to 700 up to 1100 photons which saturates the sensor dynamic as shown in Figure 6.7. This confirms also that the benefit using LGSO scintillators for the detection of low energy gamma rays comes from the consideration that the amplitude of the signal generated by a SiPM is proportional to the emission rate of the crystal and not to the total amount of photons emitted.

6.7 Summary and Conclusion

An extensive characterisation of a Silicon Photomultiplier produced by FBK-irst has been performed. The sensor is shown to provide a very high SNR for gamma photons with an energy range from 60 to 122 keV; in addition, good energy resolutions and linearity are demonstrated, compared with other results reported in literature [137, 144, 145], especially when coupled to an LGSO scintillator and used in detecting low energy gamma radiation. The use of a LGSO scintillator for detection of low energy gamma rays has been adopted because the low (β)-activity of the crystal does not corrupt the energy resolution of the detector and the extremely low dead time of the LGSO-SiPM system prevents a long acquisition period during the analysis of the patient, considering the low activity of the radioactive source used usually in medical applications. The low bias voltage, insensitivity to magnetic field and compact layout make this detector an attractive alternative to PMTs for both high and low energy gamma imaging (PET and $^{125}\mathrm{I}$ imaging) or for low dose rate brachytherapy with $^{125}\mathrm{I}$[1].

The scintillated gamma spectroscopy which was conducted by attaching an LGSO crystal to the SiPM detector indicated very good energy resolution (30 keV) at 122 keV. The spectroscopic results obtained from $^{241}\mathrm{Am}$ and $^{109}\mathrm{Cd}$ sources (24 keV and 29 keV FWHM respectively) makes this detector a viable choice for low energy gamma ray instrumentation.

All devices tested (planar PIN, PIN+JFET and SiPM) would offer adequate energy resolution for PET (although energy resolution is a secondary consideration for PET as a wide range of photon energies will need to be accepted if Compton-scattered photons are to be utilised. A scintillator from the LSO family such as LGSO offers high light output and a short time constant; NaI or CsI are less-well suited for PET due to their long time constant despite their high light output.

[1] CMRP is one of the pioneers in research and development of specialised detectors for use in low dose rate brachytherapy [146, 147]

The SiPM offers numerous advantages over the other two devices characterised in Chapters 4 and 5 in relation to PET applications. The planar PIN device has no intrinsic gain, while the PIN detector with integrated JFET is not well-suited to applications requiring a scintillator (the JFET also only provides limited intrinsic gain). The SiPM offers a very fast rise time and extremely linear output (in terms of photon energy) up to the point of saturation. Importantly, the signal to noise ratio of the SiPM device is very good. With the low bias voltage and insensitivity to magnetic fields, the flexibility of this device makes it a very good detector candidate. Therefore, the SiPM, coupled with an LSO-family scintillator is selected as the central device around which the remainder of the PET system to be developed in this Thesis is designed.

Chapter 7

Design and Simulation of CMRPET: A High Resolution Solid-State PET Scanner with DoI

The previous chapters studied several silicon-based solid state detector technologies which would be suitable for the next generation of compact high-resolution PET scanners. This chapter presents a design for a low cost, high-resolution PET scanner for small volumes, featuring variable gantry geometry, depth of interaction capabilities and magnetic field compatibility. The scanner architecture, including hardware and software components will be described in detail, and specific elements of the system will be experimentally characterised and evaluated. Monte Carlo simulations of a scanner with operational parameters based on these experimental measurements demonstrate the feasibility of the design. Experimental evaluation of a practical realisation of CMRPET will then be presented in Chapter 8.

The proposed Compact Millimetre-Resolution Positron Emission Tomography (CMRPET) system is a high spatial resolution positron emission tomography (PET) scanner with full depth of interaction capability and an adjustable gantry diameter (80 mm to 202 mm). Its edge-on pixellated scintillator/detector architecture allows the depth of interaction (DoI) of each 511 keV gamma ray event to be localised to a $3 \times 3 \times 3$ mm^3 scintillator voxel. The edge-on detector module configuration includes an

4×4 array of voxels which ensures the high gamma ray detection efficiency is not compromised. The incorporation of DoI in the design results in minimal degradation of the spatial resolution in the reconstructed PET image across the field of view (FoV) of the scanner.

Detailed Monte Carlo computer simulations of the scanner with point source and a model of an Ultra Micro Jaszczak phantom are conducted in the GEANT4 Application for Tomographic Emission (GATE) to establish expected count rates, detector sensitivity and the spatial resolution realised under ideal conditions in the simulator [148].

7.1 CMRPET Design Overview

The complete CMRPET scanner, together with the radial-axial stage, is shown in Figure 7.1. The current experimental prototype features a variable diameter gantry (80 mm to 202 mm, electronically adjustable), comprised of a pair of opposed coplanar rings. Each ring includes a radial actuator which can adjust the radial position of a detector array module in steps of 12.5 μm over a range of 61 mm, and a rotational actuator which can set the angle of axial rotation of the ring with a precision of 1.8 minutes of arc. Axial and radial positions may be independently adjusted for each ring (subject to physical limits of motion), allowing flexibility in the geometry of the gantry and the position of the detector modules for imaging different sized objects while maximising the sensitivity of the scanner. Due to this flexibility, the system is an ideal experimental platform for new radio tracer performance evaluation and detector module design testing and optimisation.

Each detector module consists of a 4×4 array of 3×3 mm^2 silicon photomultiplier (SiPM) detectors (SENSL ArraySL) optically coupled to a matching array of $3 \times 3 \times 3$ mm^3 LYSO scintillators, sealed in a lightproof plastic enclosure and mounted on a differential preamplifier board [145]. The detector arrays are placed in an edge-on configuration, parallel to the transaxial plane (Figure 7.2). This configu-

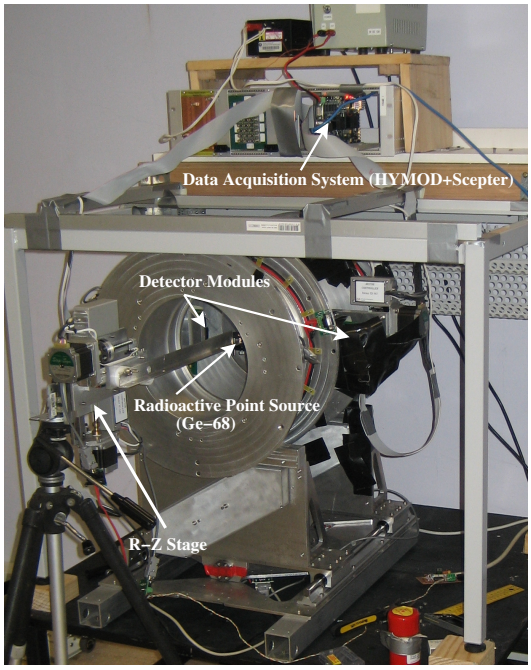

Figure 7.1 CMRPET Scanner and Radial-Axial Stage

ration provides a DoI resolution of 3 mm, since the DoI is implicitly obtained from the 4×4 transaxial arrangement of the pixels. An example CMRPET detector array configuration is shown in Figure 7.3, where the FoV diameter is set to 44.784 mm with 12 radial sectors (rsectors). The Crystal ID number for a detected event indicates the location of photon interaction in the array, quantised to a cubic voxel 3 mm wide in all dimensions. The image is reconstructed by mapping the activated pixels in coincident events to their proper pixels in corresponding detector arrays and drawing the Lines of Response (LoR) depending on the position of the detector heads around the gantry. It is noted that in its initial prototype, CMRPET only provides a single image slice; however the architecture can easily be extended to provide multiple detector rings, or the gantry can be translated in the axial direction to acquire multiple non-simultaneous image slices. The detector and scintillator will be discussed in detail in Section 7.1.1, while the differential preamplifier chain is discussed in Section 7.1.2.

All electronic actuators, together with an axial-radial stage on which the object to be

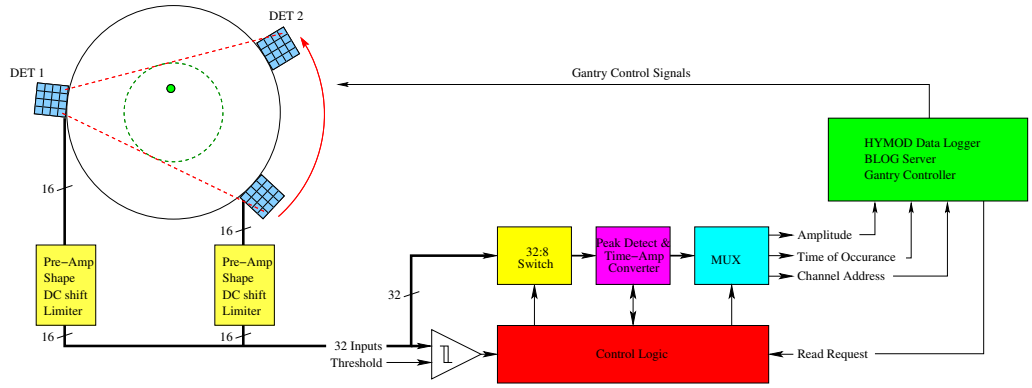

Figure 7.2 Block diagram of the CMRPET scanner, depicting the detectors in edge-on configuration and the associated DAQ. The figure illustrates the sweeping motion of one detector relative to the other to cover the entirety of the FoV.

imaged is mounted, are controlled over an I^2C serial bus by integrated gantry control and data-logging software. This controller is programmed to set the ring radius to the desired value and then conduct a full sweep across the field of view to cover all possible LoRs, emulating a fully-populated ring of detector modules (7.2). The gantry and electromechanical control system are described in detail in Section 7.1.5, while the associated control software is described in Section 7.1.6.

The exposure time in each position is calculated to compensate for the chosen radioisotope's half life (decay) and the time it takes to move the detectors to their new positions, such that each exposure should correspond to the same expected number of decay events. Data logging is synchronised with the movement control, ensuring that logging is suspended during movements and resumed following completion of the movement operation. The new position of the detector heads is recorded in the log after the movement is complete.

The detector modules are interfaced to a multichannel mixed analog/digital application specific integrated circuit (ASIC) and an FPGA-based digital data acquisition (DDAQ) system. The SCEPTER ASIC was originally developed for soft X-ray detection at Brookhaven National Laboratory and is based on a unique architecture incorporating multiple peak detectors and time-to-amplitude converters [73, 149, 150].

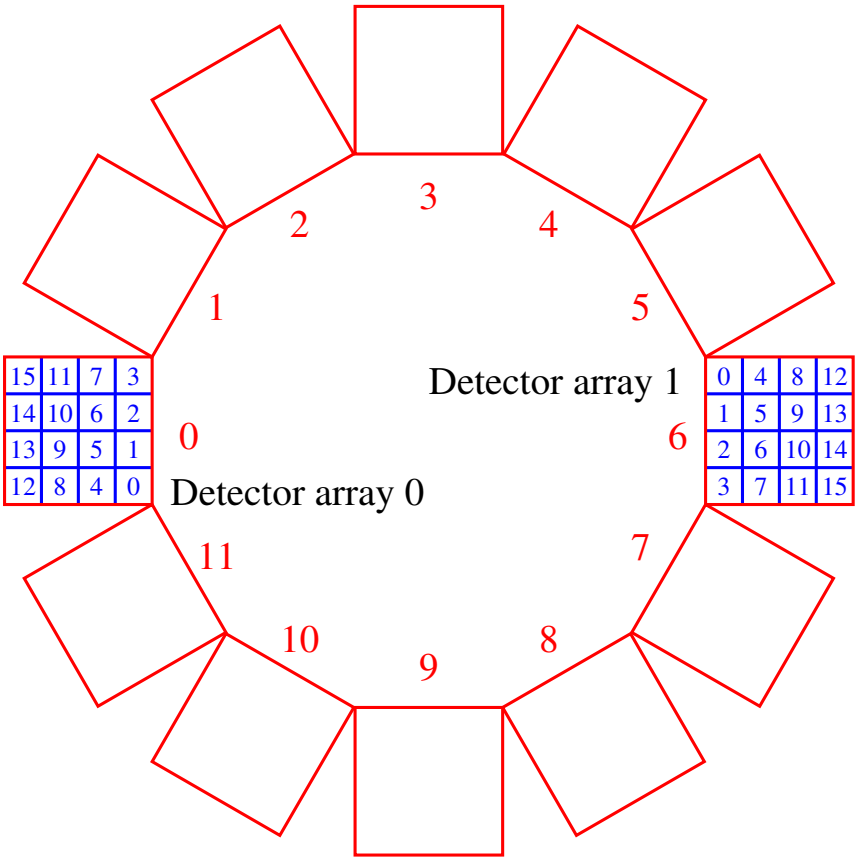

Figure 7.3 DoI encoding scheme. Crystal ID numbers are shown in blue, radial sector (rsector) numbers are shown in red. The two detector heads are currently placed at rsector 0 and 6. In this configuration, CMRPET has been configured to have a FoV with a diameter of 44.784 mm, with 12 rsectors. Note that the actual SCEPTER channel address is not the same as the Crystal ID number in each head due to the unusual ordering of signal routing on the SensL preamplifier board. For this reason, the channel address is mapped to the proper detector head and Crystal ID during the initial coincidence detection phase of offline data analysis.

It offers an extremely low dead time, making it ideal for PET signal acquisition. The time of arrival and energy of each event are measured by the ASIC, the event is time-stamped by the HYMOD digital data acquisition (DDAQ) system and sent to the integrated movement control and log server. Events are stored in list mode for later offline processing for coincidence detection and subtraction of random coincident events. Finally, coincident events are used to reconstruct an image using a direct backprojection algorithm [151]. SCEPTER is described in detail in Section 7.1.3, the HYMOD DDAQ system is described in Section 7.1.4, and data analysis and image reconstruction are described in Section 7.1.7 and 7.1.8 respectively.

7.1.1 Detector and Scintillator

The detector selected for this project is a commercial ArraySL-4 SiPM device manufactured by SenseL [145]. This device is a 4×4 array of matched discrete 3.05×3.05 mm SiPMs packaged into a single module. The individual pixels contain 4774 individual sub-cells; the reported peak photon detection efficiency is 14% at 500 nm [145]. The device was chosen because

- It is commercially available at a reasonable price (approximately $A3000 per unit when CMRPET was designed);
- It is sensitive to wavelengths from 400 to 850 nm, with peak sensitivity at 500 ns, which is compatible with LSO-family scintillators [145];
- It has a high pixel gain of 2.4×10^6 at room temperature [145];
- As each SiPM pixel is a discrete device (the module is an array of individual flip-chip SiPMs bonded to a carrier package), the pixels are be individually matched to minimise the pixel-to-pixel variation in energy resolution and photon detection efficiency (shipped devices are certified to have a total variation in optical of less than 20% of the standard deviation to median ratio for either quantity) [145]; and

- The device was also available in other array configurations, and the manufacturer is willing to custom-build arrays for specific applications. This is an important consideration for future development of the CMRPET design.

A scintillator was chosen from the LSO family for use with this detector, as LSO scintillators emit light at a wavelength compatible with the ArraySL-4 SiPM device[1]. Cerium-doped LYSO ($Lu_{1.8}Y_{0.2}SiO_5(Ce)$) was ultimately chosen due to its compatibility with the SiPM, availability and cost. It has the following desirable properties [11, 12]:

- High density (7.1-7.3 g.cm^{-3});
- Fast decay time (41 ns);
- High light yield (75% of NaI);
- Optical output wavelength compatible with the SensL SiPM detector (420 nm, which is close to the SensL ArraySL-4's wavelength of maximal sensitivity of 500 nm); and
- Relatively high effective atomic number (65).

The $3 \times 3 \times 3$ mm^3 scintillator crystals are packed into a 4×4 array. Each crystal is covered on 5 sides by reflective teflon tape and optically coupled to the SiPM on the remaining side with optical grease. The entire block (scintillators and detectors) is encased in a light-proof black plastic enclosure. This assembly is shown in Figure 7.4.

[1]Note that although the peak PDE of the SiPM is quoted at 14% at 500 nm, at 420 nm the PDE is significantly lower (approximately 4%). This was true of all SiPM devices commercially available at the time at which CMRPET was originally designed, which were optimised for green scintillators. It is quite straightforward to replace the ArraySL-4 module with more recent devices such as SensL's B-series, which are specifically optimised for use with LYSO scintillators.

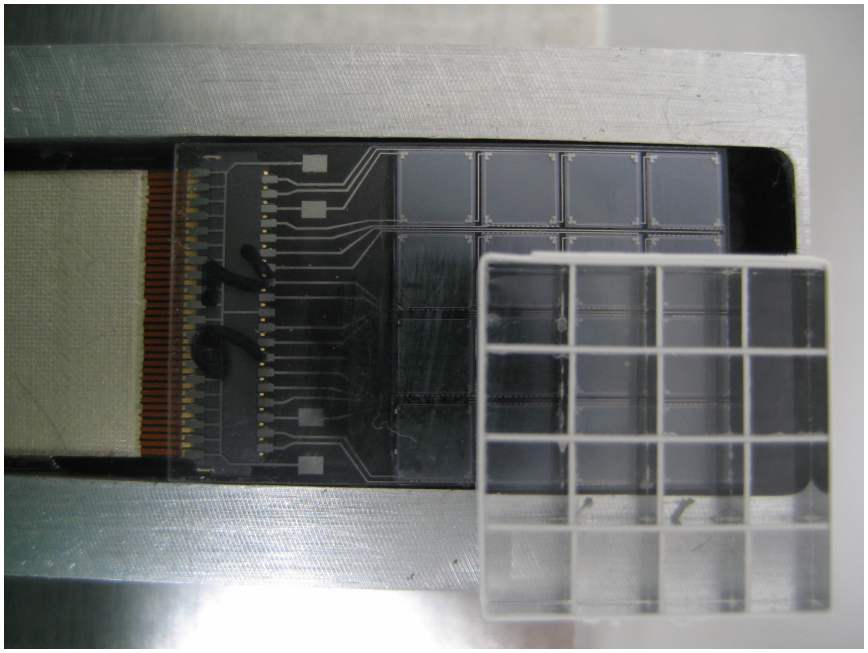

Figure 7.4 SiPM detector arrays and LYSO scintillator array

7.1.2 Differential Amplifier / Shaper

The detector module is connected to a manufacturer-supplied 16-channel transimpedance preamplifier module via a short flexible ribbon cable. This preamplifier (SensL SPMArray2-A0) has an input impedance of 47 Ω and provides a fixed differential DC gain of 2000 Ω (or a differential DC voltage gain of 42.553 if viewed as a voltage amplifier) with an shaping time constant of 4.7 ns. It provides a differential voltage output pair for each detector pixel suitable for connection to a short 50 Ω transmission line. To condition the output signal from this circuit such that it is suitable for acquisition with the chosen nuclear pulse processing ASIC (see Section 7.1.3), it is necessary to provide additional gain and pulse shaping, as well as converting the differential signal to a single-ended output.

The output from the preamplifier is connected to a non-inverting AC-coupled differential integrator with a DC gain of 2 and a time constant of 10 ns, followed by a non-inverting amplifier/adder with a DC/signal gain of 3 and an offset voltage of 0.3 V. The complete circuit is shown in Figure 7.5(a). As the output stage of the

circuit is supplied by rails of +3.3 V/0 V, and the amplifier is rail-to-rail capable and rail-clamping, the output voltage is intrinsically limited to a safe voltage range of 0 V to 3.3 V, which is compatible with the SCEPTER IC connected to V_{out}. The simulated op-amp in this circuit has a large-signal gain-bandwidth product of 190 MHz and a slew rate of 1500 V/μs, corresponding to the characteristics of the AD8036 amplifier used in the final design.

Simulated typical input and output waveforms are shown in Figure 7.5(b). The common-mode noise source is set to zero in this example (however, the design has also been simulated with a variety of common-mode noise sources; the amount of common-mode noise reaching the output is essentially zero). Positive and negative differential inputs waveforms are shown as p_{in} and n_{in} respectively, representing stylised SiPM pulses received from the end of a short 50 Ω transmission line connected to the SensL preamplifier. The output voltage is V_{out}.

The complete detector/preamplifier/pulse shaper is shown in Figure 7.5 along with the associated power supply circuit.

7.1.3 SCEPTER CMOS Pulse Processing ASIC

Analysis of incoming nuclear pulses is performed using the SCEPTER 32-channel hybrid analog/digital CMOS IC. SCEPTER was selected due to its ability to buffer up to 8 events per readout clock cycle, low power consumption (less than 2 mW/channel), multi-channel capabilities (32), good linearity (0.05% deviation) and high absolute timing and energy accuracy (nominal maximum error of 0.3% of full scale; this can be improved by calibration, as used in CMRPET). It also has the advantage of previously being used in an unrelated nuclear signal processing project in combination with the HYMOD data acquisition platform (to be discussed in Section 7.1.4. Each of SCEPTER's 32 channels is connected to one of the single-ended outputs of the differential amplifier described in the previous section; thus a single SCEPTER ASIC can acquire pulses from two 4×4 detector arrays. SCEPTER is described in detail in Section 2.4.6.

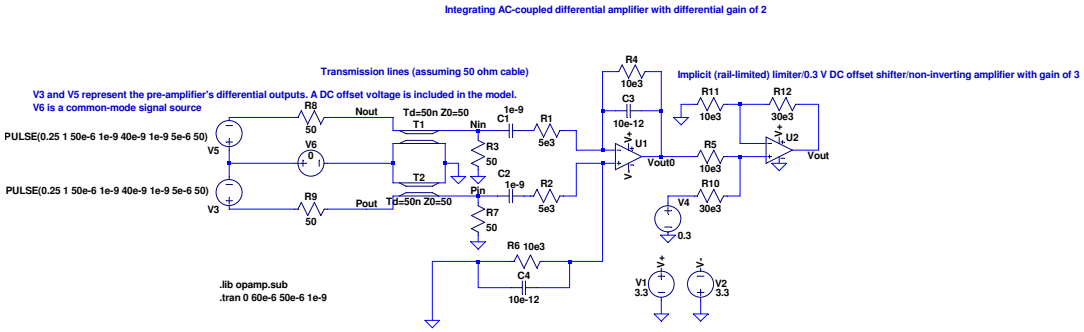

(a) Differential wideband amplifier/shaper (pseudo-integrator) schematic

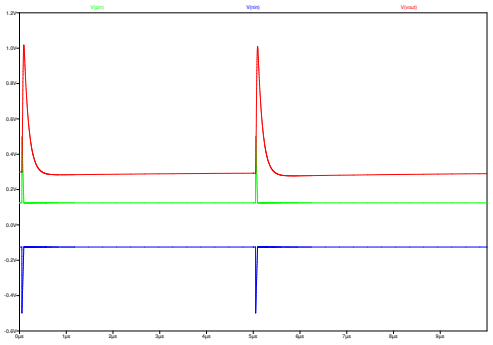

(b) Simulated differential input pulse and single-ended shaped output pulse

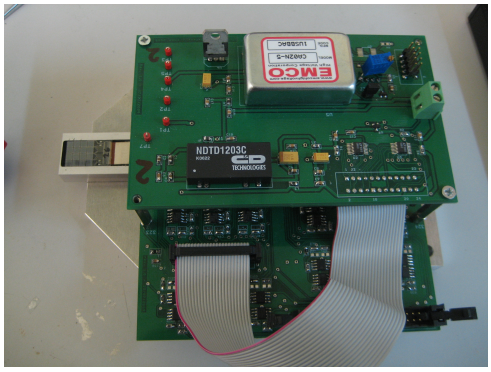

(c) Complete assembly showing SiPM detector and its associated preamplifier circuit

Figure 7.5 Preamplifier system

For PET applications, the key information provided by SCEPTER is an energy measurement of the pulse, and a timestamp (in the form of a global read request clock plus an analog time-to-amplitude conversion, which starts at zero at the time of the event and increases linearly up to the point of readout or saturation). With appropriate calibration of both timing and energy information on each channel (energy measurements are also affected by channel inhomogeneity in the analog preamplifier stages), it is possible to very precisely characterise incoming pulses at an event rate of up to 1.6 MHz [73].

By sequentially analysing the timestamps and pulse energies of each recorded nuclear event, it is possible to identify coincidences (defined as two or more events occurring within a specified timing and energy window), allowing LoRs to be constructed for sinogram binning and image reconstruction.

7.1.4 HYMOD Data Acquisition System and Binary Logger

HYMOD was selected as the appropriate data acquisition platform, since it already had been successfully used with SCEPTER, was capable of handling a very high rate of events and used a simple and well-known binary log format for storage of the resulting data [64].

The energy (pulse height) and time of arrival (TOc) outputs from SCEPTER are converted to a digital representation by dual 14-bit fast synchronous ADCs. These are coupled to a HYMOD board, which digitises the analog representations of pulse height and time of arrival, acquires the channel addresses and generates the required control signals for SCEPTER (including the read request clock). Each event is then represented as a series of 32-bit words encoding energy, time of arrival and channel index, formatted into a TCP/IP packet and sent over the network to a binary log server running on a remote Linux PC [152]. The complete architecture is shown in Figure 7.6.

The binary log server records all incoming events from HYMOD or from other data

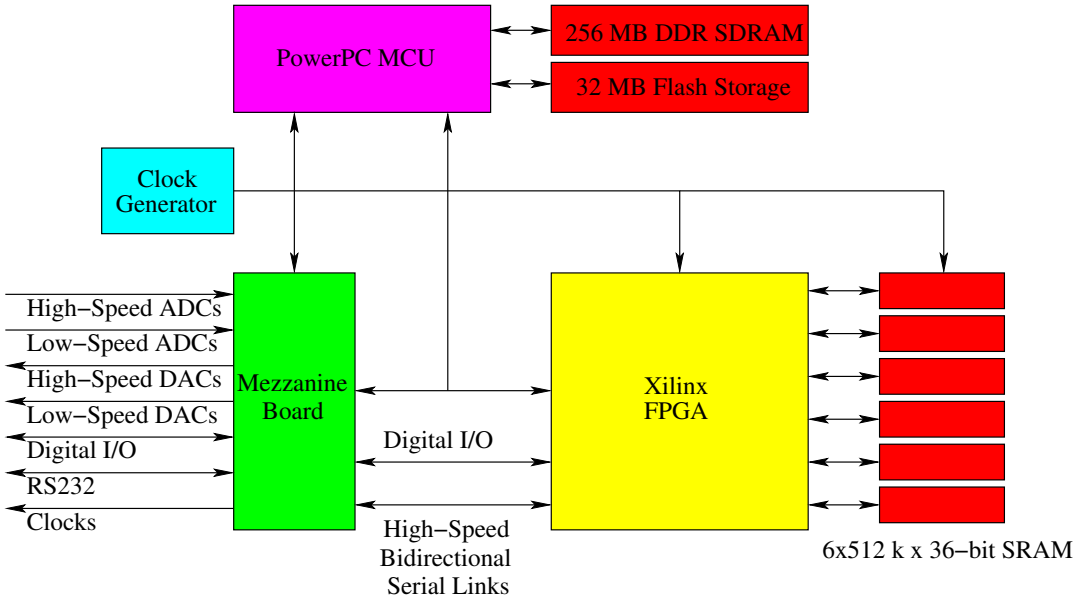

Figure 7.6 HYMOD Data Acquisition System

sources (See Section 7.1.5 as binary records; these are stored as a sequence of files on local hard drives and can later be analysed offline for coincidence detection or spectroscopy.

7.1.5 Gantry and Electromechanical Control System

The electromechanical design of the CMRPET scanning gantry is adapted from an earlier gantry developed at CMRP, whose principal application was SPECT imaging [153–155]. The original gantry included a single ring, capable of rotation through 360 degrees with a resolution of 0.03 degrees per step. This ring could be translated axially along a set of rails with a resolution of 0.0125 mm per step. Four mounting points were available on the ring, intended to accept a radial actuator on which detector, collimators, sources and other devices could be mounted. These radial actuators also provide a resolution of 0.0125 mm per step with approximately 70 mm of linear travel. While this arrangement was adequate for SPECT, a PET system requires either a full ring of detectors or a means to simulate such a ring using a smaller number of detectors which can be moved. Due to the costs of detectors and

scintillators, a fully populated ring was not feasible for this project. Therefore, it was necessary to effectively simulate a full detector ring by using only a single pair of detectors which could be independently moved to different positions around the ring. Two functional gantry rings were mounted co-axially on one set of rails. Since radial actuators could be mounted on either face of the gantry rings, it is possible to mount two actuators such that in the home position of both rings, the detectors (mounted on the actuator platforms which are in turn attached to the rings) are be directly opposite one another. The precise alignment can be adjusted by locking one of the rings in place and adjusting the position of the second ring until proper alignment is achieved. Axial movement is not required for this project - although it would be easy to add, scan times would be impractically long due to the short half-life of typical clinical positron emitters (such as ^{18}F). Therefore, axial movement is currently disabled. Steel counterweights are mounted on each ring on the opposite side to the detector assemblies in order to properly balance each ring, reducing angle-dependent torque but increasing the overall moment of inertia.

Both the revolute actuators (which adjust the angular position of each ring) and the radial actuators (used to adjust the radial position of each detector assembly) use exactly the same logical and electrical interface. Each actuator is driven by a single two-phase (6-wire) stepper motor, connected to a driver module consisting of an Philips P82B96 I2C bus transceiver, Philips PCA9554(A) I2C programmable I/O register and a set of four MOSFET power switches. Current through each of the four stepper motor half-windings can be independently applied by setting bits on the output port of the I/O register. Motors are therefore moved by rotating a 4-bit pattern across the four output lines (bits 1-4) which corresponds to the magnetised windings required for either one-phase, two-phase or half-step stepper motor control. Motor speed is determined by the pulse frequency (i.e. the rate at which the 4-bit pattern is rotated), and motor direction is determined by the direction of the 4-bit bit rotation (left or right rotation).

Revolute actuators include a single optical limit switch, while linear actuators include

two mechanical limit switches, one at each end of travel. The status of these switches may be determined by reading from the PCA9554(A) I/O port. Each driver module has its own I2C address; as the I2C I/O register chip is available in two variants, each with their own base address (0x20 and 0x38 respectively), and each chip has a three-bit address setting, it is possible to address up to 16 driver modules in total. The use of the bus transceiver allows higher bus voltages than the normal supply rails of the gantry; consequently, the data cable cable can be significantly extended and susceptibility to interference is considerably reduced. The original gantry design exploited this capability to allow the radial actuators to remain permanently connected to both power and the I2C bus. However, in CMRPET, radial adjustments are only made at the start of a scan. Therefore, to simplify cabling on the double-ring gantry, the connection to the power and I2C distribution network is detached for normal gantry operation. It is possible to do this safely while the entire system is powered up, as all linear actuator motor windings are automatically de-energised between movements (since their coefficient of static friction is sufficient to prevent unwanted movement of the load). Therefore, there is no risk of high-voltage arcing when the highly inductive motors are disconnected. This has the added advantage of reducing the idle current drawn from the power supply, since a stepper motor draws significant current when it is energised but stationary.

An additional pair of linear actuators are used to adjust the position of the object to be imaged; this pair are the key elements of a structure known as the *stage* which is affixed to the base of the gantry and allows the position of the object to be adjusted vertically and axially. The vertical actuator of the stage may be mechanically translated in the vertical direction in 30 mm increments in order to cover a larger range of positions than is possible with the actuator alone; the entire assembly may also be translated horizontally by means of a hand-operated screw. The stage actuators are connected to the same I2C bus as the gantry actuators, allowing all motors to be controlled by a single piece of control software.

Motors may be controlled via a stand-alone microcontroller; this was the original

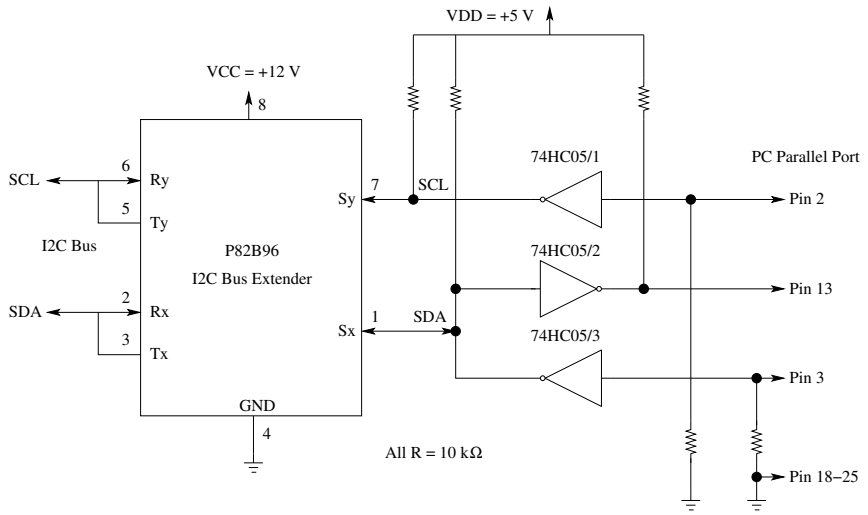

Figure 7.7 Parallel port I2C interface

control mechanism for the CMRP gantry design. However, CMRPET requires that movements be performed under the control of an external computer, and that the movements are recorded using the same binary logging system as the detected nuclear events, such that data collected while the gantry is in motion may be discarded, and the exact position of the detectors is known at all times during the acquisition process. Therefore, the stand-alone microcontroller module has been replaced with a simple parallel port I2C interface designed to work with the Linux parallel port I2C device driver (Figure 7.7). This interface is powered by an independent 12 volt power supply to ensure that even when high levels of current are drawn from the motor supply (leading to possible supply rail voltage glitches), this will not affect the reliability of communications.

7.1.6 Control Software Design

Operation of the gantry is managed by a TCP/IP server called `supergantry`, written in C. `supergantry` runs on the host PC (which doubles as a datalogger), listening for incoming connections on TCP port 5555. It uses a command syntax which is similar to that originally used on the stand-alone microcontroller formerly used to operate the CMRP gantry. Several commands are available, and are listed in Table

Table 7.1 Table of `supergantry` commands

Command	Function
h<N>	Simultaneously move all motors to the home position - due to simultaneous movement requirement, acceleration is abrupt rather than smooth. Optional: request movement of motor N only
s	Request current motor positions
MX NNNN	Move motor X to absolute position NNNN

7.1.

A key feature of `supergantry` is its ability to provide smooth acceleration of the motor from standstill to maximum velocity and then back down to standstill. This is necessary because unless a stepper motor operates within a narrow band on its torque-speed curve, the torque supplied by the motor will be insufficient to prevent slip, particularly during start/stop when the load has a large moment of inertia. Slip prevention is achieved by implementing a variable step-time. Acceleration and deceleration follow an asymptotic exponential function of the form $\omega = \omega_{min} + (1 - e^{-t/\tau}) \times \Delta\omega$. Thus, the motor starts at ω_{min} and asymptotically approaches $\omega_{min} + \Delta\omega$; however the acceleration stops at the half-way point of the operation. The acceleration profile is then reversed until the point that the motor has returned to ω_{min} at which point it is stopped. The time constant, initial angular velocity and maximum change in angular velocity $\Delta\omega$ are all configurable parameters, and have been empirically tuned to ensure that the gantry operates slip-free.

The control modules inherited from the original CMRP SPECT gantry do not implement any stepping logic internally; instead, all stepping is performed over the I2C bus, one step at a time. This is a straightforward task on a microcontroller, which does not have an operating system and does not need to deal with the complexities of multitasking. On a dedicated host PC, as used in CMRPET, special care must be taken to provide smooth stepping - particularly when smooth acceleration is required. This is provided by running `supergantry` in *soft real-time mode*, in which `supergantry` runs as the sole real-time task under a simple soft real-time sched-

uler (POSIX `SCHED_RR`, which implements deterministic round-robin scheduling with fixed time-slices). With this scheduler in operation, a real-time task with the highest priority on the system cannot be interrupted by any other task when it is able to run. This is ideal for pulsing a stepper motor, since most of the time the process is simply waiting for a timer to expire. When a request arrives over the network for one or more motors to move, if smooth acceleration is enabled, the request is broken down into individual motor movements which are executed sequentially. The motor to be moved is pulsed, then `supergantry` sets a real-time hardware timer (POSIX `CLOCK_MONOTONIC`) and waits for it to expire. The delay is set to the maximum inter-step delay, corresponding to the initial minimum angular velocity of the stepper motor. After the timer expires, the motor is again pulsed, the timer is set to expire after a slightly shorter interval, then `supergantry` again waits for the timer to expire. This process continues until half of the pending steps have been completed, after which steps continue with ever-longer intervals between them, achieving smooth deceleration back to standstill.

`supergantry` runs at an elevated privilege level and executes requests for motor movement in real-time for non-real-time client software. To control CMRPET, a second client program called `gantryctl.pl` has been written in the Perl scripting language. This program parses a configuration file describing the geometry of the scanner, the desired exposure time in each position, the half-life of the isotope (if a short-lived isotope such as ^{18}F is to be used), and a variety of other configuration parameters. It also reads a 'movement plan' for the sequence of positions that the rings are to execute during a scan, plus a plan for movement of the radial-axial stage if required. The movement plan can be generated manually, or with the aid of an additional Perl script called `gantryplan.pl` which calculates a suitable series of ring positions based on the geometry of the scanner and the maximum radius of the subject. These positions are stored in a plain text file which may be edited or otherwise modified by hand prior to execution if desired. `gantryctl.pl` will initially adjust the radial actuators on which the detector assemblies are mounted, pause to allow the radial actuators to be disconnected, then step through the positions described

in the movement plan (and stage plans, if used). The exposure time between motor steps is continuously adjusted to account for the half-life of the isotope, such that each position results in approximately the same number of recorded events. The requested scan is simulated prior to execution to ensure that it is feasible for the scan to be completed prior to the decay of all significant quantities of the available radioisotope. The operator may then adjust the desired initial exposure time if the initial value is invalid.

At the beginning of each scan, all parameters are recorded using the same binary logging service as used by HYMOD to record detected nuclear events, in the form of a 'logged comment'. This is timestamped, and is used to identify the start of the operation in the recorded data stream during the data analysis phase. A similar comment is inserted in the log before the start and after the end of any motor operation, such that the data between these points may later be discarded. Finally, any error (or operator interruption) causing premature termination of the scan is logged; if no error occurs then the successful completion of the scan is logged and `gantryctl.pl` terminates.

As soon as CMRPET has completed a scan, `gantryctl.pl` automatically executes the entire post-processing data analysis chain and generates a preliminary image for quick visual verification. This image is automatically e-mailed to a list of operator addresses specified in the configuration file, along with a summary of the parameters of the run and all key configuration files, providing a convenient timestamped record of the scan to interested users.

7.1.7 Data Analysis

All detected events are stored in list mode, together with a synchronised record of motor movements. For each event, the following information is recorded:

- A measurement of the peak pulse amplitude, corresponding to photon energy, represented as a 12 bit number;

- The value of the read request counter, which is a cyclic 24-bit number; and
- A measurement of the time-to-amplitude converter value, which is a 12-bit number that starts at zero at the time of the event and continues to increase linearly until the pulse is read out (by the next read request) or saturation ($2^{12}-1$) is reached.

7.1.7.1 Energy Calibration

Raw pulse amplitude measurements need to be calibrated in order for an accurate estimate of photon energy. ^{137}Cs (β^-/γ) and ^{68}Ge (β^+/γ) sources were used to acquire a pair of gamma spectra for each pixel in each detector array. The pulse amplitudes corresponding to the centroid of Gaussian curves fitted to the photopeaks were used as reference points for energy calibration of each analog channel. This calibration was subsequently applied to each pixel to ensure the consistency of energy windowing.

To evaluate the uniformity of the response of detector arrays across all pixels, energy resolution was calculated in terms of photopeak full width at half maximum (FWHM) (expressed as a percentage) for the calibrated ^{137}Cs spectra for each pixel in each detector module. The mean energy resolution was $18\%\pm4\%$. Full results for all channels are shown in Table 7.2.

Overall calibrated energy spectrum of ^{68}Ge and ^{18}F sources, averaged over all 32 channels of the detector, are shown in Figure 7.8.

7.1.7.2 Timing Calibration and Parameter Selection

The time to amplitude conversion process varies slightly from channel to channel. The TAC is essentially a ramp function which starts rising from zero when the pulse peak is detected, and stops rising when either saturation is reached or the pulse is read out [73]. Therefore, a combination of the digitised value of the TAC and the read request clock value (which must be unwrapped as the read request counter is

Table 7.2
Energy resolution homogeneity across all detector pixels - ^{137}Cs source (662 keV), measured at 20 °C

Detector head	Pixel	Channel	Energy Resolution (%)
1	1	0	15
	2	1	20
	3	2	20
	4	3	20
	5	4	16
	6	5	17
	7	6	18
	8	7	17
	9	8	20
	10	9	18
	11	10	17
	12	11	17
	13	12	19
	14	13	23
	15	14	20
	16	15	20
2	1	16	17
	2	17	17
	3	18	19
	4	19	21
	5	20	18
	6	21	17
	7	22	15
	8	23	14
	9	24	16
	10	25	17
	11	26	14
	12	27	15
	13	28	17
	14	29	17
	15	30	18
	16	31	20

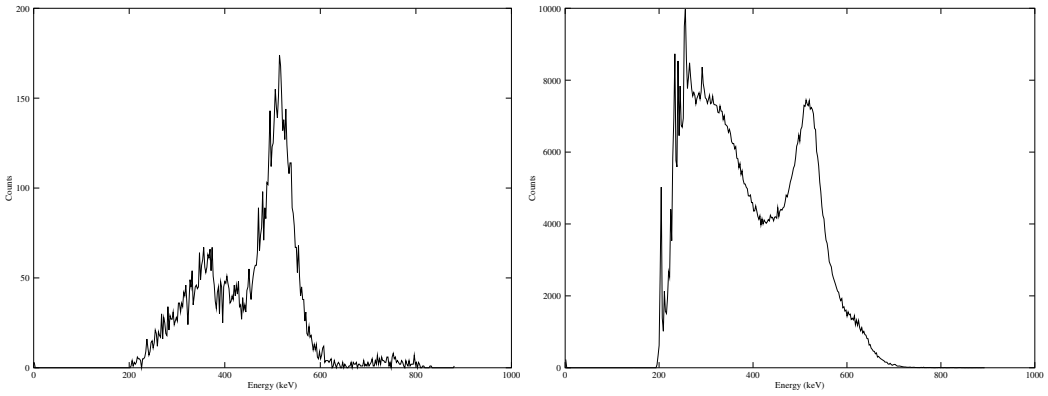

(a) ^{68}Ge (b) ^{18}F

Figure 7.8 Calibrated spectra recorded using CMRPET, averaged over all 32 channels. The ^{18}F source is surrounded by a scattering medium (solid water), while the ^{68}Ge source is surrounded by air (resulting in minimal scattering). Compton-scattered photons are present in the lower-energy part of the ^{18}F spectrum but not in the ^{68}Ge spectrum.

only 24 bits wide) is sufficient to provide the time of arrival of each pulse. The slope of the TAC ramp can be adjusted in software, however the adjustment is rather coarse, and due to variations in the value of the monolithic analog components in the TAC circuit, the slope varies somewhat. Therefore, this must be properly calibrated.

Firstly, an appropriate value for the read request clock and TAC slope must be chosen. In order to obtain the maximum dynamic range for the TAC, it should be set as low as possible for a particular value of the TAC slope. To obtain the best possible timing resolution, the TAC slope should be set as high as practically possible. TAC slope is adjusted by setting the SCEPTER parameter t_{ds}, which controls the time taken for the TAC to reach the saturation value of $2^{12} - 1$. It can be set to values from the set $\{0.32, 0.63, 0.83, 1.25, 2.5, 4.9, 9.8, 19.4\}$ μs. However, in practice SCEPTER was found to have stability problems if t_{ds} was set to values less than 1.25 μs. Therefore, t_{ds} was set to 1.25 μs.

Having chosen t_{ds}, the read request frequency should be set as low as possible. In order to detect coincidence pairs, which will be read out in consecutive read request intervals, the ideal read request frequency would be set such that the TAC will saturate just after two complete read request periods. For a t_{ds} value of 1.25 μs, this

Table 7.3 Read request frequency vs. recorded event rate; 688 MBq ^{18}F source

Read Request Clock (MHz)	Count rate (s^{-1})
1.0000	1014678
1.4000	1485898
2.0645	2069326
2.5000	2554510
3.0467	3029284
3.7000	3618048
4.9000	3984380
5.8182	4014664
7.1111	4001632
9.1429	3985574

corresponds to a minimum read request frequency of 400 kHz. However, this is not the only consideration; if the rate of detected events is too high, some potential coincidences may be lost. This is clearly demonstrated by a simple experiment in which a high-activity source (688 MBq, ^{18}F loaded into an ultra-micro Jaszczak phantom placed approximately 100 mm from both detector heads) is used with various read request clock rates. The observed event rate is shown in Table 7.3, and clearly peaks when the read request clock frequency is 4.9 MHz; no further significant increase results from further increases in read request frequency. The observed rate of approximately four million events per seconds corresponds to the true detected event rate. At lower read request frequencies, the 8-event buffer is often completely occupied, leading to many events being missed. Therefore, depending on the activity of the source and the anticipated maximum count rate, the read request clock may need to be set to a higher frequency. For the remainder of this Thesis, a read request clock frequency of 3.0467 MHz is used unless otherwise specified; this is a reasonable compromise between dynamic range of the TAC and the ability to process a high event rate.

Once TAC slope and read request frequency are defined, individual channels need to be calibrated, as the actual TAC slope varies slightly from channel to channel. This is achieved by observing the maximum TAC values observed on all channels using

a high-activity source. When multiple events occur within a single read request interval, the lower channel will be read out first (on the next rising read request clock edge) followed by the higher channel. The detector heads are placed in 180-degree opposition and a positron emitter is placed between them. Since channels 0-15 are on one detector head and 16-31 are on the other, the TAC values observed on each channel 0-15 will be uniformly distributed between the TAC values corresponding $t = 0$ and that corresponding to one full read request period ($t = T_{RR}$) for that particular channel. Since a certain number of events will be coincidences, the values observed on channel 16-31 will be distributed between the value corresponding to $t = 0$ and the TAC value corresponding to $t = 2T_{RR}$ for those channels (of course, since most events will be singles, the majority of observed TAC values will be uniformly distributed between the TAC value corresponding to $t = 0$ and $t = T_{RR}$, with the small fraction corresponding to coincidences occupying the remainder). Therefore, the difference between the maximum and minimum TAC values observed for each channel can be equated to either one or two full read request periods (depending on the channel), thus achieving the required timing calibration. The standard deviation in TAC slope was found to be approximately 1.5% of the mean across all channels, with a maximum deviation of 3.3%. One read request period at 3.0467 MHz corresponds to an average TAC range of 759.73, therefore a one-bit change in TAC value would correspond to a timing increment of 0.44075 ns. In practice, other sources of timing jitter result in a significantly lower actual timing resolution.

7.1.7.3 Timing Characterisation of Acquisition System

The timing and energy resolutions were obtained using a ^{22}Na source with the following experimental configuration: a photomultiplier tube (Hamamatsu R2300 biased at 850 V) in coincidence with the SensL SiPM photodetector. Each detector is coupled to a $3 \times 3 \times 3$ mm^3 LYSO scintillator via optical grease. The resulting timing histograms, with various values of read request clock frequency, are shown in Figure 7.9. The TAC full scale rise time (T_{ds}) is set to 1.25 μs.

To evaluate the timing resolution of the pulse processing and data acquisition system

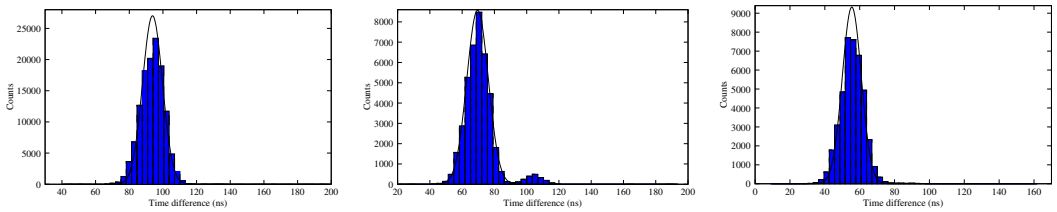

(a) 3.0476 MHz (b) 5.8182 MHz (c) 9.1429 MHz

Figure 7.9 Coincidence timing spectra (SiPM/LYSO - PMT/LYSO) for three different values of read request clock rate.

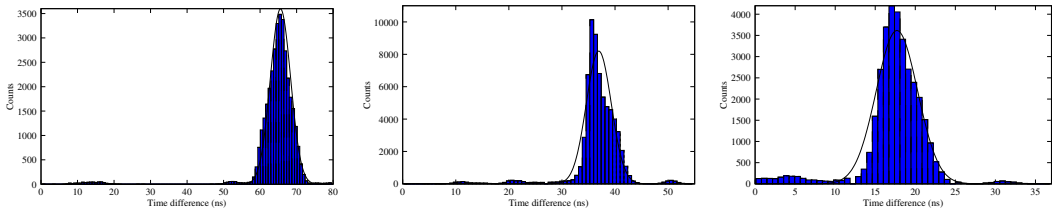

(a) 3.0476 MHz (b) 5.8182 MHz (c) 9.1429 MHz

Figure 7.10 Coincidence timing spectra (pulser) for three different values of read request clock rate.

alone, the signal processing chain was also tested with an integrated pulser. Results are shown in Figure 7.10, and the corresponding resulting timing resolutions are presented in Table 7.4. For comparison, results obtained with the same detector combination using standard NIM-based analog coincidence detection resulted in timing resolution of 3.65 ns FWHM.

There are several possible avenues for improvement to the timing resolution of the SCEPTER system. It would be desirable to further increase the slope of the linear

Table 7.4
Timing resolution, SiPM-PMT and pulser with SCEPTER/HYMOD ($t_{ds} = 1.25\mu$s, read request clock frequency = 3.0467 MHz)

	Timing Resolution (ns)	
F_{clock} **(MHz)**	**SiPM-PMT**	**Pulser**
3.0476	13.9	6.5
5.8182	15.6	5.5
9.1429	12.8	6.1

TAC; this would enable the full dynamic range of the timing ADC to be utilised and potentially improve the timing resolution. The present version of SCEPTER becomes unstable when T_{ds} was reduced to less than 1.25 μs. Small improvements may also be obtained by increasing the resolution of the analog to digital converter (ADC) which is used to acquire the value of the time to amplitude converter; however, no benefit can be realised if the analog noise on the TAC output is greater than the quantisation noise of the ADC. With the current version of SCEPTER, it appears that moving beyond a 12 bit ADC will be of little value for this reason.

The estimated timing resolutions that were obtained are sufficient for a non-time-of-flight (non-ToF) PET system, which only requires an intrinsic timing resolution of the order of 10 ns [156]. It is expected that this will be achievable with SiPM-SiPM coincidences, given the performance of SCEPTER/HYMOD with the pulser and the fact that SiPM and PMT pulse shapes are significantly different. As the full detector arrays were not available at the time of this test, it was not possible to do a SiPM-SiPM coincidence test at this stage of the project.

7.1.7.4 Coincidence Detection

Once CMRPET has been properly calibrated for energy and timing for the chosen read request clock frequency and TAC slope, the binary log data is parsed and the actual energy and time of occurrence of each event is calculated. A configurable timing and energy window are applied in order to identify potential coincidences; these are typically set at 5 ns and $[300, 700]$ keV respectively (the wide energy resolution allows some Compton-scattered photons to be utilised). Additional logic eliminates impossible coincidences (where the coincident events are recorded between two pixels in the same detector head). The position of both detector heads is tracked by the log-parsing software; events recorded during movement operations are automatically discarded. Valid coincidences are formatted into an ASCII text file in the same format as that produced by the GATE simulation framework; this simplifies the application of reconstruction software.

It is noted that the potential exists for multiple interactions within one or both crystal arrays. In this case, due to a Compton scattering process, multiple voxels will detect gamma photons with energies significantly less than 511 keV within the coincidence timing window. The coincidence detection algorithm is capable of detecting these events and classifying them as true coincidences, potentially allowing a kinematic approach to estimate the original point of interaction; however, in practice it was observed that coincidences involving the activation of more than one voxel in a detector head constituted a very small fraction of total events (significantly less than one percent). Therefore, due to the complexity of computing the point of origin of multi-photon coincidences (and the low probability of detecting all scattered photons), these multi-photon events are ignored. Simulations indicate that this does not have a significant effect on the performance of the scanner.

One final point to note: due to the unusual routing of signals from the SensL preamplifier module, the order of SCEPTER's channels is different to that assumed by the reconstruction software and simulator. Therefore, it is necessary to perform a re-mapping procedure as part of the coincidence identification procedure. This is implemented via a configuration file; an example is provided in Appendix A.

7.1.8 Image Reconstruction

Having obtained the Crystal ID and radial sector numbers for the coincidence, the exact (x, y, z) coordinates of each point of interaction may be calculated and the line of response (LoR) drawn between the two points. The point of origin is taken as the coordinates of the centre of the front face of the activated voxel, as the probability of interaction is greatest near the front of the crystal.

A number of alternative image reconstruction techniques may be used once the coincident event pairs are identified. The classical approach is filtered backprojection (FBP), in which a sinogram is constructed and transformed to the image domain via an inverse Radon transform (IRT). Iterative approaches (which typically use a FPB reconstruction as an initial starting point) offer reduced levels of imaging artefacts,

at the cost of significantly more processing time. An alternative to these techniques which does not require the use of an IRT to reconstruct the image is direct backprojection, in which anti-aliased lines are drawn directly between coincident detector voxels in a floating-point spatial image domain, and accumulated using a floating-point summation, followed by two-dimensional Gaussian filtering. This essentially constructs an image where each pixel value represents the level of activity of the corresponding voxel in the object.

This method results in a bias to higher apparent activity at the periphery of the FoV, which is a function of gantry and detector geometry. It is a straightforward matter to equalise this non-uniformity, by generating an image of a flood-filled cylindrical volume source and computing an inverse intensity response function. Alternatively, the equalisation function can also be derived analytically for a given geometry, or computed using a simulated uniform phantom with the same detector geometry in GEANT4/GATE. As the latter approach is simple and yields a quick result without the need to handle large quantities of radioactive liquid, this is the method which has been adopted in this project.

It is noted that image reconstruction is not the focus of this research and any of the algorithms discussed above could be used as the data is provided in a simple list mode format. If computational workload is not a limiting factor, it is likely that the best results will be obtained by an iterative reconstruction technique. It is also noted that the image reconstruction software generates a traditional sinogram in addition to the direct reconstruction results, permitting the use of iterative or filtered backprojection techniques if desired.

7.1.9 Estimation of Random Coincidences

The most commonly used approach for random coincidence correction is to delay one channel by significantly more than the coincidence timing window (to exclude all true coincidences) and then produce an image based on any resulting coincidences. This image may then be subtracted from the one reconstructed from the prompts (i.e.

all coincidences occurring within the coincidence timing window) with a weighting based on the ratio of the rate of random to prompt coincident events. In practice, this method results in a significant noise enhancement due to a low random count over the duration of the exposure. To avoid this problem, the method proposed by Divoli et al. is adopted, in which random coincidence events are synthesised by combining events from consecutive pairs of prompt coincidences [157]. This technique produces an estimate of the expected spatial distribution of random coincident events with a significantly lower SNR than is possible with the classical technique (generating uncorrelated events at up to half of the rate of prompt events). However, in order to correctly estimate the appropriate weighting for the random image, the relative rate of random to prompt coincident events must still be estimated using statistics generated from the classical random estimation method. In CMRPET, data are collected in list mode, therefore this estimate is performed offline; the additional computational complexity of synthesising the additional pseudo-random coincidences is negligible.

A Monte Carlo simulation to evaluate the performance of the Divoli method in comparison with the classical random correction technique is described in Section 7.2.1.2, while the simulation results demonstrating the efficacy of this approach will be presented in Section 7.2.2.1.

7.2 Monte Carlo Simulations

A Monte Carlo model was developed for GEANT4 Application for Tomographic Emission (GATE) (version 6.1) to simulate the CMRPET scanner, including a full model of the scanner geometry and the associated signal processing chain [148]. Models for the point source and Jaszczak phantom were constructed and added to the simulation, replicating the physical configuration discussed in Section 7.1. Simulation output is in the form of time-stamped coincidence events pulses with the crystal and detector block identification number (ID), essentially identical to that generated by the experimental hardware.

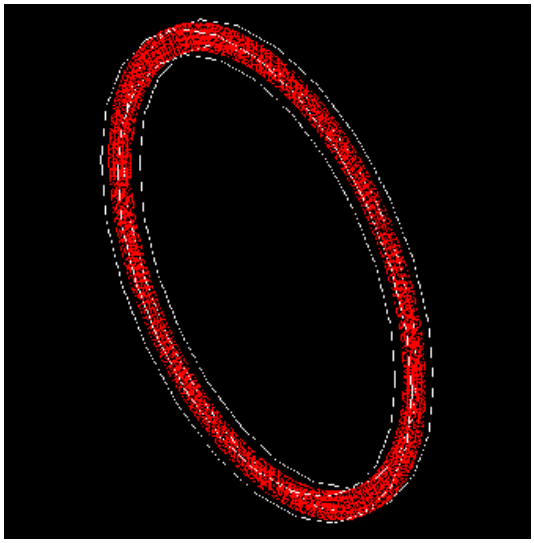

Figure 7.11 The Simulated CMRPET scanner geometry based on 12 mm long DoI detectors.

A fully-populated simulation of the CMRPET scanner is shown in Figure 7.11. A total of 53 detector arrays were placed around the detector ring, where each detector was modelled on the experimental detectors with $3 \times 3 \times 3$ mm^3 LYSO crystals in a 4×4 array. The simulated scanner has an inner diameter of 202.56 mm and an outer diameter of 226.56 mm (the specific inner ring diameter allows an integer number of 12 mm detector modules to form a complete ring). The recorded events were searched for coincidence pairs by applying a coincidence time window of 10 ns and an energy window of 300 to 700 keV (a wide energy window was chosen to allow some experimentation with utilising photons which have undergone Compton scattering, resulting in the presence of lower-energy photons - it is possible to narrow the energy window later in software). The same parameters will be adopted in Chapter 8 for the physical realisation of CMRPET.

7.2.1 Simulation Methodology

7.2.1.1 Source and Phantom

A simulated positron-emitting point source was custom-designed for this simulation campaign. It consists of a cylindrical region (1 mm in diameter and 2 mm in length)

containing 3.5 MBq of ^{15}O. ^{15}O was chosen as an alternative for ^{68}Ga (which will be used in later experiments in the form of a ^{68}Ge point source generator) as it was the most similar isotope to ^{68}Ga that is currently available in GATE in terms of maximum positron energy (1.72 MeV, compared to 1.90 MeV for ^{68}Ga). The source was surrounded by a 0.5 mm thick steel sheath and placed in a large cylindrical volume of water, with a diameter of 200 mm and a thickness of 20 mm.

7.2.1.2 Validation of Divoli Random Correction Method

To demonstrate the effectiveness of the Divoli technique, a 60 second acquisition of the ^{15}O point source offset by 10 mm from the centre of the field of view was simulated in GATE/GEANT4. Classical random correction and the Divoli random correction technique were then applied and the results compared by comparing the resulting images, which were additionally profiled horizontally and vertically. Symmetry of the resulting image was also assessed in the horizontal and vertical direction, and the different random correction techniques compared.

7.2.1.3 Spatial Resolution

The simulated point source was initially placed at the centre of the FoV, and moved in 10 mm increments along the radial direction, along the centre of the axial FoV. At each point source location, events were acquired for 300 seconds. Random coincident correction was performed and spatial resolution estimates were performed in radial and tangential directions. These simulations will be repeated experimentally in Chapter 8.

Simulation studies of the effects of photon attenuation, photon scatter and random coincidences were also performed using an accurately modelled Ultra Micro Jaszczak phantom, consisting of a cylinder with an outside diameter of 3.5 cm and an inside diameter of 2.8 cm. The diameters of the resolution elements (rods) vary from 0.5 mm to 2 mm in diameter, filled with ^{18}F. The activity of the source was volumetrically normalised for each rod, with a simulated total activity of 720 MBq. This high ac-

tivity level was used since the simulated prototype scanner, like the actual system, only includes two detector arrays which are moved to different positions during the simulation. Therefore, only a small fraction of gamma photons are actually detected. This fraction would increase significantly in a fully populated production version of the instrument.

7.2.1.4 Sensitivity and Counting Rate Performance

The previously defined ^{15}O source was employed to evaluate the sensitivity of the simulated CMRPET system. Sensitivity is defined as the ratio of measured true coincidence rate to point source activity in positron annihilation events per second. For an accurate estimate of sensitivity, the prompt coincidence rate must be measured and corrected for random events. The rate of random coincidences may be estimated off-line for either using the standard delayed-channel coincidence method, previously described in Section 7.1.9, and subtracted to obtain an estimate of the rate of true coincidences.

7.2.2 Simulations Results

This section presents the results of the Monte Carlo simulation campaign. All measurement errors provided are two standard deviations, representing a 95% confidence interval.

7.2.2.1 Validation of Divoli Random Correction Method

The original image is shown in Figure 7.12(e), with images of the distribution of randoms resulting from the classical and Divoli methods shown in Figures 7.12(a) and 7.12(c) respectively. Finally corrected images are shown in Figures 7.12(b) and 7.12(d) respectively.

It is difficult to see the specific performance improvements from the results shown in Figure 7.12. The horizontal and vertical profiles of the uncorrected, classically corrected and Divoli-corrected point source image are shown with a logarithmic scale

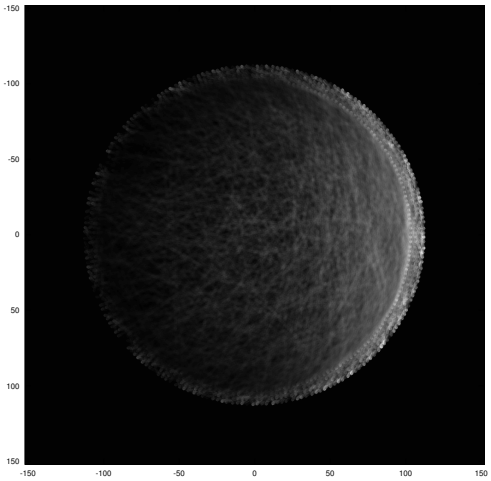

(a) Classical random distribution

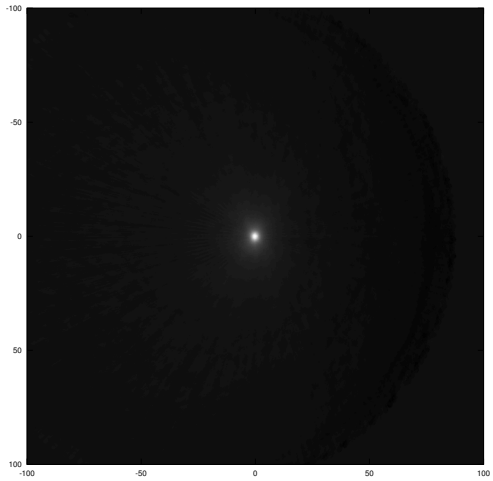

(b) Classical random correction

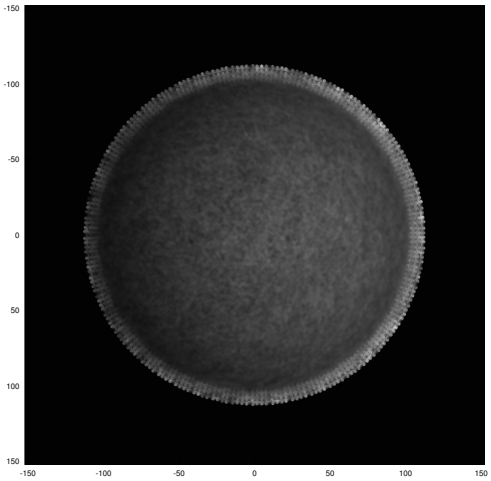

(c) Divoli random distribution

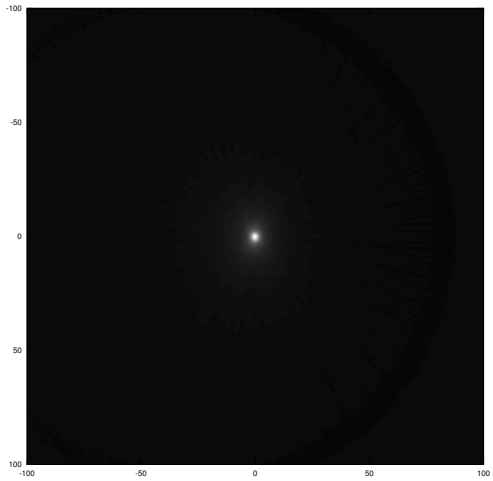

(d) Divoli random correction

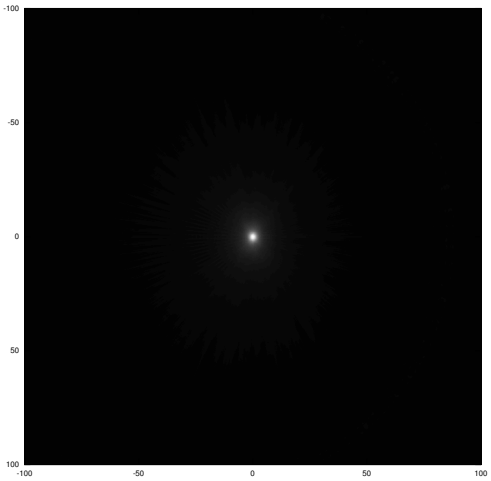

(e) Original uncorrected image

Figure 7.12 Reconstructed point source image, with no correction, classical and Divoli correction. The intensity distribution of randoms is also shown.

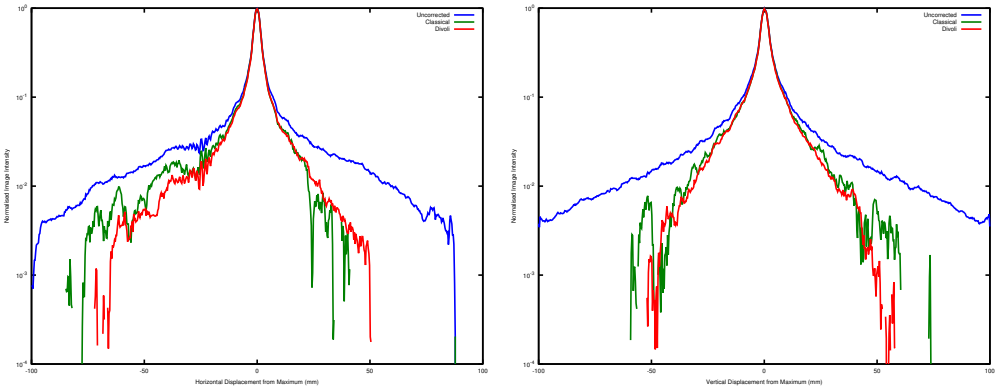

(a) Horizontal (b) Vertical

Figure 7.13 Profile of a point source, with no correction, classical correction and Divoli correction. The intensity scale is logarithmic.

in Figure 7.13. The Divoli method is superior in removing the background halo due to the randoms; however the improvement is quite modest.

It is noted that the random distribution produced by the classical technique is skewed in the direction of the offset of the point source from the CFoV. This is shown in Figure 7.14, in which symmetry in the horizontal direction (i.e. around the vertical axis) is shown to be significantly better with the Divoli method than with classical random correction. Little difference is observed in the vertical direction (i.e. symmetry about the horizontal axis); this is because the point source is centred on the horizontal axis and is therefore vertically symmetric. Although it the cause for this aberration is not known, it is suspected to be due to the equal weight given to low-probability pseudo-coincidences near the very periphery of the FoV in the classical approach. By contrast, the Divoli method favours creating pseudo-coincidences with a similar distribution to real coincidence data since all data is taken from events constructed from pairs of real coincidences, thus avoiding an artificial enhancement of apparent activity near the edge of the FoV. It is noted that a suitable probability density function could be used to correctly bias the weightings given to the classical method, which should result in similar results to the Divoli approach.

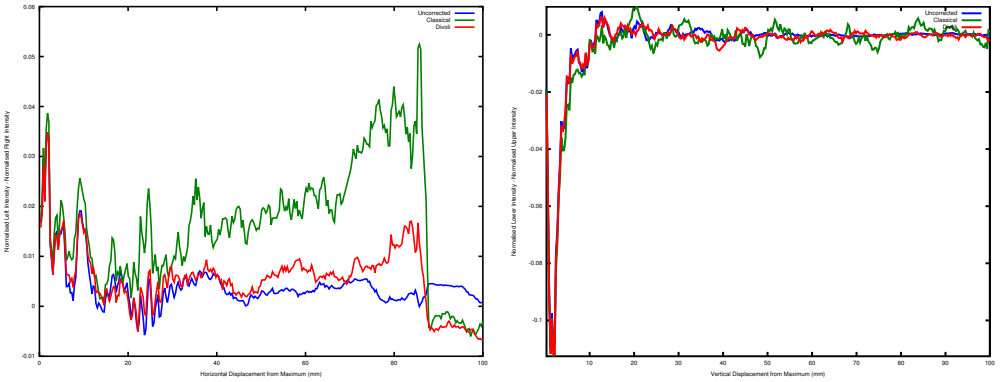

(a) Horizontal (b) Vertical

Figure 7.14 Improvements in symmetry of a nominally symmetric point source profile obtained using the Divoli method.

7.2.2.2 Spatial Resolution

The simulated ^{15}O point source images reconstructed with the direct-backprojection algorithm are shown in Figure 7.15. Radial and tangential point source profiles acquired from the reconstructed images of ^{15}O point source are plotted versus the radial offset from the centre (Figure 7.16). Additionally, fitted Gaussians are shown in Figure 7.17. Spatial resolution was then computed using all available depth of interaction information[2], and also with events rebinned to a 4×1 array of $3\times3\,times12$ mm^3 crystals, with a matching 4×1 detector, to simulate a scanner with an equivalent crystal volume but with no DoI information. Image reconstruction and other relevant parameters are shown in Table 7.5.

The FWHMs of the profiles shown in Figure 7.16 were calculated as a measure of the intrinsic resolution of the CMRPET detector modules and are plotted in Figure 7.18 as a function of radial position in the central transverse slice of CMRPET. Maximum, minimum and mean spatial resolutions are also shown in Table 7.6, measured in both the radial and tangential dimension, with and without the use of depth of interaction information. Clearly, utilising DoI information results in a significant improvement

[2]The exact (x, y, z) point of interaction was not used (although this information is available in GATE) - only the crystal index, in order to properly model the behaviour of a practical implementation of CMRPET

Table 7.5
Direct backprojection (and sinogram) image reconstruction parameters; Other geometric and imaging parameters.

Parameter	Value	Units
x resolution	0.303843	mm/pixel
y resolution	0.303843	mm/pixel
Nominal chord width	4.24	mm FWHM
Sinogram angle steps	512	(unused; for reference only)
Sinogram radial steps	512	(unused; for reference only)
Timing window	± 5	ns
Timing window offset	0	ns
Energy window	300-700	keV
Radial sectors	53	–
FoV diameter	202.562	mm
Voxel width/height/depth	3	mm
Axial rings	1	–

Table 7.6
Spatial resolution in radial and tangential directions, with and without DoI, obtained from Monte Carlo simulations. 95% confidence intervals are 2σ across all point source positions.

	Radial Resolution (mm)		Tangential Resolution (mm)	
	DoI	**No DoI**	**DoI**	**No DoI**
Maximum (worst)	2.3	3.8	3.9	6.1
Minimum (best)	1.6	1.6	1.7	1.7
Mean	2.0	2.8	2.6	3.0
95% CI	0.4	1.4	1.2	2.6

in spatial resolution, particularly close to the edge of the field of view.

A GATE simulation of the Ultra Micro Jaszczak phantom and CMRPET was also performed. The resulting image, reconstructed using the direct-backprojection method, is shown in Figure 7.19. The smallest resolvable hole has a diameter of 2 mm.

7.2.2.3 System Sensitivity

The true coincidence count rate for a 3.5 MBq ^{15}O point source is approximately 10000 coincidences per second. Using the energy window of 300 to 700 keV, the sensitivity estimate obtained from the simulation was 0.41%. This is a rather poor

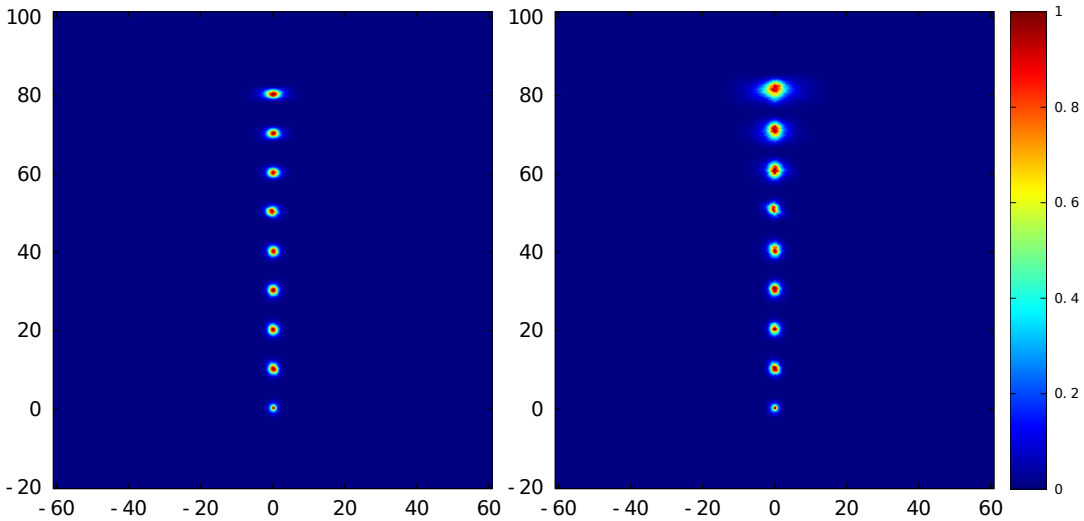

(a) DoI (b) No DoI

Figure 7.15 Images of the simulated ^{15}O point source at different radial offsets from CFoV (located near left-most point) reconstructed by the direct-backprojection algorithm. All dimensions in mm; intensity is normalised to maximum activity.

system sensitivity, which is a consequence of the very narrow edge-on profile of the detector modules. The simplest method for improving sensitivity is to stack multiple rings in the axial direction.

7.3 Discussion

The effectiveness of the edge-on detector configuration is clearly established through the simulations conducted in this Chapter. The utilisation of DoI information significantly enhances the uniformity of spatial resolution across the field of view; this effect is noted both in the radial and tangential dimension. The Divoli method for random correction is shown to be effective and moderately superior to the classical delayed-channel approach.

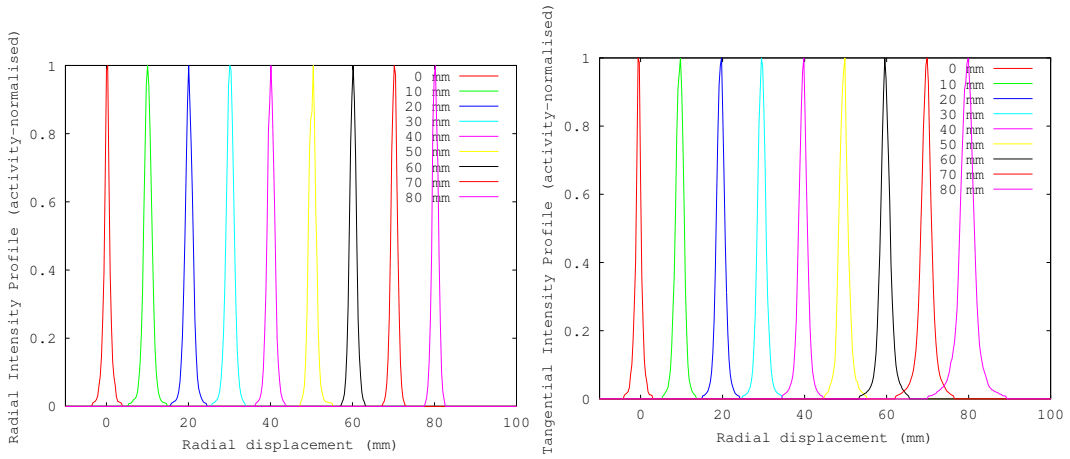

(a) Radial - DoI

(b) Tangential - DoI

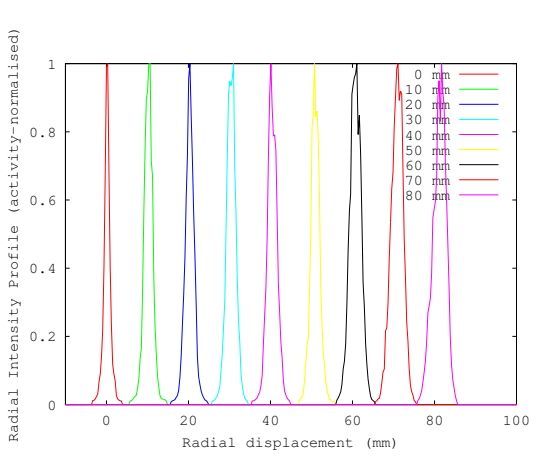

(c) Radial - No DoI

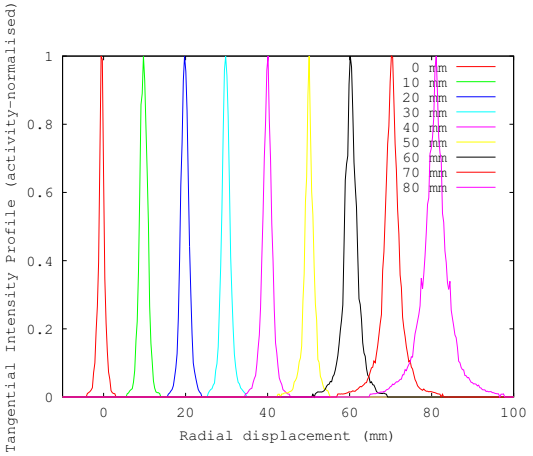

(d) Tangential - No DoI

Figure 7.16 Profiles of a simulated ^{68}Ge point source as a function of radial displacement across the FoV.

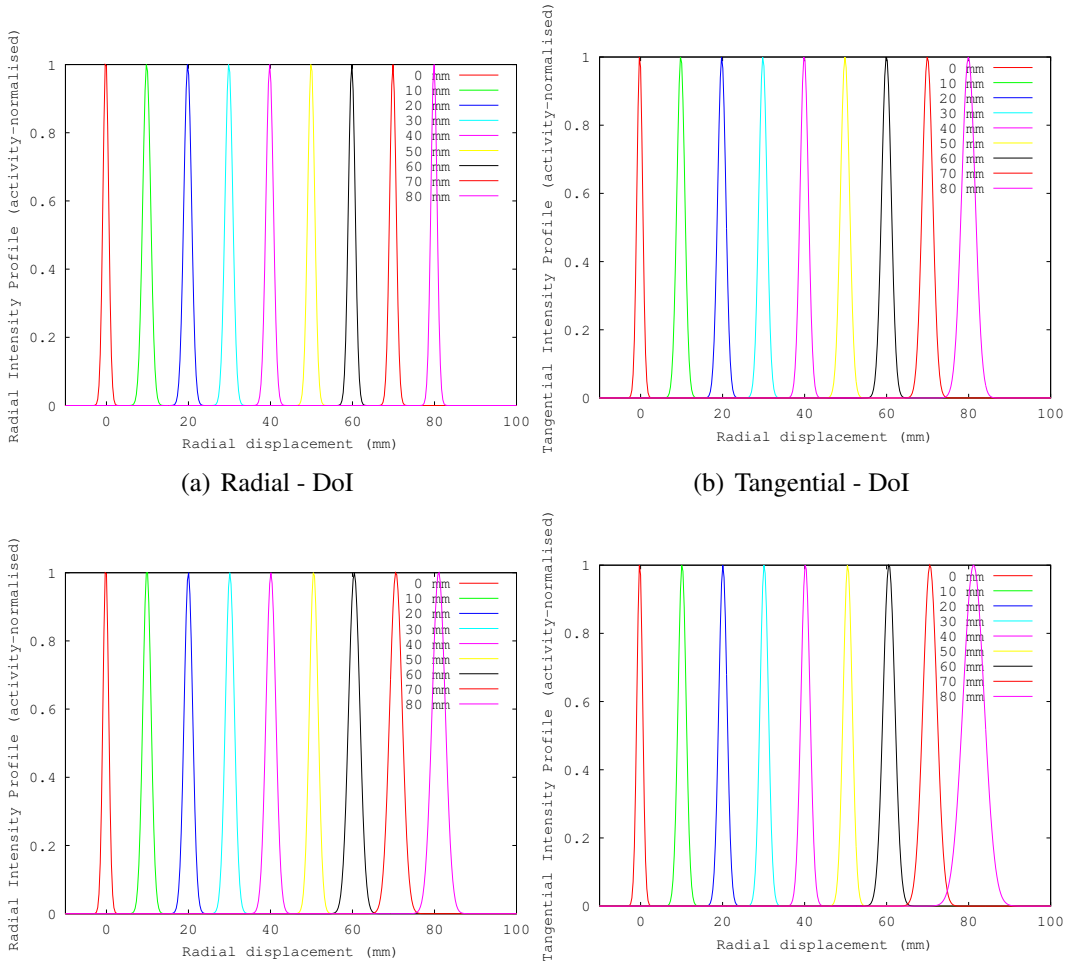

(a) Radial - DoI

(b) Tangential - DoI

(c) Radial - No DoI

(d) Tangential - No DoI

Figure 7.17 Gaussian profiles fitted to the simulation data from Figure 7.16

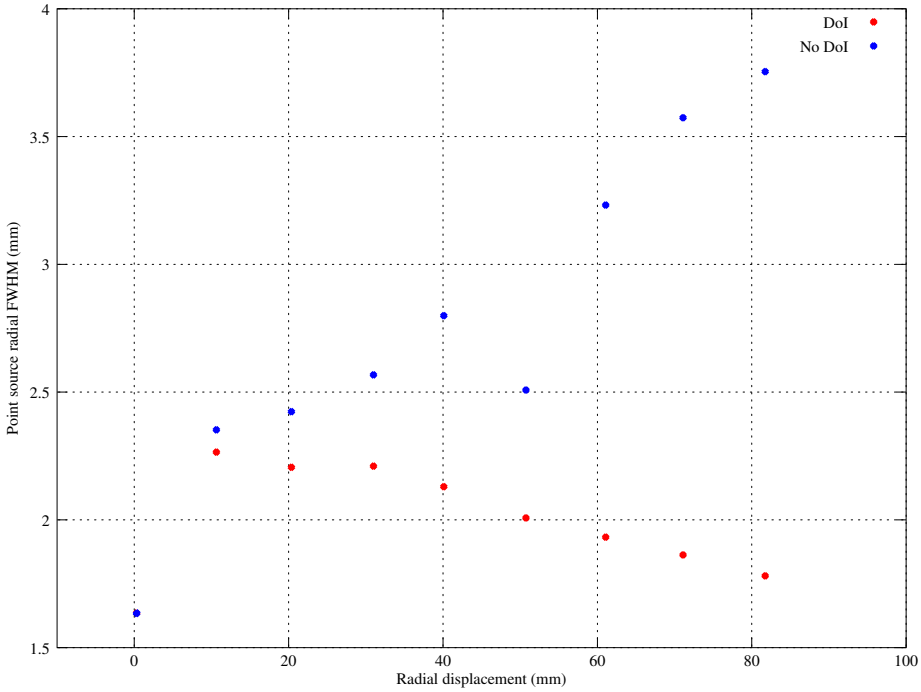

(a) Radial

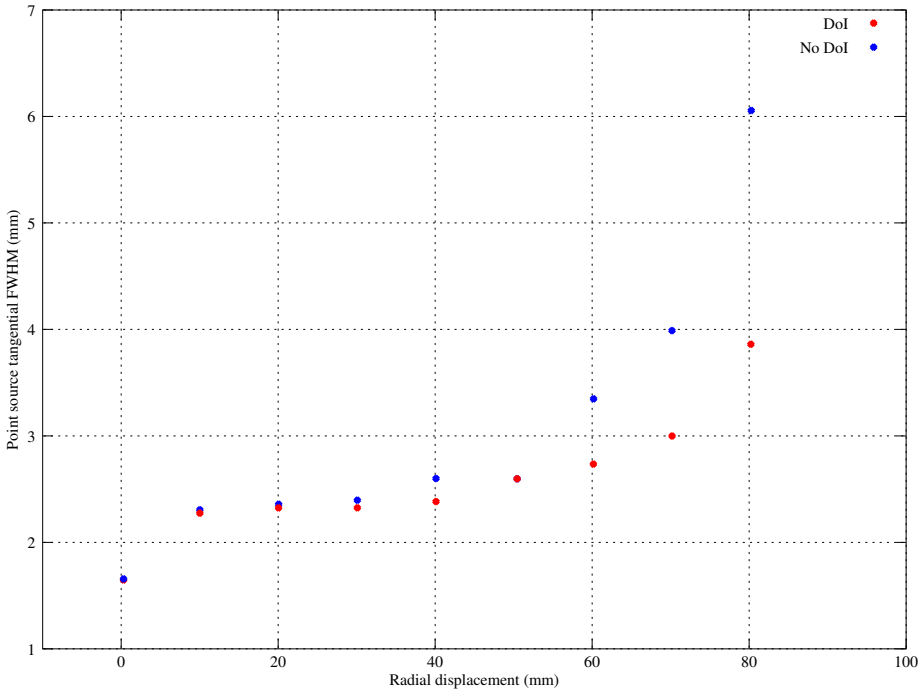

(b) Tangential

Figure 7.18 FWHM of the Gaussian profiles fitted to the simulated ^{68}Ge point source as a function of radial displacement (with and without DoI).

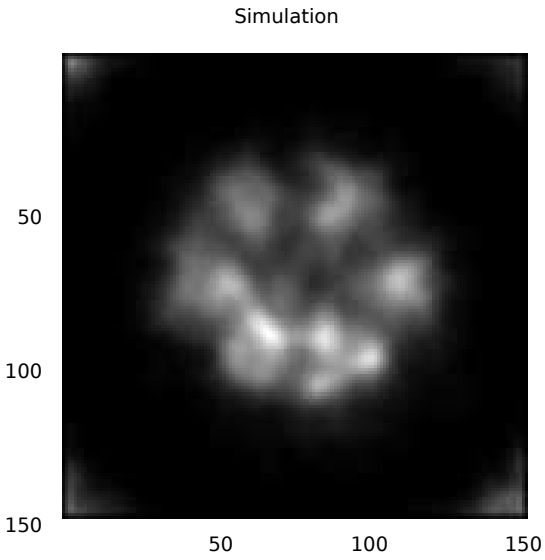

Figure 7.19 Reconstructed image of simulated Ultra Micro Jaszczak phantom and modelled CMRPET in GATE/GEANT4 and reconstructed by the direct-backprojection algorithm with full use of DoI information. Diameters of the rods in each of six segments were 2.0, 1.5, 1.25. 1.0, 0.75 and 0.50 mm, respectively. Centre to centre spacing is twice the rod diameter.

7.4 Conclusion

A low-cost variable-geometry PET system for small volume imaging has been designed and constructed. Key components have been characterised an validated; energy and timing resolution measurements have also been performed. Detailed GATE simulations of point sources at various positions inside the field of view have been completed, both validating the post-acquisition processing chain and verifying that there is minimal degradation in resolution near the edge of the field of view when DoI information is utilised. A realistic simulated phantom has also been imaged using the simulated CMRPET system. Finally, system sensitivity has been estimated for CMRPET in simulation.

Chapter 8 presents experimental results obtained using a prototype realisation of the CMRPET design configured identically to the model used in the simulation, and under near-identical experimental conditions.

Chapter 8

Experimental Characterisation of CMRPET

This Chapter presents experimental results obtained from the prototype system described and simulated in Chapter 7. Note that all measurement errors provided are given as two standard deviations, representing a 95% confidence interval.

The spatial resolution of CMRPET is experimentally evaluated in Section 8.2.1 using two approaches: firstly by translating a low-activity ^{68}Ga (^{68}Ge generator) point source to different positions inside the field of view, and secondly by using a Ultra Micro Jaszczak phantom filled with a high activity Fluorodeoxyglucose solution (FDG; ^{18}F). Spatial resolution estimates previously obtained from simulation studies were confirmed. The average spatial resolution achieved using CMRPET was 2.0$\pm$0.4 mm in the radial dimension and 2.0$\pm$0.2 mm in the tangential dimension, measured using the ^{68}Ga point source placed at different radial displacements inside the FoV. The best radial and tangential spatial resolutions observed were 1.8 mm in both cases. Initial images of phantoms are also acquired and are presented in Section 8.2.1. Spatial resolution estimates were confirmed by measuring the diameter of the smallest resolvable region in an FDG-filled Ultra Micro Jaszczak phantom, which was found to be 2.0 mm. Results are shown to be comparable to those obtained in simulation. Sensitivity estimates are reported in Section 8.2.2.

8.1 Experimental Methodology

8.1.1 Spatial Resolution

The spatial resolution was measured using a 3.5 MBq ^{68}Ga (^{68}Ge generator) point source placed on the radial-axial stage. The inner diameter of the gantry was set to 202 mm. The source has a nominal diameter of 1.2 mm and is embedded in a stainless steal sheath. It was initially positioned close to the centre of the FoV and then moved radially in steps of 10 mm to a maximum radius of 90 mm. At each position, data were acquired for 300 seconds for each pair of possible detector positions. The count rate profiles of the reconstructed point sources for every position were plotted in radial and tangential directions, and corrected for random coincident events as described in Section 7.1.9. The resulting profiles were fitted with a Gaussian function, and the FWHM of each fitted curve was calculated as a measure of the spatial resolution in the radial and tangential directions. Spatial measurements were not corrected for source dimensions (i.e. by deconvolution) or acollinearity.

The effect of having good DoI resolution is demonstrated by reconstructing images from the same raw data, with and without the DoI information. In non-DoI mode, the end points of a LoR are mapped to the front faces of the corresponding crystal columns in its radial sector, regardless of the measured DoI. This is the procedure generally adopted by commercial PET systems with deep crystals; the justification is that a photon interacting with the scintillator is most likely to do so near the front of the crystal due to the high Z_{eff} of the LYSO scintillator material. By contrast, when DoI information is used, the LoR is mapped to the front of corresponding crystal in its proper row and column within each radial sector, resolving its DoI to within 3 mm.

Additional measurements of the spatial resolution in the transverse plane were performed using a hot rod Ultra Micro Jaszczak (hot spot emission computed tomography) phantom. The phantom consists of a cylinder with an outer diameter of 3.5 cm and an inner diameter of 2.8 cm. The diameters of the resolution elements (rods)

vary from 0.5 mm to 2 mm in diameter. The phantom was filled with a uniform fluid distribution of ^{18}F with total activities of 300 MBq to 500 MBq at the start of the measurement. The scan was performed for up to 5 half lives (550 minutes). This was to eliminate statistical fluctuations due to the small size of the detectors and the limited solid angle. The exposure time was progressively increased as the scanning proceeded to compensate for the continuous reduction of the source activity. A total of 53 individual radial sector positions were used to allow for scanning the full FoV. The images were reconstructed using the method described in Section 7.1.8.

8.1.2 Sensitivity and Count Rate Performance

The aforementioned ^{68}Ga point source was moved radially in the transverse plane in small increments. The prompt coincidence count rate from the source was measured for 300 seconds at each position. The rate of random coincidences were estimated and subtracted using the same approach as described in Section 7.2.1.4.

8.2 Experimental Results

8.2.1 Spatial Resolution

A combined image of all exposures of the ^{68}Ga point source, moved across the FoV in 10 mm increments were reconstructed with and without DoI information. The results are shown in Figure 8.1. Image reconstruction and other relevant parameters are the same as for the simulations in Chapter 7 detailed in Table 7.5.

The radial and tangential image profiles of the point source images (with and without DoI) are shown in Figure 8.2. The curves are not normalised for detector efficiency, source dimensions, or acollinearity, however they are normalised for maximum image intensity.

The FWHMs of the profiles shown in Figure 8.2 were calculated as a measure of the intrinsic resolution of the CMRPET detector modules and are plotted in Figure 8.4 as

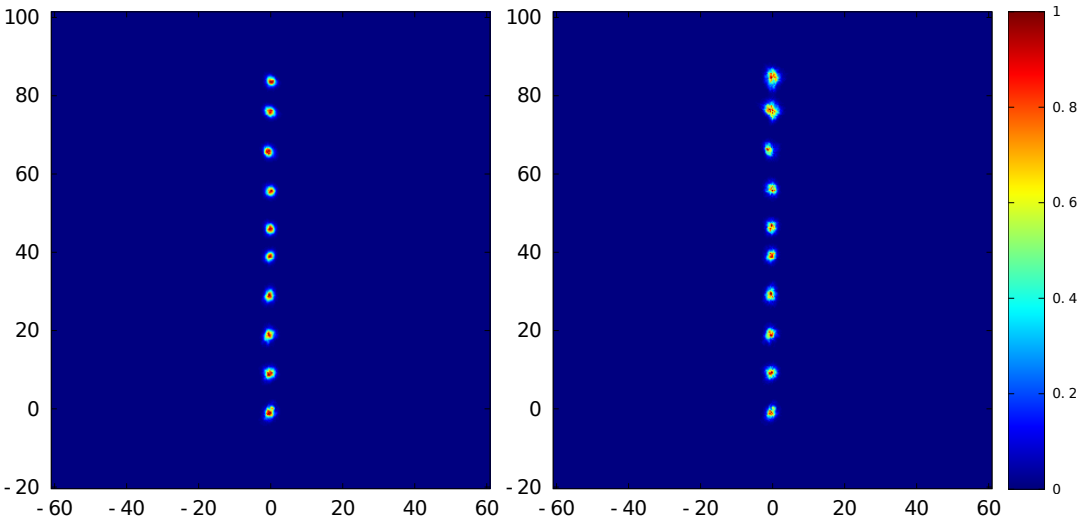

(a) DoI (b) No DoI

Figure 8.1 Images of the ^{68}Ga point source at different radial offsets from CFoV (located near left-most point) reconstructed by the direct backprojection algorithm. All dimensions in mm; intensity is normalised to maximum activity.

a function of radial position in the central transverse slice of CMRPET. Maximum, minimum and mean spatial resolutions are also shown in Table 8.1, measured in both the radial and tangential dimension, with and without the use of depth of interaction information.

The effect of ignoring DoI information becomes apparent once the point source moves more than 20 mm from the centre. The effect is observed to be slightly stronger in the tangential direction; this result mirrors the observations in the Monte Carlo simulations discussed in Chapter 7. It is noted that while there is some statistical fluctuation in the radial and tangential measurements, the size of the point source is consistently over-estimated unless DoI is enabled.

When depth of interaction information is not utilised, both radial and tangential spatial resolution degrade very rapidly as radial displacement increases. The minimum values are very similar to those observed when DoI information is used, as expected. However, the maximum values observed (at the periphery of the field of view) and the overall mean are significantly worse, both in radial and tangential dimensions.

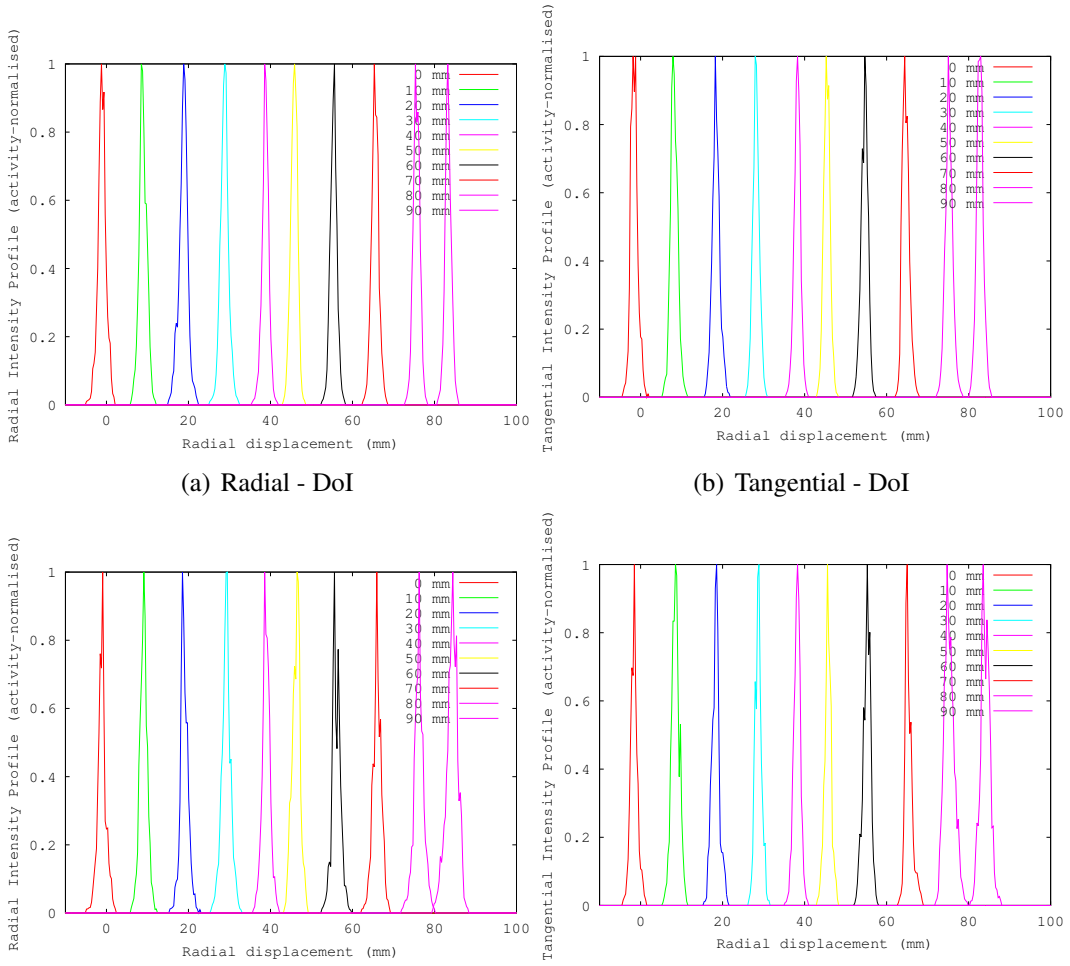

(a) Radial - DoI

(b) Tangential - DoI

(c) Radial - No DoI

(d) Tangential - No DoI

Figure 8.2 Profiles of a ^{68}Ga point source as a function of radial displacement across the FoV.

Table 8.1
Spatial resolution in radial and tangential directions, with and without DoI, obtained from experiments conducted using the prototype realisation of CMRPET. 95% confidence intervals are 2σ across all point source positions.

	Radial Resolution (mm)		**Tangential Resolution (mm)**	
	DoI	**No DoI**	**DoI**	**No DoI**
Maximum (worst)	2.3	3.3	2.3	3.0
Minimum (best)	1.8	1.8	1.8	1.8
Mean	2.0	2.6	2.0	2.2
95% CI	0.4	0.8	0.2	0.8

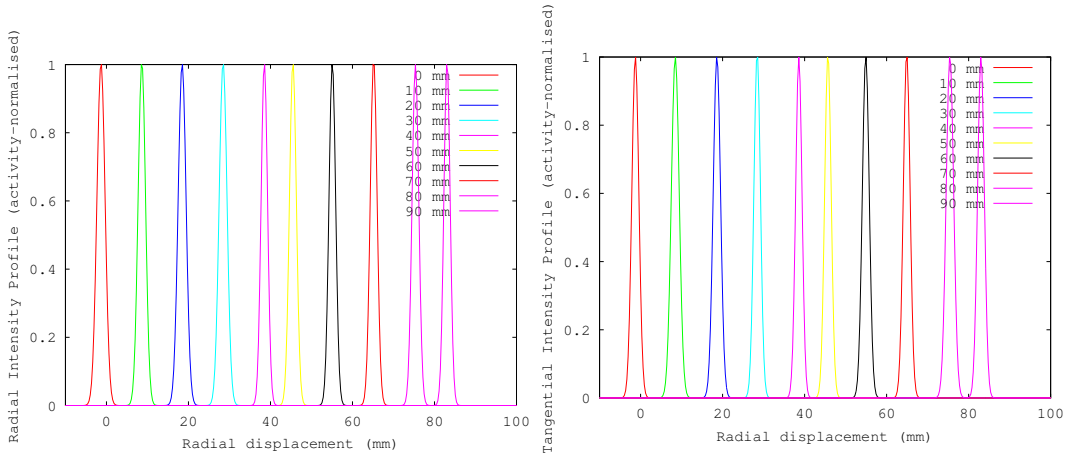

(a) Radial - DoI (b) Tangential - DoI

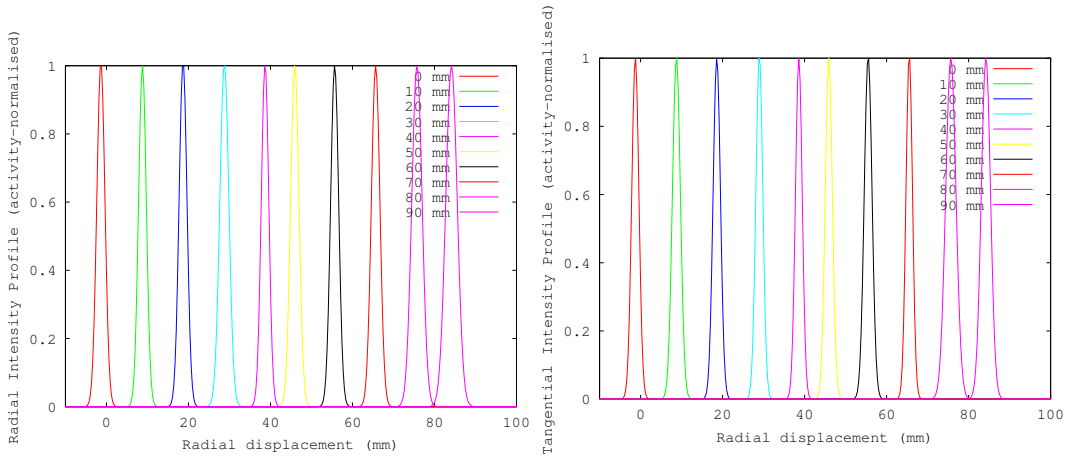

(c) Radial - No DoI (d) Tangential - No DoI

Figure 8.3 Gaussian profiles fitted to the experimental data from Figure 8.2

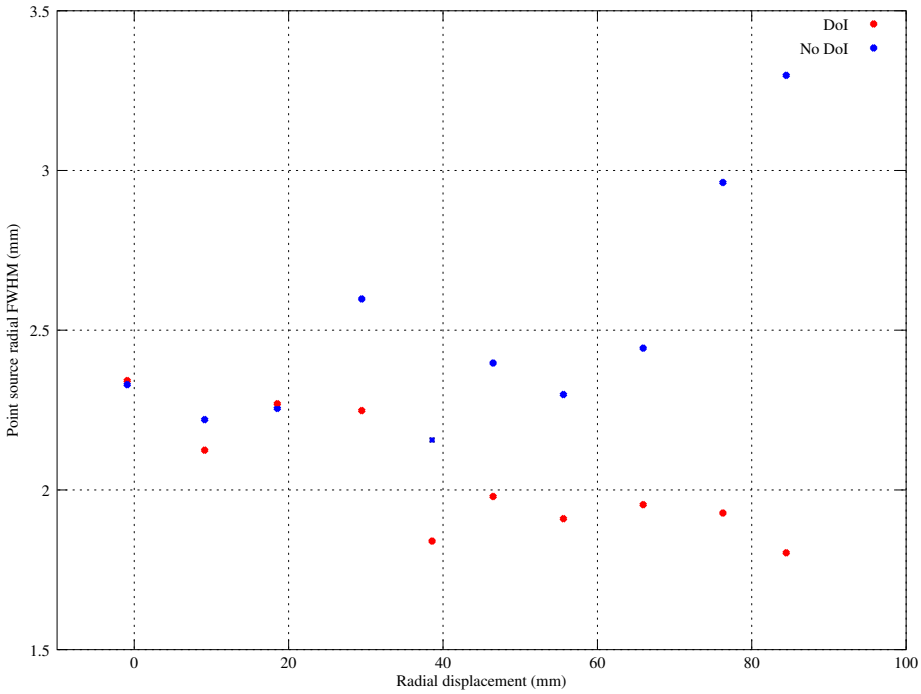

(a) Radial

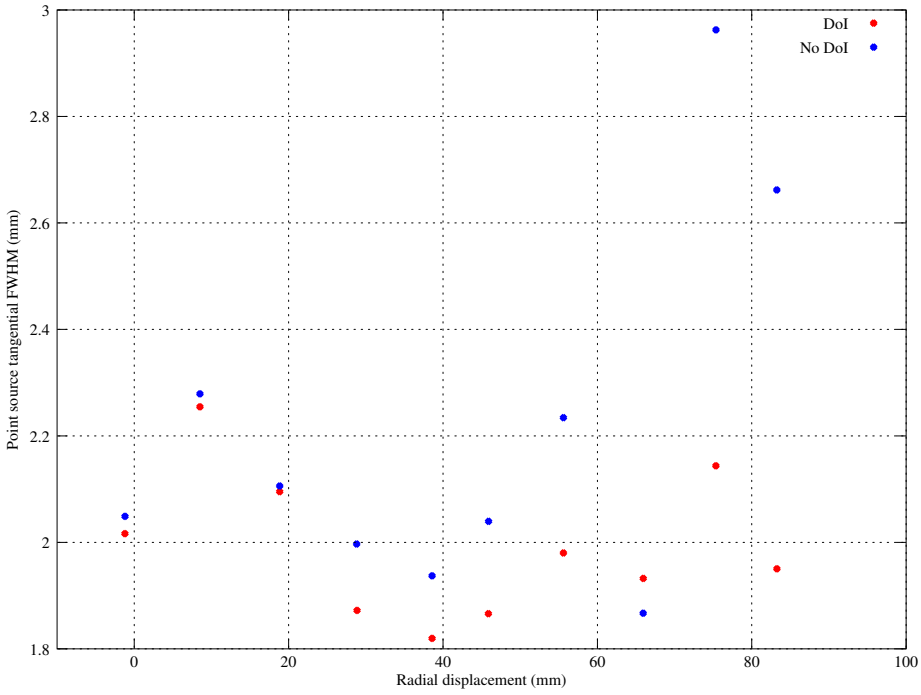

(b) Tangential

Figure 8.4 FWHM of the Gaussian profiles fitted to the ^{68}Ge point source as a function of radial displacement (with and without DoI).

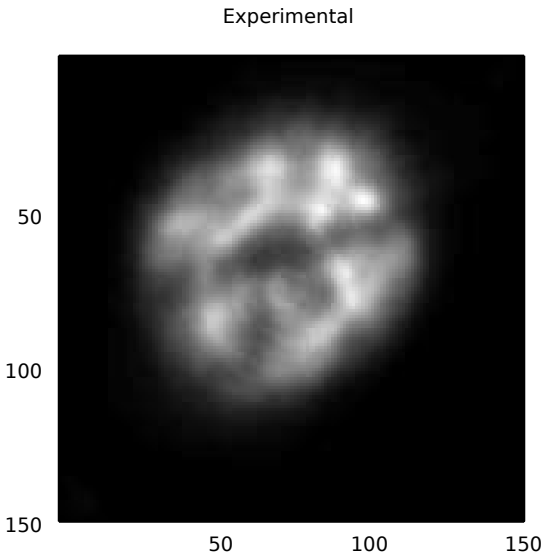

Figure 8.5 Reconstructed image of the Ultra Micro Jaszczak phantom acquired by CMRPET scanner and reconstructed by the direct-backprojection algorithm with full use of DoI information. Diameters of the rods in each of six segments were 2.0, 1.5, 1.25. 1.0, 0.75 and 0.50 mm, respectively. Centre to centre spacing is twice the rod diameter.

Therefore, the use of DoI information provides a significantly more consistent spatial resolution across the field of view.

A reconstructed image of a transverse slice of the Ultra Micro Jaszczak phantom acquired with CMRPET is shown in Figure 8.2.1. The smallest resolvable hole in the reconstructed image (using the direct backprojection method) has a diameter of 2 mm.

8.2.2 System Sensitivity

The true coincidence count rate for a 3.5 MBq ^{68}Ge point source is approximately 10000 coincidences per second. The sensitivity of the prototype CMRPET scanner, using an energy window of 200 keV centred on 500 keV was measured as 0.35%.

8.3 Discussion

The measured mean spatial resolution at the CFoV (with no correction for finite source size) is in good agreement with the best possible theoretical spatial resolution for a PET system with gantry radius of 202 mm and a detector pixel pitch of 3 mm with an ^{15}O point source at the CFoV. Assuming a block field factor of zero ($b = 0$):

$$\mathrm{FWHM} = 1.25\sqrt{\left(\frac{D_{crystal}}{2}\right)^2 + (0.0022D_{system})^2 + s^2 + b^2} \tag{8.1}$$

The theoretical spatial resolution is predicted to be 2.0 mm. The equation includes the degrading effects of the FWHM attributable to positron range (s), system (gantry) diameter (D_{system}), and finite crystal size ($D_{crystal}$).

The results show that the obtained spatial resolution is essentially the same as its theoretically predicted value. Figure 8.4 also show good agreement with the simulation results previously shown in Figure 7.18, again demonstrating the effectiveness of the DoI estimation in achieving a relatively uniform spatial resolution across the entire FoV. The spatial resolution near the centre of the FoV (CFoV) is essentially the same regardless of the use of DoI information. As the point source is moved radially from the centre to the periphery of the FoV, spatial resolution begins to deteriorate. This deterioration is reduced by utilising the DoI information, enabling a 30-40% improvement in spatial resolution at the edge of the FoV. Therefore, in a scanner using DoI information, the radial resolution degrades more slowly with increasing radial source position than in a scanner with identical geometry but without this capability. The significantly improved spatial resolution in the periphery of the FoV makes this scanner configuration an attractive choice for small animal and positron emission mammography (PEM) imaging, where the subject occupies the full FoV.

It is noted that the degradation in the tangential dimension observed in the simulation is significantly worse than that observed in practice - the cause of this effect is not known at this time. However, employment of DoI greatly improves the consistency

of spatial resolution even in this case. Other differences between the experimental and simulated results for system sensitivity may be a result of imperfect SiPM optical coupling or light spreading/leakage in the experimental apparatus. A comparison of the experimental and simulated sensitivity indicates an actual efficiency factor of 85%.

8.4 Conclusion

A fully functional high resolution PET scanner has been developed at CMRP. Preliminary experimental phantom and point source images have been acquired and reconstructed, and validated against simulation results. Application of depth of interaction data has been shown to provide an improvement in the uniformity of spatial resolution across the FoV.

The largest drawback of CMRPET is the lengthy acquisition time for each run. Sensitivity of a PET system is affected by several factors, including solid angle, packing fraction and scintillator efficiency for 511 keV photons. The current form of CMRPET is somewhat limited by its poor solid angle, which is due to the limited number of detector modules. It is straightforward to improve both the acquisition time and the system sensitivity by extending the design to multiple rings of multiple detector modules. An increase in system sensitivity from 0.35% to 4% would be obtained by using a fully-populated system with 8 parallel rings. Additional future work includes investigation of alternative image reconstruction techniques (iterative, OSEM etc.) to further improve image quality.

Chapter 9

Summary of Contributions and Future Research

A prototype DoI enabled PET scanner based on SiPM arrays placed in an edge-on configuration (CMRPET) have been successfully developed. The performance of scanner clearly has been demonstrated through simulation and experimental evaluation. In particular, the effectiveness of the edge on placement of the detectors in resolving DoI is shown, with a uniform spatial resolution achieved across the whole FoV.

9.1 Contributions

A thorough review of the current trends in detector technology, associated read out and data acquisition systems was completed, results of which were summarised in Chapter 2. A number of key technologies suitable for advanced compact PET systems were identified, including LSO-family scintillators (such as LGSO and LYSO), solid-state detectors and silicon photomultipliers (SiPMs) in particular, the SCEPTER nuclear pulse processing ASIC and HYMOD data acquisition platform.

Three silicon detectors were characterised in terms of their energy (spectroscopic), timing (transient response), noise (ENC) and charge collection (IBIC) and their performance were compared in Chapters 4, 5 and 6. It was concluded that the a pixel-

lated SiPM detector provides the best solution for a dedicated small FoV PET system.

The read out circuitry and its associated ASIC were selected based on the system requirements such as low noise, minimum dead time, and sufficient bandwidth for handling the anticipated event rate. A read out system based on the mixed mode SCEPTER ASIC from Brookhaven National Laboratory and the HYMOD data acquisition system developed at CSIRO satisfy the aforementioned criteria and are discussed in detail in Chapter 7. A thorough evaluation of the DAQ system was carried out and it was optimised for use with the SiPM detectors. A low noise discrete element analogue pulse conditioning (shaping and DC shifting/limiting) circuit was designed to interface the SiPM detectors to SCEPTER and DDAQ. The resulting design, incorporating all of these elements was named CMRPET, and was simulated in GATE. Its performance was evaluated in terms of sensitivity, energy, timing and spatial resolution by reconstructing a simulated ^{15}O point source, stepped across the FoV radially (Chapter 7). To demonstrate the effectiveness of DoI in improving the system performance, the point source was reconstructed with and without the DoI information. It was found that the DoI-enabled system improves the spatial resolution by $\approx$30% at the edge of the FoV.

A prototype CMRPET scanner with two fully assembled SiPM modules mounted on a gantry was constructed for experimental work, and the associated control systems and software were developed. The detectors were mounted on two rotationally independent gantry heads and thus were used to simulate a fully populated ring. The spatial resolution was evaluated in two ways, firstly by scanning a ^{18}Ge point source which was stepped across the FoV radially and secondly, by imaging an ultra micro Jaszczak filled with a high activity FDG (^{18}F) solution. The radial spatial resolution at the CFoV was found to be 2 mm (Chapter 8).

9.2 Future Work

There are a number of technical restrictions in the current system which limit its usefulness:

1. Image acquisition time is limited by the availability of only two detector modules and the need to emulate a full detector ring;
2. Noise and timing uncertainty arise due to long cables currently which need to be used to connect detectors to the data acquisition system; and
3. The potential for positioning uncertainty exists in the system due to lack of feedback and mechanical limitations of the variable-geometry rotating gantry on which the detectors are mounted.

Upgrades to a number of the gantry's mechanical components (such as adding a shaft encoder to the gantry stepper motors) will result in a more accurate positioning and an improvement in image quality and a reduction in imaging artefacts. In order to improve the speed of image acquisition, the gantry ring needs to be fully populated with detectors and the associated scintillator crystals and support electronics. A fully populated ring will consist of between 16 and 50 detector modules, depending on the chosen gantry radius. A key preparatory step towards fully populating the ring is to develop a scalable distributed analog/digital signal acquisition system based on the application-specific integrated circuit (ASIC) used in the current prototype, which will be able to cope with the very high volume of data produced by a fully populated ring. This will have the added benefit of reducing signal path lengths compared to the current prototype, minimising noise and pulse distortion issues. The current system uses SCEPTER ASIC attached to an FPGA-based data acquisition system. Each chip supports up to 32 inputs, such that one chip is sufficient for two 4×4-pixel arrays. In the current prototype, SCEPTER is connected to the detector arrays via a pair of 1.5 metre ribbon cables, which complicate rotation of the gantry and introduce noise and

pulse distortion (hence impairing image quality). The upgraded design will integrate one SCEPTER between each pair of adjacent detectors, mounted directly on the gantry ring. This will reduce the noise and distortion issues significantly and greatly simplify cabling arrangements. This design will scale over a wide variety of gantry radii, with each pair of detectors added to the system allowing increased resolution and reduced acquisition time. These benefits can be experimentally confirmed with the addition of a second detector pair to the current prototype system. The result will a PET system with greatly improved image acquisition speed (subject to full population of the detector ring) which requires much lower activity levels to perform imaging, such that it is ready for use in studies involving live animal models.

Bibliography

[1] M. N. Wernick and J. N. Aarsvold, *Emission Tomography, The Fundamentals of PET and SPECT*. Elsevier, 2004.

[2] F. M. Khan, *The Physics of Radiation Therapy*, 3rd ed. Lippincott Williams & Wilkins, 2003, ch. 8, pp. 148–151.

[3] G. F. Knoll, *Radiation Detection and Measurements*, 3rd ed. Wiley, 2000.

[4] PerkinElmer, "Avalanche photodiodes: A user guide," Online [last accessed 12/08/2013]; http://www.perkinelmer.com/CMSResources/Images/44-6538APP_AvalanchePhotodiodesUsersGuide.pdf, 2010.

[5] S. R. Cherry, J. A. Sorenson, and M. E. Phelps, *Physics in Nuclear Medicine*, 3rd ed. Saunders (Elsevier), 2003.

[6] H. S. S. Division, "Characteristics and Use of Charge Amplifier - Technical Information SD-37," Hamamatsu Photonics K. K., Tech. Rep., Oct. 2001.

[7] Amptek, "A250 Specifications," Online [last accessed 22/07/2013]; http://www.amptek.com/pdf/a250.pdf, May 2013.

[8] A. Fazzi, G. F. D. Betta, and G. U. Pignatel, "PIN Diode and Integrated JFET on High Resistivity Silicon: a New Test Structure," in *Nuclear Science Symposium Conference Record*, vol. 1. IEEE, nov 2001, pp. 219–222.

[9] J. L. Humm, A. Rosenfeld, and A. D. Guerra, "From PET detectors to PET scanners," *European Journal of Nuclear Medicine and Molecular Imaging*, vol. 30, no. 11, pp. 1574–1597, Nov. 2003.

[10] M. Korzhik, A. Fedorov, A. Annenkov, A. Borissevitch, A. Dossovitski, O. Missevitch, and P. Lecoq, "Development of scintillation materials for PET scanners," *Nuclear Instruments and Methods in Physics Research Section A: Accelerators, Spectrometers, Detectors and Associated Equipment*, vol. 571, no. 1-2, pp. 122–125, 2007.

[11] T. Kimble, M. Chou, and B. H. Chai, "Scintillation properties of LYSO crystals," in *Nuclear Science Symposium Conference Record, 2002 IEEE*, vol. 3. IEEE, 2002, pp. 1434–1437.

[12] S. Derenzo, M. Boswell, M. Weber, and K. Brennan, "Scintillation properties," Online [last accessed 01/08/2013]; http://scintillator.lbl.gov/, 2013.

[13] Wendie A. Berg and Irving N. Weinberg and Deepa Narayanan and Mary E. Lobrano and Eric Ross and Laura Amodei and Lorraine Tafra and Lee Adler and Joseph Uddo and William Stein and Edward A. Levine, "High-resolution fluorodeoxyglucose positron emission tomography with compression ("positron emission mammography") is highly accurate in depicting primary breast cancer." *Breast Journal*, vol. 12, no. 4, pp. 309–323, Jul-Aug 2006.

[14] C. Woody, A. Kriplani, P. O'Connor, J.-F. Pratte, V. Radeka, S. Rescia, D. Schlyer, S. Shokouhi, S. Stoll, P. Vaska, A. Villaneuva, N. Volkow, and B. Yu, "RatCAP: a small, head-mounted PET tomograph for imaging the brain of an awake RAT," *Nuclear Instruments and Methods in Physics Research A*, vol. 527, pp. 166–170, Jul. 2004.

[15] P. Vaska, C. L. Woody, D. J. Schlyer, S. Shokouhi, S. P. Stoll, J.-F. Prate, P. O'Connor, S. S. Junnarkar, S. Rescia, B. Yu, M. Purschke, A. Kandasamy, A. Villanueva, A. Kriplani, V. Radeka, N. Volkow, R. Lecomte, and R. Fontaine, "RatCAP: Miniaturized Head-Mounted PET for Conscious Rodent Brain Imaging," *IEEE Transactions on Nuclear Science*, vol. 51, no. 5, pp. 2718–2722, Oct. 2004.

[16] J.-F. Pratte, G. D. Geronimo, S. Junnarkar, P. O. Connor, B. Yu, S. Robert, V. Radeka, C. Woody, S. Stoll, P. Vaska, A. Kandasamy, R. Lecomte, and R. Fonaine, "Front-End Electronics for the RatCAP Mobile Animal PET Scanner," *IEEE Transactions on Nuclear Science*, vol. 51, no. 4, pp. 1318–1323, Aug. 2004.

[17] S. Shokouhi, P. Vaska, D. J. Schlyer, S. P. Stoll, A. V. Jr., A. Kriplani, and C. L. Woody, "System Performance Simulations of the RatCAP Awake Rat Brain Scanner," *IEEE Transactions on Nuclear Science*, vol. 52, no. 5, pp. 1305–1310, Oct. 2005.

[18] J. T. Bushberg, J. A. Seibert, A. M. Leidholdt, and J. M. Boone, *The Essential Physics of Medical Imaging*, 2nd ed. Lippincott Williams & Wilkins, 2002.

[19] J. Douglas, C. Moisan, and J. Rogers, "Investigating the Impace of LSO on the Count Rate of Wholebody PET Tomographs," *IEEE Transactions on Nuclear Science*, vol. 44, no. 3, pp. 1219–1224, Jun 1996.

[20] E. R. Powsner, *Essentials of Nuclear Medicine Physics*. Blackwell Publishing, 1998.

[21] M. Phelps, E. Hoffman, S. Huang, and M. Ter-Pogossian, "Effect of positron range on spatial resultion," *J. Nucl. Med*, vol. 16, pp. 649–652, 1975.

[22] S. R. Cherry, J. A. Sorenson, and M. E. Phelps, *Physics in Nuclear Medicine*, 3rd ed. Saunders (Elsevier), 2003, ch. 18, pp. 325–359.

[23] W. W. Moses, "Trends in PET Imaging," *Nuclear Instruments and Methods*, vol. A, no. 471, pp. 209–214, 2001.

[24] V. Astakhov, P. Gumplinger, C. Moisan, T. Ruth, and V. Sossi, "Effect of Depth of Interaction Decoding on Resolution in PET: A Simulation Study," *IEEE Transactions on Nuclear Science*, vol. 50, no. 5, pp. 1373–1376, oct 2003.

[25] M. Conti, L. Eriksson, H. Rothfuss, and C. C.L. Melcher, "Comparison of Fast Scintillators With TOF PET Potential," *Nuclear Science, IEEE Transactions on*, vol. 56, no. 3, pp. 926 –933, june 2009.

[26] C. L. Melcher, "Scintillation Crystals for PET," *Journal of Nuclear Medicine*, vol. 41, no. 6, pp. 1051–1055, Jun. 2000.

[27] F. Daghighian, P. Shenderov, K. S. Pentlow, M. C. Graham, B. Eshaghian, C. L. Melcher, and J. S. Schweitzer, "Evaluation of Cerium Doped Lutetium Oxyorthosilicat (LSO) Scintillation Crystal for PET," *IEEE Transactions on Nuclear Science*, vol. 40, no. 4, pp. 1045–1047, Aug. 1993.

[28] C. L. Melcher and J. S. Schweitzer, "Cerium-doped Lutetium Oxyorthosilicate: A Fast, Efficient New Scintillator," *Nuclear Instruments and Methods in Physics Research Section A*, vol. 314, no. 1, pp. 212–214, Apr. 1991.

[29] Yamamoto, Seiichi and Horii, Hitoshi and Hurutani, Mitsuru and Matsumoto, Keiichi and Senda, Michio, "Investigation of single, random, and true counts from natural radioactivity in LSO-based clinical PET," *Annals of Nuclear Medicine*, vol. 19, no. 2, pp. 109–114, Apr. 2005.

[30] R. R. Raylman, S. Majewski, M. F. Smith, R. Wojcik, A. G. Weisenberger, B. Kross, V. Popov, and J. J. Derakhshan, "Comparison of Scintillators for Positron Emission Mammography (PEM) Systems," *IEEE Transactions on Nuclear Science*, vol. 50, no. 1, pp. 42–49, Feb 2003.

[31] J. Martinez, J. Benlloch, J. Cerda, C. Lerche, N. Pavon, and A. Sebastia, "High Speed Data Acquisition and Digital Signal Processing System for PET Imging Techniques Applied to Mammography," *IEEE Transactions on Nuclear Science*, vol. 51, no. 3, pp. 407–412, Jun 2004.

[32] P. Lecoq and M. Korzhik, "New inorganic scintillation materials development for medical imaging," *Nuclear Science, IEEE Transactions on*, vol. 49, no. 4, pp. 1651–1654, aug 2002.

[33] S. Weber, D. Christ, M. Kurzeja, R. Engels, G. Kemmerling, and H. Halling, "Comparison of LuYAP, LSO, and BGO as scintillators for high resolution PET detectors," *Nuclear Science, IEEE Transactions on*, vol. 50, no. 5, pp. 1370–1372, oct. 2003.

[34] C. W. E. van Eijk, "Radiation detector developments in medical applications: inorganic scintillators in positron emission tomography," *Radiation Protection Dosimetry*, vol. 129, no. 1-3, pp. 13–21, 2008.

[35] W. W. Moses, S. E. Derenzo, and T. F. Budinger, "PET detector modules based on novel detector technologies," *Nuclear Instruments and Methods in Physics Research Section A: Accelerators, Spectrometers, Detectors and Associated Equipment*, vol. 353, no. 1-3, pp. 189–194, 1994.

[36] A. D. Guerra, N. Belcari, M. G. Bisogni, F. Corsi, M. Foresta, P. Guerra, S. Marcatili, A. Santos, and G. Sportelli, "Silicon Photomultipliers (SiPM) as novel photodetectors for PET," *Nuclear Instruments and Methods in Physics Research Section A: Accelerators, Spectrometers, Detectors and Associated Equipment*, vol. 648, Supplement 1, no. 0, pp. S232–S235, 2011.

[37] G. Hall, "Semiconductor particle tracking detectors," *Rep. Prog. Phys.*, vol. 57, pp. 481–531, 1994.

[38] S. Sze and K. Ng, *Physics of Semiconductor Devices*, 3rd ed. Wiley, 2007.

[39] F. Smith, *Applied Radiation Physics*, 3rd ed. World Scientific, 2003, ch. 5, pp. 185–196.

[40] W. W. Moses, S. E. Derenzo, R. Nutt, W. M. Digby, C. W. Williams, and M. Andreaco, "Performance of a PET Detector Module Utilizing an Array of Silicon Photodiodes to Identify the Crystal of Interaction," *IEEE Transactions on Nuclear Science*, vol. 40, no. 4, pp. 1036–1040, Aug. 1993.

[41] W. W. Moses, I. Kipnis, and M. H. Ho, "A 16-Channel Charge Sensitive Amplifier IC for a PIN Photodiode Array Based PET Detector Module," *IEEE Transactions on Nuclear Science*, vol. 41, no. 4, pp. 1469–1472, Aug. 1994.

[42] S. Holland, "An IC-compatible detector process," *IEEE Trans. Nucl. Sci.*, vol. 36, no. 1, pp. 283–289, feb 1989.

[43] S. E. Holland, D. E. Groom, N. P. Palaio, R. J. Stover, and M. Wei, "Fully Depleted, Back-Illuminated Charge-Coupled Devices Fabricated on High-Resistivity Silicon," *IEEE Trans. Nucl. Sci.*, vol. 50, no. 1, pp. 225–238, jan 2003.

[44] B. Patt, J. Iwanczyk, C. Tull, J. Segal, L. MacDonald, M. Tornai, and C. Kenny, "Fast-Timing Silicon Photodetectors," *IEEE Transactions on Nuclear Science*, vol. 47, no. 3, pp. 957–964, jun 2000.

[45] E. Sciacca, A. C. Giudice, D. Sanfilippo, F. Zappa, S. Lombardo, R. Consentino, C. D. Franco, M. Ghioni, G. Fallica, G. Bonanno, S. Cova, and E. Rimini, "Silicon Planar Technology for Single-Photon Optical Detectors," *IEEE Transactions on Electron Devices*, vol. 50, no. 4, pp. 918–925, Apr. 2003.

[46] P. Bérard, M. Bergeron, C. Pepin, J. Cadorette, M. Tétrault, N. Viscogliosi, R. Fontaine, H. Dautet, M. Davies, P. Deschamps, and R. Lecomte, "Development of a 64-channel APD detector module with individual pixel readout for submillimetre spatial resolution in PET," *Nuclear Instruments and Methods in Physics Research Section A: Accelerators, Spectrometers, Detectors and Associated Equipment*, vol. 610, no. 1, pp. 20–23, 2009.

[47] P. Buzhan, B. Dolgoshein, A. Ilyin, V. Kantserov, V. Kaplin, A. Karakash, A. Pleshko, E. Popova, S. Smirnov, Y. Volkov, L. Vilatov, S. Klemin, and F. Kayumov, "An Advanced Study of Silicon Photomultiplier," *ICFA Instrumentation Bulletin*, vol. 23, no. 1, Fall 2001.

[48] P. Buzhan, B. Dolgoshein, L. Filatov, A. Ilyin, V. Kantzerov, V. Kaplin, A. Karakash, F. Kayumov, S. Klemin, E. Popova, and S. Smirnov, "Silicon

photomultiplier and its possible applications," *Nucl. Instr. and Meth. A*, vol. 504, pp. 48–52, 2003.

[49] A. N. Otte, B. Dolgoshein, H. G. Moser, R. Mirzoyan, and M. Teshima, "Status of Silicon Photomultiplier Developments as optical Sensors for MAGIC/EUSO-like Detectors," in *29th International Cosmic Ray Conference, Part 2: future plans and developments*, vol. 5. International Union of Pure and Applied Physics Commission on Cosmic Rays, Aug. 2005, pp. 211–214.

[50] M. Danilov, "Novel photo-detectors and photo-detector systems," *Nuclear Instruments and Methods in Physics Research Section A: Accelerators, Spectrometers, Detectors and Associated Equipment*, vol. 604, no. 1-2, pp. 183–189, 2009.

[51] R. Pestotnik, S. Korpar, H. Chagani, R. Dolenec, P. Križan, and A. Stanovnik, "Silicon photo-multipliers as photon detectors for PET," *Nuclear Instruments and Methods in Physics Research Section A: Accelerators, Spectrometers, Detectors and Associated Equipment*, vol. 623, no. 1, pp. 594–596, 2010.

[52] A. Akindinov, A. Martemianov, P. Polozov, V. Golovin, and E. Grigoriev, "New results on mrs apds," *Nuclear Instruments and Methods in Physics Research Section A: Accelerators, Spectrometers, Detectors and Associated Equipment*, vol. 387, no. 1-2, pp. 231 – 234, 1997, new Developments in Photodetection. [Online]. Available: http://www.sciencedirect.com/science/article/pii/S0168900296012016

[53] C. Piemonte, "A new Silicon Photomultiplier structure for blue light detection," *Nucl. Instr. and Meth. A*, vol. 568, no. 1, pp. 224–232, nov 2006.

[54] T. K. Lewellen, "Investigation of Depth-of-Interaction by Pulse Shape Discrimination in Multicrystal Detectors Read Out by Avalanche Phtodiodes," *American Journal of Roentgenology*, vol. 195, pp. 301–309, aug 2010.

[55] W. W. Moses and S. E. Derenzo, "Design Studies for a PET Detector Module Using a PIN Photodiode to Measure Depth of Interaction," *IEEE Transactions on Nuclear Science*, vol. 41, no. 4, pp. 1441–1445, Aug. 1994.

[56] P. Beltrame, E. Bolle, A. Braem, C. Casella, E. Chesi, N. Clinthorne, R. D. Leo, G. Dissertori, L. Djambazov, V. Fanti, C. Joram, H. Kagan, W. Lustermann, F. Meddi, E. Nappi, F. Nessi-Tedaldi, J. Oliver, F. Pauss, M. Rafecas, D. Renker, A. Rudge, D. Schinzel, T. Schneider, J. Séguinot, P. Solevi, S. Stapnes, and P. Weilhammer, "Demonstration of an Axial PET concept for brain and small animal imaging," *Nuclear Instruments and Methods in Physics Research Section A: Accelerators, Spectrometers, Detectors and Associated Equipment*, vol. 628, no. 1, pp. 426–429, 2011.

[57] S. Hong, C. Kim, S. Cho, H. Woo, G. Ko, S. Kwan, J. Rhee, I. Song, and J. Lee, "A Feasibility Study on the Use of Optical Fibers for the Transfer of Scintillation Light to Silicon Photomultipliers," *Nuclear Science, IEEE Transactions on*, vol. 58, no. 3, pp. 579–589, Jun. 2011.

[58] P. Beltrame, E. Bolle, A. Braem, C. Casella, E. Chesi, N. Clinthorne, R. D. Leo, G. Dissertori, L. Djambazov, V. Fanti, M. Heller, C. Joram, H. Kagan, W. Lustermann, F. Meddi, E. Nappi, F. Nessi-Tedaldi, J. Oliver, F. Pauss, M. Rafecas, D. Renker, A. Rudge, D. Schinzel, T. Schneider, J. Sguinot, P. Solevi, S. Stapnes, and P. Weilhammer, "The AX-PET demonstratorDesign, construction and characterization," *Nuclear Instruments and Methods in Physics Research Section A: Accelerators, Spectrometers, Detectors and Associated Equipment*, vol. 654, no. 1, pp. 546–559, 2011.

[59] S. R. Cherry, Y. Shao, R. W. Silverman, K. Meadors, S. Siegel, A. Chatziioannou, J. W. Young, W. F. Jones, J. C. Moyers, D. Newport, A. Boutefnouchet, T. F. Farquhar, M. Andreaco, M. J. Paulus, D. M. Binkley, R. Nutt, and M. E. Phelps, "MicroPET: A High Resolution PET Scanner for Imaging Small Animals," *IEEE Transactions on Nuclear Science*, vol. 44, no. 3, pp. 1161–1166, Jun. 1997.

[60] Y.-C. Tai, A. F. Chatziioannou, R. W. Silverman, K. Meadors, S. Siegel, D. F. Newport, Y. Yang, J. Stickel, and S. R. Cherry, "microPET II: An Ultra-high Resolution Small Animal PET System," in *Nuclear Science Symposium Conference Record*, vol. 3. IEEE, Nov. 2002, pp. 1848–1852.

[61] I. C. S. L. S. Committee, *IEEE Standard for Information technology - Telecommunications and information exchange between systems - Local and metropolitan area networks - Specific requirements, Part 3: Carrier sense multiple access with collision detection (CSMA/CD) access method and physical layer specifications*. IEEE, 2005.

[62] K. Nguyen, I. Mohor, and T. Markovic, "Ethernet MAC 10/100 Mbps," http://www.opencores.org/projects.cgi/web/ethmac/overview [last accessed: 1/11/2006], 2006.

[63] T. K. Lewellen, C. M. Laymon, R. S. Miyaoka, K. S. Lee, and P. E. Kinahan, "Design of a Firewire Based Data Acquisition System for use in Animal PET Scanners," in *Nuclear Science Symposium Conference Record*, vol. 4. IEEE, Nov. 2001, pp. 1974–1978.

[64] C. Ryan, D. Siddons, G. Moorhead, R. Kirkham, P. Dunn, A. Dragone, and G. Degeronimo, "Large detector array and real-time processing and elemental image projection of X-ray and proton microprobe fluorescence data," *Nuclear Instruments and Methods in Physics Research Section B: Beam Interactions with Materials and Atoms*, vol. 260, no. 1, pp. 1–7, Jul. 2007.

[65] H. Spieler, "Radiation Detectors and Signal Processing," Lecture Notes - VII. Heidelberger Graduate Lectures in Physics, Oct. 2001.

[66] A. Bertuccio and A. Pullia, "A Method for Determination of the Noise Parameters in Preamplifying Systems for Semiconductor Radiation Detectors," *Review of scientific instruments*, vol. 64, pp. 3294–3298, Nov. 1993.

[67] V. Radeka, "Low-Noise Techniques in Detectors," *Annual Review of Nuclear and Particle Science*, vol. 38, pp. 217–277, 1988.

[68] F. C. GmbH, "CR-200 Gaussian shaping amplifier (Rev. 2): application guide," Cremat, Tech. Rep., Oct. 2001.

[69] Adel S. Sedra and Kenneth C. Smith, *Microelectronics*, 5th ed. Oxford University Press, 2004.

[70] Paul Horowitz and Winfield Hill, *The Art of Electronics*, 2nd ed. Cambridge University Press, 1999.

[71] A. Dragone, G. De Geronimo, J. Fried, A. Kandasamy, P. O'Connor, and E. Vernon, "The PDD ASIC: highly efficient energy and timing extraction for high-rate applications," in *Nuclear Science Symposium Conference Record, 2005 IEEE*, vol. 2, Oct. 2005, pp. 914–918.

[72] P. O'Connor, G. D. Geronimo, and A. Kandasamy, "Amplitude and time measurement ASIC with analog derandomization: first results," *IEEE Trans. Nucl. Sci.*, vol. 50, no. 4, pp. 892–897, aug 2003.

[73] P. O'Connor, G. De Geronimo, and A. Kandasamy, "Amplitude and time measurement ASIC with analog derandomization: first results," *Nuclear Science, IEEE Transactions on*, vol. 50, no. 4, pp. 892–897, aug. 2003.

[74] W. W. Moses, P. R. G. Virador, S. E. Derenzo, R. H. Huesman, and T. F. Budinger, "Design of a High-Resolution, High-Sensitivity PET Camera for Human Brains and Small Animals," *IEEE Transactions on Nuclear Science*, vol. 44, no. 4, pp. 1487–1491, Aug. 1997.

[75] N. C. Rouze, M. Schmand, S. Siegel, and G. D. Hutchins, "Design of a Small Animal PET Imaging System With 1 Microliter Volume Resolution," *IEEE Transactions on Nuclear Science*, vol. 51, no. 3, pp. 757–763, Jun. 2004.

[76] J. A. Correia, C. A. Burnham, D. Kaufman, and A. J. Fischman, "Development of a Small Animal PET Imaging Device with Resolution Approaching 1mm," *IEEE Transactions on Nuclear Science*, vol. 46, no. 3, pp. 631–635, Jun. 1999.

[77] J. A. Correia, C. A. Burnham, D. Kaufman, A.-L. Brownell, and A. J. Fischman, "Performance Evaluation of MMP-II: A Second-Generation Small Animal PET," *IEEE Transactions on Nuclear Science*, vol. 51, no. 1, pp. 21–26, Feb. 2004.

[78] H. Li, Y. Liu, T. Xing, Y. Wang, S. Xie, J. Uribe, H. Baghaei, R. Ramirez, S. Kim, and W.-H. Wong, "Electronics Design for a Low-Cost High-Sensitivity Rodent-Research PET (RRPET)," in *Nuclear Science Symposium Conference Record*, vol. 4. IEEE, Oct. 2003, pp. 2267–2271.

[79] Y.-C. Tai, A. F. Chatziioannou, Y. Yang, R. W. Silverman, K. Meadors, S. Siegel, D. F. Newport, J. R. Stickel, and S. R. Cherry, "MicroPET II: Design, Development and Initial Performance of an Improved MicroPET Scanner for Small-Animal Imaging," *Physics in Medicine and Biology*, vol. 48, no. 11, pp. 1519–1537, May 2003.

[80] R. Miyaoka, C. Laymon, M. Janes, K. Lee, P. Kinahan, and T. Lewellen, "Recent progress in the development of a micro crystal element (MiCE) PET system," in *Nuclear Science Symposium Conference Record, 2002 IEEE*, vol. 2, nov. 2002, pp. 1287–1291.

[81] E. P. Visser, J. A. Disselhorst, M. Brom, P. Laverman, M. Gotthardt, W. J. Oyen, and O. C. Boerman, "Spatial Resolution and Sensitivity of the Inveon Small-Animal PET scanner," *Journal of Nuclear Medicine*, vol. 50, no. 1, pp. 139–147, jan 2009.

[82] J. S. Kim, J. S. Lee, K. C. Im, S. J. Kim, S.-Y. Kim, D. S. Lee, and D. H. Moon, "Performance Measurement of the microPET Focus 120 Scanner," *Journal of Nuclear Medicine*, vol. 48, no. 9, pp. 1527–1535, sept 2007.

[83] Y. Wang, J. Seidel, B. M. Tsui, J. J. Vaquero, and M. G. Pomper, "Performance Evaluation of the GE Healthcare eXplore VISTA Dual-Ring Small-Animal PET Scanner," *Journal of Nuclear Medicine*, vol. 47, no. 11, pp. 1891–1900, nov 2006.

[84] Y. Yang and S. S. Cherry, "Observations Regarding Scatter Fraction and NEC Measurements for Small Animal PET," *IEEE Transactions in Nuclear Sciences*, vol. 53, no. 1, pp. 127–132, feb 2006.

[85] A. Chatziioannou, R. W. Silverman, K. Meadors, T. H. Farquhar, and S. R. Cherry, "Techniques to Improve the Spatial Sampling of MicroPET - A High Resolution Animal PET Tomograph," *IEEE Transactions on Nuclear Science*, vol. 47, no. 2, pp. 422–427, Apr. 2000.

[86] R. Laforest, D. Longford, S. Siegel, D. F. Newport, and J. Yap, "Performance Evaluation of the microPET®-Focus-F120," in *Nuclear Science Symposium Conference Record*, vol. 5. IEEE, Oct. 2004, pp. 2965–2969.

[87] T. K. Lewellen and R. L. Harrison and S. Vannoy, *The SimSET Program*. Medical Science Series, 1998, pp. 77–92.

[88] H. Feick, E. Fretwurst, M. Moll, and G. Lindstrom, "Correlation of radiation damage effects in high resistivity silicon detectors with results from deep level spectroscopy," *Nuclear Science, IEEE Transactions on*, vol. 44, no. 3, pp. 825–833, 1997.

[89] D. Passeri, P. Ciampolini, G. Bilei, and F. Moscatelli, "Comprehensive modeling of bulk-damage effects in silicon radiation detectors," *Nuclear Science, IEEE Transactions on*, vol. 48, no. 5, pp. 1688–1693, 2001.

[90] M. Petasecca, F. Moscatelli, D. Passeri, and G. Pignatel, "Numerical Simulation of Radiation Damage Effects in p-Type and n-Type FZ Silicon Detectors," *Nuclear Science, IEEE Transactions on*, vol. 53, no. 5, pp. 2971–2976, 2006.

[91] M. Benoit, A. Lounis, and N. Dinu, "Simulation of guard ring influence on the performance of ATLAS pixel detectors for inner layer replacement," *J. Inst.*, vol. 4, no. 3, 2009. [Online]. Available: {http://iopscience.iop.org/1748-0221/4/03/P03025}

[92] ——, "Simulation of Radiation Damage Effects on Planar Pixel Guard Ring Structure for ATLAS Inner Detector Upgrade," *Nuclear Science, IEEE Transactions on*, vol. 56, no. 6, pp. 3236–3243, 2009.

[93] B. E. A. Saleh and M. C. Teich, *Fundamentals of Photonics*. John Wiley & Sons, Inc., 1991, pp. 693–694.

[94] "IEEE NPSS Short Course - Radiation Detection and Measurement - Pulse Processing and Analysis," Online [last accessed 29/01/2013]; http://www-physics.lbl.gov/~spieler, Nov. 2002.

[95] C. Allier, H. Valk, J. Huizenga, V. Bom, R. Hollander, and C. van Eijk, "Comparative Study of Silicon Detectors," *IEEE Transactions on Nuclear Science*, vol. 45, no. 3, pp. 576–580, jun 1998.

[96] R. Orito, H. Nishimura, K. Hattori, H. Kubo, K. Miuchi, T. Nagayoshi, Y. Okada, H. Sekiya, A. Takada, A. Takeda, and T. Tanimori, "Performance of large area Si PIN photo diode array," in *IEEE Nuclear Science Symposium Conference Record*, vol. 5. IEEE, oct 2005, pp. 2993–2997.

[97] T. Frach, W. Ruetten, K. Flieder, G. Maehlum, T. Solf, and A. Thon, "Assessment of Photodiodes as a Light Detector for PET scanner," in *IEEE Nuclear Science Symposium Conference Record*, vol. 7. IEEE, oct 2004, pp. 4177–4181.

[98] L. Rossi, P. Fischer, T. Rohe, and W. Wermes, *Pixel Detectors, From Fundamentals to Applications*. Springer, 2006.

[99] C. Delaney and E. Finch, *Radiation Detectors, Physical Principles and Applications*, 1st ed. Oxford Science Publications, 1992.

[100] W. Shockley and W. Read, "Statistics of the Recombinations of Holes and Electrons," *Physical Review*, vol. 87, pp. 835–842, Sep. 1952.

[101] B. M. Noisecom, *7200 Series Capacitance Meter*, Wireless Telecom Group.

[102] S. Ramo, "Currents Induced by Electron Motion," *Proc. IRE*, vol. 27, p. 584585, 1939.

[103] W. Shockley, "Currents to conductors induced by a moving point charge," *J. Appl. Phys.*, vol. 9, pp. 635–636, 1938.

[104] G. Gilmore, *Practical Gamma-ray Spectrometry*, 2nd ed. WILEY, 2008.

[105] M. Jakšic, I. Bogdanović, M. Bogovac, S. Fazinić, S. Galassini, K. Kovačević, C. Manfredotti, and E. Vittone, "Testing of radiation detectors by IBIC imaging," *Nucl. Instr. Meth. B*, vol. 113, pp. 378–381, 1996.

[106] G. Eichholz and J. Poston, *Principles of Nuclear Radiation Detection*, 1st ed. Ann Arbor Science, 1979.

[107] R. Siegele, D. D. Cohen, and N. Dytlewski, "The ANSTO high energy heavy ion microprobe," *Nucl. Instr. Meth. B*, vol. 158, pp. 31–38, 1999.

[108] W. Moses, S. Derenzo, C. Melcher, and R. A. Manente, "A room temperature LSO/PIN photodiode PET detector module that measures depth of interaction," *Nuclear Science, IEEE Transactions on*, vol. 42, no. 4, pp. 1085–1089, 1995.

[109] V.Saveliev, "The recent development and study of silicon photomultiplier," *NIM*, vol. NIM, no. 1-2, pp. 528–532, dec 2004.

[110] G. D. Betta, G. Pignatel, G. Verzellesi, M. Boscardin, A. Fazzin, and L. Bosisio, "Monolithic integration of Si-PIN diodes and n-channel double-gate JFET's for room temperature X-ray spectroscopy," *NIM*, vol. 458, no. 1-2, pp. 275–280, feb 2001.

[111] J. Kemmer and G. Lutz, "New detector concepts," *NIM. A*, vol. 253, p. 365, 1987.

[112] J. Kemmer, G. Lutz, U. Prechtel, K. Schuster, M. Sterzik, L. Strüder, and T. Ziemann, "Experimental confirmation of a new semiconductor detector

principle," *Nuclear Instruments and Methods in Physics Research A*, vol. 288, pp. 92–98, Mar. 1990.

[113] S. Carrato, G. Cautero, F. Corsi, G. DallaBetta, A.Dragone, A. Fazzi, F. Garibaldi, C. Marzocca, M. Petasecca, G. Pignatel, L. Stebel, A. Tauro, V. Varoli, and N. Zorzi, "A functionally reconfigurable detector head for scintimammography," *NIM*, vol. 571, no. 1-2, pp. 369–371, feb 2007.

[114] V. Mishra, V. Srivastava, and S. Kataria, "Role of guard rings in improving the performance of silicon detectors," *PRAMANA Journal of Physics*, vol. 65, no. 2, pp. 259–272, aug 2005.

[115] L. Stebel, S. Carrato, G. Cautero, M. Petasecca, G. Pignatel, C. Marzocca, A. Tauro, A. Dragone, F. Corsi, G. Betta, A. Fazzi, and N. Zorzi, "Development of a prototype detector for use in scintimammography imaging," *Microelectronics Journal*, vol. 37, no. 12, pp. 1598–1609, dec 2006.

[116] M. L. Lerch, A. B. Rosenfeld, P. E. Simmonds, G. N. Taylor, S. R. Meikle, and V. L. Pervertailo, "Spectral Characterisation of a Blue-Enhanced Silicon Photodetector," *IEEE Transactions on Nuclear Science*, vol. 48, no. 4, pp. 1220–1224, Aug 2001.

[117] M. L. Lerch, R. Ward, P. E. Simmonds, V. L. Pervertailo, S. R. Meikle, G. N. Taylor, and A. B. Rosenfeld, "Readout of LYSO using a new silicon photodetector for positron emission tomography," in *Nuclear Science Symposium Conference Record*, vol. 2. IEEE, Oct 2003, pp. 1408–1412.

[118] *ISE-TCAD Manual*, 6th ed., Integrated System Engineering (ISE), 1999.

[119] F. Lemeilleur, M. Glaser, E. H. M. Heijne, P. Jarron, C. Soave, C. Leroy, J. Rioux, P. Roy, M. Siad, and I. Trigger, "Charge transport in silicon detectors," in *1st International Conference on Large-Scale Applications and Radiation Hardness of Semiconductor Detectors*, 1994. [Online]. Available: \url{http://preprints.cern.ch/cgi-bin/setlink?base=preprint\&categ=CM-P\&id=CM-P00060336}

[120] M. Moszyńuski, M. Kaputsa, M. Mayhugh, D. Wolski, and S. Flyckt, "Absolute light output of Scintillators," *IEEE Transactions on Nuclear Science*, vol. 44, no. 3, pp. 1052–1061, jun 1997.

[121] M. A. Green, "Self-consistent optical parameters of intrinsic silicon at 300k including temperature coefficients," *Solar Energy Materials and Solar Cells*, vol. 92, no. 11, pp. 1305 – 1310, 2008. [Online]. Available: http://www.sciencedirect.com/science/article/pii/S0927024808002158

[122] *SmartGel: Optical Coupling Technology*, Nye Lubricant Inc., 12 Howland Road, Fairhaven, MA 02719, USA, 2005.

[123] V. Radeka, P. Rehak, S. Rescia, E. Gatti, A. Longoni, M. Sampietro, G. Bertuccio, P. Holl, L. Struder, and J. Kemmer, "Implanted Silicon JFET on Completely Depleted High-Resistivity Devices," *IEEE Electron device Lett.*, vol. 10, no. 2, pp. 91–94, feb 1989.

[124] E. Pinotti, H. Bräuninger, N. Findeis, H. Gorke, D. Hauff, P. Holl, J. Kemmer, P. Lechner, G. Lutz, W. Kink, N. Meidinger, G. Metzner, P. Predehl, C. Reppin, L. Strüder, J. Trümper, C. v. Zanthier, E. Kendziorra, R. Staubert, V. Radeka, P. Rehak, G. Bertuccio, E. Gatti, A. Longoni, A. Pullia, and M. Sampietro, "The pn-CCD on-chip electronics," *Nucl. Instr. and Meth. A*, vol. 326, no. 1-2, pp. 85–91, mar 1993.

[125] E. Gatti, P. Rehak, A. Longoni, J. Kemmer, P. Holl, R. Klanner, G. Lutz, A. Wylie, F. Goulding, P. N. Luke, N. W. Madden, and J. Walton, "Semiconductor Drift Chambers," *IEEE Trans. Nucl. Sci.*, vol. 32, no. 2, pp. 1204–1208, apr 1985.

[126] G.-F. D. Betta, M. Boscardin, L. Bosisio, P. Gregori, L. Pancheri, C. Piemonte, L. Ratti, G. Verzellesi, and N. Zorzi, "Monolithic integration of detectors and transistors on high-resistivity silicon," *Nucl. Instr. and Meth. A*, vol. 579, pp. 658–663, 2007.

[127] G. F. D. Betta, G. Verzellesi, G. U. Pignatel, S. Amon, M. Boscardin, and G. Soncini, "Design of an n-channel JFET on high-resistivity silicon for radiation-detector on-chip front-end electronics," *Nucl. Instr. and Meth. A*, vol. 567, pp. 368–371, 2006.

[128] G.-F. D. Betta, C. Piemonte, M. Boscardin, P. Gregori, N. Zorzi, A. Fazzi, and G. U. Pignatel, "An improved PIN photodetector with integrated JFET on high-resistivity silicon," *Nucl. Instr. and Meth. A*, vol. 567, pp. 368–371, 2006.

[129] G. Bondarenko, P. Buzhan, B. Dolgoshein, V. Golovin, E. Guschin, A. Ilyin, V. Kaplin, A. Karakash, R. Klanner, V. Pokachalov, E. Popova, and K. Smirnov, "Limited Geigermode microcell silicon photodiode: new results," *Nucl. Instr. and Meth. A*, vol. 442, pp. 187–192, 2000.

[130] V. M. Golovin, Russian Patent nr. 1644708, Class 6 H 01 L 31/06 // BI, 1999, no. 33., 1999.

[131] V. Golovin and V. Saveliev, "Novel type of avalanche photodetector with Geiger mode operation," *Nucl. Instr. and Meth. A*, vol. 518, no. 1-2, pp. 560–564, feb 2004.

[132] T. Frach, G. Prescher, C. Degenhardt, R. de Gruyter, A. Schmitz, and R. Ballizany, "The digital silicon photomultiplier; Principle of operation and intrinsic detector performance," in *Nuclear Science Symposium Conference Record (NSS/MIC), 2009 IEEE*, Nov. 2009, pp. 1959–1965.

[133] M. Petasecca, B. Alpat, G. Ambrosi, P. Azzarello, R. Battiston, M. Ionica, A. Papi, G. U. Pignatel, and S. Haino, "Thermal and Electrical Characterization of Silicon Photomultiplier," *IEEE Trans. Nucl. Sci.*, vol. 55, no. 3, pp. 1686–1690, jun 2008.

[134] C. Piemonte, R. Batiston, M. Boscardin, G. F. D. Betta, A. D. Guerra, N. Dinu, A. Pozza, and N. Zorzi, "Characterization of the First Prototypes of Silicon Photomultiplier Fabricated at ITC-irst," *IEEE Trans. Nucl. Sci.*, vol. 54, no. 1, pp. 236–244, feb 2007.

[135] N. Dinu, R. Battiston, M. Boscardin, G. Collazuol, F. Corsi, G. D. Betta, A. D. Guerra, G. Llosá, M. Ionica, G. Levi, S. Marcatili, C. Marzocca, C. Piemonte, G. Pignatel, A. Pozza, L. Quadrani, C. Sbarra, and N. Zorzi, "Development of the first prototypes of Silicon PhotoMultiplier (SiPM) at ITC-irst," *Nucl. Instr. and Meth. A*, vol. 572, no. 1, pp. 422–426, mar 2007.

[136] D. P. McElroy, V. Saveliev, A. Reznik, and J. A. Rowlands, "Evaluation of silicon photomultipliers: A promising new detector for MR compatible PET," *Nucl. Instr. and Meth. A*, vol. 567, no. 1-2, pp. 106–109, feb 2007.

[137] M. McClish, P. Dokhale, J. Christian, C. Stapels, and K. Shah, "Characterization and scintillation studies of a solid-state photomultiplier," *Nucl. Instr. and Meth. A*, vol. 572, no. 3, pp. 1065–1070, mar 2007.

[138] G. Collazuol, G. Ambrosi, M. Boscardin, F. Corsi, G. F. D. Betta, A. D. Guerra, N. Dinu, M. Galimberti, D. Giulietti, L. A. Gizzi, L. Labate, G. Llosa, S. Marcatili, F. Morsani, C. Piemonte, A. Pozza, L. Zaccarelli, and N. Zorzi, "Single photon timing resolution and detection efficiency of the IRST silicon photo-multipliers," *Nucl. Instr. Meth. A*, vol. 581, no. 1-2, pp. 461–464, oct 2007.

[139] G. Bertuccio and R. Casiraghi, "Study of silicon carbide for x-ray detection and spectroscopy," *Nuclear Science, IEEE Transactions on*, vol. 50, no. 1, pp. 175–185, 2003.

[140] N. Otte, B. Dolgoshein, J. Hose, S. Klemin, E. Lorenz, R. Mirzoyan, E. Popova, and M. Teshima, "The Potential of SiPM as Photon Detector in Astroparticle Physics Experiments like MAGIC and EUSO," *Nuclear Physics B Proceedings Supplements*, vol. 150, pp. 144–149, Jan. 2006.

[141] P. Buzhan, B. Dolgoshein, A. Ilyin, V. Kantserov, V. Kaplin, A. Karakash, A. Pleshko, E. Popova, S. Smirnov, Y. Volkov, L. Filatov, S. Klemin, and F. Kayumov, "An advanced study of silicon photomultiplier," *ICFA Inst. Bull*, vol. 21, p. 28, 2001.

[142] C. M. Pepin, P. Berard, and R. Lecomte, "Comparison of LSO, LGSO and MLS scintillators," in *Nuclear Science Symposium Conference Record*, vol. 1. IEEE, nov 2001, pp. 124– 128.

[143] *GaAs Detectors*, Space Research Centre of University of Leicester, mar 2008, http://www.src.le.ac.uk/instrumentation/solid_state/semiconductors/gaas.html.

[144] *Scintillator Readout with SPM*, 1st ed., SensL, mar 2008, www.sensl.com/pdfs/SPM_Tech_App_Notes/AN_ScintReadout.pdf.

[145] *ArraySL-4 Scalable Silicon Photomultiplier Array Datasheet*, SENSL, may 2011. [Online]. Available: http://sensl.com/documentation

[146] A. B. Rosenfeld, "Electronic dosimetry in radiation therapy," *Radiation Measurements*, vol. 41, no. Supplement 1, pp. S134–S153, dec 2006.

[147] ——, *Radiation Detectors for Medical Applications*. Springer Netherlands, nov 2006, ch. SEMICONDUCTOR DETECTORS IN RADIATION MEDICINE: RADIOTHERAPY AND RELATED APPLICATIONS, pp. 111–147.

[148] S. J. *et al*, "Gate: a simulation toolkit for pet and spect," *Physics in Medicine and Biology*, vol. 49, no. 19, Oct 2004. [Online]. Available: http://iopscience.iop.org/0031-9155/49/

[149] G. De Geronimo, E. Vernon, K. Ackley, J. Fried, P. O'Connor, A. Dragone, Z. He, C. Herman, and F. Zhang, "Readout ASIC for 3D position-sensitive detectors," in *Nuclear Science Symposium Conference Record, 2007. NSS '07. IEEE*, vol. 1, nov 2007, pp. 32 –41.

[150] G. De Geronimo, E. Vernon, K. Ackley, A. Dragone, J. Fried, P. O'Connor, Z. He, C. Herman, and F. Zhang, "Readout ASIC for 3D Position-Sensitive Detectors," *Nuclear Science, IEEE Transactions on*, vol. 55, no. 3, pp. 1593 –1603, jun 2008.

[151] A. J. Reader and H. Zaidi, "Advances in pet image reconstruction," *PET Clinics*, vol. 2, no. 2, pp. 173 – 190, 2007. [Online]. Available: http://www.sciencedirect.com/science/article/pii/S1556859807000193

[152] M. Safavi-Naeini, D. Franklin, M. Petasecca, M. Lerch, R. Kirkham, G. Moorhead, P. Dunn, G. De Geronimo, and A. Rosenfeld, "SiPM based detector module and digital data acquisition system for PET: Initial results," in *Nucl Sci Symp Conf Rec (NSS/MIC)*. IEEE, nov 2009, pp. 2679 –2682.

[153] J. Brady, *Scanning Gantry System Electronics Design Manual*, 1st ed., 2004. [Online]. Available: http://home.exetel.com.au/jbrady/HTMLobj-175/gantry_design.pdf

[154] ——, *Scanning Gantry Users' Manual*, 1st ed., 2004. [Online]. Available: http://home.exetel.com.au/jbrady/HTMLobj-176/User_Manual.pdf

[155] J. Brady, M. Lerch, J. Bourke, P. Anthony, and A. B. Rozenfeld, "Modular design of a multi-modal, small animal scanning gantry," Centre for Medical Radiation Physics, Tech. Rep., 2004. [Online]. Available: http://home.exetel.com.au/jbrady/HTMLobj-177/Lite_Gantry.pdf

[156] N. Clinthorne, "Methods for high resolution pet," Online [last accessed 01/08/2013]; http://www-group.slac.stanford.edu/ais/publicDocs/presentation113.pdf, Apr. 2009.

[157] A. Divoli, K. Erlandsson, J. Dickson, M. A. Flower, and R. J. Ott, "Estimation of random coincidences from the prompt PET data," in *Nuclear Science Symposium Conference Record, 2007. NSS '04. IEEE*, vol. 1, nov 2004, pp. 3703–3707.

[158] G. Wang and J. Qi, "Direct reconstruction of dynamic pet parametric images using sparse spectral representation," in *Biomedical Imaging: From Nano to Macro, 2009. ISBI '09. IEEE International Symposium on*, 2009, pp. 867–870.

[159] J. E. Carroll, *Physical Models for Semiconductor Devices*, 1st ed. Edward Arnold Ltd, 1974.

[160] S. Holland, N. Wang, and W. Moses, "Development of Low Noise, Back-Side Illuminated Silicon Photodiode Arrays," *IEEE Transactions on Nuclear Science*, vol. 44, no. 3, pp. 443–447, jun 1997.

[161] G. F. D. Betta, G. U. Pignatel, G. Verzellesi, M. Boscardin, A. Fazzi, and L. Bosisio, "Monolithic integration of Si-PIN diodes and n-channel double-gate JFET's for room temperature X-ray spectroscopy," *Nucl. Instr. and Meth. A*, vol. 458, pp. 275–280, 2001.

[162] A. Fazzi, G. U. Pignatel, G. F. D. Betta, M. Boscardin, V. Varoli, and G. Verzellesi, "Charge Preamplifier for Hole Collecting PIN Diode and Integrated Tetrode N-JFET," *IEEE Trans. Nucl. Sci.*, vol. 47, no. 3, pp. 829–833, jun 2000.

[163] M. Safavi-Naeini, M. L. F. Lerch, M. Petasecca, G. U. Pignatel, and A. B. Rosenfeld, "Evaluation of pixellated, back-sided planar photodetectors for high-resolution imaging instrumentation," *Nucl. Instr. Meth. A*, vol. 589, pp. 259–267, 2008.

[164] G. Lutz, *Semiconductor Radiation Detectors*, 1st ed. springer, 1999, ch. 8, pp. 229–238.

[165] N. Pavlov, G. Maehlum, and D. Meier, "Gamma Spectroscopy using a Silicon Photomultiplier and a Scintillator," in *Nuclear Science Symposium Conference Record*. IEEE, oct 2005, pp. 173–180.

[166] Y. Shaoa, H. Li, and K. Gao, "Initial experimental studies of using solid-state photomultiplier for PET applications," *Nucl. Instr. and Meth. A*, vol. 580, no. 2, pp. 944–950, 2007.

[167] D. Herbert, S. Moehrs, N. D'Ascenzo, N. Belcari, A. D. G. F. Morsani, and V. Saveliev, "The Silicon Photomultiplier for application to high-resolution

Positron Emission Tomography," *Nucl. Instr. and Meth. A*, vol. 573, no. 1-2, pp. 84–87, apr 2007.

[168] M. Moszynski, M. Kapusta, M. Mayhugh, D. Wolski, and S. O. Flyckt, "Absolute light output of scintillators," *IEEE Trans. Nucl. Sci.*, vol. 44, no. 3, pp. 1052–1061, jun 1997.

[169] E. Hoffman, S. Huang, M. Phelps, and D. Kuhl, "Quantitation in positron emission computed tomography: 4. Effect of accidental coincidences," *J Comput. Assist. Tomogr.*, vol. 5, no. 3, pp. 391–400, jun 1981.

[170] D. Brasse, C. Comtat, R. Trebossen, M. Tararine, and Q. Nguyen, "Correction for the random coincidences in dual head gamma camera imaging," in *IEEE Nucl Sci Symp Conf Rec (NSS)*, vol. 3, 1999, pp. 1229 –1233.

[171] Y. Zhang, H. Li, S. Liu, S. An, C. Wang, H. Baghaei, R. Ramirez, and W.-H. Wong, "The systematic errors in the random coincidence estimation using a delayed window," in *IEEE Nucl Sci Symp Conf Rec (NSS/MIC)*, nov 2009, pp. 3897 –3899.

[172] D. Brasse, C. Comtat, R. Trebossen, M. Tararine, Q. Nguyen, and B. Bendriem, "Correction for the random coincidences in dual-head gamma camera imaging," *IEEE Trans Nucl Sci*, vol. 48, no. 3, pp. 864 –871, jun 2001.

[173] E. Hoffman and *et al*, "Quantification in positron emission computed tomography: 4. Effect of accidental coincidences," *J Comput. Assist. Tomogr.*, vol. 5, no. 3, pp. 391–400, Jun 1981.

[174] D. Brasse and *et al*, "Correction Methods for Random Coincidences in Fully 3D Whole-Body PET: Impact on Data and Image Quality," *J Nucl. Med.*, vol. 46, no. 5, pp. 859–867, May 2005.

[175] K. Schilling, P. Conti, , L. Adler, and L. Tafra, "The role of positron emission mammography in breast cancer imaging and management," *Applied Radiology*, vol. 37, no. 4, pp. 26–36, apr 2008.

[176] Y. C. Tai, A. F. Chatziioannou, Y. F. Yang, R. Silverman, K. Meadors, S. Siegel, D. F. Newport, J. R. Stickel, and S. R. Cherry, "MicroPET II: design, development and initial performance of an improved microPET scanner for small-animal imaging," *Physics in Medicine and Biology*, vol. 48, no. 11, pp. 1519 – 1537, 2003.

[177] S.-K. Woo, K. Kim, T. Lee, J. Kim, J. Jung, K. Woo, W. Jung, J. Kang, G. Cheon, C. Choi, and S. Lim, "Experimental condition and registration method for the tumor detection of lung metastasis small animal PET and CT whole body images," in *Nuclear Science Symposium Conference Record, 2007. NSS '07. IEEE*, nov 2007, pp. 3372 –3375.

[178] H. Mizuma, M. Shukuri, T. Hayashi, Y. Watanabe, and H. Onoe, "Establishment of In Vivo Brain Imaging Method in Conscious Mice," *J Nucl Med*, vol. 51, no. 7, pp. 1068–1075, jul 2010.

[179] Y.-C. Tai1, A. F. Chatziioannou, Y. Yang, R. W. Silverman, K. Meadors, S. Siegel, D. F. Newport, J. R. Stickel, and S. R. Cherry, "MicroPET II: design, development and initial performance of an improved microPET scanner for small-animal imaging," *Phys Med Biol*, vol. 48, no. 11, pp. 1519 – 1537, 2003.

[180] R. Myers, "The biological application of small animal PET imaging," *Nucl Med Biol*, vol. 28, no. 5, pp. 585 –593, jul 2001.

[181] N. Cesca, N. Auricchio, G. D. Domenico, G. Zavattini, R. Malaguti, R. Andritschke, G. Kanbach, and F. Schopper, "Silipet: Design of an ultra-high resolution small animal pet scanner based on stacks of semi-conductor detectors," *Nuclear Instruments and Methods in Physics Research Section A: Accelerators, Spectrometers, Detectors and Associated Equipment*, vol. 572, no. 1, pp. 225–227, 2007.

[182] S. Jan, G. Santin, D. Strul, S. Staelens, K. Assi, D. Autret, S. Avner, R. Barbier, M. Bardis, P. M. Bloomfield, D. Brasse, V. Breton, P. Bruyndonckx,

I. Buvat, A. F. Chatziioannou, Y. Choi, Y. H. Chung, C. Comtat, D. Donnarieix, L. Ferrer, S. J. Glick, C. J. Groiselle, D. Guez, P.-F. Honore, S. Kerhoas-Cavata, A. S. Kirov, V. Kohli, M. Koole, M. Krieguer, D. J. van der Laan, F. Lamare, G. Largeron, C. Lartizien, D. Lazaro, M. C. Maas, L. Maigne, F. Mayet, F. Melot, C. Merheb, E. Pennacchio, J. Perez, U. Pietrzyk, F. R. Rannou, M. Rey, D. R. Schaart, C. R. Schmidtlein, L. Simon, T. Y. Song, J.-M. Vieira, D. Visvikis, R. V. de Walle, E. Wiers, and C. Morel, "GATE: a simulation toolkit for PET and SPECT," *Physics in Medicine and Biology*, vol. 49, no. 19, p. 4543, 2004.

[183] C. C. Yang, jianhua Yu, J. J. Lee, and B. M. Tsui, "Monte Carlo Simulation of a GE eXplore VISTA System for Quantitative Small Animal PET Imaging," *Nuclear Medicine Communications*, vol. 31, no. 1, pp. 32–38, 2010.

[184] A. D. Guerra and N. Belcari, "State-of-the-art of pet scanners for small animal and breast cancer imaging," *Nuclear Instruments and Methods in Physics Research Section A: Accelerators, Spectrometers, Detectors and Associated Equipment*, vol. 580, no. 2, pp. 910 – 914, 2007.

[185] A. Saoudi, C. M. Pepin, F. Dion, Bentoukia, R. Lecomte, M. Anreaco, M. Casey, R. Nutt, and H. Dautet, "Investigation of Depth-of-Interaction by Pulse Shape Discrimination in Multicrystal Detectors Read Out by Avalanche Phtodiodes," *IEEE Transactions in Nuclear Sciences*, vol. 46, pp. 462–467, 1999.

[186] A. Braem, M. Chamizo, E. Chesi, N. Colonna, F. Cusanno, R. D. Leo, F. Garibaldi, C. Joram, S. Marrone, S. Mathot, E. Nappi, F. Schoenahl, J. Seguinot, P. Weillhammer, and H. Zaidi, "Novel design of a parallax free compton enhanced pet scanner," *Nuclear Instruments and Methods in Physics Research A*, vol. 525, pp. 268–274, 2004.

[187] Y. Yang, Y. Wu, S. S. James, H. De, P. A. Dokhale, K. S. Shah, R. Farrel, and S. S. Cherry, "A Prototype PET Scanner with DOI-encoding Detectors," *J. Nucl. Med.*, vol. 49, no. 7, pp. 1132–1140, jul 2008.

[188] S. S. James, Y. Yang, Y. Wu, R. Farrel, P. Dokhale, K. S. Shah, and S. S. Cherry, "Experimental Characterization and System Simulations of Depth of Interaction PET detectors using 0.5 mm and 0.7 mm LYSO," *Phys. Med. Biol.*, vol. 54, pp. 4605–4619, jun 2009.

[189] M. Soret, S. L. Bacharach, and I. Buvat, "Partial-Volume Effect in PET Tumor Imaging," *J. Nucl. Med.*, vol. 48, no. 6, pp. 933–945, jun 2007.

[190] J. W. Marshall Leach, "Fundamentals of Low-Noise Analog Circuit Design," *Proceedings of the IEEE*, vol. 82, no. 10, pp. 1514–1538, Oct. 1994.

[191] R. Brooks, U. Sank, G. DiChiro, W. Friauf, and S. Leighton, "Design of a High Resulotion Positron Emission Tomograph: The Neuro-PET," *J. Comput. Assist. Tomogr*, vol. 4, pp. 5–13, 1980.

[192] R. Fontaine, F. Bélager, J. Cadorette, J. D. Leroux, J.-P. Martin, J.-B. Michaud, J.-F. Pratte, S. Robert, N. Viscogliosi, and R. Lecomte, "A Data Acquisition Sub-System for Distributed, Digital, Computational, APD-Based, Bimodal PET/CT Architecture for Small Animal Imaging," in *Nuclear Science Symposium Conference Record*, vol. 4. IEEE, Oct. 2004, pp. 1733–1737.

[193] G. Hegyesi, J. Imrek, G. Kalinka, J. Molnár, D. Novák, J. Végh, L. Balkay, M. Emri, S. A. Kis, G. Molnár, L. Trón, I. Valastyán, I. Bagaméry, T. Bükki, S. Rózsa, Z. Szabó, and A. Kerek, "Ethernet Based Distributed Data Acquisition System for a Small Animal PET," *IEEE Transactions on Nuclear Science*, vol. 53, no. 4, pp. 2112–2117, Aug. 2006.

[194] A. Rudge, "Some Notes On The System of Readout of The VIKING Chip," Sep. 1994, private communication.

[195] S. Gregory, "VA2 Interface Board (Hybrid Card)," Oct. 2006, revision V1.3.

[196] O. Toker, "VIKING, a CMOS Low Noise Monolithic 128 Channel Frontend for Si-strip Detector Readout," *Nuclear Instruments & Methods in Physics Research*, vol. A, no. 340, pp. 572–579, 1994.

[197] *TRA-DUCT 2902: Room Temperature Conductive Silver Epoxy Adhesive*, TRA-CON Inc., 45 Wiggins Avenue, Bedford, MA 01730, USA, Oct 2002.

[198] J. S. Iwanczyk and B. E. Patt, *Semiconductors for Room Temperature Nuclear Detector Applications*, 1st ed. Academic Press, 1995, vol. 43, ch. 14, pp. 531–559.

[199] *NIM Model 821, Quad Discriminator*, LeCroy, 700 Chestnut Ridge Road, Chestnut Ridge, NY 10977, Oct 1996.

[200] *VA2, Specifications*, Ideas ASA, Vertiasveien 9, Bosx 315, N-1323 Høvik, Norway.

[201] *MODEL V550, 2 Channel CAEN Readout for Analog Multiplexed Signals (C-RAMS)*, CAEN Technologies, Inc., 1140 Bay Street, Suite 2C, Staten Island, NY 10305, USA, May 1998.

[202] *MODEL V 262, Multipurpose I/O Register*, CAEN Technologies, Inc., 1140 Bay Street, Suite 2C, Staten Island, NY 10305, USA, Jun 1998.

[203] M. Safavi-Naeini, M. Lerch, M. Petasecca, G. Pignatel, M. Reinhard, and A. Rosenfeld, "Evaluation of pixellated, back-sided planar photodetectors for high-resolution imaging instrumentation," *Nuclear Instruments and Methods in Physics Research Section A: Accelerators, Spectrometers, Detectors and Associated Equipment*, vol. 589, no. 2, pp. 259–267, 2008. [Online]. Available: {http://www.sciencedirect.com/science/article/pii/S0168900208002179}

[204] M. Safavi-Naeini, D. Franklin, M. Lerch, M. Petasecca, G. Pignatel, M. Reinhard, G.-F. Betta, N. Zorzi, and A. Rosenfeld, "Evaluation of Silicon Detectors

With Integrated JFET for Biomedical Applications," *Nuclear Science, IEEE Transactions on*, vol. 56, no. 3, pp. 1051–1055, Jun. 2009.

[205] M. Safavi-Naeini, G. Deeley, D. Franklin, M. Lerch, G. P. M. Petasecca, M. Reinhard, and A. Rosenfeld, "TCAD and IBIC charge collection modelling of a novel Silicon detector for use in medical imaging," *Nuclear Instruments and Methods in Physics Research Section A: Accelerators, Spectrometers, Detectors and Associated Equipment*, vol. 624, no. 1, pp. 73–77, Dec 2010.

[206] M. Safavi-Naeini, D. R. Franklin, M. L. F. Lerch, M. Petasecca, G. U. Pignatel, M. Reinhard, R. Siegele, and A. B. Rosenfeld, "IBIC Characterisation of Novel Silicon Detectors for Imaging Applications," in *Nuclear Science Symposium Conference Record (NSS/MIC), 2008 IEEE*, Nov 2008, pp. 63–67.

[207] M. Safavi-Naeini, D. Franklin, M. Petasecca, M. Lerch, R. Kirkham, G. Moorhead, P. Dunn, G. De Geronimo, and A. Rosenfeld, "SiPM based detector module and digital data acquisition system for PET: Initial results," in *Nuclear Science Symposium Conference Record (NSS/MIC), 2009 IEEE*, Nov. 2009, pp. 2679–2682.

[208] M. Safavi-Naeini, D. R. Franklin, M. Lerch, M. Petasecca, G. Moorhead, R. Kirkham, P. Dunn, G. O'Keefe, G. Degeronimo, and A. B. Rosenfeld, "Preclinical Studies Using a Prototype High-Resolution PET System with Depth of Interaction," in *Nuclear Science Symposium Conference Record (NSS/MIC), 2011 IEEE*, Nov 2011.

[209] M. Safavi-Naeini, D. R. Franklin, M. Petasecca, M. L. F. Lerch, R. Kirkham, G. Moorhead, P. Dunn, G. D. Geronimo, and A. B. Rosenfeld, "Prototype High-Resolution PET System with DoI," *Journal of Instrumentation*, 2013 (submitted).

[210] M. Safavi-Naeini, D. R. Franklin, M. Petasecca, M. L. F. Lerch, and A. B. Rosenfeld, "Comparison of Correction Methods for Random Coincidence in CMRPET," *Nuclear Instruments and Methods in Physics Research Section*

A: Accelerators, Spectrometers, Detectors and Associated Equipment, 2013 (submitted).

Appendix A

Software Documentation

This chapter documents the software developed for this project, including configuration files and command-line arguments. An overview of the process of setting up a scan is provided along with example configuration files. Documentation for individual supporting programs is also provided.

A.1 Overview

The process of performing a tomographic scan is managed from a single embedded Linux PC.

A.1.1 Hardware Startup

This subsection describes the procedure for correctly starting the hardware from a complete power-off state.

1. Power up the management PC;
2. Plug in and turn on the gantry;
3. Power up the detector heads;
4. Once the PC has booted (it automatically logs you in), plug in the USB-serial

converter, attach it to the SPI programmer, and start 'minicom'. Ensure local echo is enabled so you can see what you are typing (**ctrl-a e**);

5. Plug the SPI programmer in to the first detector head DAC. Program the desired offset voltage. Normally this is done with the command `A0800`. The red light on the programmer should toggle on or off. There is no harm in sending this command multiple times[1].

6. Repeat for the second detector head;

7. Disconnect the SPI programmer and exit minicom. You may unplug the SPI programmer and USB-serial converter;

8. Power up the HYMOD/SCEPTER board; and

9. You *may* need to re-start the CSIRO SCEPTER control script (`medm`). The CSIRO control scripts start automatically start as part of the automatic login procedure, however they may not function correctly if SCEPTER/HYMOD are powered off at boot-up time. If in doubt, close all CSIRO SCEPTER control windows (or issue `killall mdem` and re-start (you can use the command `start_medm`, or manually execute

   ```
   medm -x -macro prefix=uowblog $HOME/csiro-blogd.adl &
   medm -x $HOME/pm-medm/pm.adl &
   ```

   from the default user's home directory.

A.1.2 Autostarted Functions

This section briefly describes elements which are started during normal host boot procedure.

[1] This procedure is obviously something of a hack. Originally it was intended to program the detector head DAC voltages via a built-in SPI port on HYMOD; however this turned out to be hazardous as it depended on HYMOD/SCEPTER being powered up before the correct DAC voltage is set, which is potentially dangerous to SCEPTER. Therefore, this procedure was developed as a temporary work-around. The permanent solution is to use a DAC with programmable non-volatile memory (or add a simple AVR or similar microcontroller) so that it sets the correct voltage automatically on power-up.

1. Two CSIRO services are started automatically via scripts in `/etc/init.d`:

   (a) `csiro-blogd`, the binary logging daemon, which is a TCP/IP service used to log data to disk. Data is currently stored in `/data1`. This may be configured by editing `/etc/csiro-blogd.conf` and executing `/etc/init.d/csiro-blogd restart`; and

   (b) `csiro-blogioc`, which manages I/O with HYMOD/SCEPTER and can be controlled via a CSIRO-supplied scripted GUI. `csiro-blogioc` is started in a `screen` session as root - if you wish to interact directly with its command interpreter, you can execute `screen -r` as root (or run `sudo screen -r` as a normal user). This can be configured by editing `/etc/csiro-blogioc.conf`, however to restart csiro-blogioc you should kill the service manually and then start it again using the init script.

2. Two CSIRO-provided scripted GUIs are provided - one to manage the blog server, the other to control the settings for SCEPTER. These are `pm.adl` and `csiro-blogd.adl`, and are started automatically from the correct location by running `start_medm`. If necessary, they can be stopped simply by closing all `medm` windows.

To verify that all hardware is functioning as expected, use the `pm.adl` configuration GUI to set up the desired SCEPTER parameters. The 6th entry in the top-level menu launches the SCEPTER control panel. Parameters suitable for a scan of a low-activity point source (such as the small ^{68}Ge (Ga generator) source in the lab) are shown in Table A.1. The only variables which may need to be modified are the read request clock frequency and T_{ds}. T_{ds} is the nominal time for the time-to-amplitude converter to saturate from zero and can be decreased to provide better timing resolution; however SCEPTER seems to have difficulty with $T_{ds} < 1.25$ μs. The read-request clock may need to be increased if a high-activity source is being used, in order to avoid event-rate saturation of SCEPTER.

Table A.1
Configuration parameters for SCEPTER (set via `pm.adl`). T_{ds} is set to the minimum stable value; read request clock frequency is sufficient for a low-activity point source.

Parameter	Appropriate settings for CMRPET
`tdm`	`occurrence`
`tds` (T_{ds}	1.25 μs
`tos`	9.3 μs
`trk`	`disabled`
`trke`	`disabled`
Read request clock	3.0476 MHz
`aux`	`aao`
`lock`	`disabled`
`bla`	0

It is necessary to ensure that the pulse threshold is set to a reasonable value (one volt is normal). The detector should be set to time of occurrence mode (`tdm = occurrence`), and the read request clock and SCEPTER data should be enabled. T_{rk} and T_{rke} should be disabled. Scepter Data should be enabled. `aux` should be set to `aao`, `lock` should be disabled and `bla` should be zero.

Placing a low-activity gamma source near one of the detector heads should result in an increase in activity levels (for example, should be able to register activity rates in the order of 700-2000 counts per second). If this is working, the detector signal processing chain is working and ready for scanning.

A.2 CMRPET Movement Control and Data Logging

This section describes the major functional components responsible for moving and coordinating the scanner and data logging procedure.

A.2.1 `supergantry`

Low-level motor operations are performed by the `supergantry` program, which communications with the motor controller modules via an I2C bus on the management PC's parallel port. Note: this could easily be replaced with a different I2C

Table A.2 `supergantry` command-line options

Command	Description
`--help/-h`	print out this help message
`--version/-v`	print out version string
`--simultaneous/-s`	allow simultaneous motor movement (but no smooth acceleration)
`--port/-p NNNN`	specify TCP port to listen for control connections [5555]
`--device/-d /dev/i2c-N`	specify i2c device node [/dev/i2c-0]
`--movement | -m onephase | twophase (default) | halfstep`	specify stepper motor drive strategy

port, for example a USB-based I2C bus interface, provided that it has Linux support. `supergantry` runs as a real-time Linux process and must therefore be executed as root via `sudo` or installed setuid root (`` `which supergantry` `` simply returns the current path to `supergantry`):

```
sudo chown root.root `which supergantry`
sudo chmod a+s `which supergantry`
```

`supergantry` may be started with a number of command-line options. Executing `supergantry` with the `--help` option will provide the list of current options shown in Table A.2.

`supergantry` defaults to non-simultaneous movement, TCP port 5555, i2c device node `/dev/i2c-0` and `twophase` movement (which gives maximum torque).

Commands are issued to `supergantry` via a TCP connection to the management server on port 5555 by default. This may be performed manually via a telnet client. A summary of the commands which may be performed through this interface are listed in Table A.3. Note that multiple movement commands may be issued through a single command (e.g. `m0 500 m1 1000`).

Table A.3
`supergantry` commands (issued via a TCP connection to the server port, 5555 by default)

Command	Description	Sample Output
`s[N]`	Status (optional: motor N)	`M0 3623 M1 5774 M2 600 M4 1520`
`h[N]`	Home (optional: motor N)	`0` (on completion)
`mN X`	Move motor `N` by `X` steps	`0` (on completion)

During normal scanning procedures, `supergantry` will be commanded to move the motors into different positions by `gantryctl.pl`.

A.2.1.1 Build Dependencies

- `libconfig` (note: on some machines this may be called `libconfig8` or `libconfig9`)
- `libconfig-dev` (as above)

A.2.2 `gantryctl.pl`

This is the toplevel script which moves the motors into position using `supergantry` and logs data to the CSIRO binary logging daemon. `gantryctl.pl` requires one configuration file (normally called `gantryctl.conf`), a gantry plan file (typically called `something.plan`) and an optional stage plan file, if source-holding stage needs to be moved during the scan (e.g. for using a point source in multiple positions in the one scan).

- `gantryctl.conf` is rather complex and is best described by way of a commented example:

```
# Initial position for two gantry rings -
# normally home position (0)

# Starting position for both rings (normally zero)
```

```
initial_rotation_1: 0
initial_rotation_2: 0

# Configured motor speed (obsolete, but we need a
# number here to estimate execution time)
motor_speed: 55.5555555555556

# Don't move beyond this angle (safety issue)
final_angle: 184.0

# Maximum angular distance between detector
# heads (i.e. no collision)
safe_separation_angle: 51

# Do you want the radial motors to move initially?
# If you are doing multiple scans with a constant
# gantry diameter, don't bother.  If you set this to
# TRUE, make sure you power the motors up before
# running the script (and disconnect them when
# prompted during the scan).

do_initial_radial_movement: FALSE

# Geometric configuration parameters: used by
# gantryplan.pl and related tools. Everything is in mm.

maximum_subject_diameter: 80
point_source_location_x: 0
point_source_location_y: 50
minimum_gantry_diameter: 200
detector_head_width: 12

# Either specify this (CURRENTLY DISABLED!):
#source_half_life: 100000000000

# OR this (use this one for now!)
dwell_time: 300

# Only if testing
dry_run: FALSE

# Put an upper limit on scan time, in order to test
# feasability of the scan (currently not used)!
maximum_total_exposure_time: 500000
```

```
# TRUE or FALSE, generally we use this (note: in
# reality this is no longer a 'remote serial port',
# rather it is supergantry listening on a TCP port.
remote_serial: TRUE

# ID of serial port (for USB use ttyUSB0). Ignored
# if above is TRUE
port_name: /dev/ttyS0

# Serial (supergantry) port address and port (if
# remote_serial is TRUE)
serialserver: 127.0.0.1
serial_tcp_port: 5555

# CSIRO binary log server address and port
blogserver: 192.168.2.254
blog_port: 9000

# Post-processing paths, configuration files etc.
# + details for e-mailing of results
emails: mitra.safavi@gmail.com,mitra@uow.edu.au
datadir: /data1/data-2010-03-09/
analysisdir: /home/mitra/results/
analysis_template_dir: /home/mitra/analysis_template
parse_blogfile_conf: parse_blogfile_antiplanar.conf
energy_cal_file: energy_calibration.dat
timing_cal_file: timing_cal_3MHz.dat
sinogram_doi_conf: sinogram_doi.conf
sinogram_nodoi_conf: sinogram_nodoi.conf
```

- The gantry plan file is generated by `gantryplan.pl`, a one-off script which reads `gantryctl.conf` to obtain the geometry of the scanner and the volume to be scanned, and writes a plan describing the different gantry positions through which the gantry rings will be stepped so as to cover all of the field of view covered by the target volume. A sample (partial) plan file is shown below:

```
n_steps: 53
n_steps_B: 14
r_actual: 101.28184344644
initial_radial_steps: 97
0: 0, 20, 0, 2.37101332346399
```

```
1: 0, 21, 0, 2.48956398963719
2: 0, 22, 0, 2.60811465581039
3: 0, 23, 0, 2.72666532198359
4: 0, 24, 0, 2.84521598815679
5: 0, 25, 0, 2.96376665432999
6: 0, 26, 0, 3.08231732050319
7: 0, 27, 0, 3.20086798667639
8: 0, 28, 0, 3.31941865284959
...
373: 26, 55, 3.08231732050319, 6.52028663952599
374: 26, 56, 3.08231732050319, 6.63883730569919
375: 26, 57, 3.08231732050319, 6.75738797187239
376: 26, 58, 3.08231732050319, 6.87593863804558
377: 26, 59, 3.08231732050319, 6.99448930421879
configmd5: d4c19248dfc761823a5f35b9fb44c103
```

The first two lines specify the number of radial steps needed in one full rotation; the second indicates the number of steps for the second ring for every position of the first ring. At present, the first ring is rotated to each new position sequentially. A future optimisation of this step (achieved by modifying `gantryplan.pl` will be to alternate between clockwise and counter-clockwise movement of the second ring to slightly reduce transit time.

The third line indicates the actual radius that will be used during scanning, a little greater than the desired ring radius specified in `gantryctl.conf` due to the finite width of the detector heads (12 mm). Although CMRPET can theoretically utilise overlapping radial sectors, and therefore use any ring radius desired, this would not be possible in a fully populated ring. If desired, this limitation may be removed in the future.

The fourth line indicates the position that the radial motors should be stepped to prior to starting the scan. This should only need to be done once for a series of scans with a given radius - you can disable the initial movement by editing `gantryctl.conf`.

The remaining lines (apart from the MD5 checksum at the end) describe the position combinations. Each line starts with a sequential position index, fol-

lowed by the desired radial sector (starting from zero) for each ring, followed by the actual angle in radians to which this position corresponds.

The last line is an MD5 checksum of the preceding data - it is not currently used.

The final (optional) configuration file for `gantryctl.pl` determines the positions through which the stage will be cycled for each gantry position. This is useful if you wish to conduct a campaign of multiple point source images with a single point source. An example configuration file is shown below:

```
zero_axial: 1520
zero_radial: 4600
direction_axial: +1
direction_radial: -1
0: 0, 30
```

The first two lines indicate the 'zero' position for the axial and radial actuators. These should be the step values which will position the point source in the exact centre of the ring.

The next two lines indicate whether a positive displacement in millimetres corresponds to stepping forward (+) or backward (-).

The remaining lines are simply a sequential position index followed by linear offsets in millimetres for axial and radial actuators.

A.3 CMRPET Scanning Workflow

A.3.1 Configuring the Scanner

Prior to starting a scan, it is necessary to edit the configuration files needed for `gantryplan.pl`. The first and last of these have already been described in Section A.2.2; the second must be generated via the command

```
gantryplan.pl gantryctl.conf gantryplan.plan
```

This will read `gantryctl.conf` and write `gantryplan.plan` (make sure you do not overwrite an existing plan file that you want to keep!).

You should also verify that events are still being detected (via the `medm` GUI script for controlling SCEPTER).

A.3.2 Pre-Scan Tasks

The following procedures are recommended for operating CMRPET.

1. From a terminal, start a `screen` session. Create three windows (issue the command `ctrl-a c` three times; you can switch between windows with the commands `ctrl-a n` and `ctrl-a p`)

2. In the first `screen` window, run `sudo supergantry`. You should see some debug messages indicating that the expected number of motors (typically four) have been detected.

optional In the second window (or in a different terminal session), open a `telnet` session to port 5555 via the command `telnet localhost 5555`. Press `h` to home the gantry. This will take a maximum of about a minute. During this time it is recommended that you monitor the gantry's progress and ensure that no cables are being tangled or pulled or that the detector heads are not going to collide. If this happens, kill `supergantry` immediately. After the gantry is in the home position (you can verify by issuing the `s` command to check the status) you can disconnect the telnet session (`ctrl-]`). This procedure is optional as it will happen automatically when you run `gantryctl.pl`, but it is recommended to do it manually on the first run so you can monitor the process.

CMRPET is now ready for scanning.

A.3.3 Performing and Monitoring a Scan

In the second `screen` window prepared above (remember, you should have closed the telnet session if you used one!), execute `gantryctl.pl` as follows:

```
gantryctl.pl gantryctl.conf
    gantryplan.plan stage_plan.plan
```

The following sequence of events take place:

1. The gantry is moved to the home position;
2. If requested (via `gantryctl.conf`), the radial actuators will be stepped to the initial positions (if you do this, don't forget to disconnect them from the power/i2c bus following this initial movement - there should be no problem with inductive load since the radial actuators are automatically powered down after movement
3. The user is prompted to press ENTER to begin the scan.

At this point, the scanner will sequentially step through each position combination specified in `gantryplan.pl`. If a stage plan has also been specified, then for each gantry position, the stage will step through each of the positions defined in the stage plan file. This sequence will be repeated for each gantry ring position until the scan is completed.

If you want to verify that data is being logged, you should be able to see a new directory (with an incremented run number) in `/data/data-2010-03-09`, and the first segment in this directory growing steadily.

A.3.4 Post-Processing

CMRPET will automatically perform basic post-processing and analysis of data, e-mailing the results to you and storing the coincidence data in a convenient location for later detailed analysis. The following section discusses the steps which are followed; you may perform them manually instead or in addition if desired. However, generally only the coincidence data will be of interest.

A.3.4.1 Input file concatenation

The CSIRO binary logger logs data to `/data1/data-2010-03-09` by default (the last part can be changed via the blog control `medm` script). Each run is stored in its own directory (corresponding to the run number and incremented on each new run). A run consists of multiple segments of up to 50-60 MB; periodically the blog server starts a new segment. At the completion of a run, all of these segments should be concatenated to a single binary log file - the original segments can then be deleted if no longer required.

The following command will perform this step manually:

```
cat 468.? 468.?? 468.??? > 468.bin
```

A.3.5 Extracting time-calibrated coincidence data

```
parse_blogfile parse_blogfile.conf
    energy_calibration.dat blog_filename
    timing_calibration.dat [> timing_histogram.dat]
```

This process reads the concatenated blog file, extracts events and comments (which contain gantry position information), searches for potential coincidence pairs which have occurred in each position, and writes a a series of output files containing only those events.

If the file `timing_calibration.dat` does *not* exist, `parse_blogfile` is being run in *calibration* mode; the calibration `timing_calibration.dat` file will be **created** and a timing histogram for each channel constructed and printed to standard output for later processing. Refer to Section 7.1.7.2 for the details of how to process the raw data from this procedure to generate a proper timing calibration file (note: you cannot use the file without some further processing!).

If the file already exists, `parse_blogfile` will be run in `analysis` mode. A series of output files will be generated, `coincidence0.dat, coincidence1.dat, ...` etc. - one file for each position index in the stage plan file. This allows individual point source measurements to be conveniently separated. These coincidence files are formatted identically to the output from GATE.

A.3.5.1 Inputs

- `parse_blogfile.conf` contains a mapping of pixels to channels and specifies the RR clock frequency `F_rr`. An example is as follows:

```
// Format is (Scepter Channel #, Head #, pixel #
// (pixels numbered 0-15 as per Lucky's mapping))
pixel_map = (
// detector head 0
        (0, 1, 0),
        (1, 1, 1),
        (2, 1, 3),
        (3, 1, 2),
        (4, 1, 4),
        (5, 1, 5),
        (6, 1, 7),
        (7, 1, 6),
        (8, 1, 8),
        (9, 1, 9),
        (10, 1, 11),
        (11, 1, 10),
        (12, 1, 12),
        (13, 1, 13),
        (14, 1, 15),
        (15, 1, 14),
// detector head 1
        (16, 0, 12),
```

```
        (17, 0, 13),
        (18, 0, 15),
        (19, 0, 14),
        (20, 0, 8),
        (21, 0, 9),
        (22, 0, 11),
        (23, 0, 10),
        (24, 0, 4),
        (25, 0, 5),
        (26, 0, 7),
        (27, 0, 6),
        (28, 0, 0),
        (29, 0, 1),
        (30, 0, 3),
        (31, 0, 2)
);

F_rr = 3.0476e6;
```

The last line of this file is VERY IMPORTANT - it specifies the read request clock frequency which you have used for the run (in hertz).

- `energy_calibration.dat` contains a table of calibration points for your energy spectrum, per channel (i.e. 32 lines). It should look like this:

```
0 2900 0 0.511
0 3018 0 0.511
0 3167 0 0.511
0 2797 0 0.511
0 3072 0 0.511
0 3326 0 0.511
0 3495 0 0.511
0 3500 0 0.511
0 2602 0 0.511
0 3383 0 0.511
0 1851 0 0.511
0 2459 0 0.511
0 1553 0 0.511
0 3387 0 0.511
0 3183 0 0.511
0 3454 0 0.511
0 1000 0 0.511
0 3386 0 0.511
```

```
0 3240 0 0.511
0 3313 0 0.511
0 3641 0 0.511
0 1000 0 0.511
0 2895 0 0.511
0 3217 0 0.511
0 3530 0 0.511
0 1915 0 0.511
0 2547 0 0.511
0 3227 0 0.511
0 3683 0 0.511
0 3224 0 0.511
0 3188 0 0.511
0 3216 0 0.511
```

The format is `raw_0, raw_1, real_energy_0, real_energy_1`. Actual energies are specified in MeV.

- `blogfile.bin` is your concatenated blogfile as prepared in A.3.4.1.
- `timing_calibration.dat` contains a table of calibration points for the timing. When this file is used as an *INPUT ONLY* it should have the following format:

```
0 530 1276 2034
1 524 1274 2037
2 524 1274 2046
3 514 1272 2027
4 524 1274 2034
5 515 1273 2004
6 517 1273 1994
7 512 1273 1999
8 524 1274 2040
9 517 1273 1992
10 513 1273 2039
11 505 1272 2038
12 520 1272 2030
13 509 1273 2002
14 507 1273 2044
15 503 1272 1997
16 0 0 0
17 518 1273 1966
18 518 1273 2033
```

```
19 508 1272 2028
20 515 1273 2032
21 0 0 0
22 509 1272 2013
23 504 1272 2013
24 519 1274 2031
25 511 1273 1925
26 509 1273 2032
27 503 1272 1997
28 510 1272 2031
29 503 1272 2005
30 506 1272 2032
31 502 1271 2031
```

The `tacN` fields are the limits of the TAC. For multi-event bursts, if the first event occurs on this channel, then the TAC will be in the range from `tac1` to `tac2`. If it is the second event, it will be in the range `tac2` to `tac3`.

A.3.5.2 Outputs

- `timing_calibration.dat` - raw timing calibration data. Confusingly (it's PhD code, OK?), this is NOT in the same format as when this file is present and usable as an input. So DON'T think you can just run `parse_blogfile` once to generate this data and then apply it immediately! You need to do some more work. This file contains a lot of information that you are probably not interested in;

- Standard Output (redirected to `timing_histogram.dat` in this example) - will have 32 rows, each row being 4096 elements long (TAC values are 12 bits). The histograms can be used to establish timing ranges.

  Processing with Matlab function `process_timing_calibration`, which takes a single argument (the histogram matrix generated above) and returns a 32×4 timing calibration matrix which may be used as the *INPUT* timing calibration file. HOWEVER you need to manually go through and check the values - the estimation process is inherently a little fuzzy and there might be a

few dead channels which can produce garbage results (you can manually clear these by editing the resulting matrix).

- Coincidence output files `coincidenc0.dat, coincidence1.dat, ...` etc. These are formatted exactly as per GATE ASCII coincidence output; please refer to GATE documentation for details [148].

A.3.5.3 Build Dependencies

- `libconfig` (note: on some machines this may be called `libconfig8` or `libconfig9`)
- `libconfig-dev` (as above)

A.3.6 Sinogram/Linogram reconstruction

```
sinogram sinogram.conf coincidences.dat
```

This process traditionally took the coincidence data and constructed a sinogram for later reconstruction via IRT or some other tool. However, as an alternative, a direct linogram implementation was developed using OpenCV, which returns both an image for quick viewing and also a floating-point image in the form of a textual .dat file for manululation in Matlab/Octave. No intensity normalisation is performed at this stage.

A.3.6.1 Inputs

- `sinogram.conf` - contains all key sinogram parameters. The main parameter that you will need to adjust is the number of rsectors and the gantry radius - most of the other parameters remain fixed for a given detector. An example configuration file is as follows:

```
# Resolution of sinogram output

sino_radial = 512;
```

```
sino_angles = 512;

# Resolution of linogram output
lino_nx = 512;
lino_ny = 512;

# Crystals are assumed to be cubic.
# This is the side length in millimetres
crystal_size = 3;

# inner ring radius, mm
ring_radius = 101.281;

# Number of radial sectors
# (should be the same as gantryctl.conf)
n_rsectors = 53;

# Starting from
first_rsector = 0;

# Finishing at
last_rsector = 53;

# Head geometry
crystals_in_axial_dimension = 1;
crystals_in_radial_dimension = 4;
crystals_in_tangential_dimension = 4;

# Single ring for CMRPET
n_rings = 1;
allow_multi_ring_coin = 0;
max_ring_difference = 0;

# Set to 4 to disable DoI and emulate long crystals
upsampling_factor = 1;

# 1 to use crystal id as co-ordinate; 0 to use exact
# location (from simulation only!)
use_coords_or_det_ids = 1;
rebinned_num_layers = 4;

# booleans = 1 for yes, 0 for no
# generally leave these alone!
have_annihilation_pos_info = 0;
have_energy_info = 1;
```

```
have_rotating_gantry = 0;
have_compton_scatter = 0;
compton_scatter_weighting = 0;

# Energy thresholds in MeV
e_lower = 0.3;
e_upper = 0.7;

# 1 if you want an energy histogram output file
do_energy_hist = 1;

# Line width for linogram
d_pixels = 5.0;

# Timing window
t_window = 5e-9;

# Timing offset (set to > 100 ns
# for generating the randoms map)
t_centre = 0.0;

# Optional; filter out events in the wrong order
strict_order = -1;

# How often to update the graphical display
# (every this many events)
update_period = 10000;
```

Refer to Lakshal Perera's PhD thesis for details of the various parameters (this sinogram software has been greatly extended and enhanced since he developed the original version).

- `coincidences.dat` are the coincidences detected by `parse_blogfile`. Most likely you will only process one of these at a time, but it is possible to specify multiple files on one command line if needed.

A.3.6.2 Outputs

Many output files are generated - they are not all of interest to this project, and you cannot directly specify most of the output filenames. However, some are particularly useful/interesting:

- `linogram_float.dat` - the directly-reconstructed image, in the spatial domain. This is an ASCII text file and is ready for direct loading into Matlab/Octave.

- `linogram.png` - a grayscale linogram as a PNG image for quick viewing. As it is limited to 8-bit precision, this has limited analytical value.

- `sino_WxHxDmm_radiallayer_M_axialslice_N_energywindow_MIN-MAX.dat` - this file (or one like it) contains the raw **sinogram** data. To make your life easier (i.e. for importing into Matlab/Octave), make a symbolic link to this file:

  ```
  ln -sf long_file_name.dat sino.dat
  ```

  and then load in Matlab/Octave. This file is what should be used if you intend to reconstruct your image using FBP or MLEM from inside Matlab/Octave. The sinogram resolution may be adjusted by editing parameters `sino_angles` and `sino_radial` in `sinogram.conf`; generally both dimensions should have the same resolution.

- `sino_WxHxDmm_radiallayer_M_energywindow_MIN-MAX.dat` - not to be confused with the previous file, this only contains a textual dump of some information about the run. Probably of limited interest. Do not attempt to load this into Matlab/Octave - this should only be read with a plain-text editor.

- `energy_histogram_WxHxDmm_energywindow_MIN-MAX.dat` - an energy histogram in ASCII text, ready to be loaded into Matlab/Octave.

A.3.6.3 Build Dependencies

- `libconfig8`

- `libconfig8-dev`

- `libcv-dev`

- `libhighgui-dev`

Note that on some systems you may need to link against `libopencv` instead of `libcv`. This can be adjusted in the Makefile.

A.3.7 Image Normalisation

Prior to any image analysis, it is necessary to perform intensity normalisation with flood data (this may be produced from a simulation; ideally it would be generated from experimental flood data). Two normalisation-adjustment algorithms are provided by the same function `geomcorrect` - the first is a linear correction and the second is multiplicative. Generally the multiplicative correction produces superior results.

```
[cimlin, cimmul] =
    geomcorrect (image, flood, factor, xdim, ydim);
```

The element-by-element mathematical operations performed by geomcorrect are as follows:

$$cimlin = image - factor \times flood;$$
$$cimmul = image/(flood^{factor});$$

A.3.7.1 Input parameters

- `image` is the uncorrected image (resulting from running `sinogram` on experimental data;
- `flood` is an (uncorrected) image resulting from sinogram reconstruction of a uniform phantom occupying the entire field of view. This may be generated via a GATE simulation with exactly the same gantry geometry as your experimental configuration (as it is essentially an analytic result). However, GATE

has an annoying tendency to crash before sufficient data is collected to produce a smooth image. Therefore, a (lumpy) simulation can be randomly rotated and accumulated several times (possibly low-pass filtered) to smooth out irregularities in the resulting image. Both `image` and `flood` must have the same dimension.

- `factor` is an optional scaling factor (it defaults to 1). Its interpetation depends on the correction algorithm; simple linear scaling or multiplicative scaling.

- `xdim, ydim` are the (optional) width and height of the output image. This essentially means that a region of `xdim` × `ydim`, whose centre coincides with the geometric centre of `image` and `flood`, will be adjusted to generate the output. Output images will correspond to these coordinate ranges. If not specified, the entire image is processed.

A.3.7.2 Outputs

- `cimlin` - the linearly-corrected image; generally inferior to the multiplicative approach (but try adjusting the `factor` parameter to optimse)

- `cimmul` - the multiplicatively corrected image; generally produces a better result (again, try adjusting `factor`).

A.3.7.3 Build Dependencies

None per se.

A.3.8 Measuring Point Source FWHM

```
[fh, fv, mh, mv] =
    measure_2Dfwhm (im, W, H, xrange, yrange)
```

Give an image containing a point source (or multiple point sources), `measure_2Dfwhm` will attempt to fit a Gaussian to the point, and return the FWHM in the horizontal

and vertical dimension as well as the centroid of the Gaussian which has been fitted to the point source.

A.3.8.1 Inputs

- `im` is the image containing one or more point sources;
- `W, H` are the full image dimensions in arbitrary units (e.g. millimetres)
- `xrange, yrange` are tuples (pairs of values) corresponding to the x and y limits that will be searched for a Gaussian peak.

A.3.8.2 Outputs

- `fh, fv` are the resulting FWHMs (in the same units as `W, H`)
- `mh, mv` are the coordinates of the centroid of the peak (again, in the same units as `W, H`)

A.3.8.3 Dependencies

- `est_gaussian.m` - support function which calculates the centroid, standard deviation and FWHM of a one-dimensional Gaussian pulse which optimally fits supplied x vs y data.

Appendix B

Hardware Documentation

This appendix briefly documents the schematics which were produced for this project.

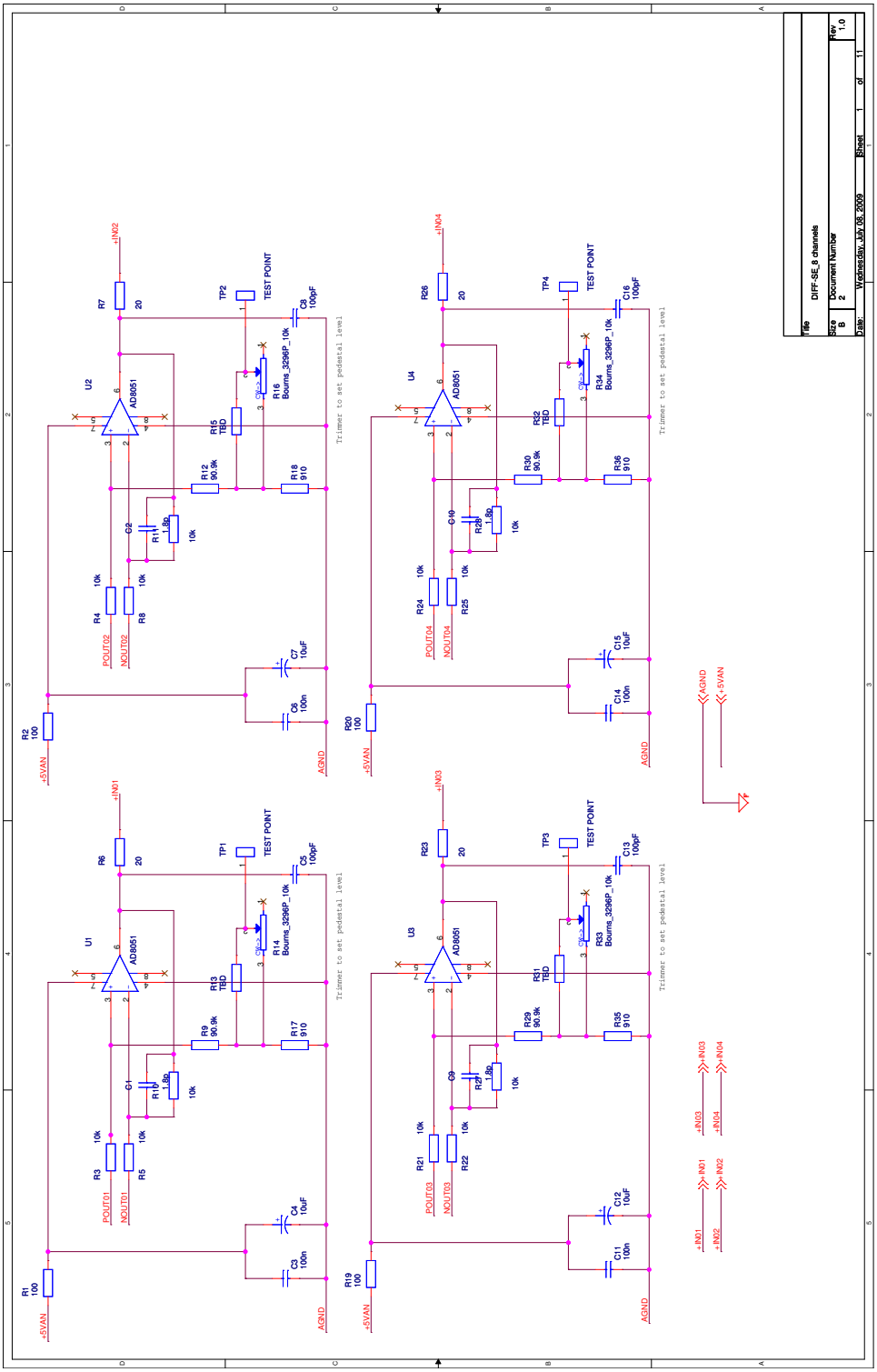

Figure B.1 CMRPET interface board (final design) between SENSL preamplifier and SCEPTER

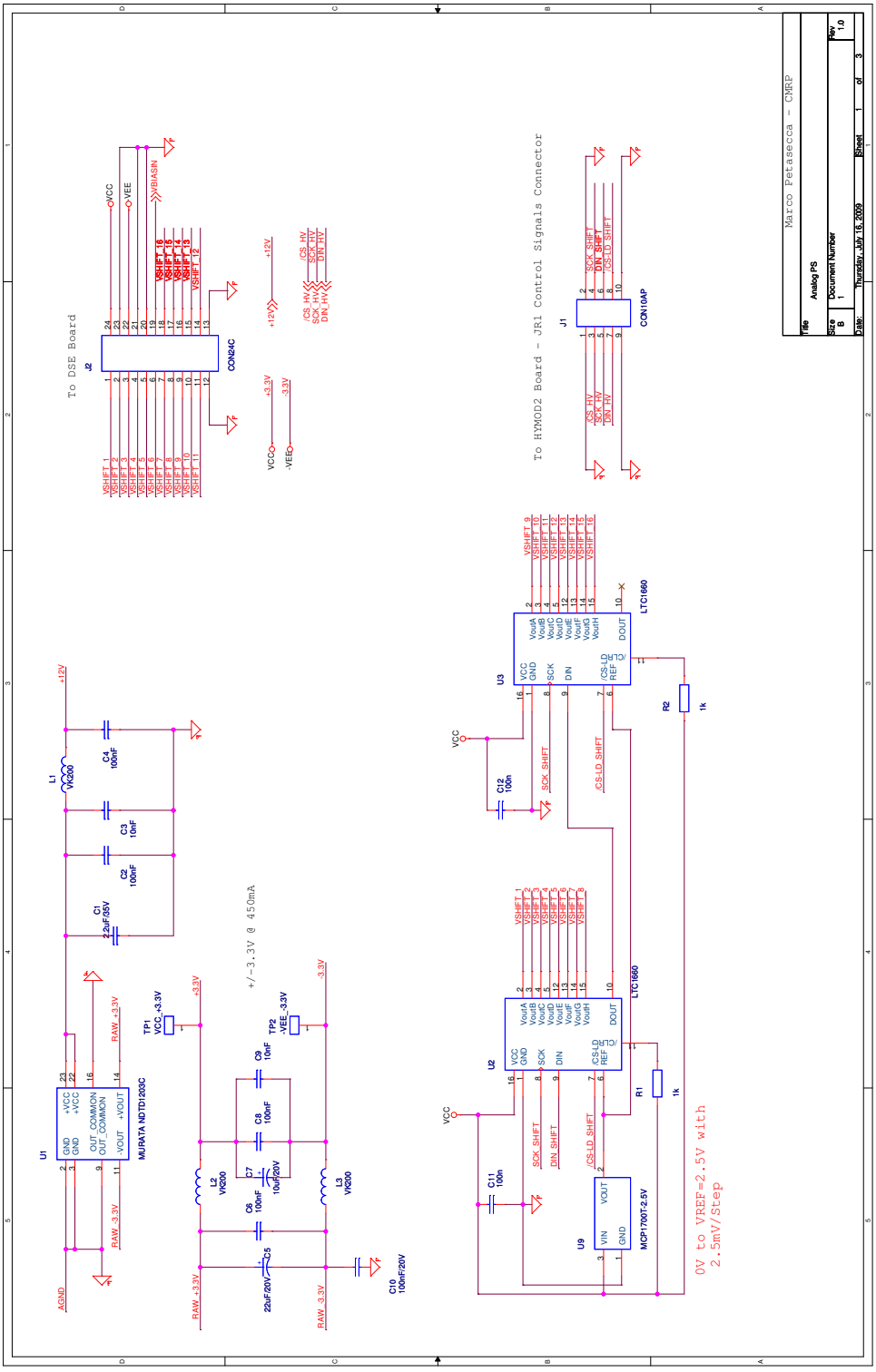

Figure B.2 SiPM power supply board